Research in Computational Methods for Structural Acoustics

Final Report

Department of the Navy Reference:	N00014-92-J-1774
ONR Program Manager	Dr. Luise Couchman
Funding Dates	05/01/92 to 03/31/96
Date of Report:	July 6, 1996

Principal Investigator: Peter M. Pinsky
Department of Civil Engineering
Stanford University
Stanford, CA 94305-4020
tel: (415) 723-9327
e-mail: pinsky@cive.stanford.edu
fax: (415) 723-7514

Co-Principal Investigator: Thomas J.R. Hughes
Department of Mechanical Engineering
Stanford University

Research Assistants: Karl Grosh
Isaac Harari
Manish Malhotra
James R. Stewart
Lonny L. Thompson

DEPARTMENT OF THE NAVY
OFFICE OF NAVAL RESEARCH
SEATTLE REGIONAL OFFICE
1107 NE 45TH STREET, SUITE 350
SEATTLE WA 98105-4631

IN REPLY REFER TO:

4330
ONR 247
11 Jul 97

From: Director, Office of Naval Research, Seattle Regional Office, 1107 NE 45th St., Suite 350, Seattle, WA 98105
To: Defense Technical Center, Attn: P. Mawby, 8725 John J. Kingman Rd., Suite 0944, Ft. Belvoir, VA 22060-6218

Subj: RETURNED GRANTEE/CONTRACTOR TECHNICAL REPORTS

1. This confirms our conversations of 27 Feb 97 and 11 Jul 97. Enclosed are a number of technical reports which were returned to our agency for lack of clear distribution availability statement. This confirms that all reports are unclassified and are "APPROVED FOR PUBLIC RELEASE" with no restrictions.

2. Please contact me if you require additional information. My e-mail is *silverr@onr.navy.mil* and my phone is (206) 625-3196.

ROBERT J. SILVERMAN

Contents

Chapter 1

Introduction

The study of structural acoustics and fluid-structure interaction involves the solution of problems of acoustic radiation and scattering, elastic and structural wave propagation, and their interaction. Only relatively few, simple cases can be solved analytically and when the wavelength is of the same order as characteristic length scales asymptotic methods usually cannot be employed. Thus, most configurations of practical interest must be solved by standard computational tools such as boundary element, finite difference and finite element methods. Exterior problems of wave propagation pose a unique challenge to computation since the unbounded region is inappropriate for direct implementation of computational techniques. The derivation of mathematically sound continuous formulations that provide suitable bases for the computation of solutions to exterior problems of acoustics is not a trivial task. The performance of numerical methods that are then based on such a formulation, in terms of accuracy and convergence, as well as computational cost-effectiveness, also requires careful consideration. This work reviews recent developments in numerical methods that address these issues.

Acoustic problems, in addition to being of interest in their own right, can also be considered as scalar models for elastic and structural waves. The time-harmonic case is governed by the Helmholtz equation (or the reduced wave equation), with solutions describing propagating and evanescent waves in acoustic fluids. In the evanescent mode, time-harmonic acoustics are described by equations similar to many singular diffusion problems. The solutions to these problems may contain sharp boundary layers, as in heat conduction with temperature-dependent strong sources due to chemical reactions, diffusion problems in semiconductors and elastic materials on elastic supports. There is also general interest in the Helmholtz equation in an abstract setting because of stability problems that are associated with its operator, namely, there is potential loss of ellipticity with increasing wave number in the propagation region, and a diminishing capability to characterize derivatives of the solution with increasing decay rate (stability in the H^1 sense).

Numerical solutions to the reduced wave equation in exterior domains have been sought primarily via techniques that are based on Helmholtz integral representations of the problem, relating quantities on the *physical boundary* of the problem. Such formulations are obtained by using fundamental solutions as weighting functions and

employing Green's theorem, a procedure that typically is restricted to linear, isotropic and homogeneous problems. These equations lead to direct [20] and indirect boundary element methods [101] (see also the survey in [137]), with the benefit of *a priori* satisfaction of the radiation condition at infinity, and the advantage of seeking solutions over a domain that is of one dimension lower than the original form of the problem. On the other hand, methods of this kind are known to encounter difficulties, such as potential non-uniqueness of the solution of the *continuous* boundary integral equations at characteristic wave numbers of corresponding, but physically unrelated, interior problems. This is *not* a property of *exact* solutions of the boundary-value problem (see [139, p. 297], [153, pp. 55–60], and references therein), and will lead to ill-conditioned discrete equations if left uncorrected. Countering this drawback requires considerable ingenuity since the distribution of critical values becomes progressively more dense for higher wave numbers and elongated geometries. In Chapter 3, results pertaining to the uniqueness of boundary integral representations are reviewed in detail. Although these results are well known, the manner by which they arise does not appear to be fully appreciated. The resulting restriction of the application of these methods in their original form to problems with wave numbers below a critical limit has been recognized practically since their inception ([22], [104, pp. 128–136], and [105, pp. 498–500]), and over the years numerous remedies have been attempted.

Foremost among these are the following three approaches: The CHIEF method, due to Schenck [130], in which the integral formulation is modified by adding equations to enforce solutions to vanish at points in the interior, thereby differentiating fictitious solutions from the desired one; the advantage of solving the resulting overdetermined system of equations without significant addition in cost or complexity is counteracted by the lack of rigorous criteria for selecting interior points and determining the limit of stability. The interior points must be sufficient in number and judiciously located on one hand, yet too many points can degrade the conditioning of the linear equations. The Burton-Miller approach [19] of combining the integral equation with its normal derivative theoretically precludes non-unique solutions; while conventional formulations lead to excessive computational cost of equation formation (the impact of computations performed in [6] is examined in Chapter 7), recent work [107] indicates that this difficulty may be overcome, although some implementational issues (such as the need for C^1 interpolation) remain unresolved. The third approach is to replace the fundamental solution in the boundary integral equation with a modified Green function, [95] and [102]; however, this scheme is not simple to implement and a correlation between the number of terms employed in the kernel and the modes of fictitious solutions that are suppressed is not generally accepted.

Despite ongoing efforts, a satisfactory resolution is apparently yet to be recognized by the computational acoustics community, as evidenced by the profusion of recent and current literature dealing with these topics, e.g., [26, 54, 100, 133]. Burton-Miller formulations, when properly employed, appear to offer the most promising basis for boundary-based computation in that non-unique solutions are rigorously excluded. Traditional implementations of this procedure suffer from the shortcoming of attempting to numerically integrate hyper-singular kernels, thereby exacerbating an existing difficulty of boundary element methods in integrating weakly singular kernels

(which come about by the use of fundamental solutions. and are analytically integrable but often cause numerical difficulties. in particular when higher-order interpolation functions are employed). These issues are circumvented in [107] by transforming the Burton-Miller formulation into one in which no hyper-singular kernels remain, greatly enhancing the appeal of this approach. An alternative is to employ a weak form of the Burton-Miller approach which allows consistent use of C^0 approximation while potentially remaining theoretically sound yet computationally competitive [97].

In this work we take a different course and review developments in finite element methods for the Helmholtz equation in unbounded domains. Having reached a high degree of mathematical and algorithmic sophistication, finite element methods, which are based on variational formulations, have become the numerical technique of choice for numerous classes of boundary-value problems, and are emerging as strong challengers to entrenched traditional approximate solution methods in many others. Finite element methods are not restricted to homogeneous, isotropic, linear problems, which is often the case for boundary elements. When applicable, boundary elements do have an ostensible advantage. For example, in three dimensions they require only surface discretization as compared to volumetric in the case of finite elements, thereby reducing the number of equations to be solved. However, the resulting systems of equations are nonsymmetric and dense, as opposed to symmetric and banded in finite elements. The computational advantage in processing time and storage requirements that would be expected intuitively is therefore not always realized in the ranges of problem size to which direct and iterative solution strategies are each applicable, rendering the two methods economically competitive for large-scale computation (as demonstrated in Chapter 7). Nevertheless the task of discretization is substantially simpler for boundary element methods, an important consideration in model preparation. In contrast to boundary element methods which are often based on collocation and hence may be difficult to analyze, finite elements have a rich mathematical background which can be used to prove convergence of numerical solutions to the exact solution with mesh refinement (in Chapter 6), and at times aid in method design (see Chapter 5). Finally, there is no theoretical limitation on the applicability of finite element methods to high wave numbers in exterior problems, as one encounters in boundary integral equations in their original form. The Galerkin finite element method is capable of modeling increasingly higher wave numbers by refining the mesh. However, this may become prohibitively expensive, and we will explore in depth herein methods of achieving this goal by less costly means.

In the field of structural acoustics, the use of finite element methods in modeling elastic solids is on the rise, coupled with (and on occasion supplanting) boundary element methods to model the acoustic fluid, e.g., [8, 29, 117]. Two fundamental impediments to the direct application of finite element methods to modeling acoustic fluids are the unbounded domain and the stability issues discussed above. The utilization of exponential shape functions in so-called infinite elements was suggested as a means to circumvent the difficulty associated with the exterior domain [17], see Chapter 3. Other approaches convert the boundary-value problem to formulations that are defined over bounded regions by introducing an artificial external boundary with appropriate boundary conditions. Proper representation of the radiation

condition then becomes the crucial issue. One approximation to the radiation condition was obtained by employing an asymptotic expansion of the far-field solution to generate a sequence of local boundary operators [15]. In a recent implementation of this scheme, finite elements were used to model the transient response of an acoustic fluid in an exterior domain coupled to a viscoelastic structure [123]. Numerous other schemes have been proposed, many of which are surveyed in the exhaustive reviews [1, pp. 95–116] and [40]. Once a boundary-value problem is formulated in a bounded region, finite element methods may be employed for computation, taking advantage of the wide range of applicability and rich mathematical structure inherent in these techniques.

In this work, a computational formulation is derived by the DtN method proposed by Givoli and Keller [41] for converting boundary-value problems defined over large or unbounded domains to formulations that are suitable for domain-based computation. This procedure formulates a boundary-value problem in a bounded region by imposing a relation between the function and its normal derivative on an artificial boundary. The goal is for the solution of the DtN formulation to be the restriction of the exact (and unique) solution of the original problem to this bounded domain. The investigation in Chapter 3, which rigorously shows that the DtN method achieves this goal by devising an *exact* and non-reflective boundary condition that is imposed on the exterior of the computational domain, was prompted by experience with the difficulties related to non-uniqueness of boundary integral representations. Simple criteria guaranteeing the uniqueness of solutions in practical implementation are also presented in Chapter 3 and local approximations of DtN boundary conditions are characterized. (A modified DtN boundary condition has been developed to circumvent these criteria yet lead to well-posed problems [53].) This study indicates that DtN formulations provide a suitable basis for domain-based computation of solutions to exterior problems. Employing DtN boundary conditions enables the development of finite element methods that converge with mesh refinement for *fixed* computational domains. Other details on the DtN procedure and its application to problems of time-harmonic acoustics in exterior domains are presented in Chapter 3.

The degradation of stability that arises in the type of problems discussed herein, and the resulting numerical pathologies, are addressed by employing a general technique that was developed precisely to counteract such difficulties and specializing it to this application. This methodology, in which the process of designing finite elements is based on understanding the underlying mathematical framework, has given rise to a profusion of new classes of methods, e.g., [27, 34, 35, 36, 71, 72, 76, 77, 87]. In such cases, additional quantities are introduced into the formulation in order to demonstrate convergence of numerical solutions to the exact solution. By endowing the method in this manner with a sound mathematical foundation its performance on general configurations is guaranteed, and stability properties are enhanced while maintaining higher-order accuracy.

Such ideas were developed by Hughes and Brooks for problems of convective transport [72], and originally referred to as 'streamline-upwind/Petrov-Galerkin' (SUPG, also called 'streamline-diffusion' and 'anisotropic balancing diffusion'). These methods were later extended to advective-diffusive systems [78, 93], applied to Stokes [75],

and compressible and incompressible flows, e.g., [79, 87, 94], and have since undergone extensive refinement and mathematical analysis (for a review see [70], and Johnson [88, pp. 181–188, 199–204 and 259–268], and references therein).

In a more recent development, the concept of 'Galerkin/least-squares' has arisen as a generalization of these ideas. This methodology is obtained by appending terms in *least-squares form* to the standard Galerkin formulation. The added terms contain *residuals of the Euler-Lagrange equations* of the boundary-value problem usually evaluated over element interiors, thereby preserving the *consistency* inherent in the Galerkin method (an important ingredient in obtaining improved convergence rates with higher-order interpolation) as well as respecting regularity requirements on the functions employed. The notion of Galerkin/least-squares crystallized in [76] and in the application of ideas of this sort to abstract mixed problems by Franca and Hughes (see [36] and references therein) and their colleagues, and was the key to recognizing these techniques as part of a general framework.

In fluid mechanics, Galerkin/least-squares methods are identical to SUPG for hyperbolic cases, but the analysis in the presence of diffusion is simpler [76]. For mixed problems, critical stability conditions governing well-posedness are violated in the Galerkin framework by many practically convenient interpolations. Under the Galerkin/least-squares umbrella, general combinations of interpolations (including equal-order ones) become convergent, either by *circumventing* the stability conditions in the case of Stokes [73], compressible and incompressible elasticity [37], Reissner-Mindlin plate [74] and contact problems [12] (in which the constraints are on the boundaries), or by *satisfying* these conditions in the application of variational principles (such as Hellinger-Reissner formulations) to compressible and incompressible elasticity [33], and structural models (see [36] and references therein). In a similar application, mixed variational principles of linear elasticity with independent rotation fields are modified to engender displacement-type formulations that converge for all combinations of interpolations [71]. These formulations lead to membrane elements with drilling (in-plane rotational) degrees of freedom in the two-dimensional case, which may be employed to facilitate the analysis of shells. Galerkin/least-squares methods have also been implemented as a crucial stabilizing ingredient in space-time finite element methods both for first-order [76] and [93] and second-order hyperbolic equations [77]. Parameters that are employed in many of these methods were characterized in [61].

An initial investigation employing Galerkin/least-squares technology to relax wave-resolution requirements for problems of time-harmonic acoustics is presented in Chapter 5. This work is later generalized in Chapter 6 exploiting the mathematical structure inherent in finite elements to design and analyze the methods proposed. The demonstrated success of Galerkin/least-squares methodology in generating mixed finite element formulations that are mathematically rigorous, simple to implement and computationally efficient is particularly promising in considering problems of structural acoustics and fluid-structure interaction, in which the coupling terms are similar in nature to those found in abstract mixed problems.

Other alternatives to the basic Galerkin formulation may be constructed without upsetting consistency. Douglas and Wang modified the Galerkin/least-squares

method for Stokes flow presented in [73] by altering the *weighting* of the additional terms [27]. This nonsymmetric formulation, which is stable under more lenient conditions than its Galerkin/least-squares counterpart, was later extended to advection-diffusion problems [35]. A modification to the treatment of the jump terms in [73] is presented in [138]. Franca and Dutra do Carmo introduced a method they called 'Galerkin/gradient least-squares' in which the least-squares terms contain residuals of the *gradient* of the governing differential equation [34]. This method is intended for modeling complex boundary layer phenomena, such as arise in the analysis of thin structures, and thus far was successfully applied to scalar singular diffusion problems (also related to evanescent time-harmonic acoustics). In Chapter 5 the performance of Galerkin/gradient least-squares methods on problems of time-harmonic acoustics is evaluated and found to be comparable to Galerkin/least-squares in the entire range of decay and in a portion of the range of propagation.

In Chapter 2 boundary-value problems of structural acoustics in exterior domains are introduced. Problems that are suitable for domain-based computation, obtained via the DtN method, are characterized in Chapter 3 and properties of resulting continuous and discrete formulations are reviewed. Galerkin, Galerkin/least-squares and Galerkin/gradient least-squares finite element methods are presented in Chapter 4.

In Chapter 5 we consider simplified inhomogeneous radiation problems—radiation loading of acoustic media by prescribed boundary conditions as induced by the vibration of a structure (thereby emphasizing boundary conditions of the Neumann type), with particular reference to exterior domains. We work in one dimension for simplicity, but never embark on a course that would preclude multi-dimensional generalizations. Model problems are employed to examine the numerical formulations and design the Galerkin/least-squares operator. We concentrate on Galerkin/least-squares methods, but also examine the application of Galerkin/gradient least-squares operators to this class of problems. In recent years, there has been a resurgence of interest in the use of hierarchical p-version finite elements and spectral elements to obtain high-resolution numerical solutions for structural acoustics. Results from a complex wavenumber dispersion analysis provide a guide for the design of p- and hp-version adaptive schemes, high-order preconditioners for iterative solution methods and the selection of optimal Galerkin/least-squares mesh parameters for elements using high-order basis functions.

The initial work presented in Chapter 5 is then extended to more general settings. The effect of nodal spacing and the performance of the methods proposed in multidimensional configurations are investigated in Chapter 6, and the general convergence of solutions obtained by Galerkin/least-squares finite element methods is presented, with error bounds obtained for the case of unresolved waves, guaranteeing the performance of these methods on configurations of practical interest. The performance of the methods proposed is validated by numerical examples.

Cost-effectiveness of numerical schemes is a primary concern in method design, since it determines both the economics of computation and the limit of problem-solving capabilities on existing computer technology. The demand for large-scale problem-solving capabilities is growing with increasing interest in the numerical modeling of realistic configurations, driving the development of sophisticated algorithms

that are amenable to efficient implementation on modern vector and parallel platforms. In Chapter 7 computational attributes of boundary element and finite element methods are examined. Direct solution techniques are reviewed, and the cost of employing such techniques to solve the equations arising from boundary element and finite element analyses of a wide range of geometric configurations is evaluated and compared. This study is repeated for iterative solvers, employing the GMRES procedure as a representative technique. The two solution strategies are then compared, and the cost of equation formation is examined. This work clearly demonstrates that finite element methods are economically competitive with boundary element methods for obtaining solutions to problems of time-harmonic acoustics.

Finite element methods are capable of modeling problems of structural acoustics at arbitrarily high wavenumbers providing that an appropriate level of mesh refinement is employed. However, direct solution techniques become prohibitively expensive for the level of mesh refinement necessary at high wavenumbers. Iterative solution strategies are an attractive alternative in these situations. Efficient methods for the solution of large-scale matrix problems that arise from finite element methods for structural acoustics are presented in Chapter 8. Results from a number of numerical tests on both sequential and parallel computers are presented to highlight the superior performance of methods considered.

The Galerkin/least-squares method for the Helmholtz equation provides accuracy and stability with lower resolution than the Galerkin method. A second mechanism for enhancing accuracy is *adaptivity*, which is the subject of Chapter 9. An a posteriori error estimator and adaptive strategy are derived specifically for the Helmholtz equation and the role of adaptivity in reducing the cost of computation is addressed.

Galerkin/generalized least-squares methods are developed and applied to model the steady-state response of *in vacuo* and fluid-loaded Timoshenko beams in Chapter 10. The goal of the new methods is to decrease the computational burden required to achieve a desired accuracy level at a particular frequency thereby enabling larger scale, higher frequency computations for a given platform. Methods for the *in vacuo* response of beams are first presented. Numerical and analytic results for the method are then presented and compared to standard approaches. Methods for the coupled problem are presented next followed by results.

Chapter 11 presents the design of new space-time finite element formulations for the solution of transient structural acoustics problems in exterior domains. The formulation is based on a time-discontinuous Galerkin/least-squares variational equation for both the structure and the acoustic fluid together with their interaction. The result is an algorithm for time-dependent wave propagation with the desired combination of good stability and high accuracy. New time-dependent non-reflecting boundary conditions for the acoustic wave equation are developed based on the exact impedance relation of the Dirichlet-to-Neumann (DtN) map in the frequency domain. Time-dependent counterparts are obtained through an inverse Fourier transform procedure. Optimal stability estimates and convergence rates are reported together with a discussion of the positive form of the resulting space-time matrix equations. Representative numerical examples involving transient radiation achieved by the new method for structural acoustics.

have presented.

Chapter 2

Boundary Value Problems for Time-harmonic Structural Acoustics

First, the boundary value problem for the coupled system is given. The acoustic domain of the original problem is infinite. Using the DtN boundary condition, an equivalent problem on a finite domain is obtained which is amenable to computation. The weak form of the problem is given next.

2.1 Strong Form of the Exterior Problem

Consider an elastic body immersed in an infinite acoustic medium. The elastic body occupies the domain $\Omega_s \subset \mathbb{R}^d$, where $d = 2$ or 3 is the number of spatial dimensions (Fig. 2.1). If the dynamics of the elastic body are to be approximated by a reduced shell or plate theory, as will be the case in this paper, then the elastic domain is parameterized by a surface if $d = 3$ or a curve if $d = 2$. The interior surface of the structure is denoted by Γ^-. The domain interior to Ω_s is assumed to be evacuated; therefore only mechanical forces act on Γ^-. The surface exterior to Ω_s is denoted by Γ. This surface (or curve) is the fluid-structure interface (sometimes called the wet surface) where the acoustic pressure loads the structure. The unit normal outward from the structure (inward toward the fluid) on Γ is $\hat{\mathbf{n}} \in \mathbb{R}^d$. The infinite domain exterior to the surface Γ is denoted by $\mathcal{R} \subset \mathbb{R}^d$. In Fig. 2.1, a finite fluid domain, defined by the region $\Omega_f \subset \mathcal{R}$ is pictured. Ω_f occupies the region between the surfaces Γ and $\partial\mathcal{B}_R$, where $\partial\mathcal{B}_R$ is the truncation boundary of the fluid.

The boundary Γ is assumed to admit the nonoverlapping partition

$$\Gamma = \overline{\Gamma_g^f \cup \Gamma_h^f} \quad . \tag{2.1}$$

The boundary of the structural domain admits the partitions

$$\partial\Omega_s = \overline{\Gamma_{g_i}^s \cup \Gamma_{h_i}^s} \quad , \tag{2.2}$$

where $i = 1, \ldots, n_{dof}$ with n_{dof} being the number degrees of freedom of the structural model.

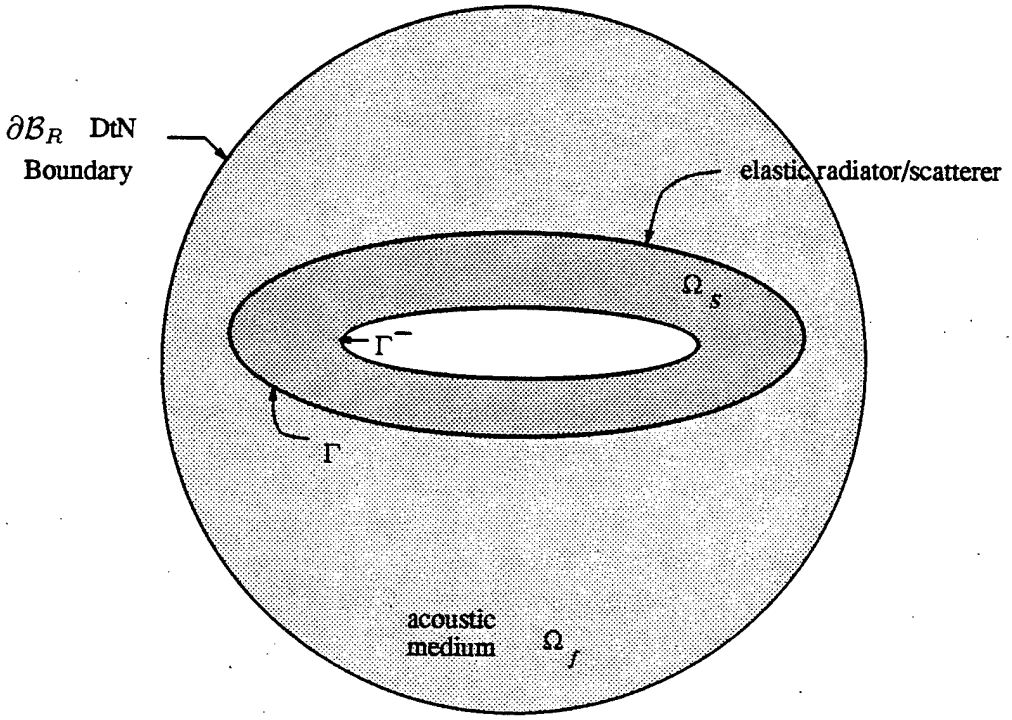

Figure 2.1: Geometry for elastic structure in acoustic medium.

All variables are assumed to undergo time harmonic vibrations of the form $e^{-i\omega t}$ where $i = \sqrt{-1}$ and ω is the angular frequency. With the geometrical definitions in hand we move to the formal statement of the strong form and the definitions involved therein.

The strong form of the exterior structural acoustics problem is: find the displacement vector $\mathbf{u} : \overline{\Omega}_s \mapsto \mathbb{C}^{n_{dof}}$ and the acoustic pressure $p : \overline{\mathcal{R}} \mapsto \mathbb{C}$ satisfying: the governing differential equations:

$$\mathcal{L}_f p = f \quad \text{in } \Omega_f \text{ and } \mathcal{R} \ , \tag{2.3}$$

$$\mathcal{L}_s \mathbf{u} = \mathbf{q} - \hat{\mathbf{n}}^s p|_\Gamma \quad \text{in } \Omega_s \ , \tag{2.4}$$

essential and natural boundary conditions:

$$p = g \quad \text{on } \Gamma_g^f \ , \tag{2.5}$$

$$p_{,n} = h \quad \text{on } \Gamma_h^f \ , \tag{2.6}$$

$$u_i = g_i \quad \text{on } \Gamma_{g_i}^s \quad i = 1, \ldots, n_{dof} \ , \tag{2.7}$$

$$\mathcal{B}_i \mathbf{u} = h_i \quad \text{on } \Gamma_{h_i}^s \quad i = 1, \ldots, n_{dof} \ , \tag{2.8}$$

plus a consistency condition relating Γ_h^f and $\Gamma_{g_{normal}}^s$, see below;
continuity of normal displacement at the fluid-solid interface:

$$\hat{\mathbf{n}} \cdot \nabla p = \rho_0 \omega^2 \hat{\mathbf{n}}^s \cdot \mathbf{u} \quad \text{on } \Gamma \ ; \tag{2.9}$$

and radiation conditions expressed either as:

$$\lim_{r \to \infty} r^{(d-1)/2}(p_{,r} - ik_0 p) = 0 \tag{2.10}$$

or through the Dirichlet-to-Neumann map as:

$$p_{,n} = -Mp \quad \text{on } \partial\mathcal{B}_R \ . \tag{2.11}$$

The pressure, p, satisfies the Helmholtz equation, (2.3), where $\mathcal{L}_f := -\nabla^2 - k_0^2$, ∇^2 is the Laplacian, the acoustic wave number is defined as $k_0 = \omega/c_0$ where c_0 is the speed of sound in the fluid medium, ρ_0 is the density of the fluid, and $f : \Omega_f \mapsto \mathbb{C}$, the acoustic sources are restricted to Ω_f.

The structural matrix differential operator, $\mathcal{L}_s$, is left as generic; symbolically it represents the governing differential equations of the structure which interface the fluid on Γ and all attached substructures. The structural response may be modeled using the equations of linear elasticity; this case is presented in the thesis of Abboud [1]. The applied mechanical forces are given by $\mathbf{q} : \Omega_s \mapsto \mathbb{C}^{n_{dof}}$. As the displacement vector may contain rotational and translational degrees of freedom, we define $\hat{\mathbf{n}}^s \in \mathbb{R}^{n_{dof}}$, the unit vector which when dotted with the displacement vector yields the normal displacement. The effect of the acoustic pressure acting in the normal direction on Γ is denoted by $\hat{\mathbf{n}}^s p|_\Gamma$.

The given functions which define the boundary conditions are $g : \Gamma_g^f \mapsto \mathbb{C}$, $h : \Gamma_h^f \mapsto \mathbb{C}$, $g_i : \Gamma_{g_i}^s \mapsto \mathbb{C}$ and $h_i : \Gamma_{h_i}^s \mapsto \mathbb{C}$. The normal derivative is defined as $p_{,n} := \nabla p \cdot \mathbf{n}$ where $\mathbf{n}$ is the unit outward pointing normal from the domain Ω_f, ∇ is the gradient operator and the inferior comma denotes differentiation. On the fluid-structure interface, there is a consistency condition relating natural boundary conditions on the pressure (on Γ_h^f) to essential boundary conditions on the normal structural displacement (define as $\Gamma_{g_{normal}}^s$). For the remainder of this paper, we enforce natural boundary conditions on the pressure through the essential boundary

conditions on the normal component of the displacement. The components of $\mathbf{u}$ are u_i. $\mathcal{B}_i$ is vector differential operator which operates on the displacement to yield the natural boundary condition. However, the exact form of the natural boundary conditions in (2.8) cannot be explicitly written down until we fix the governing differential equations for the structure (this is just a consequence of the abstract and formal nature of the presentation given in this chapter; these terms will be explicitly defined when applied to a problem).

The radiation condition, (2.10) , (see e.g., [96]) is stated in terms a radial variable, r, where r is the distance from the origin of a spherical or polar coordinate system. This condition requires that the scattered pressure is outgoing at infinity. Application of this form of the radiation condition, however, is not suitable for domain based calculations. Therefore, an artificial boundary, $\partial\mathcal{B}_R$, is introduced. The artificial boundary is obtained by holding constant the radial variable of a Helmholtz separable [114] coordinate system (e.g., the radius for a spherical system). On this special class of boundaries, one may write the exact impedance boundary condition, (2.11), imposition of which results in an problem equivalent to the original one posed on the infinite domain, $\mathcal{R}$. The integral operator which relates the Dirichlet pressure data to the Neumann normal derivative data on the separable surface is the Dirichlet-to-Neumann (or DtN) map, is M. The use of the DtN map to truncate finite element calculations for exterior acoustics was probably first described by Feng [30], but the methodology was crystallized in the work of Givoli and Keller [41, 98]. The application of the DtN for exterior acoustics problems is discussed in detail [56, 41, 98]. The DtN formulation is valid only for acoustic sources $f \in \Omega_f$.
Remark:

1. The above formulation assumes that p is purely outgoing. The inclusion of plane wave excitation of the structure and fluid is straightforward. First one sets $p = p^{scat} + p^{inc}$ where p^{scat} is the unknown scattered pressure and p^{inc} is the known incident plane wave field. By using the fact that p^{inc} satisfies the homogeneous Helmholtz equation, a formulation for p^{scat} and $\mathbf{u}$ which now includes inhomogeneous terms due to the incident pressure is obtained.

2.2 Weak Form of the Exterior Problem

The weak form of the exterior structural acoustics problem is given next. Denote the space of square integrable functions on Ω as $L^2(\Omega)$ and the Sobolev space $H^m(\Omega)$ as the space of functions with all derivatives up to the mth derivative in $L^2(\Omega)$.

First we define the variational spaces necessary for the structural variables. Let the space of solution vectors for the displacement be denoted by $\mathcal{S}_\mathbf{u}$ where $\mathcal{S}_\mathbf{u} = \{\mathbf{u}|\mathbf{u} : \Omega_s \mapsto \mathbb{C}^{n_{dof}}, u_i \in H^{m_i}(\Omega_s), u_i = g_i \text{ on } \Gamma_{g_i} \text{ where } i = 1, \ldots, n_{dof}\}$. The theory used to describe the structural response determines the value of m_i for the ith component of $\mathbf{u}$. The space of weighting functions, $\mathcal{V}_\mathbf{u}$, to which $\overline{\mathbf{u}}$ belongs, differs from $\mathcal{S}_\mathbf{u}$ only in that the components of $\overline{\mathbf{u}}$, defined by $\overline{u}_i$, satisfy homogeneous essential boundary conditions on Γ_{g_i}. Let the solution space for the acoustic pressure be denoted by $\mathcal{S}_p$ where $\mathcal{S}_p = \{p|p : \Omega_f \mapsto \mathbb{C}, p \in H^1(\Omega_f), p = g \text{ on } \Gamma_g\}$. The space of weighting

functions for the pressure, $\mathcal{V}_p$, is the same as $\mathcal{S}_p$ except that homogeneous boundary conditions are indicated for the functions in $\mathcal{V}_p$ on Γ_g.

The weak form of the problem is: Given $\mathbf{q}$, f, g, h, g_i and h_i for $i = 1, \ldots, n_{dof}$ find $\mathbf{u} \in \mathcal{S}_\mathbf{u}$ and $p \in \mathcal{S}_p$ such that for all $\overline{\mathbf{u}} \in \mathcal{V}_\mathbf{u}$ and $\overline{p} \in \mathcal{V}_p$

$$a^f(\overline{p}, p) + (\overline{p}\hat{\mathbf{n}}^s, \rho_0\omega^2\mathbf{u})_\Gamma + (\overline{p}, \mathrm{M}p)_{\partial\mathcal{B}_R} = \mathrm{L}^f(\overline{p}) \quad , \tag{2.12}$$

$$a^s(\overline{\mathbf{u}}, \mathbf{u}) + (\overline{\mathbf{u}}, \hat{\mathbf{n}}^s p)_\Gamma = \mathrm{L}^s(\overline{\mathbf{u}}) \quad , \tag{2.13}$$

where

$$a^f(\overline{p}, p) := (\nabla\overline{p}, \nabla p)_{\Omega_f} - k_0^2(\overline{p}, p)_{\Omega_f} \quad , \tag{2.14}$$

$$L^f(\overline{p}) := (\overline{p}, f)_{\Omega_f} \quad , \tag{2.15}$$

$$L^s(\overline{\mathbf{u}}) := (\overline{\mathbf{u}}, \mathbf{q})_{\Omega_s} + \sum_{i=1}^{n_{dof}} (\overline{u}_i, h_i)_{\Gamma_{h_i}} \quad , \tag{2.16}$$

and

$$(\overline{\mathbf{u}}, \mathbf{q})_\Omega = \int_\Omega \overline{\mathbf{u}}^H \mathbf{q} d\Omega \quad , \tag{2.17}$$

the superscript ^{H} indicates the Hermitian of the vector. The structural operator, $a^s(\cdot, \cdot)$ represents an integral of the the potential and kinetic energy densities for the structure which cannot be explicitly defined until governing equations for the structure are given. Note that all of the operators are sesquilinear (i.e., conjugate linear in the first slot and linear in the second).

Chapter 3

Analysis of Formulations Underlying Computation

In the following, we analyze formulations for domain-based acoustic computation that are derived by the DtN method for exterior problems. The acoustic field variable in the Helmholtz equation is denoted ϕ, representing the acoustic pressure of velocity potential. The analytical results are derived in [58] and the numerical studies are presented in [63]. The DtN method was developed by Givoli and Keller [41] for converting boundary-value problems defined over large or unbounded domains to formulations that are suitable for numerical analysis. The DtN method typically employs artificial boundaries of relatively simple geometric shape, allowing the problem in the exterior of the artificial boundary to be solved analytically. A relation between the function and its normal derivative is thus obtained, and imposed on the artificial boundary as an *exact* boundary condition to the computational formulation. Experience with the difficulties related to non-uniqueness of boundary integral representations demonstrates the importance of investigating the *continuous* formulations underlying computation.

The DtN formulation is shown to possess non-reflective boundary conditions and to give rise to exact (and, by implication, unique) solutions. Truncating the DtN operator, which is often expressed in terms of an infinite series, may cause loss of uniqueness at characteristic wave numbers of higher harmonics. Simple expressions are derived to determine a sufficient number of terms in the operator for unique solutions at any given wave number. Numerical studies confirm these results. A local counterpart of the DtN map is shown to be unique for all wave numbers.

3.1 Properties of the DtN Formulation

We wish to compare solutions of the DtN problem in the computational domain Ω_f with boundary condition (2.11) to the solution of the exterior problem with the radiation condition (2.10).

Theorem *The DtN boundary-value problem has a unique solution for all wave numbers. Furthermore, this solution is the restriction of the solution to the original problem in the unbounded domain to the computational domain.*

Proof *See [58].*

Being a differentiation operator, the DtN map is an unbounded linear operator, and in addition

$$M \neq 0 \tag{3.1}$$

for all finite values of kR.

To verify these properties we examine the operator more closely. In two dimensions, the DtN map is given by

$$Mp = \sum_{n=0}^{\infty}{}'\alpha_n \int_0^{2\pi} \cos n(\theta-\theta')\, p(R,\theta')\, d\theta' \tag{3.2}$$

where the prime on the sum indicates that the first term is halved. The coefficients are

$$\alpha_n := -\frac{k}{\pi}\frac{H_n^{(1)\prime}(kR)}{H_n^{(1)}(kR)} \tag{3.3}$$

where $H_n^{(1)}$ are Hankel functions of the first kind and the prime on functions denotes differentiation with respect to the argument. (A general reference for properties of cylindrical and spherical eigenfunctions of the Helmholtz equation is [114, Chapter 11]) Hankel functions of the first kind correspond to outgoing cylindrical waves and are defined as

$$H_n^{(1)}(r) := J_n(r) + iY_n(r) \tag{3.4}$$

in terms of the linearly independent Bessel functions J_n and Weber functions Y_n. Thus

$$\begin{aligned} -\frac{\pi}{k}\alpha_n &= \frac{J_n'(kR)+iY_n'(kR)}{J_n(kR)+iY_n(kR)} \\ &= \frac{J_n'(kR)J_n(kR)+Y_n'(kR)\,Y_n(kR)}{J_n^2(kR)+Y_n^2(kR)} \\ &\quad +i\,\frac{(Y_n'(kR)J_n(kR)-J_n'(kR)\,Y_n(kR))}{J_n^2(kR)+Y_n^2(kR)} \end{aligned} \tag{3.5}$$

By Abel's identity for the Wronskian of an ordinary differential equation, since J_n and Y_n are linearly independent solutions to Bessel's equation

$$Y_n'J_n - J_n'Y_n = c\exp\left(-\int\frac{dr}{r}\right) \tag{3.6}$$

with the constant $c \neq 0$. Evaluating the right-hand side for this case yields

$$Y_n'(kR)J_n(kR) - J_n'(kR)Y_n(kR) = \frac{2}{\pi kR} > 0 \tag{3.7}$$

indicating that there is no finite value of kR for which J_n and Y_n are simultaneously zero. In particular,

$$\left|H_n^{(1)}(kR)\right|^2 = J_n^2(kR)+Y_n^2(kR) > 0 \tag{3.8}$$

for all $kR > 0$, and hence $Im\,\alpha_n < 0$ and is bounded. The coefficients α_n are bounded for all finite n and $kR > 0$, with asymptotic approximations of the magnitudes

$$|\alpha_n| \sim \frac{n}{\pi R}, \qquad 2n+1 \gg kR \tag{3.9}$$

Analogs of the above properties for the three-dimensional case are presented in [58].

Thus, M is not the zero operator. These properties corroborate the statement made in [98] that *there are no restrictions on permissible values of R for exterior problems*. Another consequence is that the DtN map is one-to-one, and thus has an inverse (Neumann-to-Dirichlet) operator, a linear *bounded* (and hence continuous) operator with a norm of $\min|\alpha_n|$. We use the fact that $Im\,\alpha_n \neq 0$ in subsequent sections.

3.2 The Truncated DtN Map

The DtN map is represented by an infinite series. (See, e.g, (3.2) for the two-dimensional case.) In practice the map is approximated by truncating the series. We wish to examine the effect of this truncation on uniqueness of the solution of the computational problem. Let M^N denote the DtN map truncated after N terms.

3.2.1 Conditions for uniqueness

In contrast to the full DtN map, the truncated map is a bounded linear operator with a norm of, e.g., in two dimensions, $\max\limits_{n<N}|\alpha_n|$, where,

$$\max_{n<N}|\alpha_n| = |\alpha_{N-1}| \sim \frac{N-1}{\pi R}, \qquad 2N-1 \gg kR \tag{3.10}$$

cf. (3.9).

Let v be the difference between two solutions to the DtN boundary-value problem with the DtN map in (2.11) replaced by M^N. This function satisfies the homogeneous problem. The complex conjugate of v satisfies this boundary-value problem with the DtN map replaced by $\bar{M}^N$.

$$\begin{aligned} 0 &= \int_{\Omega_f} (\bar{v}\,\mathcal{L}_f v - v\,\mathcal{L}_f \bar{v})\, d\Omega \\ &= \int_{\partial\mathcal{B}_R} \left(\bar{v}\frac{\partial v}{\partial n} - v\frac{\partial \bar{v}}{\partial n}\right) d\Gamma \\ &= -\int_{\partial\mathcal{B}_R} \left(\bar{v}\,M^N v - v\,\bar{M}^N \bar{v}\right) d\Gamma \\ &= -2i \int_{\partial\mathcal{B}_R} Im\left\{\bar{v}\,M^N v\right\} d\Gamma \end{aligned} \tag{3.11}$$

Uniqueness hinges on the effectiveness of the truncated DtN formulation of the free-space problem, i.e., in precluding modes of the Laplacian in the entire ball $\mathcal{B}_R$. Boundary conditions on the wet surface Γ have no effect on this statement.

To interpret the statement of zero energy flux through the artificial boundary in the context of the truncated DtN map we consider examples in two dimensions. (Similar results for the three-dimensional case are in terms of spherical harmonics [58].) The first is the one-term approximation

$$M^1 v(R,\theta) \quad = \quad \frac{\alpha_0}{2} \int_0^{2\pi} v(R,\theta')\, d\theta' \tag{3.12}$$

For this case

$$\begin{aligned} 0 \quad &= \quad \int_0^{2\pi} Im\left\{\bar{v} M^1 v\right\}\, d\theta \\ &= \quad \frac{Im\,\alpha_0}{2} \left| \int_0^{2\pi} v(R,\theta)\, d\theta \right|^2 \end{aligned} \tag{3.13}$$

and since $Im\,\alpha_0 \neq 0$

$$\int_0^{2\pi} v(R,\theta)\, d\theta \quad = \quad 0 \tag{3.14}$$

i.e., the one-term approximation admits all eigenfunctions of the Laplacian in the entire circle of radius R with a *Neumann* boundary condition on the artificial boundary, except for the first mode. (A general reference for characterization of solutions of eigenvalue problems of differential equations is [23, Chapter VI].)

Similarly, the two-term approximation

$$M^2 v(R,\theta) \quad = \quad M^1 v(R,\theta) + \alpha_1 \int_0^{2\pi} \cos(\theta - \theta')\, v(R,\theta')\, d\theta' \tag{3.15}$$

imposes (3.14) and since $Im\,\alpha_1 \neq 0$

$$\int_0^{2\pi} v(R,\theta) \cos\theta\, d\theta \quad = \quad 0 \tag{3.16}$$

$$\int_0^{2\pi} v(R,\theta) \sin\theta\, d\theta \quad = \quad 0 \tag{3.17}$$

suppressing the first two modes of the Laplacian in the entire circle with a Neumann boundary condition on the artificial boundary, but admitting all others. Approximations with more terms follow along the same lines, yielding

$$\sum_{n=0}^{N-1}{}' Im\,\alpha_n \left(\left| \int_0^{2\pi} v(R,\theta)\, \cos n\theta\, d\theta \right|^2 + \left| \int_0^{2\pi} v(R,\theta)\, \sin n\theta\, d\theta \right|^2 \right) \quad = \quad 0 \tag{3.18}$$

(Recall that $Im\,\alpha_n \neq 0$.) It is clear from this expression that the full map enforces uniqueness.

In general, the N-term approximation suppresses the first N modes of the Laplacian in the entire ball $\mathcal{B}_R$ with a Neumann boundary condition on the artificial boundary, but admits all others. Thus the critical wave number for the truncated DtN formulation of the two-dimensional free-space problem is the lowest one that satisfies

$$J'_N(kR) = 0 \tag{3.19}$$

Boundary conditions on the wet surface Γ have played no role in the analysis up to this point. Accounting for these boundary conditions modifies the value of critical wave numbers (but not the fact of their existence). Equation (3.19) provides an estimate of the critical wave number, but a lower bound is needed. As a rule Dirichlet boundary conditions are the most restrictive constraints, and Neumann boundary conditions are the least restrictive. By considering eigenvalue problems as problems of minimization, it is clear that adding constraints will not reduce the characteristic value, and removing constraints will not raise it. Thus, a lower bound for the problem with a Neumann boundary condition on the physical boundary will bound the characteristic wave numbers for all boundary conditions.

We consider the annular region bounded internally by the circle of radius A (which circumscribes Γ) and externally by $\mathcal{B}_R$. Consider the homogeneous boundary-value problem in this domain with a N-term DtN boundary condition. The critical wave number for this problem will bound from below the critical wave number in Ω_f.

In two-dimensions, before imposing the internal boundary conditions, solutions have the form

$$v(r,\theta) = \sum_{n=N}^{\infty} \left(H_n^{(2)\prime}(kR) H_n^{(1)}(kr) - H_n^{(1)\prime}(kR) H_n^{(2)}(kr) \right) (a_n \cos n\theta + b_n \sin n\theta) \tag{3.20}$$

The presence of Hankel functions of the second kind, $H_n^{(2)} := \bar{H}_n^{(1)}$, which correspond to incoming waves, indicates that higher modes are partially *reflected* from the artificial boundary. Imposing the Neumann boundary condition on the circle of radius A, the critical wave number for the N-term DtN map is the lowest one that satisfies

$$Y'_N(kR) J'_N(kA) - J'_N(kR) Y'_N(kA) \quad = \quad 0 \tag{3.21}$$

All two-dimensional problems in Ω_f with an N-term DtN map are unique at least up to the lowest wave number that satisfies (3.21). Figure 3.1 shows the dependence of the geometrically nondimensionalized critical wave number on the domain for truncated DtN maps with up to four terms. This figure clearly demonstrates that *the critical wave number may be increased by reducing the size of the computational domain.* For comparison, the critical wave number for the Surface Helmholtz Equation in two dimensions is bounded from below by $kA = 2.4$. In Fig. 3.2 the critical wave number is nondimensionalized by the radius of the artificial boundary, to show that selecting

$$N \quad \geq \quad kR \tag{3.22}$$

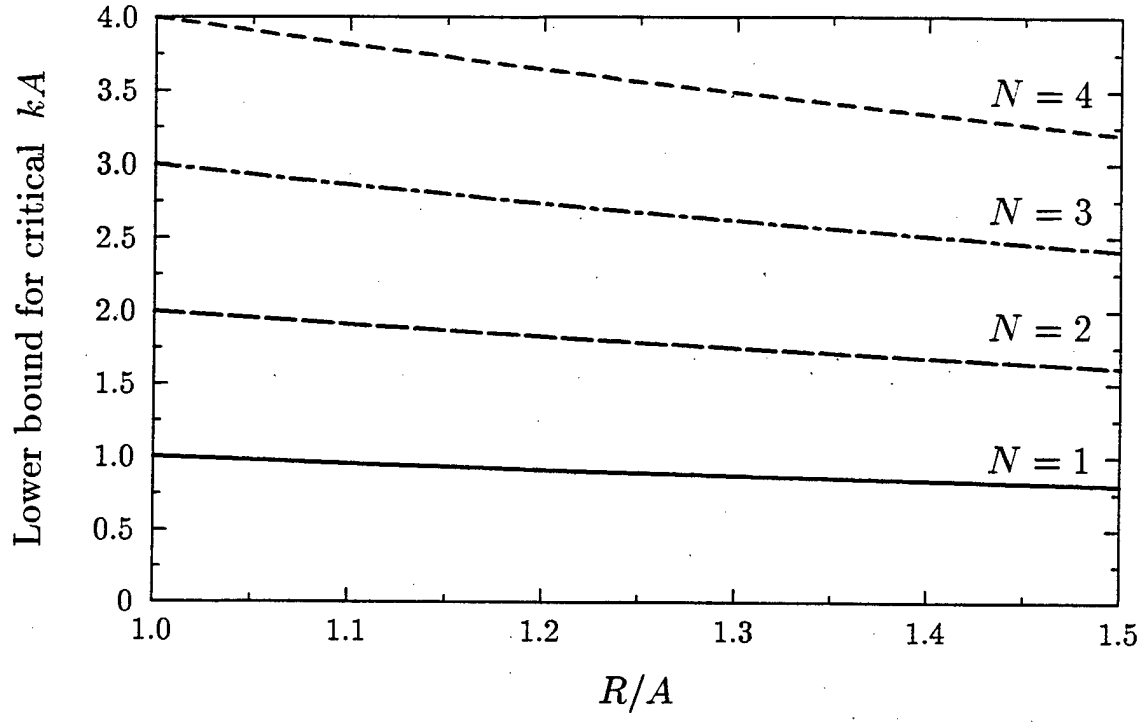

Figure 3.1: Lower bounds for critical kA of truncated DtN map in two dimensions.

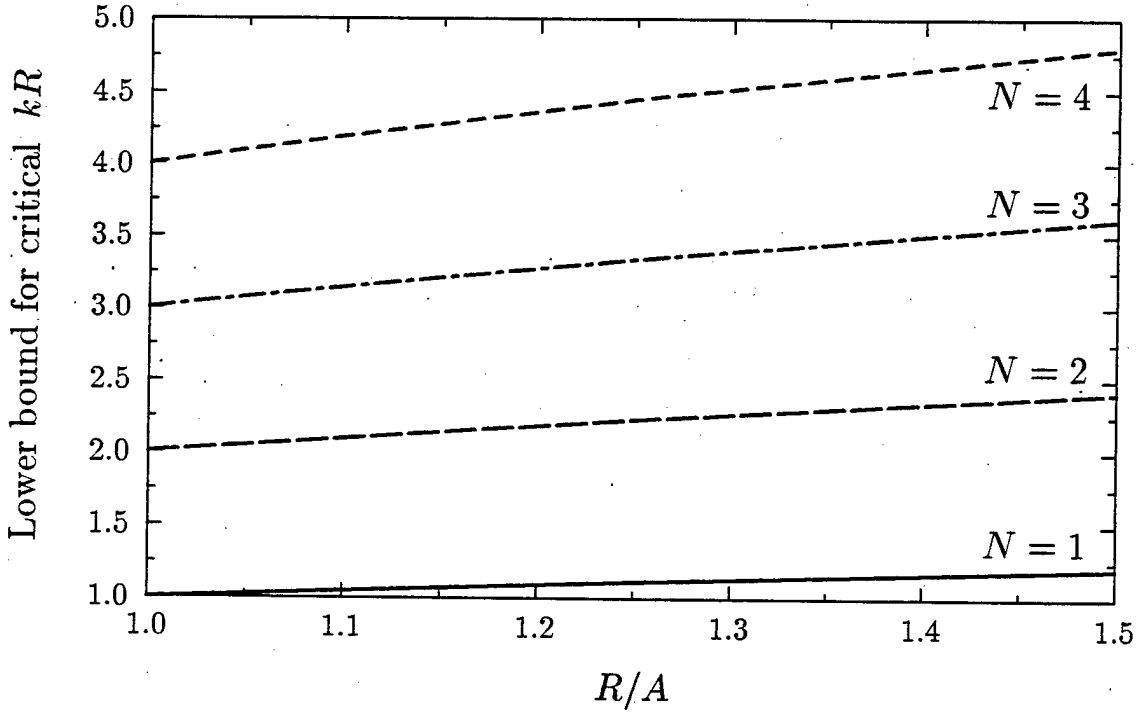

Figure 3.2: Lower bounds for critical kR of truncated DtN map in two dimensions.

guarantees uniqueness of solutions to the two-dimensional problem. (Bound (3.22) is valid for three dimensions as well [58].)

In summary, *the solution to the computational problem with the DtN map truncated after N terms is unique up to the lowest harmonic of mode $N+1$.*

Remarks.

1. The truncated boundary condition is exact for functions that consist of only the first N modes.

2. Bounds of the type (3.22) provide an important guideline to discretization, namely that from the point of view of uniqueness a smaller computational domain is more economical.

3. Grote and Keller have recently proposed a simple modification of the DtN boundary conditions leading to unique solutions at any wavenumber for any number of terms in the operator [53].

3.2.2 Numerical studies

We wish to numerically verify the validity of (3.22). A number of terms in the truncated DtN map that is insufficient for uniqueness of solutions of the continuous boundary-value problem in the computational domain will lead to ill-conditioned discrete equations. Thus the conditioning of the matrix equations is a reliable numerical measure of the uniqueness of the formulation. Since the coefficients of the equations are complex (due to the DtN contribution), the (2-norm) condition number is the square root of the ratio of the largest to smallest eigenvalues of the coefficient matrix premultiplied by its Hermitian.

Remark: The performance of iterative techniques for solving linear algebraic systems of equations is particularly sensitive to the conditioning of the coefficient matrices. In practical implementation, preconditioning and scaling are employed to improve conditioning and thereby accelerate the convergence of the approximate solution.

The numerical evaluations were all performed on two-dimensional configurations of problems representing infinite cylinders of radius a. Dirichlet boundary conditions are imposed on the cylinder surface, which is the internal boundary of the domain. DtN boundary conditions are imposed on the artificial boundary at radius R. The domain is discretized by linear quadrilateral elements, with 32 elements in a circumferential layer. The number of element layers is selected so that the element sides are roughly equal in length. For an example see Fig. 3.3.

The first series of computations, Fig. 3.4, examines the dependence of the condition number on $N/(kR)$ for various values of R. All other parameters are kept constant ($k = 3.14$, $kh = 3.14/3$ and $ka = 3.14$). At a given R the condition number has a constant, relatively high value for a small number of terms in the DtN map. As the number of terms is increased there is a sudden drop in the condition number to a second constant, relatively low value. The drop occurs at $N \approx 0.75\,kR$, which is the numerical indication of the minimum number of terms in the DtN map to assure

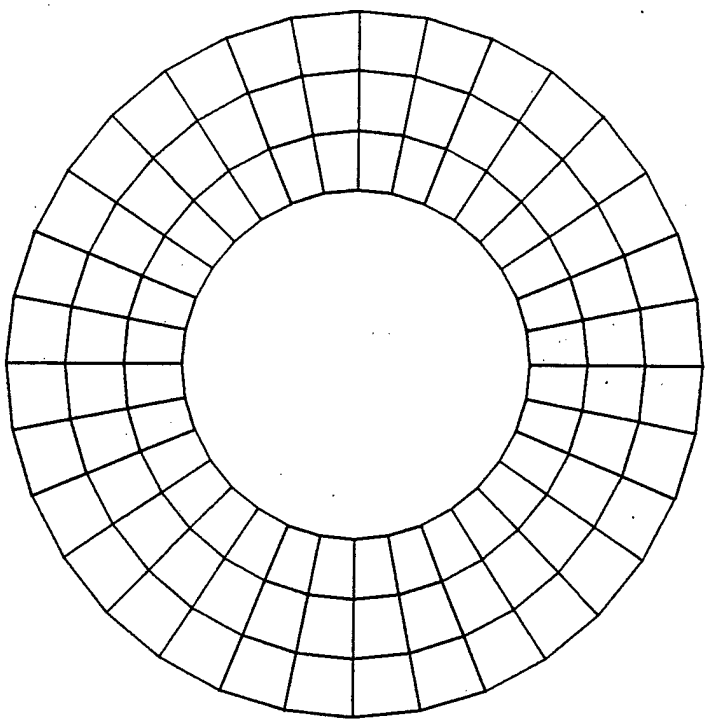

Figure 3.3: The computational domain exterior to a cylinder of radius a, with an artificial boundary at $R = 2\,a$, discretized by 3×32 linear quadrilateral elements.

uniqueness of solutions for these cases. For these configurations the bound (3.22) is somewhat conservative.

In the second series of tests we investigate the effect of large values of ka on the conditioning. According to analytical results uniqueness of solutions depends only on $N/(kR)$ and accuracy of finite element methods on kh. However, computational experience with boundary element methods indicates that difficulties may occur with increasing values of ka. These runs were performed with varying values of a, with $k = 3.14$, $kh = 3.14/3$ and $R = a + 1$. Figure 3.5 shows that the dependence of the condition number on $N/(kR)$ maintains the same trends as the previous case, in which ka was constant (Fig. 3.4). The minimum number of terms in the DtN map to assure uniqueness again occurs at $N \approx 0.75\,kR$. The values of the condition number in the region of uniqueness do not appear to depend heavily on ka. This holds for a very large range. Values up to $ka \approx 60$ were examined (see Fig. 3.6 which shows only the range of unique solutions for better resolution).

The effect of the numerically nondimensionalized wave number kh is examined next. The values of $kh/\pi = 0.50$, 0.33 and 0.25 correspond to four, six and eight elements/wave, respectively. All other parameters are kept constant ($k = 3.14$, $ka = 3.14$ and $R = 3\,a$). Again the dependence of the condition number on $N/(kR)$ maintains the same trends as in the previous cases, see Fig. 3.7. The drop in condition number occurs at $N \approx 0.85\,kR$. Overall, these computations confirm that the bound (3.22) is reliable and should be employed in practice.

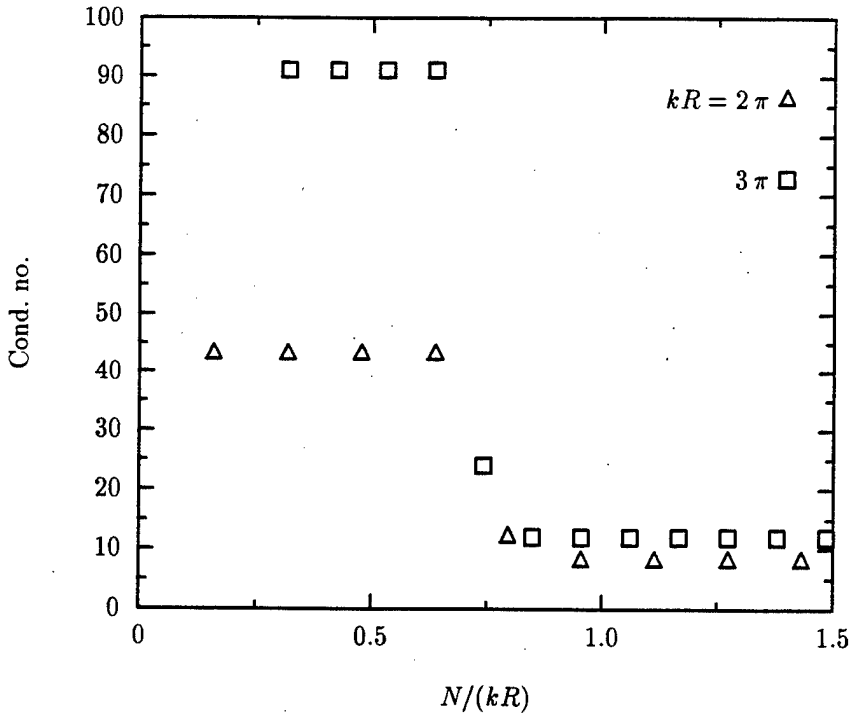

Figure 3.4: The condition number for various values of R keeping other parameters constant ($k = 3.14$, $kh = 3.14/3$ and $ka = 3.14$).

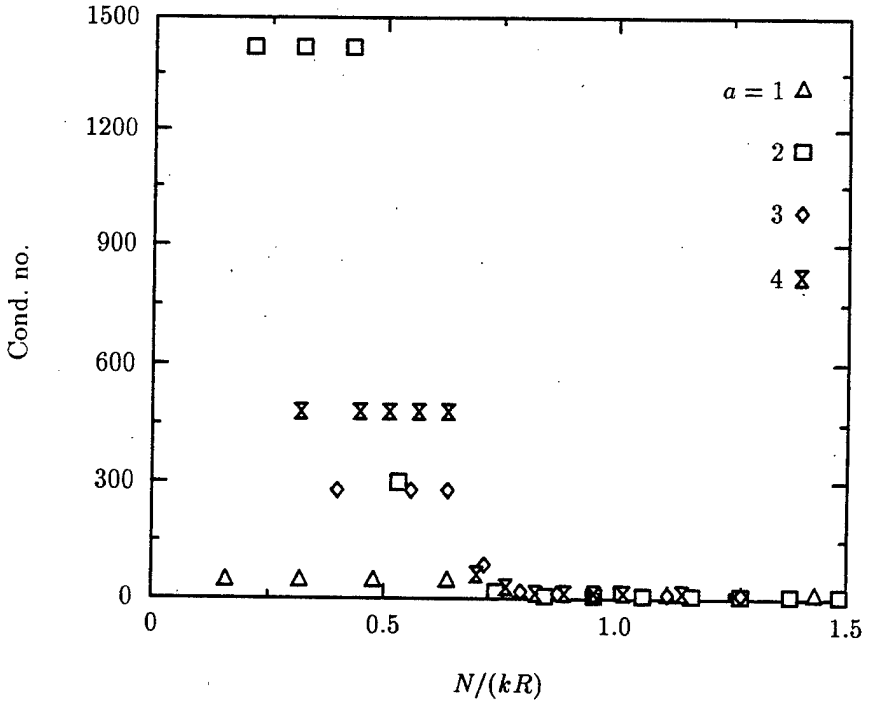

Figure 3.5: The condition number for various values of ka with $k = 3.14$, $kh = 3.14/3$ and $R = a + 1$.

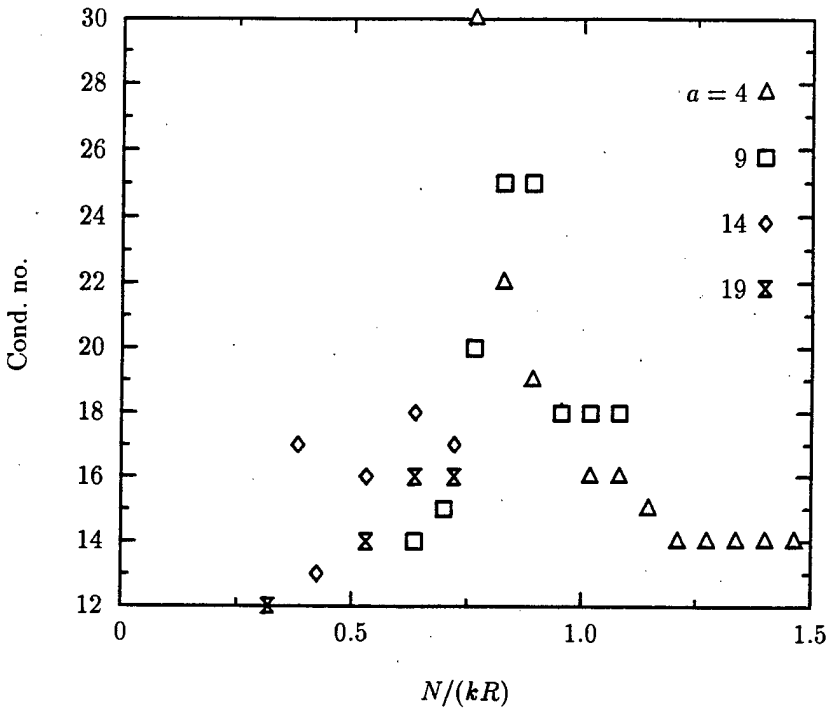

Figure 3.6: The condition number in the range of uniqueness for large values of ka with $k = 3.14$, $kh = 3.14/3$ and $R = a + 1$.

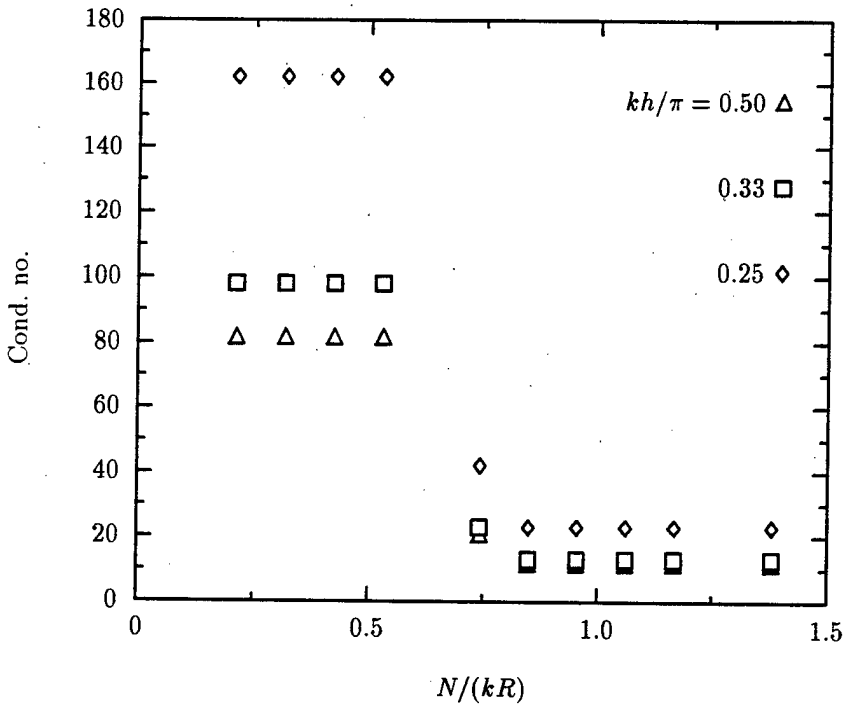

Figure 3.7: The condition number for various values of kh with $k = 3.14$, $ka = 3.14$ and $R = 3\,a$.

3.3 Local DtN Boundary Conditions

Givoli and Keller [42] have obtained a *local* counterpart of the truncated map which inherits the property that it is exact for functions that consist of only the first N modes. The resulting boundary conditions may be employed as an approximation to the full DtN map in the general case. Following the derivation in [114], we consider the first N modes in two dimensions

$$p(R,\theta) = \sum_{n=0}^{N-1}{}'(A_n \cos n\theta + B_n \sin n\theta) \tag{3.23}$$

noting that

$$(-1)^m \frac{d^{2m}p(R,\theta)}{d\theta^{2m}} = \sum_{n=0}^{N-1}{}' n^{2m}(A_n \cos n\theta + B_n \sin n\theta) \tag{3.24}$$

The DtN boundary condition is

$$\frac{\partial p}{\partial n} = -\pi \sum_{n=0}^{N-1}{}' \alpha_n (A_n \cos n\theta + B_n \sin n\theta) \tag{3.25}$$

Comparing (3.24) and (3.25) suggests expressing the coefficients as linear combinations

$$\alpha_n = \sum_{m=0}^{N-1} \beta_m n^{2m}, \qquad n = 0, 1, \cdots, N-1 \tag{3.26}$$

where β_m are obtained from solving this $N \times N$ linear system. Substitution in (3.25) yields the local expression

$$\frac{\partial p}{\partial n} = -\pi \sum_{n=0}^{N-1} (-1)^n \beta_n \frac{d^{2n}p(R,\theta)}{d\theta^{2n}} \tag{3.27}$$

Numerical evaluations of this formulation have been carried out [44].
Remarks (computational aspects)

1. The element-based data structure of finite element methods is preserved by the local representation of the DtN boundary condition.

2. The local boundary condition requires higher continuity of finite element functions in the tangential directions along the artificial boundary, commensurate with the higher tangential derivatives. Appropriate shape functions are being developed [43].

3. Evaluation of the contribution of the local boundary conditions to the discrete equations requires only integration of derivatives of finite element shape functions, which is performed numerically.

As previously noted, uniqueness of the solution is equivalent to enforcing zero energy flux through the artificial boundary. Consider the one-term local approximation in two dimensions

$$\frac{\partial p}{\partial n} = -\pi\alpha_0 p \tag{3.28}$$

This expression approximates the radiation condition for large kR [42]. Consequently, the error due to employing the local boundary conditions is reduced by increasing the size of the computational domain.

The difference between two solutions to the DtN problem with a one-term local approximation, v, must satisfy

$$\begin{aligned} 0 &= \int_0^{2\pi} -Im\{\bar{v}\,\alpha_0 v\}\,d\theta \\ &= -Im\,\alpha_0 \int_0^{2\pi} |v|^2\,d\theta \end{aligned} \tag{3.29}$$

implying, as in the case of the *full* operator, homogeneous Dirichlet and Neumann boundary conditions on the artificial boundary, which in turn imply uniqueness of solutions with a one-term local boundary condition. Adding terms to the local approximation, equivalent to adding constraints to the corresponding eigenvalue problem for the Laplacian, cannot introduce new characteristic wave numbers, and hence *any number of terms in the local boundary condition gives rise to unique solutions for all wave numbers.*

Chapter 4

Finite Element Formulations

In this chapter, the discrete approximation to the structural acoustics problem is described. Discrete methods are obtained by introducing piecewise polynomial interpolation functions over the finite element partitions of the computational domains into the variational equations. The finite element matrix equations are then obtained.

4.1 Galerkin Method

Let finite element spaces $\mathcal{S}_p^h \subset \mathcal{S}_p$, $\mathcal{V}_p^h \subset \mathcal{V}_p$, $\mathcal{S}_{\mathbf{u}}^h \subset \mathcal{S}_{\mathbf{u}}$ and $\mathcal{V}_{\mathbf{u}}^h \subset \mathcal{V}_{\mathbf{u}}$ be defined by the restriction of $\mathcal{S}_p$, $\mathcal{V}_p$, $\mathcal{S}_{\mathbf{u}}$ and $\mathcal{V}_{\mathbf{u}}$ to the space piecewise polynomials of selected order for each space, for p and $\mathbf{u}$. The discrete approximations for the pressure and for the displacement are denoted as p^h and $\mathbf{u}^h$, respectively.

The standard Galerkin finite element method is stated as: Given $\mathbf{q}$, f, g, h, g_i and h_i for $i = 1, \ldots, n_{dof}$, find $\mathbf{u}^h \in \mathcal{S}_{\mathbf{u}}^h$ and $p^h \in \mathcal{S}_p^h$ such that for all $\overline{\mathbf{u}}^h \in \mathcal{V}_{\mathbf{u}}^h$ and $\overline{p}^h \in \mathcal{V}_p^h$:

$$a^f(\overline{p}^h, p^h) + (\overline{p}^h \hat{\mathbf{n}}^s, \rho_0 \omega^2 \mathbf{u}^h)_\Gamma + (\overline{p}^h, M p^h)_{\partial \mathcal{B}_R} = L^f(\overline{p}^h) \quad , \tag{4.1}$$

$$a^s(\overline{\mathbf{u}}^h, \mathbf{u}^h) + (\overline{\mathbf{u}}^h, \hat{\mathbf{n}}^s p^h)_\Gamma = L^s(\overline{\mathbf{u}}^h) \quad , \tag{4.2}$$

where the operators in (4.1) and (4.2) are defined in Chapter 2.

4.2 Galerkin/Generalized Least-squares Methods

In this section, Galerkin Generalized Least Squares (GGLS) methods are presented for the fluid-loaded structure. The GGLS finite element method consists of the addition of a residual-proportional (and thus consistent) least-squares term to the standard Galerkin finite element method. A particular case of these methods is the classical Galerkin method, which is obtained by setting the least squares modifications to zero.

The notation $\tilde{\Omega}$ is used to denote the union of finite element interiors covering the domain Ω. The GGLS method can be stated as: Find $\mathbf{u}^h \in \mathcal{S}_{\mathbf{u}}^h$ and $p^h \in \mathcal{S}_p^h$ such that for all $\overline{\mathbf{u}}^h \in \mathcal{V}_{\mathbf{u}}^h$ and $\overline{p}^h \in \mathcal{V}_p^h$:

$$A^f_{GGLS}(\overline{p}^h, p^h) + (\overline{p}^h \hat{\mathbf{n}}^s, \rho_0 \omega^2 \mathbf{u}^h)_\Gamma + (\overline{p}^h, \mathrm{M} p^h)_{\partial \mathcal{B}_R} = L^f_{GGLS}(\overline{p}^h) \quad , \tag{4.3}$$

$$A^s_{GGLS}(\overline{\mathbf{u}}^h, \mathbf{u}^h) + (\overline{\mathbf{u}}^h, \hat{\mathbf{n}}^s p^h)_\Gamma + \sum_{i=1}^{n^s_{LS}} (\mathbf{H}^s_i \mathcal{L}_s \overline{\mathbf{u}}^h, \mathbf{H}^s_i \hat{\mathbf{n}}^s p^h)_{\tilde{\Gamma}} = L^s_{GGLS}(\overline{\mathbf{u}}^h) \quad . \tag{4.4}$$

where

$$A^f_{GGLS}(\overline{p}^h, p^h) := a^f(\overline{p}^h, p^h) + \sum_{i=1}^{n^f_{LS}} (H^f_i \mathcal{L}_f \overline{p}^h, H^f_i \mathcal{L}_f p^h)_{\tilde{\Omega}_f} \quad , \tag{4.5}$$

$$A^s_{GGLS}(\overline{\mathbf{u}}^h, \mathbf{u}^h) := a^s(\overline{\mathbf{u}}^h, \mathbf{u}^h) + \sum_{i=1}^{n^s_{LS}} (\mathbf{H}^s_i \mathcal{L}_s \overline{\mathbf{u}}^h, \mathbf{H}^s_i \mathcal{L}_s \mathbf{u}^h)_{\tilde{\Omega}_s} \quad , \tag{4.6}$$

$$L^f_{GGLS}(\overline{p}^h) := L^f(\overline{p}^h) + \sum_{i=1}^{n^f_{LS}} (H^f_i \mathcal{L}_f \overline{p}^h, H^f_i f)_{\tilde{\Omega}_f} \quad , \tag{4.7}$$

$$L^s_{GGLS}(\overline{\mathbf{u}}^h) := L^s(\overline{\mathbf{u}}^h) + \sum_{i=1}^{n^s_{LS}} (\mathbf{H}^s_i \mathcal{L}_s \overline{\mathbf{u}}^h, \mathbf{H}^s_i \mathbf{q})_{\tilde{\Omega}_s} \quad , \tag{4.8}$$

where n^f_{LS} and n^s_{LS} are the number of least-squares operators added to the standard Galerkin equations for the fluid and structural equations, respectively. At the heart of these methods is the operator H^f_i and the $n_{dof} \times n_{dof}$ matrix differential operator $\mathbf{H}^s_i$ which contain the design parameters enabling the development of new methods with enhanced accuracy characteristics. If H^f_i and $\mathbf{H}^s_i$ are set to zero, the Galerkin finite element method is recovered.

For the Helmholtz equation, two methods that have been studied previously are the Galerkin Least Squares (GLS) method which is defined by $n^f_{LS} = 1$ and

$$H^f = \sqrt{\tau_f} \quad ,$$

where τ_f is the GLS design parameter. The second is Galerkin Gradient Least Squares (G∇LS) method which is defined by $n^f_{LS} = 1$ and

$$H^f = \sqrt{\tau'_f} \nabla \quad ,$$

where τ'_f is the $G\nabla LS$ design parameter. Harari and Hughes have also studied the effect of using GLS and G∇LS together (i.e., $n^f_{LS} = 2$) for the advection diffusion equation [62]. Optimal selection of the GLS and G∇LS parameters is discussed in [34, 57].

The structural least-squares operator depends on the particular theory used. Suppose for definiteness that $n_{dof} = 2$ then the GLS method is defined by $n^s_{LS} = 1$ and

$$\mathbf{H}^s_{GLS} = \begin{bmatrix} \sqrt{\tau_1} & 0 \\ 0 & \sqrt{\tau_2} \end{bmatrix} \quad . \tag{4.9}$$

The $G\nabla LS$ method would include a gradient operator on the diagonal of the matrix in (4.9). The development of the optimal τ's for the G∇LS method applied to the vector Timoshenko beam equations is presented in [50, 52] and is a topic covered in Chapter 10.

Remark:

1. The essence of the GGLS methods is to add to the standard Galerkin finite element equations, terms proportional to the residual of the original governing differential equations integrated over element interiors. Fix $n_{LS}^f = n_{LS}^s = 1$ and drop the subscript, the GGLS equations (4.3) and (4.4) may be written as

$$
\begin{aligned}
(H^f \mathcal{L}_f \overline{p}^h, \quad & H^f(\mathcal{L}_f p^h - f))_{\tilde{\Omega}_f} + \\
& a^f(\overline{p}^h, p^h) + (\overline{p}^h \hat{\mathbf{n}}, \rho_f \omega^2 \mathbf{u}^h)_\Gamma + (\overline{p}^h, \mathrm{M} p^h)_{\partial \mathcal{B}_R} = L^f(\overline{p}^h) \quad , \\
(\mathbf{H}^s \mathcal{L}_s \overline{\mathbf{u}}^h, \quad & \mathbf{H}^s(\mathcal{L}_s \mathbf{u}^h - \mathbf{q} + \hat{\mathbf{n}}^s p^h))_{\tilde{\Omega}_s} + \\
& a^s(\overline{\mathbf{u}}^h, \mathbf{u}^h) + (\overline{\mathbf{u}}^h, \hat{\mathbf{n}}^s p^h)_\Gamma = L^s(\overline{\mathbf{u}}^h) \quad ,
\end{aligned}
$$

   where on the first line in each of these two equations is the residual proportional term and on the second line are standard Galerkin equations.

These methods are consistent by construction (i.e., the exact solution, when substituted into the numerical method (4.3) and (4.4), satisfies the equations identically). The addition of the least squares terms allows the design of methods that enhance the accuracy of the approximate solution. Care must be taken not to disturb the good properties of the original Galerkin method while still enhancing accuracy. Finally, the definition of the operators $\mathbf{H}_i^s$ and H_i^f must also satisfy conditions of rotational invariance (method independence of global coordinate frame).

Chapter 5

Acoustic Dispersion Analysis and Method Design

In the following we consider simplified inhomogeneous radiation problems—radiation loading of acoustic media by prescribed boundary conditions as induced by the vibration of a structure (thereby emphasizing boundary conditions of the Neumann type), with particular reference to exterior domains. Model problems are employed to examine the numerical formulations and design the Galerkin/least-squares operator. The acoustic field variable in the Helmholtz equation is denoted ϕ, representing the acoustic pressure of velocity potential.

5.1 A Model Problem for Radiation

Model problems based on the reduced wave equation were constructed in [57] in order to assess the performance of the numerical methods proposed. These problems, which exhibit many of the physical features of acoustic phenomena, yet still possess readily obtainable analytical solutions, are reviewed in the following. We restrict our attention to elementary solutions to *inhomogeneous Neumann problems* governed by the equations of acoustics. The domain is a half-space occupied by a *moving* acoustic fluid with a unidirectional uniform mean-flow velocity U, and constant mean-flow density, pressure and entropy (Fig. 5.1). Due to the motion in the equilibrium state of the acoustic medium the resulting differential equation involves a *convected wave operator*. All quantities are assumed to have known periodic in-plane variation as well as harmonic time dependence, with given in-plane wave numbers and frequency.

These assumptions yield the one-dimensional problem of an infinite plane radiator with a *modified wave number*. Dispersion curves that are possible within this set up are shown in [57]. In general, the wave number can be either real or imaginary. When the wave number is real, solutions maintain the character of propagating waves. When the wave number is imaginary, decay takes the place of propagation, giving rise to evanescent waves. Numerical solutions often deteriorate in the propagation region as the wave number increases due to the loss of ellipticity of the differential operator. Likewise, problems connected to modeling sharp boundary layers arise as the rate of decay increases.

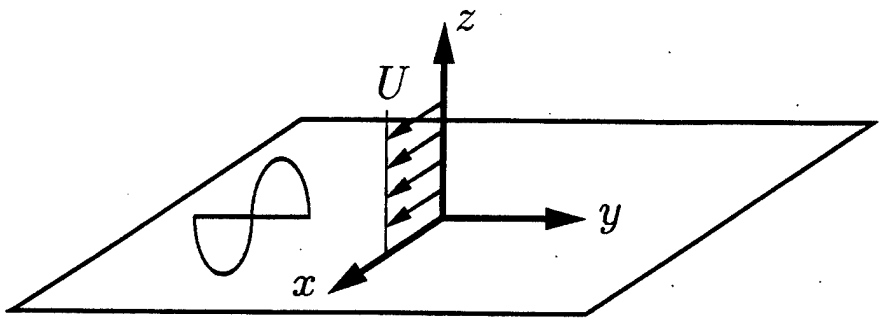

Figure 5.1: The model problem: a moving acoustic medium over an infinite plane radiator.

The performance of finite element methods is usually assessed on the basis of the value of the error and/or its derivatives measured in an integral norm. Here we refer to methods that minimize the gradient of the error, typically related to error in flux, in the L_2 norm as 'optimal methods' (distinct from optimal convergence rates). In one dimension, discrete values of the error, evaluated at the nodes, can be related to integral norms. Linear finite element functions that nodally interpolate the exact solution are optimal in the sense mentioned above. (There exist useful alternative characterizations of optimality.) Thus, nodal exactness is a *bona fide* measure of the performance of linear finite elements. The motivation for pursuing this issue is that in one dimension nodal values are often relatively easy to calculate and appraise, and hence nodal exactness, when achievable, is a desirable goal in method design.

This evaluation of the numerical solution on its own may, however, be insufficient. Consider a problem with a highly-oscillating exact solution. A computational method that yields the nodal interpolant is indeed optimal, but the solution can be quite misleading if the oscillations are not properly resolved. Figure 5.2 demonstrates the difficulty that arises in interpreting an under-resolved numerical solution. The integral measure is inappropriate for such cases. Instead, physical considerations based on the particular class of problems being addressed must be taken into account. For problems governed by the Helmholtz equation in exterior domains we want a solution that yields an accurate representation of the magnitude (related to acoustic energy) and phase of physical phenomena that are resolved, as well as the flux at the wet surface. The effect of unresolved features on the numerical solution should be minimized, particularly when dealing with problems that involve multi-scale phenomena.

Remarks: Sufficient, or proper, resolution of a wave by a numerical mesh is not an objective measure. We shall refer to ten linear elements per wave ($kh = \pi/5$) as "acceptable resolution," since this is the guideline often used by numerical analysts. The "limit of resolution" will be defined as four linear elements per wave ($kh = \pi/2$), since beyond this value the finite-dimensional functions do not even possess the required minima and maxima to model the physical features (although it is possible to envision as few as two elements per wave crudely approximating such phenomena).

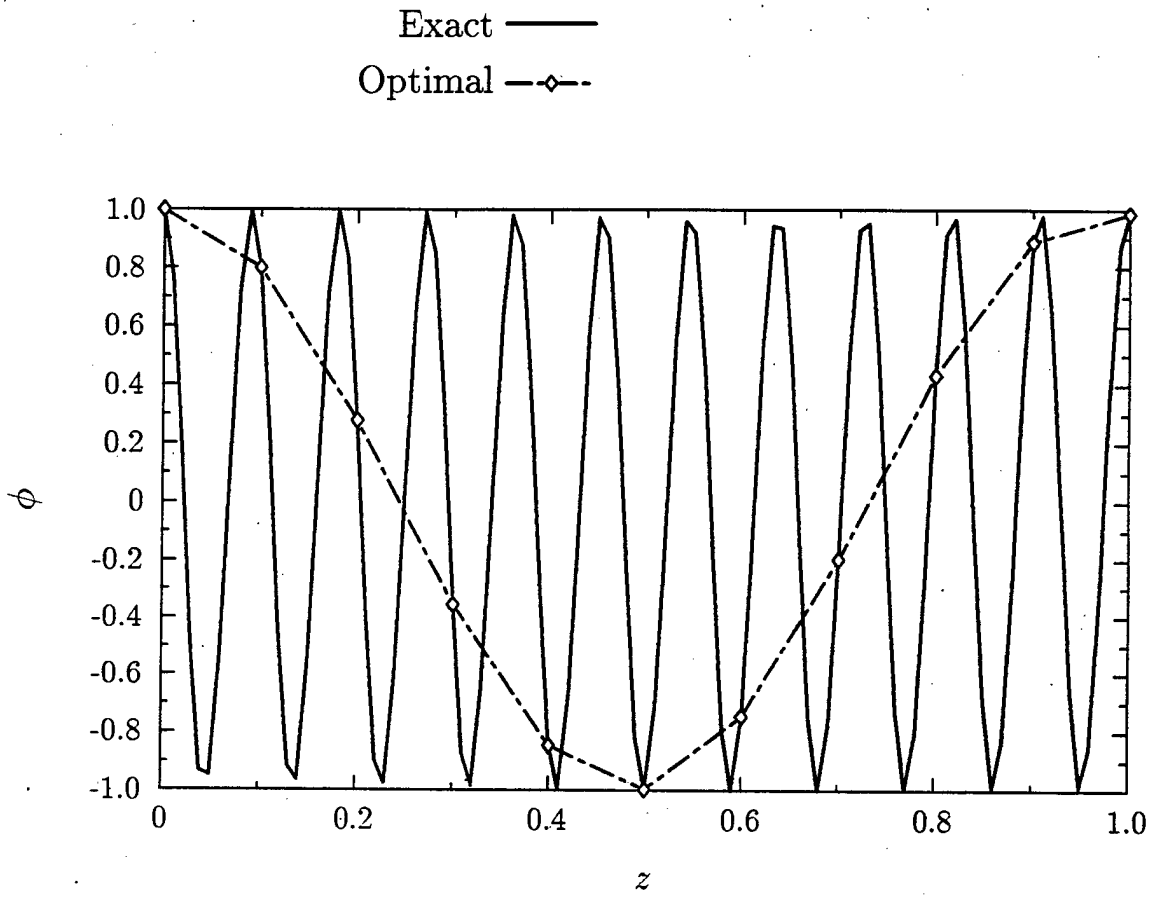

Figure 5.2: Under-resolved piecewise linear interpolant of an oscillatory function.

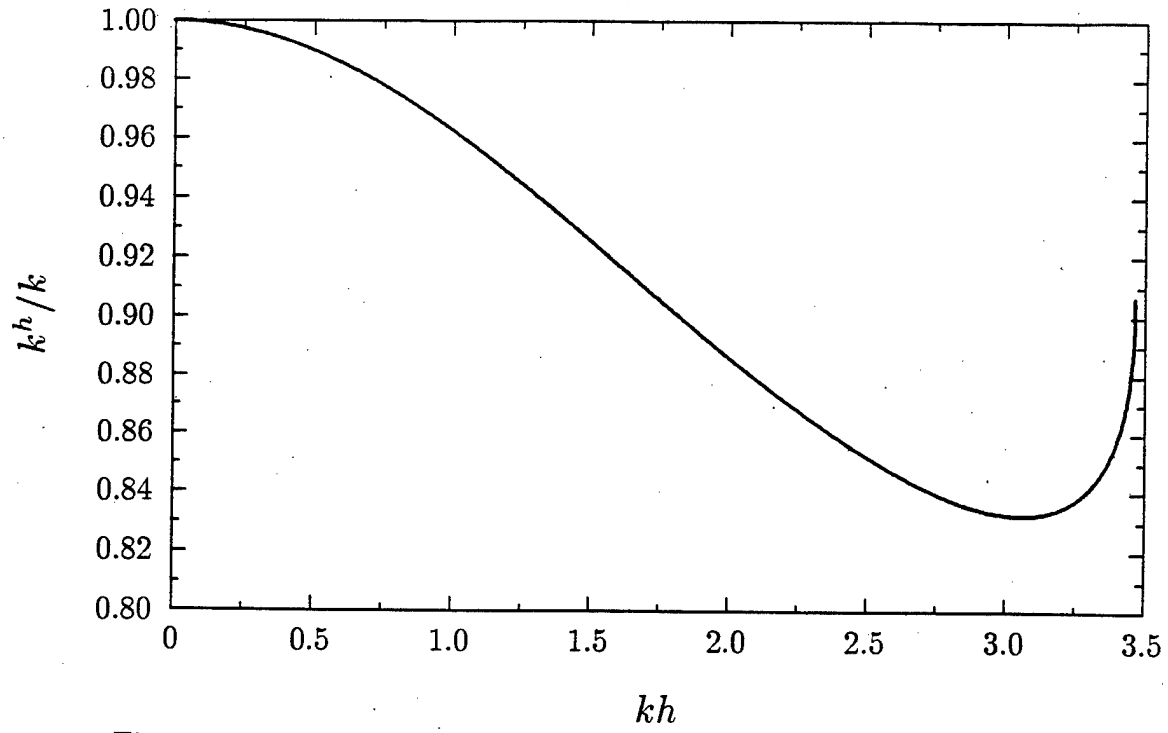

Figure 5.3: Phase error of the Galerkin formulation ($0 \leq k^h h \leq \pi$).

5.2 Plane Waves

First we wish to characterize the behavior of the numerical solution in the interior of a mesh. For this purpose we consider plane waves in an *infinite* mesh, so that only interior stencils need be investigated.

Galerkin: The performance of Galerkin solutions is conveniently characterized in terms of the numerical parameter $\alpha^h := (kh)^2/12$. When the exact solution is a propagating wave ($\alpha^h > 0$) there are two cases: For $\alpha^h \leq 1$ the magnitude of the solution is correct, but there is a *phase lag* of the approximate wave number k^h, see Fig. 5.3. The range in which the solution has the correct magnitude corresponds to $0 \leq k^h h \leq \pi$ ($\Leftrightarrow 0 \leq kh \leq \sqrt{12} \approx 3.46$). As α^h takes on values larger than one the solution decays.

Remarks.

1. The effect of increasing the wave number can always be balanced by mesh refinement since the Galerkin solution to this problem depends only on the parameter α^h.

2. The Galerkin method appears to be pointing out the appropriate strategy for handling unresolved waves, namely damping the solution, but starting the damping at too coarse a resolution (at $kh = \sqrt{12} > \pi \Leftrightarrow \alpha^h = 1$, i.e., less than two elements per wave, well below the limit of resolution for which $\alpha^h \approx 0.21$).

The performance of Galerkin solutions in the case of exponential decay ($\alpha^h < 0$) has already been studied in [34] and is reviewed here for completeness. As long as

$\alpha^h > -1/2$ there is no conceptual problem. However, for $\alpha^h < -1/2$ there are spurious *oscillations*. These oscillations are localized to the neighborhood of the boundary layer and do not pollute the entire solution. This is a clear manifestation of degradation of H^1-stability, while maintaining stability in the L_2 sense, i.e. the solution itself is approximated well, but its derivatives are approximated poorly.

In summary, the Galerkin representation of the plane wave is good in the range in which physical phenomena are well-resolved, but degrades outside of this range. The mesh needs to be refined as the wave number or decay rate is increased to maintain solution accuracy. Subject to this condition, there is no upper limit on the allowable wave number at which a good approximate solution can be obtained.

Galerkin/least-squares: For a mesh of linear finite elements the Galerkin/least-squares equations may be obtained from the Galerkin equations by replacing α^h with $\alpha_{GLS} := \alpha^h(1 - \tau k^2)$. The choice of

$$\alpha_{GLS} = \frac{1}{2}\frac{1 - \cos(kh)}{2 + \cos(kh)} \tag{5.1}$$

leads to a method for which the discrete solution is *nodally exact* in the *entire* range of phenomena under consideration, regardless of mesh refinement. In the propagation region, (5.1) leads to $0 \leq \alpha_{GLS} \leq 1$ which results in

$$1 - \frac{1}{\alpha^h} \leq \tau k^2 \leq 1 \qquad \forall \alpha^h \geq 0 \tag{5.2}$$

We may thus view the nondimensional parameter τk^2 as oscillating around $1 - \frac{1}{2\alpha^h}$. Reflecting this mean value with respect to α^h yields a valid lower bound for the decay region as well, and the upper bound may simply be extended from the region of propagation. The precise behavior of τk^2, as well as these simple expressions, is depicted in Fig. 5.4. We wish to point out the smooth transition between the decay and propagation regions. The parameter τk^2 vanishes at $\alpha^h = 0$ (which is appropriate since the Galerkin method is optimal for this case) and it has a slope of -1 at $\alpha^h = 0$. It asymptotically tends to one for both extreme values of α^h.

Remarks.

1. A Galerkin/least-squares method is quite different from a "modified wave number approach," despite some superficial similarities. The replacement of α^h by α_{GLS} is performed only for the sake of convenience in analyzing the method, and it holds only for linear elements on a uniform mesh. In general, this is not equivalent to modifying k in the governing differential equation. For higher-order elements the GLS method cannot be obtained from a Galerkin formulation simply by substituting α_{GLS} for α^h. Moreover, consistency in the sense described earlier is maintained by appropriate treatment of the right-hand side, as in eq. (4.3). This guarantees that the convergence properties will improve as the order of interpolation is increased, and superior results for all orders of interpolation can still be expected when source terms are present.

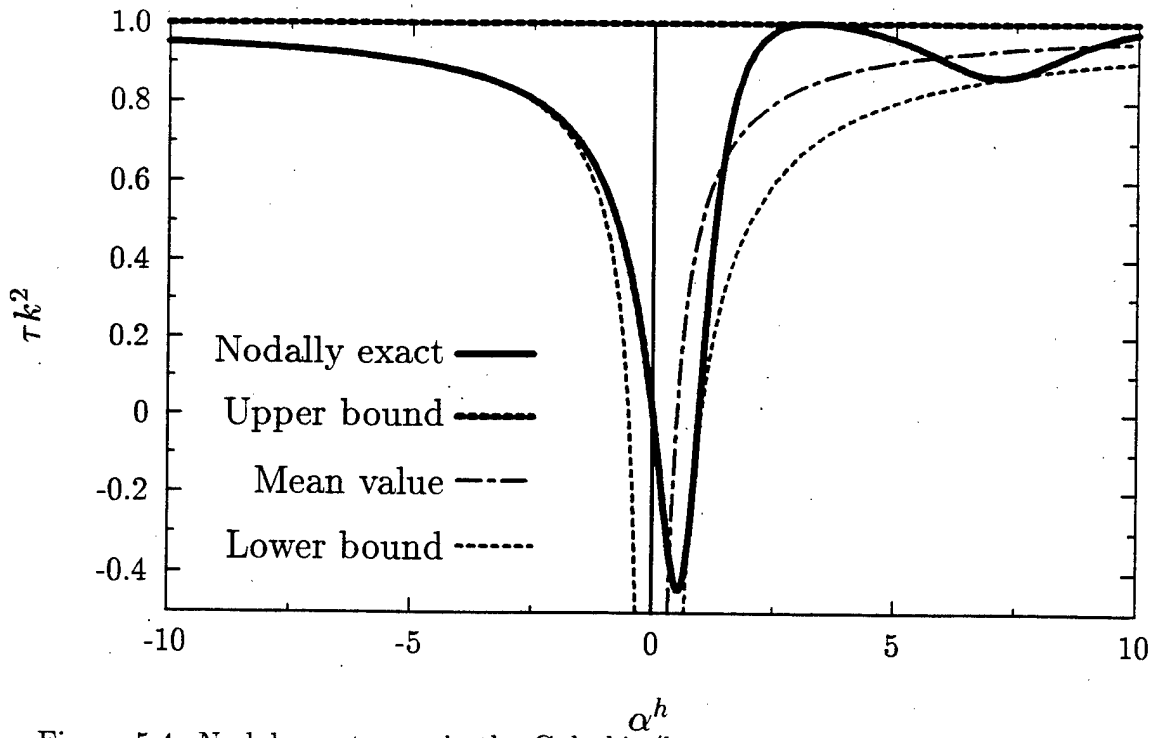

Figure 5.4: Nodal exactness via the Galerkin/least-squares method, see (5.1).

2. From the point of view of method design it is convenient to determine α_{GLS} to obtain the desired performance. However, the corresponding τ must always be examined to guarantee feasibility of implementation. For non-uniform meshes, the parameter τ which is defined on the basis of eq. (5.1) is evaluated on the element level by considering h to be the individual element size rather than the mesh parameter.

3. The aforementioned bounds suggest simple approximations to achieving nodal exactness in the region of decay, which are easily extended into the region of propagation beyond the limit of resolution, up to $\alpha^h = 1/4$. The simplest is

$$\tau k^2 = \frac{\alpha^h}{\alpha^h - 1}, \qquad \alpha^h \leq 1/4 \tag{5.3}$$

The approximation in the range of higher decay rates may be improved by

$$\tau k^2 = \begin{cases} 1 + \frac{1}{2\alpha^h}, & \alpha^h < -1 \\ \frac{\alpha^h}{\alpha^h - 1}, & -1 \leq \alpha^h \leq 1/4 \end{cases} \tag{5.4}$$

or by

$$\tau k^2 = \begin{cases} 1 + \frac{1}{2\alpha^h}, & \alpha^h < -1 \\ -\frac{1}{2}\alpha^h, & -1 \leq \alpha^h < 0 \\ \frac{\alpha^h}{\alpha^h - 1}, & 0 \leq \alpha^h \leq 1/4 \end{cases} \tag{5.5}$$

which is smoother at $\alpha^h = -1$ (see Fig. 5.5). These last two approximations correspond to $\alpha_{GLS} = -1/2$ in the range of higher decay rates, cf. (5.1). All approximations maintain continuity with (5.1) at $\alpha^h = 0$ and may be inexpensively employed in practical implementations.

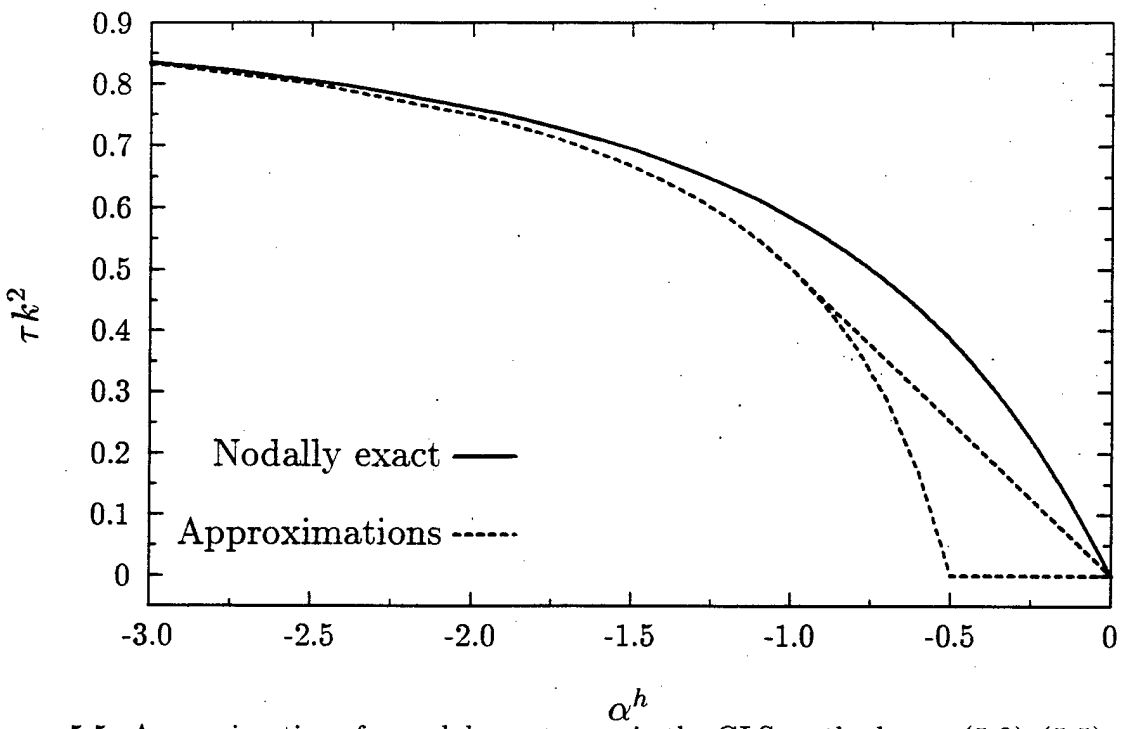

Figure 5.5: Approximations for nodal exactness via the GLS method, eqs. (5.3)–(5.5).

5.3 The Neumann Model Problem with a DtN Boundary

We now consider a model problem with a Neumann boundary condition on the wet surface of the plane radiator and the DtN boundary condition on the artificial boundary. Nodal exactness at all nodes is no longer attainable.

Galerkin: Exact solutions to boundary-value problems for the reduced wave equation in unbounded domains are unique, whereas in bounded domains such solutions are not unique at characteristic wave numbers. Due to the contribution of the DtN boundary condition, which represents the effect of the unbounded domain, there are no instabilities in the Galerkin solution. From the point of view of functional analysis this implies that stability is ensured by the presence of the DtN boundary operator, b_k, despite loss of positive-definiteness of the sesquilinear form a_k. Nevertheless, the quality of the Galerkin solution deteriorates as the absolute value of α^h increases.

In the region of propagation, outgoing and incoming waves (of incorrect phase, see Fig. 5.3) are linearly combined to satisfy the boundary conditions, resulting in spurious modulation of the amplitude. The entire solution is damped out for large values of α^h. However, before this occurs, the amplitude of the numerical solution is larger than the exact value *throughout the mesh*, and although the relative error is always bounded, it can be of several orders of magnitude. There is also severe phase error as α^h increases. For more details see [57], and subsequent numerical results and discussion.

Similarly, in the decay region, the error in the rate of decay brings about a linear combination of the part of the solution that is decaying with the part that represents

growth. Spurious oscillations in the solution start at $\alpha^h = -1/2$. The magnitude of the oscillations does not grow monotonically as $\alpha^h \to -\infty$, but rather grows and then subsides as the *entire* solution becomes trivial, losing its capability to capture the physics of the problem altogether.

Galerkin/least-squares: In this case nodal exactness can not be achieved with the type of least-squares methods presented. Consequently, in the propagation region, it is impossible to obtain correct values for both the phase and the magnitude. We examine solutions obtained by applying the Galerkin/least-squares method that was nodally exact on the infinite mesh, defined via (5.1). For this method in the propagation region the phase is exact and the magnitude is quite accurate over a wide range of α^h. The error in magnitude is virtually undetectable in the range of acceptable resolution (up to ten elements per wave, $\alpha^h \leq 0.033$) and accuracy in magnitude representation is vastly superior to that of the Galerkin solution up to the limit of resolution (four elements per wave, $\alpha^h \leq 0.2$). The maximum error in magnitude within this range for Galerkin is approximately 20%, whereas for this Galerkin/least-squares method it is about 5%, see [57]. Examples of the performance of these methods on the Neumann model problem are subsequently presented.

In the decay region the rate of exponential decay is exact. The nodal values at all of the nodes except for the one on the wet surface are quite accurate, and vanish in the limit $\alpha^h \to -\infty$, as they should. The oscillations that were seen in the Galerkin solution are precluded.

Phase accuracy is the motivation for the method defined via (5.1). Other design criteria may be employed, leading to alternative Galerkin/least-squares methods. In [57] a version of Galerkin/least-squares that minimizes the gradient of the error in the L_2 norm is derived for a single-element mesh. Although the resulting method is indeed optimal for this case, the generalization of this idea to larger meshes is almost prohibitive. However, this method is suitable for certain interaction problems in which sufficient discretization of the fluid contained within the DtN boundary is possible with a single layer of elements. An alternative in which nodal exactness at the wet surface for any uniform mesh is achieved by the simple expression

$$\alpha_{GLS} = \frac{1 - \sqrt{1 - 4\alpha^h}}{2} \tag{5.6}$$

is also presented in [57]. The use of this GLS method has a very important consequence: In the propagation region the outgoing wave satisfies the boundary conditions and in the region of decay the decaying part of the numerical solution does the same. As a result, *the magnitude of the solution is exact* in the range of propagation up to $\alpha^h < 1/4$ (where α_{GLS} is real), leading to no error in the acoustic energy.

Numerical examples: In numerical testing the Galerkin method was found to require wave resolution of about eight elements per wave (the standard guideline that is frequently employed by numerical analysts is ten elements per wave), whereas solutions obtained with Galerkin/least-squares formulations were accurate to four elements per wave [57]. As an example of numerical solutions for the Neumann model problem with a DtN boundary we show results in the propagation region over the unit interval discretized by a uniform mesh that consists of ten linear elements. The Neumann

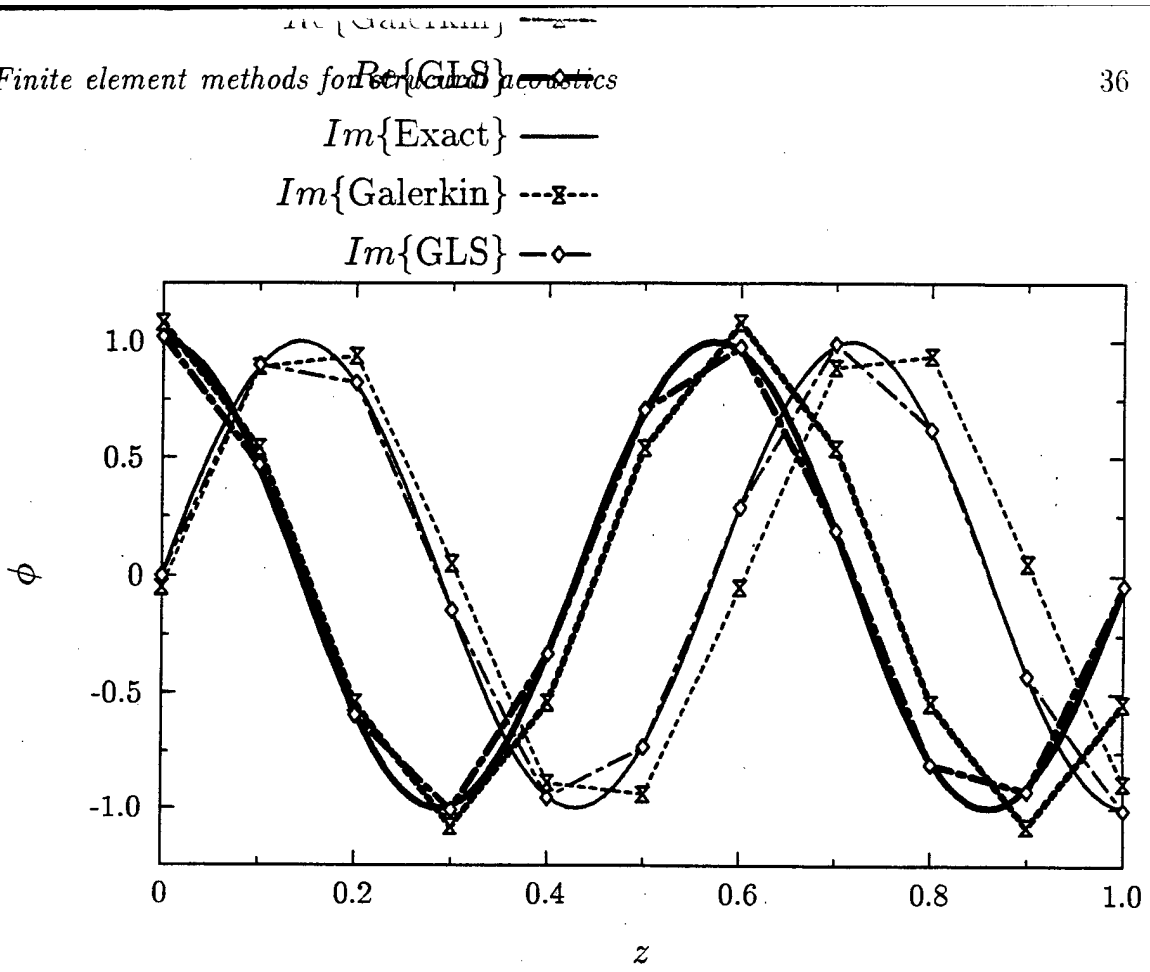

Figure 5.6: Neumann model problem with a DtN boundary condition: propagating exact solution ($\alpha^h = 1/10$, six elements per wave).

boundary condition is enforced on the wet surface ($z = 0$) and the artificial boundary is at $z = 1$. For $\alpha^h = 1/10$ we approach the limit of resolution (six elements per wave, which is between the limits of the two methods, Fig. 5.6). As expected, the Galerkin solution exhibits error in both magnitude, and in phase, which causes the loss of nodal accuracy to become more noticeable towards the DtN boundary. This is an indication of insufficient wave resolution by the numerical mesh. The Galerkin solution would improve with mesh refinement. There is no apparent error in the Galerkin/least-squares solution. Since far-field solutions are obtained by the DtN method from the numerical solution on the artificial boundary, the high degree of accuracy exhibited by the Galerkin/least-squares solution on the artificial boundary, in comparison to the Galerkin solution, is extremely important.

Damping of unresolved waves: The approximations in the region of decay to the Galerkin/least-squares method that provided phase accuracy, (5.4) and (5.5), indicate a scheme to provide damping of unresolved waves for the Neumann problem. By fixing $\alpha_{GLS} = -1/2$ after a set cut-off value of the numerically nondimensionalized wave number, e.g., the limit of resolution $kh = \pi/2$, we obtain a Galerkin/least-squares method with

$$\tau k^2 = 1 + \frac{1}{2\alpha^h} \tag{5.7}$$

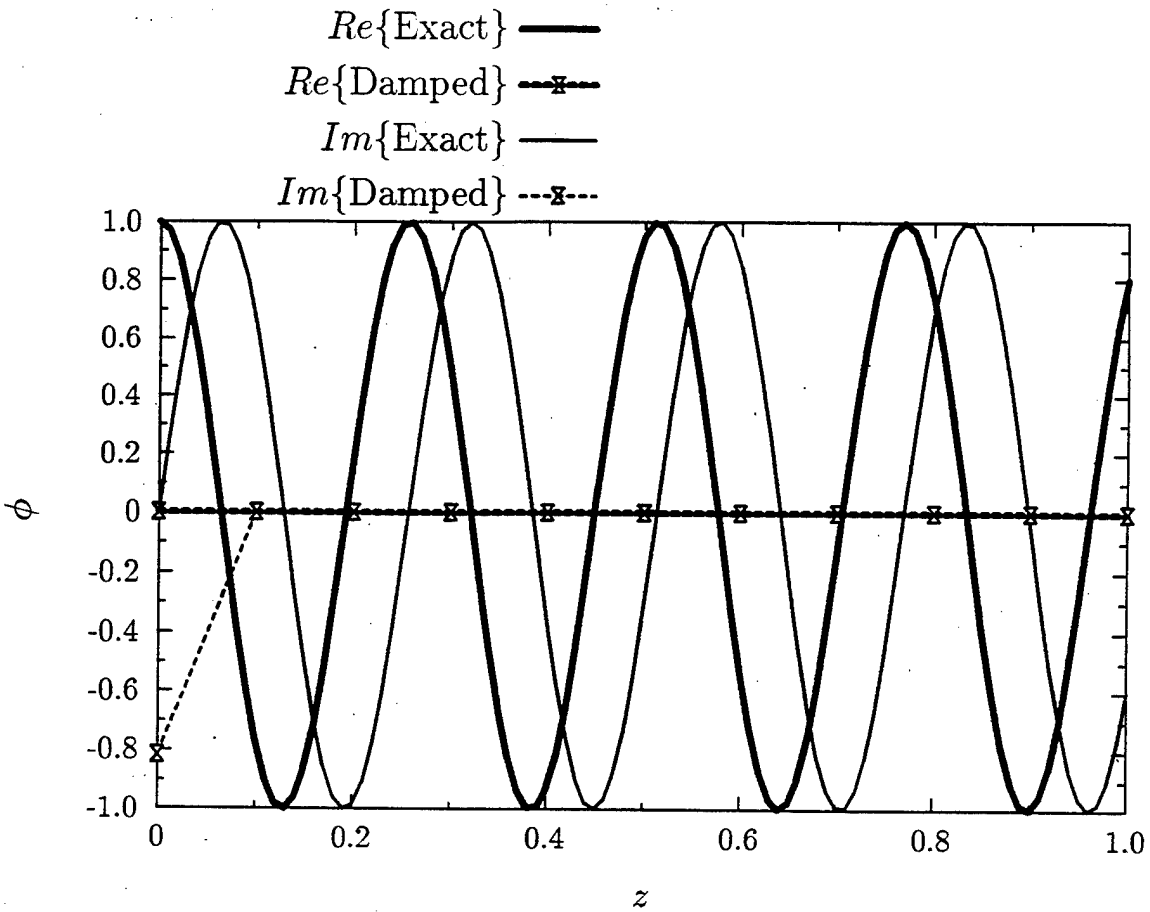

Figure 5.7: Neumann model problem with a DtN boundary condition: unresolved propagating exact solution ($\alpha^h = 1/2$, $\phi^h_{,n} = \phi_{,n}/3$ on Γ_h).

For *any* uniform mesh

$$\phi^h = \begin{cases} -\mathrm{i}h/3, & \text{on } \Gamma_h \\ 0, & \text{in } \Omega \end{cases} \tag{5.8}$$

i.e., the solution vanishes over the entire domain except for the first element, for which it is imaginary. This implies an approximation of the flux on the wet boundary, viz.,

$$\phi^h_{,n} = \phi_{,n}/3 \qquad \text{on } \Gamma_h \tag{5.9}$$

Solutions thus obtained maintain this character as the nondimensional wave number is increased indefinitely. The example depicted in Fig. 5.7 demonstrates damping of unresolved waves ($\alpha^h = 1/2$, beyond the limit of resolution). As predicted, the solution vanishes over the entire domain except for the first element, for which it is imaginary, approximating the flux on the wet boundary.

To summarize this chapter, we have reviewed the framework for *robust* finite element methods for problems of acoustics in exterior domains, including the inhomogeneous Neumann problem. Singular behavior is precluded in finite element models that are based on the DtN boundary-value problem. The Galerkin/least-squares method, with τ defined via (5.1), is accurate to the limit of resolution of four elements per wave and in the entire range of decay. Strong damping of numerical solutions for

physical phenomena that are not resolved is provided by (5.7). Superior behavior is thus exhibited in the entire range of propagation and decay.

5.4 Higher-order Elements

In recent years, there has been a resurgence of interest in the use of hierarchical p-version finite element and spectral elements to obtain high-resolution numerical solutions for structural acoustics. High-order finite element discretizations display frequency bands where the solutions are harmonic decaying waves. In these so called 'stopping' bands, the solutions are not purely propagating (real wavenumbers) but are attenuated (complex wavenumbers). In order to interpret the solution within the stopping bands, the standard dispersion analysis technique is extended to include complex wavenumbers. The results of the complex wavenumber dispersion analysis presented in this section are drawn from Thompson and Pinsky [143, 144, 147]. By allowing for complex wavenumbers, a complete characterization of high-order finite element discretizations has been obtained. Three alternatives are considered: (i) hierarchic p-version elements based on Legendre functions, (ii) new hierarchic Fourier elements based on sinusoidal functions, and (iii) spectral elements based on Lagrange interpolation in conjunction with Gauss-Lobatto quadrature. Practical guidelines for phase and amplitude accuracy in terms of the spectral order and the number of elements per wavelength are reported. Results from this analysis provide a guide for the design of p- and hp-version adaptive schemes, high-order preconditioners for iterative solution methods, and the selection of optimal Galerkin/Least-Squares (GLS) mesh parameters for elements using high-order basis functions. Further results are reported in Thompson and Pinsky [143, 144, 147].

5.4.1 Higher-order approximations

Consider the finite element approximation,

$$\phi^h(\xi) = \sum_{a=1}^{p+1} N_a(\xi)\phi_a, \qquad \xi \in [-1,1] \tag{5.10}$$

where $N_a(\xi)$ are shape functions with compact support defined in the local element coordinate ξ, and p is the spectral order.

Upon introducing (5.10) into the Galerkin least-squares variational equation (4.4) we obtain the following symmetric element impedance matrix,

$$\boldsymbol{s}^e = [s^e_{ab}] \in \mathbb{R}^{(p+1)\times(p+1)} \qquad a,b = 1:p+1 \tag{5.11}$$

$$\boldsymbol{s}^e = \boldsymbol{k}^e - (1-\tau k^2)k^2\boldsymbol{m}^e + \tau\hat{\boldsymbol{k}}^e + \tau k^2\bar{\boldsymbol{k}}^e \tag{5.12}$$

where $k = \omega/c$ and

$$\begin{aligned} k^e_{ab} &= (N_{a,x}\,,\, N_{b,x})_{\Omega_e} \\ m^e_{ab} &= (N_a\,,\, N_b)_{\Omega_e} \\ \hat{k}^e_{ab} &= (N_{a,xx}\,,\, N_{b,xx})_{\Omega_e} \\ \bar{k}^e_{ab} &= (N_{a,xx}\,,\, N_b)_{\Omega_e} + (N_a, N_{b,xx})_{\Omega_e} \end{aligned}$$

and the L_2 inner product is defined as,

$$(N_a\ ,\ N_b)_{\Omega_e} = \frac{h}{2}\int_{-1}^{1} N_a N_b d\xi \tag{5.13}$$

where h is the element length. In the above expressions, $\boldsymbol{k}^e$ and $\boldsymbol{m}^e$ are the local stiffness and mass matrices emanating from the Galerkin formulation, while the matrices $\hat{\boldsymbol{k}}^e$ and $\bar{\boldsymbol{k}}^e$ are additional contributions obtained from the Least-Squares terms.

P-version hierarchic Legendre elements

Let $\mathcal{S}^p \subset H^1$ be the finite element subspace of continuous piecewise polynomials of degree p denoted by $\mathcal{P}^p$. The basis functions used in the p-version finite element method are obtained by starting with the standard linear nodal shape functions,

$$N_a(\xi) = \frac{1}{2}(1+\xi_a\xi) \qquad a = 1,2 \tag{5.14}$$

and then adding in a hierarchical fashion internal shape functions defined in terms of integrals of Legendre polynomials.

$$N_a(\xi) := \frac{1}{||P_{a-2}||}\int_{-1}^{\xi} P_{a-2}(\xi')d\xi', \qquad a = 3,4,\cdots,p+1 \tag{5.15}$$

with the norm of the Legendre polynomial,

$$||P_{a-2}||^2 = \frac{2}{2a-3} \tag{5.16}$$

These functions are constructed such that $N_a(\pm 1) = 0$. As a result of this property the variables $\phi_1 = \phi^h(-1)$ and $\phi_2 = \phi^h(1)$ define discrete nodal variables, while the values $\phi_a, a \geq 3$ compose a set of internal variables. The derivatives of these hierarchical functions form an orthonormal basis with the property,

$$\int_{-1}^{1} \frac{dN_a}{d\xi}\frac{dN_b}{d\xi}d\xi = \delta_{ab} \qquad a,b = 3:p+1 \tag{5.17}$$

As a result of this orthogonality property, the local element stiffness matrix is diagonal beyond $a > 2$. Details on the form of these matrices are given in [143]. The element matrices are hierarchic in the sense that the matrix corresponding to $\mathcal{S}^p$ is embedded in the matrix corresponding to $\mathcal{S}^{p+1}$.

New hierarchic Fourier elements

In [144, 147] a new hierarchic trigonometric basis is constructed starting with the standard linear nodal shape functions defined in (5.14) and then adding to these in a hierarchical manner internal shape functions defined in terms of the Fourier modes,

$$N_a(\xi) = \frac{2}{(a-2)\pi}\sin((a-2)(1+\xi)\pi/2) \qquad a = 3,4,\cdots,p+1 \tag{5.18}$$

These functions satisfy $N_a(\pm 1) = 0$ and the orthogonality properties,

$$\int_{-1}^{1} N_a N_b d\xi = \frac{2}{(a-2)\pi}\delta_{ab}; \qquad \int_{-1}^{1} \frac{dN_a}{d\xi}\frac{dN_b}{d\xi} d\xi = \delta_{ab} \tag{5.19}$$

As a result of this normalization, the local element stiffness matrix is identical to the stiffness matrix obtained with the Legendre polynomial based elements. However, the use of Fourier modes changes the mass matrix.

Spectral elements

Higher-order elements based on Lagrange interpolation polynomials in conjunction with Gauss-Lobotto quadrature lead to the so-called 'spectral elements' when used with a high spectral order p. In the spectral element method, the solution variable ϕ^h is expanded within each element in terms of high-order Lagrangian interpolants, $N_a(\xi) \in \mathcal{P}^p$:

$$\{N_a(\xi) \in \mathcal{P}^p,\ N_a(\xi_b) = \delta_{ab}\ \forall a, b \in \{1, \cdots, p+1\}\} \tag{5.20}$$

evaluated at $p+1$ Gauss-Lobatto points such that $\xi_1 = -1$ and $\xi_{p+1} = 1$, with the other points being obtained as the roots of the derivative of the Legendre polynomials. In this case, the solution variables are all nodal values, $\phi_a = \phi^h(\xi_a)$, and the basis is not hierarchical. By choice of Gauss-Lobatto quadrature, the elemental mass matrix is underintegrated and diagonal.

5.4.2 Complex wavenumber Fourier analysis

In this section the complex wavenumber Fourier analysis technique developed in [144, 147] is used to investigate the dispersive and attenuation properties of higher-order finite elements. The method employs only a minor modification to the technique of real wavenumber analysis but is completely general, and can accommodate any finite element discretization and spectral order. This extension of the usual procedure involves only a slight modification to the standard Fourier analysis yet allows for a complete characterization of the 'stopping' band phenomena found in higher order finite element discretizations – a characterization that has previously escaped other analysts.

Before the assembly of the finite element equations, for hierarchical elements, it is necessary to decouple the degrees of freedom associated with the interior of the element domain from the element dynamic stiffness (impedance) matrix. The dynamic stiffness matrix $\boldsymbol{s}^e$ is partitioned into the following matrix block form,

$$\boldsymbol{s}^e = \begin{bmatrix} \boldsymbol{s}_{11} & \boldsymbol{s}_{12} \\ \boldsymbol{s}_{12}^T & \boldsymbol{s}_{22} \end{bmatrix} \in \mathbb{R}^{(p+1)\times(p+1)} \tag{5.21}$$

The matrix partition $\boldsymbol{s}_{22} \in \mathbb{R}^{(p-1)\times(p-1)}$ corresponds to interactions among internal shape functions, $\boldsymbol{s}_{12} \in \mathbb{R}^{2\times(p-1)}$ is the coupling matrix partition due to interactions between internal shape functions and nodal shape functions, and finally, $\boldsymbol{s}_{11} \in \mathbb{R}^{2\times 2}$ corresponds to interactions among the nodal shape functions N_1 and N_2. After static

condensation and assembly a tridiagonal system of linear equations in terms of nodal variables is obtained. The the nth equation of this system takes the form (see [147] for further details):

$$G_1(\alpha)\phi_{n-1} - 2G_2(\alpha)\phi_n + G_1(\alpha)\phi_{n+1} = 0 \tag{5.22}$$

In this difference stencil, the coefficients $G_1(\alpha)$ and $G_2(\alpha)$ are polynomials of degree $2p$ in the nondimensional frequency:

$$\alpha = \omega h/c \tag{5.23}$$

An exponential solution to (5.22) is assumed having the form:

$$\phi_n = Ae^{ik^h x_n}, \quad x_n = nh \tag{5.24}$$

where $k^h \in \mathbb{C}$ is the complex valued numerical wavenumber and $i = \sqrt{-1}$. Substitution of (5.24) into (5.22) results in the wavenumber-frequency relation,

$$\cos(\beta) = \lambda(\alpha) \tag{5.25}$$

where

$$\lambda(\alpha) := \frac{G_2(\alpha)}{G_1(\alpha)} \tag{5.26}$$

and β is the normalized discrete wavenumber:

$$\beta = k^h h \tag{5.27}$$

At this point, we depart from the standard finite element dispersion technique in which real frequency roots of (5.25) are sought for a given real wavenumber. Instead, we seek all the wavenumber roots of (5.25) for a given real frequency. The complex roots $\beta \in \mathbb{C}$, of (5.25) are found using the complex arc cosine; (see [143, 147] for details.

5.4.3 Dispersion and attenuation results

In this section we discuss the complex wavenumbers that arise from the Fourier analysis of high-order finite elements. It will be shown that the finite element characteristic equation (5.25) admits pure real wavenumbers, (propagating solutions) only when the frequency falls within a finite number of bands called passing bands. The number of passing bands is equal to the spectral order p of the elements in the mesh. In addition it will be shown that there are p stopping bands where the wavenumbers are complex. The results in this section apply to Galerkin finite element discretizations with $\tau = 0$.

For a uniform mesh of p–version finite elements with spectral order ($p = 2$), the frequency dependence of the real and imaginary parts of $k^h \in \mathbb{C}$ are plotted in Figure 5.8. In this case, there are two passing bands: one for frequencies between $0 < \alpha < \alpha_1$ and one for frequencies between $\alpha_2 < \alpha < \alpha_{max}$. Within these bands,

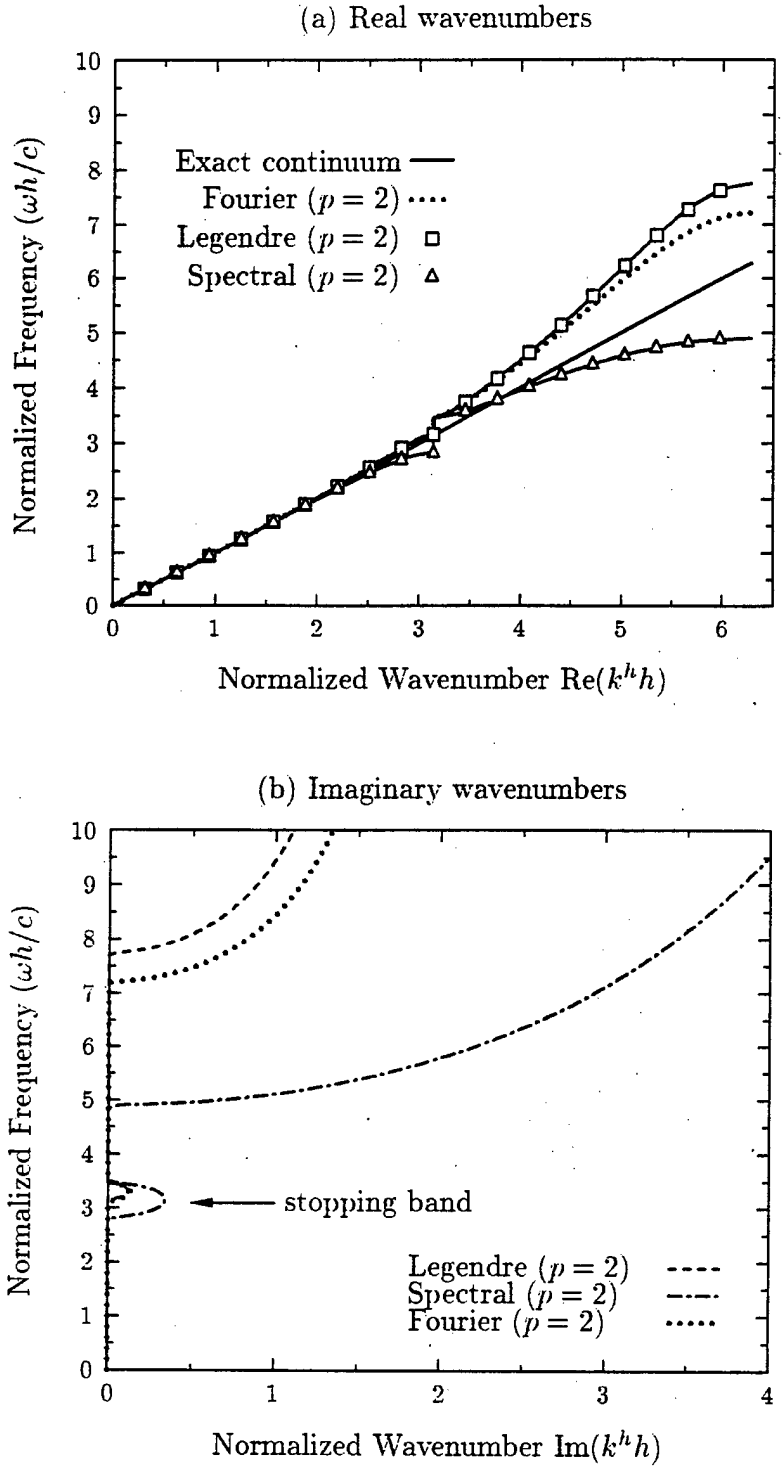

Figure 5.8: Frequency spectrum comparing quadratic finite element approximations obtained from Galerkin method: (a) Real wavenumbers, (b) Imaginary wavenumbers

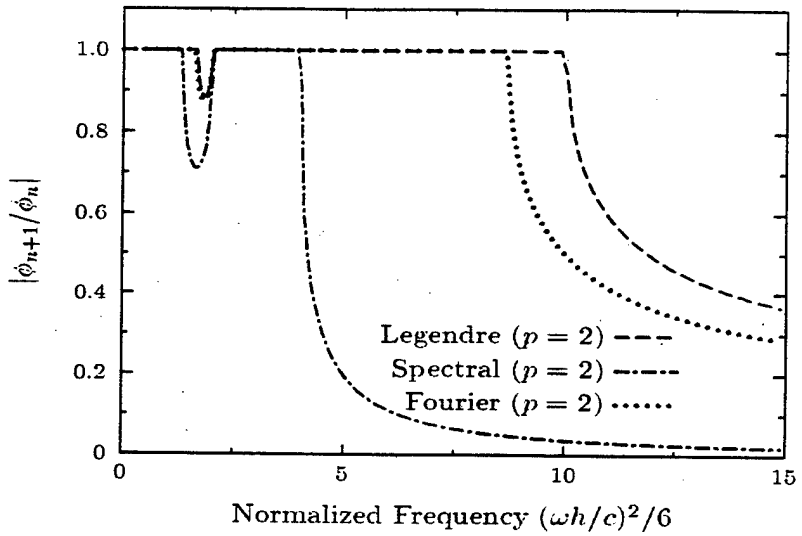

Figure 5.9: Amplitude spectrum for quadratic elements

there is a purely propagating solution with $|\lambda| < 1$ and the characteristic equation is satisfied by,

$$Re(\beta) = \cos^{-1}(\lambda), \quad \text{and} \qquad Im(\beta) = 0 \tag{5.28}$$

The dispersion curve in the lower passing band is called the acoustical branch and the upper passing band is referred to as the optical branch.

In the frequency range between these two passing passing bands, $\alpha_1 \leq \alpha \leq \alpha_2$, there is one frequency band where the numerical wavenumbers are complex. In this band, $|\lambda| > 1$ and the characteristic equation is satisfied by,

$$Re(\beta) = \pi, \quad \text{and} \qquad Im(\beta) = \cosh^{-1}(-\lambda) \tag{5.29}$$

This complex wavenumber band is called a stopping band because in this frequency range, the real part of the wavenumber is constant and the imaginary component results in an attenuated wave solution with an amplitude decay proportional to the exponential of the imaginary wavenumber.

Above the cut-off frequency, $\alpha > \alpha_{max}$, $\lambda > 1$ and the characteristic equation is satisfied by,

$$Re(\beta) = 2\pi, \quad \text{and} \qquad Im(\beta) = \cosh^{-1}(\lambda) \tag{5.30}$$

In this case, the solution propagates with a fixed wavelength equal to the limit of resolution – one quadratic element per wavelength or $Re(\beta) = 2\pi$ with strong exponential amplitude decay from node to node along the mesh.

The amplitude spectrum for $p = 2$ is plotted in Figure 5.9. The amplitude ratio is constant in the first passing band (acoustical branch) up to the complex wavenumber band where the imaginary wavenumber components produce an amplitude decay. In the stopping band, the amplitude is attenuated until a minimum is reached and then increases back up to the exact ratio of one. The amplitude ratio continues to be exact throughout the second passing band (optical branch) until it reaches the cut-off

where it is strongly attenuated. The cutoff frequency for the Spectral element falls well below that of the Legendre and Fourier elements.

Invoking a signal processing analogy, the character of this amplitude spectrum illustrates how the p–version finite element mesh acts as a band-pass filter – allowing propagation of all frequencies in the passing bands, while weakly attenuating frequencies in the complex wavenumber band, and strongly attenuating frequencies above the cut-off frequency.

As the spectral order is increased to $p = 3$, the spatial resolution limit extends to $Re(\beta) = 3\pi$. Figure 5.10 shows that there are 3 passing and 3 stopping bands present in the frequency spectrum. The first complex wavenumber band occurs when $Re(\beta) = \pi$. The frequency range for the first stopping band is very small and appears as a small perturbation in the frequency curve for the imaginary wavenumber component at approximately $\alpha = \pi$, see Figure 5.10. The second stopping band occurs when the real wavenumber component reaches 2π and is much larger, with large imaginary wavenumber components present.

As a result of these complex wavenumber bands, we observe the amplitude attenuation characteristics shown in Figure 5.11(top). The amplitude ratio is again constant in the passing bands up to the first complex wavenumber band, where there is a very small attenuation loss. Isolating this frequency region in Figure 5.11(bottom), we observe that the maximum amplitude error is only 2.5 percent for the Spectral elements and only 1 percent for Legendre and Fourier elements. Thus in this first complex wavenumber region waves propagate with constant wavenumber $Re(\beta)$ and only a very small amplitude decay. The amplitude attenuation in the second complex frequency band is very large and in practice the element size h should be chosen to avoid this nondimensional frequency range.

Results for spectral orders $p = 4$ and $p = 5$ are given in [147]. For nondimensional frequencies up to $\alpha = (p-2)\pi$, the dispersion curves approximate the exact line with slope one. As the nondimensional frequency increases, the Legendre and Spectral elements exhibit loss of accuracy in the upper two optical branches. In contrast, the Fourier element maintains accuracy up to $\alpha = (p-1)\pi$.

In conclusion, the following dispersive properties are observed: (1) There are p passing bands and p stopping bands, (2) the limit of resolution occurs at $Re(\beta) = \pi p$. In addition, the amplitude attenuation in the first few complex wavenumber (stopping) bands is very small and converges in the limit of large spectral orders to the exact amplitude ratio of one. Thus for large spectral orders the first few stopping bands are not of practical significance. As a general trend we observe that the amplitude error is greater for the Spectral elements than the Legendre and Fourier elements and the cutoff for Spectral elements always occurs before that of Legendre elements.

Analysis of phase error

Figure 5.12 shows the phase accuracy of the Galerkin finite element approximation versus a nondimensional real wavenumber $(\beta/\pi p)$. Throughout the acoustic branch, the phase error converges to the exact solution as the spectral order is increased.

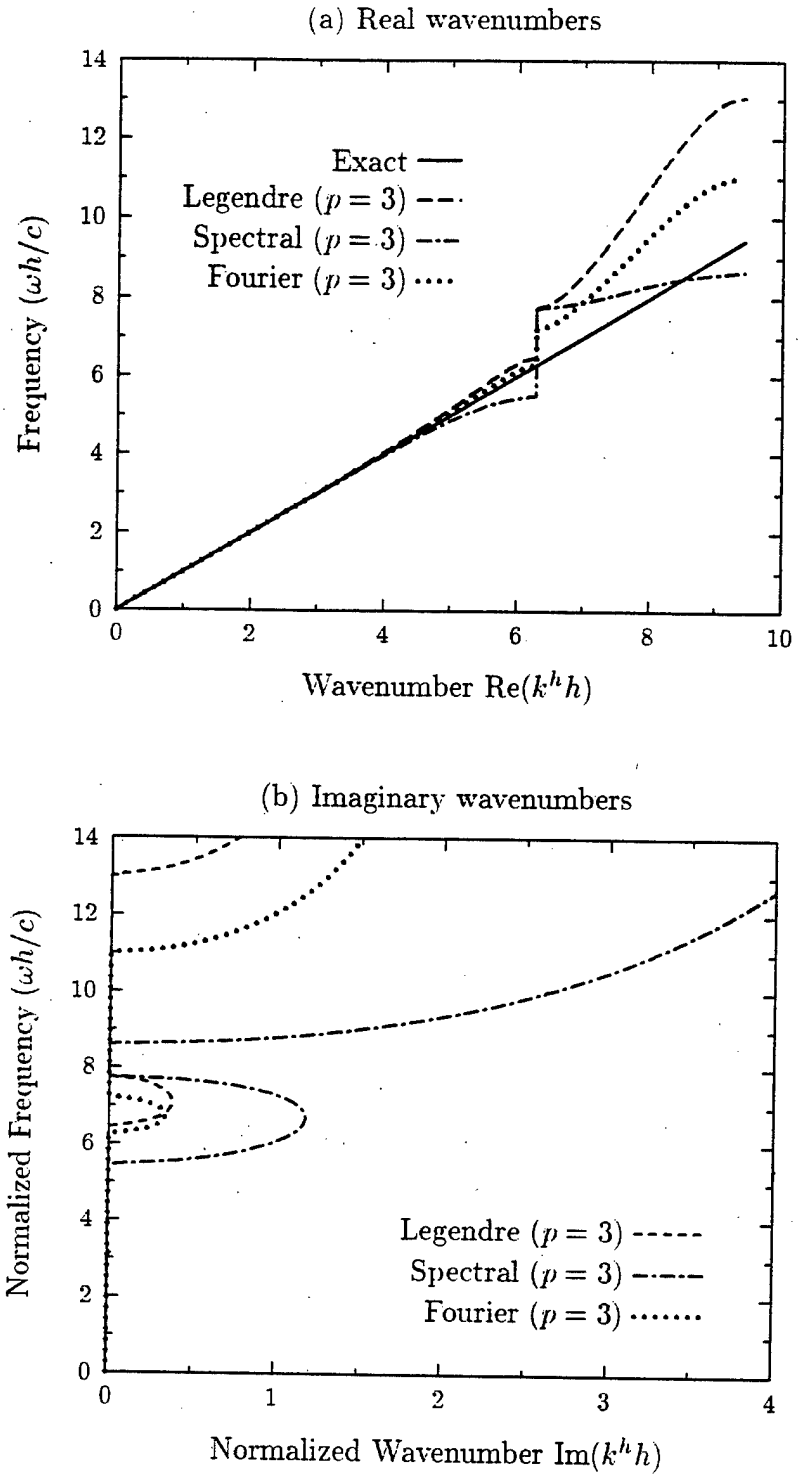

Figure 5.10: Frequency spectrum comparing cubic finite element approximations obtained from the Galerkin method: (a) Real wavenumbers, (b) Imaginary wavenumbers

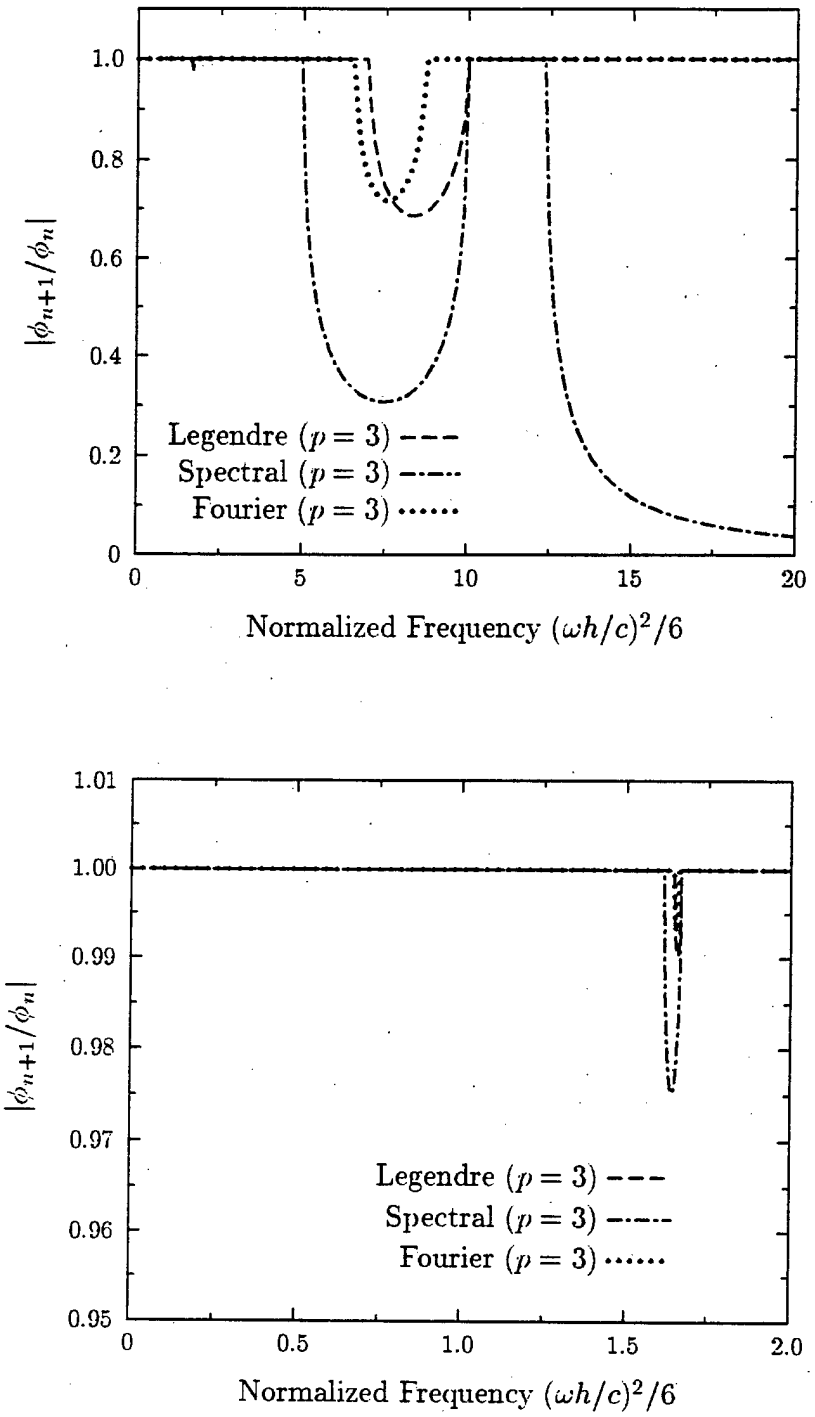

Figure 5.11: (Top): Amplitude spectrum for cubic elements. (Bottom): Isolation of amplitude spectrum near first complex wavenumber band.

Clearly, in the practical range $0 \leq k^h h/\pi p \leq .5$ the higher-order p–type elements exhibit increased accuracy compared to low-order finite elements. for the same number of degrees of freedom. In the optical branches, the dispersive errors increase. The use of trigonometric shape functions in the Fourier elements decreases the phase error found in the optical branch as compared to the Legendre case.

The convergence rate is investigated by examining the phase as the number of solution variables per wavelength is increased. In general, in the range of resolution, the phase error for spectral order p is of the order,

$$\frac{k^h}{k} - 1 = \mathcal{O}(kh)^{2p} \tag{5.31}$$

with the nodal solution,

$$\phi_n = A\mathrm{e}^{ikx_n[1\pm\mathcal{O}(kh)^{2p}]} \tag{5.32}$$

This result is verified for spectral orders of $p = 1, 2, 3$ in Figure 5.13, where the slope of the lines show the rate of convergence of the phase error to be $2p$. Additional results are reported in [147].

Analysis of attenuation

Although the amplitude from node to node is exact for frequencies within the passing bands, it is possible for the high-order finite element solution to exhibit amplitude attenuation at points internal to physical nodes. Analysis of amplitude attenuation at points internal to the physical nodes is investigated by examining quadratic elements of order $p = 2$. In this case, the dynamic stiffness matrix is assembled without condensation and the internal variable is written in terms of the center point. The resulting stencils related to equations n and $n \pm 1/2$ are of the form,

$$S(\alpha) := (K - \alpha^2 M) = 0 \tag{5.33}$$

and K and M are (2×5) stiffness and mass coefficient matrices, with solution vector,

$$\boldsymbol{\phi}^T = \begin{pmatrix} \phi_{n-1} & \phi_{n-1/2} & \phi_n & \phi_{n+1/2} & \phi_{n+1} \end{pmatrix} \tag{5.34}$$

Allowing for different amplitudes at the exterior nodes n, and element center nodes $n \pm 1/2$ we assume the complex exponential solutions,

$$\phi_n = A_1\mathrm{e}^{i\beta(n)} \tag{5.35}$$

$$\phi_{n+1/2} = A_2\mathrm{e}^{i\beta(n+1/2)} \tag{5.36}$$

Substitution of the above two solutions into (5.33) results in a symmetric characteristic matrix. Solving this system, the amplitude ratio $r = A_2/A_1$ is found. Further details for this analysis are given in [144].

Figure 5.14 shows the amplitude ratio plotted as a function of wavenumber. The curves lying above the ratio of one are acoustical branches, while those below are optical branches. For quadratic Legendre elements, amplitude attenuation is insignificant for $k^h h < 2\pi/3$ (three elements per wavelength), while for quadratic Spectral elements amplitude attenuation is insignificant for $k^h h < \pi/2$ (four elements per wavelength). Results for Fourier elements are similar to the Legendre elements. The physical interpretation of this result is discussed at length in [143].

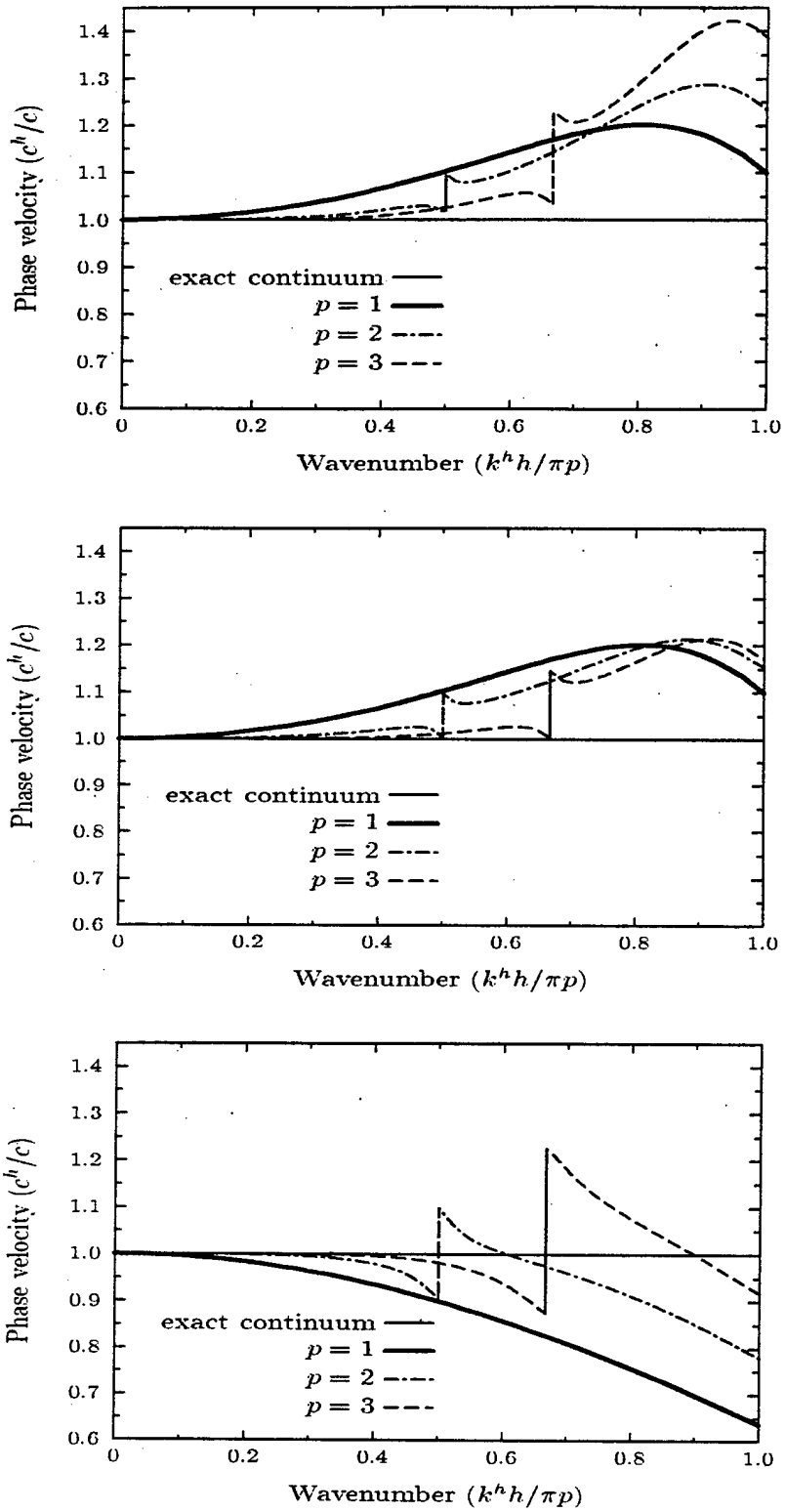

Figure 5.12: Phase error for spectral orders $p = 1, 2, 3$. (top) Legendre basis, (middle) Trigonometric basis, (bottom) Spectral basis.

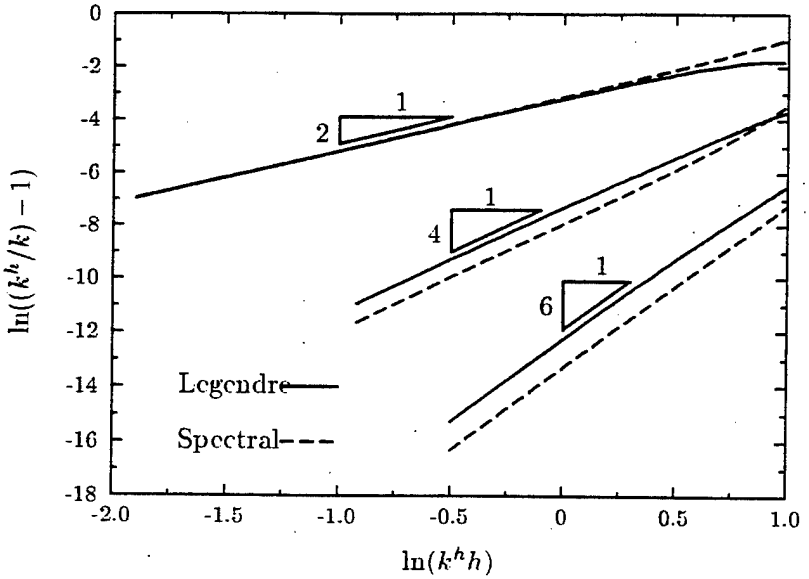

Figure 5.13: Convergence of phase error with polynomial orders $p = 1, 2, 3$.

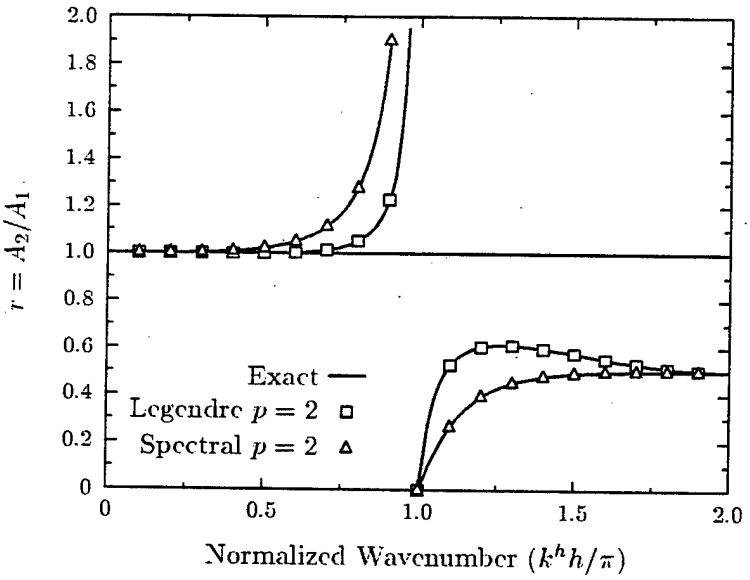

Figure 5.14: Amplitude spectrum for quadratic elements at interior nodes

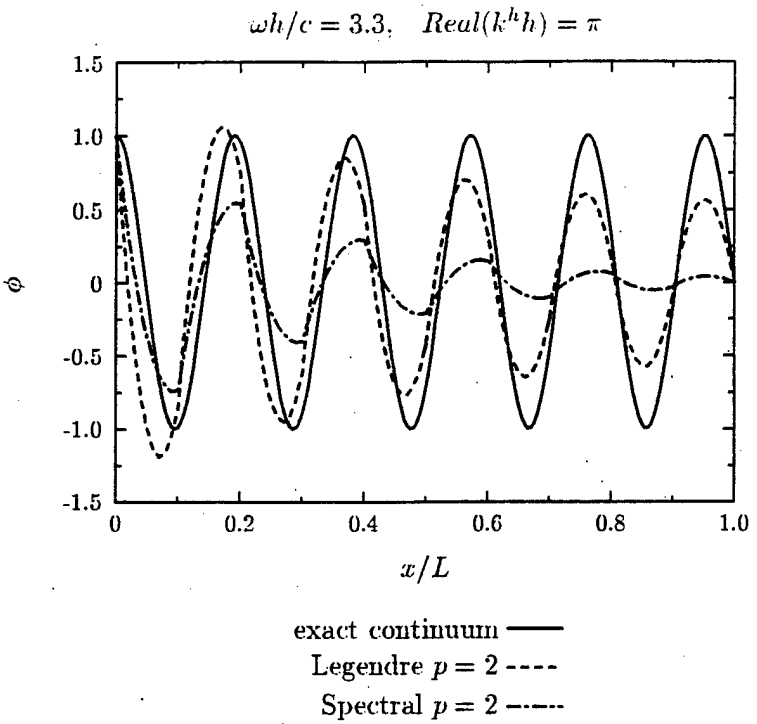

Figure 5.15: Harmonic decaying wave solution for example problem for a driving frequency in the stopping (complex wavenumber) band.

5.4.4 Illustration of the complex wavenumber band

The role that complex wavenumbers play in the practical solution of physical boundary value problems is revealed in the time-harmonic solution for the Helmholtz equation with Dirichlet boundary conditions $\phi(0) = \bar{\phi}$ and $\phi(L) = 0$, where L is the length of the domain. After discretizing with N uniformly spaced elements of length h, it can be shown that the finite element solution is,

$$\phi^h(x_n, \omega) = \bar{\phi}\frac{\sin(k^h(L - x_n))}{\sin(k^h L)} \qquad n = 0 : N \tag{5.37}$$

where k^h is the numerical wavenumber defined in (5.25) and $L = Nh$ and $x_n = nh$. The important point here is that this wave solution consists of the same numerical wavenumbers present for the infinite domain found by our Fourier analysis except that both outgoing and incoming waves are present. In Figure 5.15, the response for a frequency in the complex wavenumber stopping band is plotted. It is clear that the response has a propagating component fixed at $Re(k^h h) = \pi$ corresponding to two elements per wavelength, while the imaginary component manifests itself in the amplitude decay. The connection between the dispersion curves derived from the Fourier analysis and the discrete eigenfrequencies of this model problem is discussed in [143] together with an example of how the complex wavenumber analysis can be used as a tool to improve the solution for vibration problems.

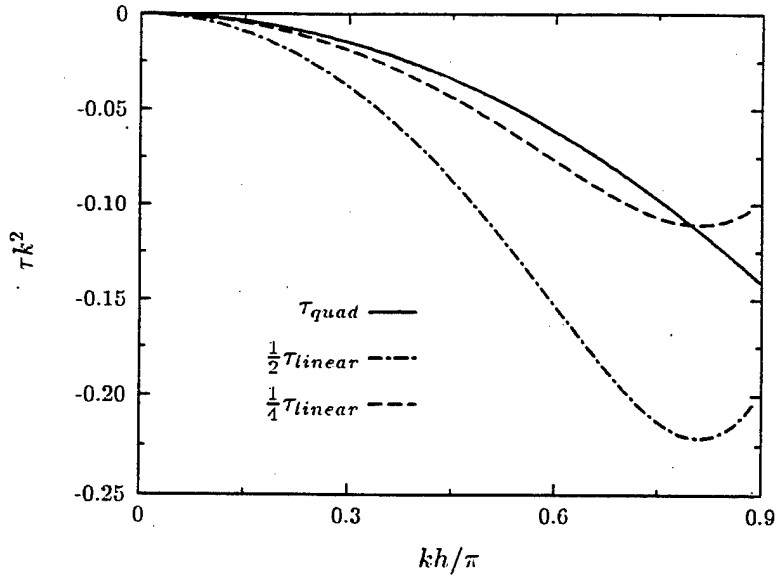

Figure 5.16: GLS mesh parameter τ_{quad} for quadratic interpolation compared to estimates based on fractions of the linear τ_{linear}.

5.4.5 Optimal GLS parameter for quadratic elements

With the aid of the complex wavenumber analysis technique described in Section 5.4.2 the optimal definition of τ_{quad} for quadratic $p = 2$ basis functions may be obtained. By substituting the exact wave number into the finite element dispersion relation for quadratic elements, and with the design criteria that the phase be exact $k^h = k$, leads to a quadratic equation for the optimal value of τ_{quad}. Defining the nondimensional parameters $\alpha := kh$, and $\hat{\tau} := \tau k^2$, the following quadratic equation is obtained:

$$c_2\hat{\tau}^2 + c_1\hat{\tau} + c_0 = 0 \tag{5.38}$$

where $c_j(\alpha)$, $j = 0, 1, 2$ are frequency dependent coefficients defined in [143]. The optimal GLS parameter τ_{quad} is obtained by solving this quadratic equation, for $\hat{\tau}$. As described earlier, for quadratic elements there are two frequency ranges where waves are allowed to propagate with real wavenumbers. In the above expression, the minus sign is used for the range $0 < kh < \pi$ while a plus sign is used for the range $\pi < kh < 2\pi$, where 2π is the limit of resolution for quadratic elements. At $kh = \pi$, there exists a discontinuity in the value of τ_{quad}. This phenomenon is related to the 'stopping bands' present in the frequency-wavenumber spectrum for high-order finite element discretizations where allowed waves possess amplitude attenuation. Figure 5.16 plots the optimal τ_{quad} obtained in [143] together with simple approximations based on fractions of the GLS parameter derived earlier for linear interpolations. Comparing these results, a practical estimate useful for computation is $0.25\tau_{linear}$.

Further details for the results obtained in this section are given [143]. Using the technique of complex wavenumber Fourier analysis the optimum GLS mesh parameter

for quadratic elements was derived. GLS finite elements for time-harmonic wave propagation using higher-order basis functions require that a suitable definition of τ be obtained for each spectral order p. In this section, it was shown that GLS parameters for elements with basis functions of high spectral order p can be approximated by simple fractions of low-order GLS parameters. In particular, for quadratic elements ($p = 2$), the value $\tau = .25\tau_{linear}$ proves to be a useful estimate.

Chapter 6

Multidimensional Configurations

In Chapter 5 we considered simplified inhomogeneous radiation problems—radiation loading of acoustic media by prescribed boundary conditions as induced by the vibration of a structure (thereby emphasizing boundary conditions of the Neumann type), with particular reference to exterior domains. In this chapter this work is extended to more general settings. The effect of nodal spacing and the performance of the methods proposed on problems with spherical-wave solutions is investigated. We examine the performance of the methods proposed in multidimensional meshes. The general convergence of solutions obtained by Galerkin/least-squares finite element methods is proved, with error bounds obtained for the case of unresolved waves, guaranteeing the performance of these methods on configurations of practical interest. The performance of the methods proposed is validated by numerical examples.

6.1 Spherical Waves

In the following we examine spherical configurations to provide a more challenging test of the performance of the numerical methods considered, since in this case propagating solutions are of decaying amplitude. Spherical waves also provide a model for three-dimensional problems on which to validate the performance of methods that were designed on basis of a plane-wave model.

We consider the domain to be discretized by a mesh of linear elements. In the absence of source terms the exact solution is

$$\phi \quad = \quad ce^{ikr}/r \tag{6.1}$$

where the constant is adjusted to satisfy either a Dirichlet or a Neumann boundary condition on the physical boundary. Nodal values of the finite element solution are denoted $\phi_A \quad = \quad \phi^h(r_A)$

6.1.1 Nodal spacing

First we wish to characterize the amplification from node to node of numerical solutions modeling waves with decaying amplitude, so that only interior stencils need be

investigated. The Ath equation of the tridiagonal system for a Galerkin solution on a uniform mesh, for which $r_A = Ah$, yields the stencil

$$\begin{aligned} &[5(3A^2 - 3A + 1) + 3\alpha^h(10A^2 - 10A + 3)] && \phi_{A-1} \\ &-2[5(3A^2 + 1) - 6\alpha^h(10A^2 + 1)] && \phi_A \\ &+[5(3A^2 + 3A + 1) + 3\alpha^h(10A^2 + 10A + 3)] && \phi_{A+1} = 0 \end{aligned} \tag{6.2}$$

In this analysis lower node numbers therefore correspond to points that are in the vicinity of a disturbance, i.e, a boundary or a source, and larger numbers represent the far field. For $A \gg 1$ this stencil tends to the stencil derived for plane waves in Chapter 5. Seeking solutions in which $\phi_A \sim \rho^A/(Ah)$ we obtain a quadratic polynomial in ρ, which represents the nodal amplification factor. It was noted in [3] that this representation of the finite element solution is inappropriate for finite node numbers when $kh \ll \pi$, since then there are wide fluctuations in the values of the coefficients of the stencil (6.2). The two solutions to the quadratic equation for ρ represent outgoing and incoming waves (or exponential growth and decay). Recall that eq. (6.2) is an interior stencil and does not take into consideration boundary conditions, which separate physical solutions from nonphysical ones. By comparison to (6.1) we see that nodal exactness would require $\rho = e^{ikh}$ However, solving the quadratic equation for ρ shows that the Galerkin formulation yields different results. We have seen from the study of plane waves that for $\alpha^h \leq 1$ the Galerkin solution maintains the character of a propagating plane wave, and decays beyond that value. In the case of spherical waves the value of α^h at which decay sets in varies from node to node (Fig. 6.1). Nevertheless, we see that for $\alpha^h \leq 1$ the Galerkin solution does maintain the character of propagating spherical waves (recall that this is well beyond the limit of resolution). Within this limit

$$\begin{aligned} |\rho|^2 &= \frac{A+1}{A-1}\frac{5(3A^2 - 3A + 1) + 3\alpha^h(10A^2 - 10A + 3)}{5(3A^2 + 3A + 1) + 3\alpha^h(10A^2 + 10A + 3)} \\ &= 1 + \frac{2}{A-1}\frac{5 + 9\alpha^h}{5(3A^2 + 3A + 1) + 3\alpha^h(10A^2 + 10A + 3)} \\ &\geq \left|e^{ikh}\right|^2 = 1 \end{aligned} \tag{6.3}$$

i.e., the amplification factor on a uniform mesh is always overestimated by the numerical solution. The error in nodal amplification is shown in Fig. 6.2, and for uniform meshes is virtually insensitive to the wave number. The largest error of approximately 5% occurs at node 2 for $kh = 0$. The amplification error is more significant for higher node numbers, since it is raised to a higher power in computing the amplitude, but the error itself is lower, more than compensating for this fact (Fig. 6.3).

The amplitude error is not substantial, but nevertheless we would like to examine the possibility of reducing it by appropriate nodal spacing. We account for arbitrary meshes by denoting the length of element e as $h^e := r_{A+1} - r_A$, and seeking solutions in which $\phi_A \sim |\rho|^{r_A/h} e^{ik^h r_A}/r_A$, where k^h allows for a phase error in the numerical solution, and, for convenience in the following analysis, h is the *local* mean element

Figure 6.1: Limit of propagation in the Galerkin solution on a uniform mesh for spherical waves: value of α^h at which decay sets in.

length. Equation (6.3) is generalized for arbitrary nodal spacing

$$|\rho|^2 = \frac{r_{A+1}h^e}{r_{A-1}h^{e-1}} \frac{\sin k^h h^{e-1}}{\sin k^h h^e} \frac{20(r_A^2 + r_A r_{A-1} + r_{A-1}^2) + (kh^{e-1})^2 (3r_A^2 + 4r_A r_{A-1} + 3r_{A-1}^2)}{20(r_{A+1}^2 + r_{A+1}r_A + r_A^2) + (kh^e)^2 (3r_{A+1}^2 + 4r_{A+1}r_A + 3r_A^2)} \quad (6.4)$$

For correct amplification we require $|\rho| = 1$. Recalling that for uniform meshes the amplification was virtually insensitive to wave number, we simplify this expression by considering the limit of well-resolved waves ($kh \to 0$ which implies that $k^h \to k$, so that $\sin k^h h^e$ may be replaced by $k^h h^e$, the first term in its Taylor series expansion at 0). Exact amplification is obtained in this case when the nodal spacing satisfies

$$r_A^2 = r_{A+1} r_{A-1} \quad (6.5)$$

which we term a 'geometric mesh'. In a spherical configuration, if a wedge is discretized radially according to this scheme, the aspect ratio is equal for all elements. Figure 6.4 shows the approximate error in amplification for the geometric mesh, neglecting the phase error. This spacing improves the amplification factor considerably for well-resolved waves. However, the error in amplification is significantly worse than that of the uniform mesh for larger numerically nondimensionalized wave numbers, particularly for larger node numbers (cf. Fig. 6.2). We therefore do not recommend

Figure 6.2: Amplification error of the Galerkin solution on a uniform mesh for spherical waves, from eq. (6.3).

the use of geometric meshes, except in the vicinity of disturbances. This conclusion is borne out by numerical experience that indicates a deterioration in the quality of solutions computed on a geometric mesh in comparison to uniform discretization.

The amplification factor might be improved for lower wave resolution by considering the first-order correction to the Taylor series expansion for the sine function, which yields

$$\frac{r_{A+1}r_{A-1} - r_A^2}{r_{A+1}^2 + r_{A+1}r_{A-1} + r_A^2} = \frac{r_{A-1}\left(k^h\right)^2 (h^e - h^{e-1})}{6 - (k^h h^{e-1})^2} \tag{6.6}$$

but it is difficult to derive the nodal spacing that satisfies this criterion.

6.1.2 Phase accuracy

We wish to characterize the phase error for the region in which the numerical solution is propagating, and examine the performance of Galerkin/least-squares, that was designed by employing plane-wave models, for problems with spherical waves.

For a uniform mesh we write

$$\rho \quad = \quad |\rho| e^{ik^h h} \tag{6.7}$$

The phase error in the Galerkin solution is shown in Fig. 6.5. The phase lag in the far field (e.g., node 50) is virtually indistinguishable from the case of plane waves

Figure 6.3: Amplitude error of the Galerkin solution on a uniform mesh for spherical waves, adjusted for position, from eq. (6.3).

(node ∞, cf. Fig. 5.3). As a matter of fact, the phase accuracy at lower node numbers is quite similar to the case of plane waves as well. As a result we expect the Galerkin/least-squares method, which was designed on the basis of consideration of phase accuracy of plane waves, in general to perform quite well for this case too. Recall that our representation of the finite element solution did not account well for the behavior at small numerically nondimensionalized wave numbers. Despite the indication in the figure to the contrary, we assert that the phase error vanishes as the mesh is refined (as verified by the convergence proof in Section 6.3).

Employing Galerkin/least-squares considerably reduces the phase error in the entire mesh, as expected. Figure 6.6 shows the phase error for the Galerkin/least-squares method that provided an exact phase for the plane wave model (see Fig. 5.4). These results are far superior to the phase error of Galerkin solutions. For example, for node 5 at $kh = \pi/2$ (which we termed the limit of resolution), the Galerkin/least-squares phase error is approximately 0.5%, whereas it is approximately 8% for the Galerkin solution (see Fig. 6.5).

6.1.3 Numerical examples

Consider a sphere of radius a pulsating uniformly. This example provides a model for validating the performance of the methods proposed on three-dimensional configurations. The exact solution to the problem is given in (6.1), where the constant is

Figure 6.4: Approximate amplification error of the Galerkin solution on a geometric mesh for spherical waves from eq. (6.4).

adjusted to satisfy the boundary conditions on the physical boundary, and for the purpose of the following calculations we set $c = 1$. The DtN boundary is positioned at $R = 2a$, and the resulting computational domain is discretized with 10 equal-length linear elements in the radial direction, taking advantage of spherical symmetry.

We examine Neumann problems in the region in which the exact solution is a propagating spherical wave, similar to the Neumann problems with propagating plane-wave solutions reported in [57]. With good resolution, approximately 18 elements per wave ($\alpha^h = 1/100$, the wave length is approximately equal to the diameter of the sphere), both the Galerkin and the Galerkin/least-squares methods give accurate results (Fig. 6.7). As α^h is increased to $1/10$ we approach the limit of resolution (six elements per wave, Fig. 6.8, the wave length is over half the radius of the sphere) and some deterioration can be seen (cf. Fig. 5.6 for the plane wave solution). As expected, the Galerkin solution exhibits error in both magnitude, and in phase. The latter causes the loss of nodal accuracy to become more noticeable towards the DtN boundary. There is little error apparent in the Galerkin/least-squares solution. In Fig. 6.9 we show the limit of resolution ($\alpha^h = 1/5$, four elements per wave, the wave length is less than half of the sphere radius), and only the real part of each solution is shown. The Galerkin solution has visibly deteriorated, but would improve with mesh refinement. The Galerkin/least-squares solution slightly overestimates the magnitude, but it is still extremely accurate. The phase lag in the Galerkin solution is apparent in this figure. The high degree of accuracy of the Galerkin/least-squares

Figure 6.5: Phase error of the Galerkin solution on a uniform mesh for spherical waves.

solution on the artificial boundary on all of these problems is particularly important for computing far-field solutions by the DtN method.

Beyond the limit of resolution we employ the Galerkin/least-squares method that damps the solution, defined in (5.7). The solution for $\alpha^h = 1/2$ (less than three elements per wave, the wave length is 1/4 of the sphere radius) is shown in Fig. 6.10. As in the case of plane waves (see Fig. 5.7), the solution essentially vanishes over the entire domain except for the element adjacent to the wet surface, thereby approximating the flux on the wet boundary (2.6), in this case

$$\phi^h_{,n} \quad = \quad ik\mathrm{h}/3.2055 \qquad \text{on } \Gamma_h \tag{6.8}$$

In summary, the Galerkin/least-squares method was designed on the basis of model problems of acoustics with plane-wave solutions. In this section we have verified that this method retains its advantageous features, namely a high degree of accuracy to the limit of resolution of four elements per wave and damping of numerical solutions beyond that resolution, on more challenging configurations. We now proceed to prove convergence of the numerical solution to the exact solution with mesh refinement.

Figure 6.6: Phase error of the Galerkin/least-squares solution on a uniform mesh for spherical waves.

6.2 Design of Galerkin/Least-squares Formulations

As discussed earlier, an important feature of Galerkin/Generalized Least-Squares methods is the introduction of a local mesh parameter into the variational equation that may be designed to provide accurate solutions with relatively coarse meshes; in effect extending the range of finite element solutions to higher frequency calculations. In the previous chapter this design goal was accomplished for one-dimensional problems using dispersion analysis. While the GLS mesh parameter obtained from a one-dimensional analysis can be used for multi-dimensional applications, it was shown in [145] that this parameter is not optimal in two- or three-dimensions. In this chapter the selection of the optimal GLS mesh parameter for the multi-dimensional Helmholtz equation is considered, and leads to elements that exhibit improved accuracy. The methods presented are mainly drawn from [143, 145, 152].

Optimal GLS methods for time-harmonic wave propagation in multi-dimensions were first investigated in Thompson and Pinsky [145] with extensions to exterior problems in [143, 152]. Although for any given direction of wave propagation, it is shown that an optimal GLS mesh parameter can be obtained, in general, the direction of wave propagation will not be known *a priori*. To remedy this difficulty, a GLS parameter is found which reduces phase error for all possible wave vector directions over an element. By performing a multi-dimensional Fourier analysis the phase accuracy and directional properties of the Galerkin Least-Squares and Galerkin/Gradient

Figure 6.7: Uniformly pulsating sphere of radius a, $R = 2a$, $ka = \sqrt{12}$, 18 elements per wave.

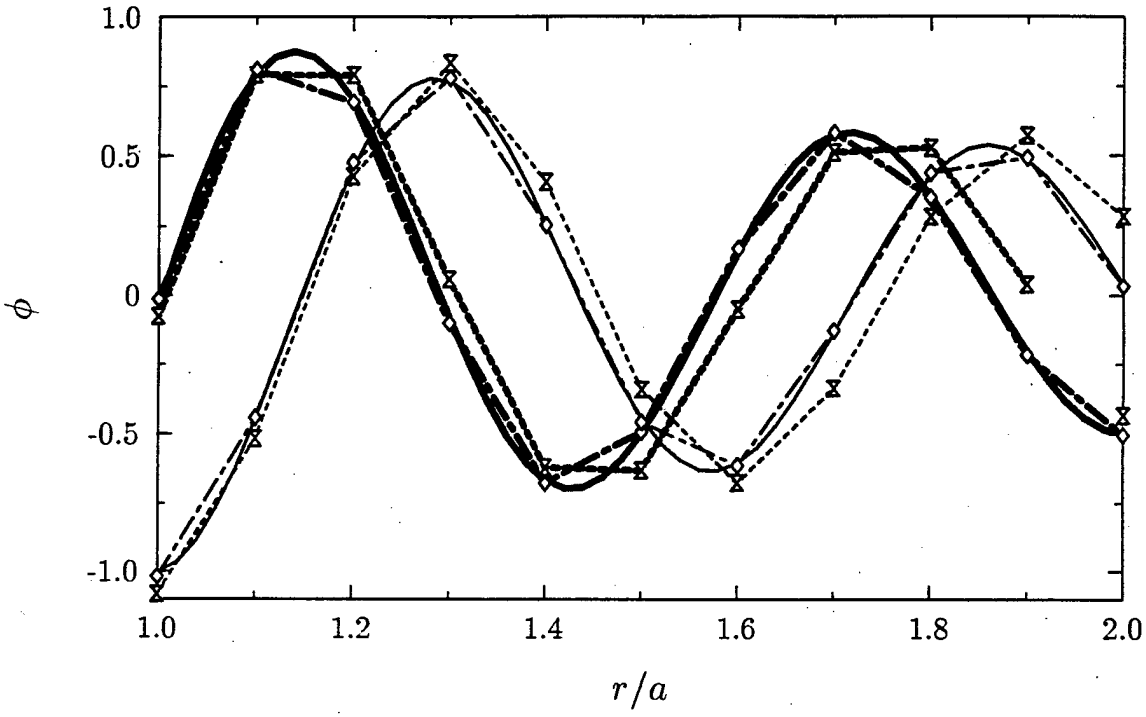

Figure 6.8: Uniformly pulsating sphere of radius a, $R = 2a$, $ka = \sqrt{120}$, six elements per wave.

Figure 6.9: Uniformly pulsating sphere of radius a, $R = 2a$, $ka = \sqrt{240}$, four elements per wave.

Figure 6.10: Uniformly pulsating sphere of radius a, $R = 2a$, $ka = \sqrt{600}$, damping of unresolved waves ($\phi^h_{,n} \propto \phi_{,n}$ on Γ_h).

Least-Squares solution is characterized over all wave vector magnitudes and directions.

To illustrate the ideas involved for the selection of optimal Galerkin Least-Squares mesh parameters for multi-dimensional wave propagation problems, consider the Helmholtz equation in two-dimensions:

$$\mathcal{L}\phi \equiv \nabla^2\phi + k^2\phi = -f \qquad \text{in } \Omega \tag{6.9}$$

where $k = .\omega/c > 0$ is the wavenumber with wavelength $2\pi/k$ and Ω is the spatial domain of interest. The Helmholtz equation in $\mathbb{R}^2$ admits the plane-wave solution,

$$\phi(x,y) = e^{i(k_x x + k_y y)} \tag{6.10}$$

where ω and the wavevector components k_x and k_y are linked by the characteristic equation,

$$\left(\frac{\omega h}{c}\right)^2 = (k_x h)^2 + (k_y h)^2 \tag{6.11}$$

and h is a problem dependent characteristic length. This nondispersive relation is satisfied by the directional wavevector components $k_x = k\cos\theta$ and $k_y = k\sin\theta$, where the normal to the plane wave is oriented at angle θ relative to the x-axis. Alternatively, the characteristic equation (6.11) can be obtained by a two-dimensional Fourier transform from physical space to wave space through the transform operation,

$$\tilde{F}(k_x,k_y) := \frac{1}{\sqrt{2\pi}} \int_{-\infty}^{\infty}\int_{-\infty}^{\infty} F(x,y)\mathrm{e}^{-i(k_x x + k_y y)}dxdy \tag{6.12}$$

The discrete counterpart to this continuous transform will be used as a tool for the design of improved finite element methods for the solution of the two-dimensional Helmholtz equation.

6.2.1 GLS Dispersion Relations

Consider a uniform mesh of bilinear elements,

$$\mathbf{R}_h^2 = \{(x,y) \in \mathbf{R}^2 = (mh_x, nh_y)\,,\ (m,n) \in \mathbf{Z}\} \tag{6.13}$$

with element sides h_x in the x-direction and h_y in the y-direction. Finite element difference relations are obtained by assembling a patch of four bilinear elements. The result is the difference stencil associated with the interior node $\phi_{m,n} = \phi^h(mh_x, nh_y)|\mathbf{R}_h^2 \mapsto \mathbb{C}$.

$$F(k) = S\phi_{m,n} - \gamma k^2 M\phi_{m,n} = 0 \tag{6.14}$$

where S and M are the two-dimensional linear difference operators emanating from the assembled stiffness (discrete Laplacian) and mass tensors respectively; see [152]. The quantity

$$\gamma := (1 - \tau k^2) \tag{6.15}$$

embodies the GLS mesh parameter τ.

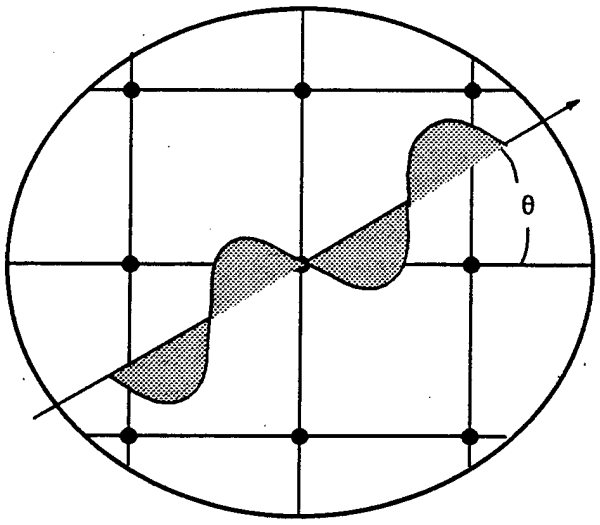

Figure 6.11: Direction of plane-wave with angle θ measured relative to mesh lines.

The GLS finite element dispersion relations are obtained by assuming a plane-wave solution propagating at an arbitrary angle relative to the mesh lines,

$$\phi_{m,n} = \mathrm{e}^{i(k_x^h h_x m + k_y^h h_y n)} \tag{6.16}$$

with $i = \sqrt{-1}$. In the above, the directional wave vector components are denoted $k_x^h = k^h \cos\theta$ and $k_y^h = k^h \sin\theta$ with numerical wavenumber k^h. The normal is oriented at angle θ relative to mesh lines, see Figure 6.11. Substituting (6.16) into (6.14) results in the GLS dispersion relation obtained in [143, 145, 152]:

$$\tilde{F}(k, k_x^h, k_y^h) = \tilde{S} - \gamma k^2 \tilde{M} = 0 \tag{6.17}$$

This equation describes the relationship between the continuous wavenumber $k = \omega/c$ and the finite element discrete wave vector components k_x^h and k_y^h. In this relation, $\tilde{S}$ and $\tilde{M}$ represent the discrete Fourier transforms of the linear difference operators S and M respectively. The transformed stiffness and mass operators are defined by:

$$\begin{aligned} \tilde{S}(k_x^h h_x, k_y^h h_y) &= \mathbf{1}_y \bar{k}_x^2 + \mathbf{1}_x \bar{k}_y^2 && (6.18) \\ \tilde{M}(k_x^h h_x, k_y^h h_y) &= \mathbf{1}_x \mathbf{1}_y && (6.19) \end{aligned}$$

where,

$$\bar{k}_x^2 = 2(1 - f_x)/h_x^2 \qquad \text{and} \qquad \bar{k}_y^2 = 2(1 - f_y)/h_y^2 \tag{6.20}$$

$$\begin{aligned} f_x &= \cos(k_x^h h_x) = \cos(k^h h_x \cos\theta) \\ f_y &= \cos(k_y^h h_y) = \cos(k^h h_y \sin\theta) \end{aligned}$$

$$\mathbf{1}_x = 1 - \frac{\epsilon}{6}(\bar{k}_x h_x)^2 \qquad \text{and} \qquad \mathbf{1}_y = 1 - \frac{\epsilon}{6}(\bar{k}_y h_y)^2 \tag{6.21}$$

The ϵ is a general quadrature parameter equal to 1 for exact Gaussian quadrature and 0 for Lobatto quadrature. The mass operator M is referred to as consistent when $\epsilon = 1$ and lumped when $\epsilon = 0$.

The characteristic equation (6.17) describes the dispersive relationship between the continuous wavenumber $k = \omega/c$ and the finite element discrete wave vector components k_x^h and k_y^h. This relation depends on both the magnitude of the discrete wavenumber $k^h := |k^h|$ and the orientation of the wavevector θ.

6.2.2 Optimal GLS mesh parameter

The optimal least-squares mesh parameter τ is obtained by requiring the phase to be exact, i.e. $k = k^h$ for any choice of wave vector angle $\theta = \theta_o$. This requirement is met by replacing k^h with the exact wavenumber, $k = \omega/c$, in the GLS finite element dispersion relation (6.17), restricting $h_x = h_y = h$, and solving for γ. With this design criteria, the optimal τ derived by Thompson and Pinsky [145, 152] is,

$$\tau k^2 := 1 - \frac{\tilde{S}(kh, \theta_o)}{k^2 \tilde{M}(kh, \theta_o)} \tag{6.22}$$

where $\tilde{S}$ and $\tilde{M}$ are defined in (6.18) through (6.21) with k^h replaced with $k = \omega/c$ and $\theta = \theta_0$. In particular, for exact 2×2 Gaussian integration, the expression for the optimal GLS mesh parameter is,

$$\tau k^2 = 1 - \frac{6(4 - f_x - f_y - 2f_x f_y)}{(kh)^2(2 + f_x)(2 + f_y)} \tag{6.23}$$

Selecting $\theta_0 = 0$, (6.22) specializes to,

$$\tau k^2 := 1 - \frac{6(1 - \cos kh)}{(kh)^2(3 - \epsilon(1 - \cos kh))} \tag{6.24}$$

which yields exact phase for plane-waves directed along uniform mesh lines for either exact integration $\epsilon = 1$ or Lobatto quadrature $\epsilon = 0$. When $\epsilon = 1$ (6.24) specializes to the GLS parameter derived by Harari and Hughes [57] in one-dimension. For comparison the GLS mesh parameter τ defined in (6.23), with $\epsilon = 1$, designed to give exact phase for plane-waves oriented along $\theta = 0$ (denoted τ_0), $\theta = 22.5$ (denoted $\tau_{22.5}$), and $\theta = 45$ (denoted τ_{45}) are plotted in Figure 6.12. At $kh/\pi = 0.4$, corresponding to five elements per wavelength, the two alternative GLS parameters show a significant difference.

6.2.3 GLS multi-dimensional dispersion analysis

In this section, the performance of alternate GLS mesh parameters based on definition (6.23), with different choices of θ_o are examined. The accuracy of the numerical solution is assessed in terms of the phase error defined by,

$$\mathrm{e}_p(k^h, \theta) := \frac{k}{k^h} \tag{6.25}$$

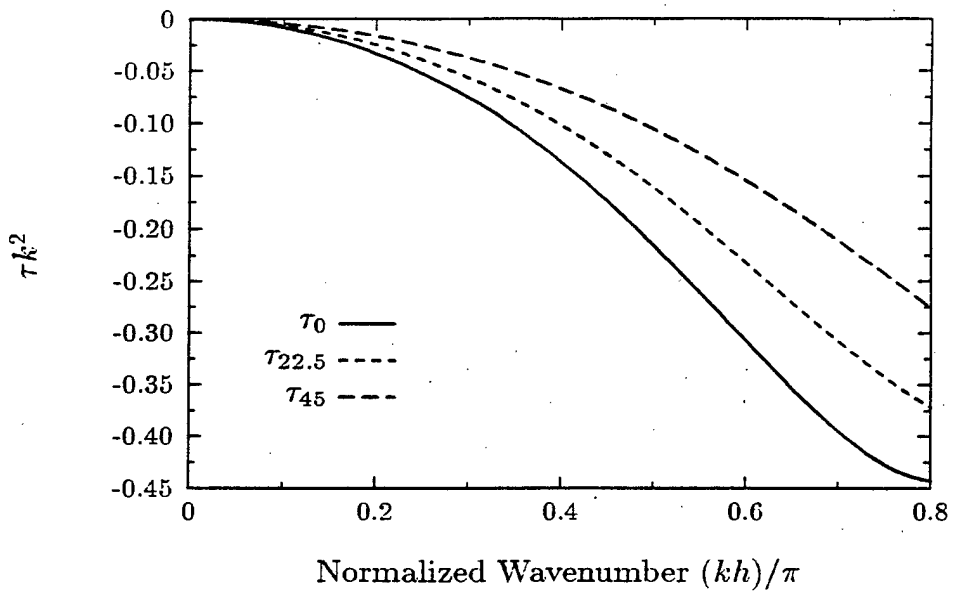

Figure 6.12: Optimal GLS parameters designed to give exact phase for plane waves directed along $\theta = 0$ (denoted τ_0), and $\theta = 22.5$ (denoted $\tau_{22.5}$).

In Figure 6.13 the phase error is plotted versus the angle of wave propagation; comparisons are made with Galerkin ($\tau = 0$) and GLS with ($\tau_{22.5}$) and (τ_0) at ten elements per wavelength (top), and four elements per wavelength (bottom). These results clearly show that the solution with $\tau_{22.5}$ gives exact phase for propagation angles $\theta = 22.5$, while the solution with τ_0 gives exact phase for propagation angles $\theta = 0$ by design. The phase error for GLS with τ_0 is a minimum (exact) at $\theta = 0$, and then increases to a maximum of 4 percent at $\theta = 45$ in the case of four elements per wavelength. Phase accuracy is improved for $\tau_{22.5}$, where the maximum error is only 2 percent at $\theta = 0$ and $\theta = 45$. By choosing the GLS parameter $\tau_{22.5}$, the envelope of the dispersion curves is centered around the exact result. As a result, the GLS solution exhibits a maximum possible error $|e_p|$ of only 2 percent at four elements per wavelength as compared to 10 percent for Galerkin. At ten elements per wavelength, GLS with $\tau_{22.5}$ has a maximum possible error of only 0.5 percent, compared to 1.6 percent for Galerkin.

In conclusion, firstly, it is clear that the least-squares addition with the family of GLS parameters τ defined by (6.23) substantially improves the phase accuracy of the finite element solution for any given wave vector orientation θ. Secondly, we find that when the direction of wave-propagation is not known *a priori*, or when it is varying over the mesh, as will generally be the case, then $\tau_{22.5}$ is optimal. Further results for GLS in two-dimensions including dispersion characteristics for other choices of τ and the effects of numerical quadrature are reported in [143, 152].

6.2.4 Three-dimensional elements

The selection of an optimal GLS parameter in three-dimensions is a simple extension of the two-dimensional case. Consider a uniform mesh of trilinear 8-node brick ele-

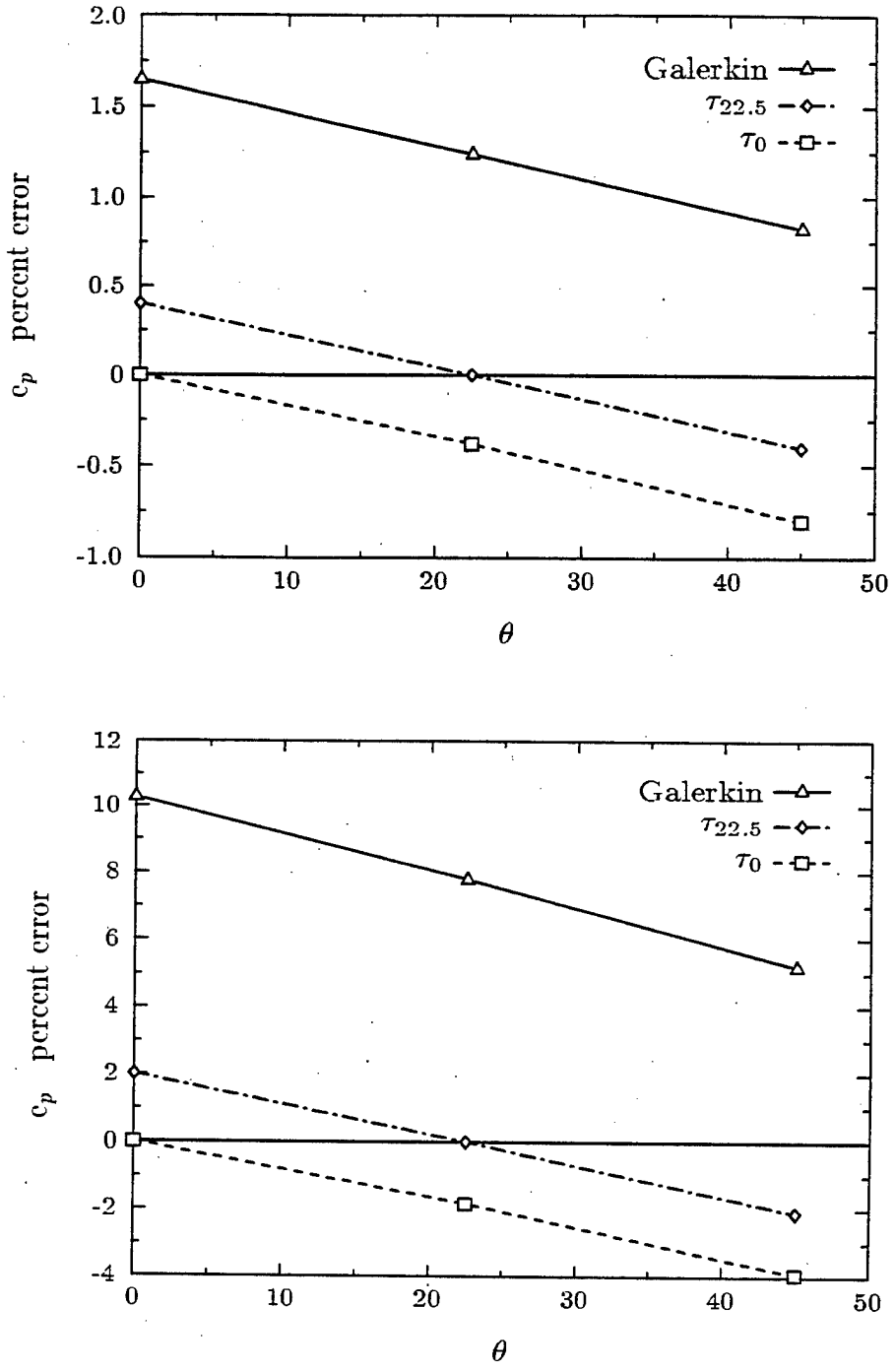

Figure 6.13: Phase error using exact integration at (top) 10 elements per wavelength, (bottom) 4 elements per wavelength.

ments with element sides h. The optimal τ in this case was obtained in [145, 143] as,

$$\tau k^2 := 1 - \frac{\tilde{S}(kh,\theta,\varphi)}{(kh)^2\tilde{M}(kh,\theta,\varphi)} \tag{6.26}$$

where $\tilde{S}$ and $\tilde{M}$ are the three-dimensional Fourier transforms of the stiffness and mass difference stencils respectively,

$$\tilde{S} = \mathbf{1}_y\mathbf{1}_z\bar{k}_x^2 + \mathbf{1}_x\mathbf{1}_z\bar{k}_y^2 + \mathbf{1}_x\mathbf{1}_y\bar{k}_z^2 \qquad \text{and} \qquad \tilde{M} = \mathbf{1}_x\mathbf{1}_y\mathbf{1}_z \tag{6.27}$$

$$\bar{k}_x^2 = 2(1-f_x) \qquad \text{and} \qquad \bar{k}_y^2 = 2(1-f_y) \qquad \text{and} \qquad \bar{k}_z^2 = 2(1-f_z) \tag{6.28}$$

$$\begin{aligned} f_x &= \cos(k_x h) = \cos(kh\cos\theta\sin\varphi) \\ f_y &= \cos(k_y h) = \cos(kh\sin\theta\sin\varphi) \\ f_z &= \cos(k_z h) = \cos(kh\cos\varphi) \end{aligned}$$

with polar angles $\theta \in [0, 2\pi]$ and meridional angles $\varphi \in [0, \pi]$ measured relative to mesh axis. By design, for $\varphi = 0 \bmod 90$, (6.26) specializes to the two-dimensional case (6.22).

6.2.5 Galerkin/generalized least-squares in two dimensions

For the Galerkin/Generalized Least-Squares (GGLS) method in two-dimensions, where the added least-squares term is in the form of the gradient of the residual, i.e. $\nabla r^h = \nabla(\mathcal{L}\phi^h + f)$ with $\mathcal{L}\phi^h = \phi^h_{,xx} + \phi^h_{,yy} + k^2\phi^h$, and $f = 0$, the dispersion relation for bilinear elements is (see [143, 145] for details):

$$(kh)^2\mathbf{1}_x\mathbf{1}_y = (1+\tau k^4)(\mathbf{1}_y\bar{k}_x^2 + \mathbf{1}_x\bar{k}_y^2) \tag{6.29}$$

which has the same form as the GLS characteristic equation (6.17) with the mesh parameter replaced with $\gamma = (1+\tau k^4)^{-1}$. In this case the optimal GGLS parameter derived in [145] is,

$$\tau k^4 := \frac{(kh)^2\tilde{M}(kh,\theta_0)}{\tilde{S}(kh,\theta_0)} - 1 \tag{6.30}$$

Examining (6.29) we conclude that for bilinear elements on a uniform grid with $f = 0$, the phase accuracy for GGLS is identical to GLS over all wave vector orientations, and no advantage results. This observation was also made by Harari [56] for the one-dimensional case.

6.3 Error Analysis of the Galerkin/Least-squares Method

The error analysis of the one-dimensional case was performed in [57]. Here we proceed along similar lines in the analysis of the multi-dimensional Galerkin/least-squares

method with DtN boundary conditions, in the entire range of propagation and decay. Special care is taken to generalize the following results to apply to problems with pure Neumann boundary conditions on the wet surface. However it should be noted that the analysis is valid for any combination of boundary conditions on the wet surface for which the exterior acoustic boundary-value problem is well defined, and by no means is it limited to Neumann problems. (Franca and Dutra do Carmo prove convergence of their Galerkin/gradient least-squares method for the decay region [34], thereby implying convergence of linear Galerkin/least-squares for Dirichlet problems in this region.) In the following we do not account directly for the Neumann problem with $k = 0$, which is not well-posed except in a limit sense. The Galerkin method is suitable for this case, in accordance with all Galerkin/least-squares methods proposed, for which $\tau k^2 = 0$ at $\alpha^h = 0$.

All the norms employed are induced by the L_2 inner products introduced previously (recall that the subscript denotes a domain of integration other than Ω, and $\tilde{\Omega}$ is the union of element interiors). The values of the constants employed may vary in specific instances of use.

6.3.1 Preliminary results

Stability of symmetric operators defined over real fields is usually expressed in terms of their bilinear forms, an essential step leading to error estimates (e.g., [88, p. 54]). Often, for operators defined over complex fields, stability is expressed in terms of the real part of the operator, which is then bounded by its modulus ([141, pp. 119–120]). However, in order to account for Neumann problems we need to include the DtN contribution, which therefore must first be characterized. We extend the analysis of the DtN operator for the Laplacian in [98] to the Helmholtz operator, relying in part on groundwork performed in [58]. The extension of any function w defined on the artificial boundary $\partial\mathcal{B}_R$ into the domain exterior to the computational domain D so that it satisfies the homogeneous Helmholtz equation $\mathcal{L}w = 0$ in D and the radiation condition at infinity is unique, and satisfies the DtN boundary condition on $\partial\mathcal{B}_R$ (since this is the manner in which the DtN operator was determined). Thus

$$\begin{aligned} b_k(w,w) &= \int_{\partial\mathcal{B}_R} \bar{w} M w \, d\Gamma \\ &= -\int_{\partial\mathcal{B}_R} \bar{w} w_{,n} \, d\Gamma \\ &= \int_D \nabla\cdot(\bar{w}\nabla w)\, d\Omega - \lim_{r\to\infty} \int_{\partial B_R} \bar{w} w_{,r} \, d\Gamma \\ &= \int_D \left(|\nabla w|^2 - k^2|w|^2\right) d\Omega - \lim_{r\to\infty} \int_{\partial B_R} \bar{w} w_{,r} \, d\Gamma \end{aligned} \tag{6.31}$$

where the normal in the second line above is outward with respect to the computational domain Ω and the last line is a consequence of the fact that w satisfies the homogeneous Helmholtz equation.

In the propagation region ($k^2 > 0$) functions are complex valued. and hence

$$\begin{aligned} 2i\, Im\, b_k(w,w) &= b_k(w,w) - \overline{b_k(w,w)} \\ &= \frac{1}{ik} \lim_{r\to\infty} \int_{\partial B_R} \left(|w_{,r}|^2 + k^2 |w|^2 \right) d\Gamma \end{aligned} \tag{6.32}$$

(6.33)

where the second line was obtained by (6.31) and the radiation condition, so that

$$\begin{aligned} -Im\, b_k(w,w) &= \frac{1}{2k} \lim_{r\to\infty} \int_{\partial B_R} \left(|w_{,r}|^2 + k^2 |w|^2 \right) d\Gamma \\ &\geq 0 \end{aligned} \tag{6.34}$$

(6.35)

By a theorem due to Rellich reported in [153, p. 56] it was shown in [58] that $Im\, b_k(w,w) = 0$ implies that $w = 0$ on $\partial\mathcal{B}_R$. This is corroborated by the investigation in [58] of the coefficients of the DtN operator demonstrating that $Im\, \alpha_n < 0$. We therefore infer that $-Im\, b_k(w,w)$ is a norm on $\partial\mathcal{B}_R$, i.e.,

$$-Im\, b_k(w,w) \geq C_{kR} \|w\|^2_{\partial\mathcal{B}_R} \qquad \forall w \in \mathcal{V} \tag{6.36}$$

where C_{kR} is a positive constant, with dimensions of inverse length, that depends only on the geometrically nondimensionalized wave number kR. For example, in two dimensions

$$\begin{aligned} b_k(w,w) &= \int_{\partial\mathcal{B}_R} \bar{w} M w \, d\Gamma \\ &= R \int_0^{2\pi} \overline{w(R,\theta)} \left(\sum_{n=0}^{\infty}{}' \alpha_n \int_0^{2\pi} \cos n(\theta - \theta')\, w(R,\theta')\, d\theta' \right) d\theta \\ &= R \sum_{n=0}^{\infty}{}' \alpha_n \left(\left| \int_0^{2\pi} w(R,\theta)\, \cos n\theta \, d\theta \right|^2 + \left| \int_0^{2\pi} w(R,\theta)\, \sin n\theta \, d\theta \right|^2 \right) \end{aligned} \tag{6.37}$$

so that, by the Parseval equality, eq. (6.36) holds with $C_{kR} = \pi \min\{-Im\, \alpha_n\}$, which justifies the assertion that C_{kR} depends only on kR, see (3.3). The three-dimensional case is similar. By direct inspection of the DtN kernels one can also show that

$$Re\, b_k(w,w) \geq 0 \qquad \forall w \in \mathcal{V} \tag{6.38}$$

In the decay region ($k^2 < 0$), by (6.31)

$$\begin{aligned} b_k(w,w) &= \int_D \left((\nabla w)^2 + |k^2| w^2 \right) d\Omega + \frac{1}{2|k|} \lim_{r\to\infty} \int_{\partial B_R} \left((w_{,r})^2 + |k^2| w^2 \right) d\Gamma \\ &\geq 0 \end{aligned} \tag{6.39}$$

and thus $\forall k^2 < 0$

$$b_k(w,w) \quad \geq \quad C_{kR}\,\|w\|^2_{\partial\mathcal{B}_R} \qquad \forall w \in \mathcal{V} \tag{6.40}$$

with $C_{kR} = \pi \min\{\alpha_n\}$, implying that $b_k(w,w)$ is a norm on $\partial\mathcal{B}_R$ in the decay region as well.

Poincaré-Friedrichs inequalities are usually stated for functions that satisfy homogeneous Dirichlet boundary conditions (see [61] and references therein for an overview and proofs of inequalities of this type). We will make use of a specialization of a Poincaré-Friedrichs inequality derived in [61]

$$\|w\|^2 \leq \frac{(2+C_{kR}R)R}{2C_{kR}d}\left(\|\nabla w\|^2 + C_{kR}\,\|w\|^2_{\partial\mathcal{B}_R}\right) \tag{6.41}$$

which holds for any boundary conditions on the wet surface, including pure Neumann boundary conditions, i.e., when $\mathcal{V} = H^1(\Omega)$.

The mesh dependent norm in which we prove convergence is induced by the following inner product

$$\left\langle w^h, \phi^h \right\rangle_{GLS} := a_{GLS}(w^h, \phi^h) + Re\, b_k(w^h, \phi^h) - Im\, b_k(w^h, \phi^h) \tag{6.42}$$

namely,

$$|||w^h|||^2_{GLS} = \left\langle w^h, w^h \right\rangle_{GLS} \tag{6.43}$$

We assume the following *least-squares bounds of the Helmholtz operator* hold $\forall k^2 \in$ R

$$L_{kh}\|\mathcal{L}w^h\|^2_{\tilde{\Omega}} \leq k^4\|w^h\|^2 \leq U_{kh}\|\mathcal{L}w^h\|^2_{\tilde{\Omega}} \qquad \forall w^h \in \mathcal{V}^h \tag{6.44}$$

This result, which is related to inverse estimates (see [61] and references therein) that are often employed in analyzing the error of finite element methods, see, e.g., [36, 76], explicates the advantageous effect of the Galerkin/least-squares term in controlling destabilizing terms. In support of the plausibility of (6.44) we note that $\|\mathcal{L}w^h\|_{\tilde{\Omega}}$ is indeed a norm since no piecewise polynomial satisfies the Helmholtz equation. Furthermore, the coefficients for several types of elements were calculated in [61] (for example, see Fig. 6.14 for the case of biquadratic rectangles of sides h_x and h_y). In general, the coefficients $0 \leq L_{kh} \leq 1 \leq U_{kh}$ depend on the numerically nondimensionalized wave number kh and the degree of interpolation. All the cases evaluated were found to depend on $(kh)^4$, i.e., to be symmetric with respect to $(kh)^2$ and behave identically in propagation and decay. The coefficients may be characterized by their asymptotic behavior

$$\left.\begin{array}{l} L_{kh} \longrightarrow 1 \\ U_{kh} \longrightarrow 1 \end{array}\right\} \qquad \text{as } (kh)^2 \to \pm\infty \tag{6.45}$$

$$\left.\begin{array}{l} L_{kh} \longrightarrow 0 \\ U_{kh} \longrightarrow \infty \end{array}\right\} \qquad \text{as } (kh)^2 \to 0 \tag{6.46}$$

For all linear elements $\Delta w^h|_{\tilde{\Omega}} = 0$ and hence $L_{kh} \equiv U_{kh} \equiv 1$. From [61] it can be shown that for $|\alpha^h| < 1$

$$L_{kh} \quad \leq \quad C_l \tag{6.47}$$

Figure 6.14: Least-squares bounds for biquadratic rectangles of varying aspect ratios (the bold lines correspond to the upper bound U_{kh}).

where the positive, nondimensional constant $C_l \geq 0$ depends only on the degree of interpolation l (and is independent of h), and for $|\alpha^h| \geq 1$

$$U_{kh} \quad \leq \quad C_l \tag{6.48}$$

See [61] for explicit definitions of L_{kh} and U_{kh}, numerical evaluations, and a discussion of results of this kind and potential implications in general settings.
Consistency condition (orthogonality of the error): Since the least-squares modification to the Galerkin formulation was in terms of residuals, the consistency possessed by the Galerkin method is inherited by Galerkin/least-squares. The Galerkin/least-squares equation is thus satisfied with the exact solution as the second argument of A_{GLS}, and so, subtracting this from the equation in its original form leads to

$$A_{GLS}(w^h, e) = 0 \qquad \forall w^h \in \mathcal{V}^h \tag{6.49}$$

where $e := \phi^h - \phi$ is the error in the finite element solution.

6.3.2 Stability condition

We treat the range of propagation and decay separately. In the range of *propagation* ($k^2 > 0$) it is not obvious that (6.43) satisfies the positive-definiteness requirement of

a norm. We show that it does, subject to the condition that

$$\tau k^2 \geq \begin{cases} L_{kh}\left(1 - \dfrac{C_{kR}d}{(2+C_{kR}R)k^2R}\right), & d \geq (2+C_{kR}R)k^2R/C_{kR} \\ U_{kh}\left(1 - \dfrac{C_{kR}d}{(2+C_{kR}R)k^2R}\right), & d < (2+C_{kR}R)k^2R/C_{kR} \end{cases} \qquad k^2 > 0 \tag{6.50}$$

Our previous analysis indicates that it is beneficial to select negative values of τ for low wave numbers (see, e.g., Fig. 5.4). We first examine $\tau \leq 0$, which, by (6.50), is restricted to $d \geq (2+C_{kR}R)k^2R/C_{kR}$

$$\begin{aligned} |||w^h|||^2_{GLS} &= \|\nabla w^h\|^2 - k^2\|w^h\|^2 + \tau\|\mathcal{L}w^h\|^2_\Omega + Re\, b_k(w^h,w^h) - Im\, b_k(w^h,w^h) \\ &\geq \|\nabla w^h\|^2 - k^2(1-\tau k^2/L_{kh})\|w^h\|^2 + C_{kR}\|w^h\|^2_{\partial\mathcal{B}_R} \\ &\geq \left(1 - \frac{(2+C_{kR}R)R}{2C_{kR}d}k^2\left(1-\frac{\tau k^2}{L_{kh}}\right)\right)\left(\|\nabla w^h\|^2 + C_{kR}\|w^h\|^2_{\partial\mathcal{B}_R}\right) \\ &\geq \frac{1}{2}\left(\|\nabla w^h\|^2 + C_{kR}\|w^h\|^2_{\partial\mathcal{B}_R}\right) \end{aligned} \tag{6.51}$$

In the above calculation we made use of (6.36), (6.38) and the least-squares bounds of the Helmholtz operator (6.44) on the second line, the Poincaré-Friedrichs inequality (6.41) on the third line, and the first case in (6.50) on the last line. For $\tau > 0$, by (6.36), (6.38) and (6.44)

$$|||w^h|||^2_{GLS} \geq \|\nabla w^h\|^2 - k^2(1-\tau k^2/U_{kh})\|w^h\|^2 + C_{kR}\|w^h\|^2_{\partial\mathcal{B}_R} \tag{6.52}$$

When $\tau k^2 \geq U_{kh}$ this expression is obviously positive. Otherwise, by (6.41)

$$\begin{aligned} |||w^h|||^2_{GLS} &\geq \left(1 - \frac{(2+C_{kR}R)R}{2C_{kR}d}k^2\left(1-\frac{\tau k^2}{U_{kh}}\right)\right)\left(\|\nabla w^h\|^2 + C_{kR}\|w^h\|^2_{\partial\mathcal{B}_R}\right) \\ &\geq \frac{1}{2}\left(\|\nabla w^h\|^2 + C_{kR}\|w^h\|^2_{\partial\mathcal{B}_R}\right) \end{aligned} \tag{6.53}$$

The second case in (6.50) was used on the last line and, since $\tau > 0$, this result is valid $\forall k^2 > 0$.

In the range of *decay* ($k^2 < 0$), (6.43) clearly satisfies the positive-definiteness requirement of a norm for $\tau > 0$, but it must be shown to hold for negative values of τ (that correspond to $\tau k^2 > 0$) as indicated by our previous analysis. In this case (6.40) and (6.44) imply

$$|||w^h|||^2_{GLS} \geq \|\nabla w^h\|^2 - k^2(1-\tau k^2/L_{kh})\|w^h\|^2 + C_{kR}\|w^h\|^2_{\partial}\mathcal{B}_R \tag{6.54}$$

which is obviously positive for $\tau k^2 \leq L_{kh}$. When $\tau k^2 > L_{kh}$ we again use (6.41) to show

$$\begin{aligned} |||w^h|||^2_{GLS} &\geq \left(1 - \frac{(2+C_{kR}R)R}{2C_{kR}d}k^2\left(1-\frac{\tau k^2}{L_{kh}}\right)\right)\left(\|\nabla w^h\|^2 + C_{kR}\|w^h\|^2_{\partial\mathcal{B}_R}\right) \\ &\geq \frac{1}{2}\left(\|\nabla w^h\|^2 + C_{kR}\|w^h\|^2_{\partial\mathcal{B}_R}\right) \end{aligned} \tag{6.55}$$

The last line was derived by posing

$$\tau k^2 \leq L_{kh}\left(1 - \frac{C_{kR}d}{(2+C_{kR}R)k^2R}\right) \qquad k^2 < 0 \tag{6.56}$$

In summary,

$$|||w^h|||^2_{GLS} \geq \frac{1}{2}\left(\|\nabla w^h\|^2 + C_{kR}\,\|w^h\|^2_{\partial\mathcal{B}_R}\right) \qquad \forall w^h \in \mathcal{V}^h \tag{6.57}$$

subject to the bounds (6.50) and (6.56) in the propagation and decay regions, respectively.

Remark: In viewing the Galerkin formulation as a special case of Galerkin/least-squares with $\tau = 0$, it becomes clear from this analysis that in the propagation region stability could be lost as the wave number increases, since (6.50), the lower bound on τ, is violated.

We now show ellipticity of the sesquilinear form. In the region of propagation

$$\begin{aligned} |A_{GLS}(w^h, w^h)|^2 &= \left(a_{GLS}(w^h, w^h) + Re\, b_k(w^h, w^h)\right)^2 + \left(Im\, b_k(w^h, w^h)\right)^2 \\ &\geq \frac{1}{2}\left(a_{GLS}(w^h, w^h) + Re\, b_k(w^h, w^h) - Im\, b_k(w^h, w^h)\right)^2 \\ &= \frac{1}{2}\left(|||w^h|||^2_{GLS}\right)^2 \qquad \forall w^h \in \mathcal{V}^h \end{aligned} \tag{6.58}$$

Ellipticity in the decay region is more direct, viz.,

$$A_{GLS}(w^h, w^h) = |||w^h|||^2_{GLS} \qquad \forall w^h \in \mathcal{V}^h \tag{6.59}$$

6.3.3 Interpolation estimates

The following results are based on standard interpolation theory (see, e.g., [21, pp. 116–131 and 230–248]), with the assumption that ϕ is sufficiently smooth. Let $\tilde{\phi}^h \in \mathcal{V}^h$ denote an interpolant of ϕ, so that the interpolation error, $\eta := \tilde{\phi}^h - \phi$, satisfies the DtN boundary condition. It is convenient to consider first the boundary terms

$$\begin{aligned} Re\, b_k(\eta, \eta) - Im\, b_k(\eta, \eta) &\leq \sqrt{2}\,|b_k(\eta, \eta)| \\ &\leq \sqrt{2}\,\|\eta\|_{\partial\mathcal{B}_R}\,\|\eta_{,n}\|_{\partial\mathcal{B}_R} \end{aligned} \tag{6.60}$$

where the second line was obtained by the Schwarz inequality. Thus

$$\begin{aligned} |||\eta|||^2_{GLS} &= \|\nabla\eta\|^2 - k^2\|\eta\|^2 + \tau\|\mathcal{L}\eta\|^2_{\tilde{\Omega}} + Re\, b_k(\eta, \eta) - Im\, b_k(\eta, \eta) \\ &\leq \|\nabla\eta\|^2 + |k^2|\|\eta\|^2 + 2\tau_+\|\Delta\eta\|^2_{\tilde{\Omega}} + 2\tau_+k^4\|\eta\|^2 + \sqrt{2}\,\|\eta\|_{\partial\mathcal{B}_R}\,\|\eta_{,n}\|_{\partial\mathcal{B}_R} \end{aligned} \tag{6.61}$$

where $\tau_+ := \max\{0, \tau\}$.

We estimate the interpolation error for $|\alpha^h| < 1$, imposing the bound $|\tau k^2| \leq \min\{6|\alpha^h|, L_{kh}\}$. By (6.61)

$$\begin{aligned} |||\eta|||^2_{GLS} &\leq 2|\tau_+ k^2| \frac{h^2}{12|\alpha^h|} \|\Delta\eta\|^2_{\tilde{\Omega}} + \|\nabla\eta\|^2 + \frac{12|\alpha^h|}{h^2}(2|\tau_+ k^2| + 1)\|\eta\|^2 + \sqrt{2}\,\|\eta\|_{\partial\mathcal{B}_R}\,\|\eta_{,n}\|_{\partial\mathcal{B}_R} \\ &\leq h^2\|\Delta\eta\|^2_{\tilde{\Omega}} + \|\nabla\eta\|^2 + \frac{12}{h^2}(2C_l + 1)\|\eta\|^2 + \sqrt{2}\,\|\eta\|_{\partial\mathcal{B}_R}\,\|\eta_{,n}\|_{\partial\mathcal{B}_R} \\ &\leq C_\phi\, h^{2l} \end{aligned} \tag{6.62}$$

where the positive constant C_ϕ depends on the exact solution. In the above calculation we used the definition of α^h in the first line, and in the second line we used $|\alpha^h| < 1$ and the bound on τ with (6.47).

For unresolved waves, $|\alpha^h| \geq 1$, we impose $|\tau k^2| \leq U_{kh}$. By (6.61)

$$\begin{aligned} |||\eta|||^2_{GLS} &\leq 2\tau_+ \left(\frac{k^2h^2}{12\alpha^h}\right)^2 \|\Delta\eta\|^2_{\tilde{\Omega}} + \frac{k^2h^2}{12\alpha^h}\|\nabla\eta\|^2 + |k^2|(2|\tau_+ k^2| + 1)\|\eta\|^2 \\ &\qquad + \sqrt{2}\,\frac{k^2h^2}{12\alpha^h}\|\eta\|_{\partial\mathcal{B}_R}\,\|\eta_{,n}\|_{\partial\mathcal{B}_R} \\ &\leq \frac{|k^2|h^4}{72}C_l\|\Delta\eta\|^2_{\tilde{\Omega}} + \frac{|k^2|h^2}{12}\|\nabla\eta\|^2 + |k^2|(2C_l + 1)\|\eta\|^2 \\ &\qquad + \frac{\sqrt{2}|k^2|h^2}{12}\|\eta\|_{\partial\mathcal{B}_R}\,\|\eta_{,n}\|_{\partial\mathcal{B}_R} \\ &\leq |\alpha^h|\, C_\phi\, h^{2l} \end{aligned} \tag{6.63}$$

Again we used the definition of α^h in the first line, and in the second line we used $|\alpha^h| \geq 1$ and the bound on τk^2 with (6.48).

Remark: For linear elements $L_{kh} = U_{kh} = 1$. Damping of unresolved waves as presented in (5.7) violates the bounds on τk^2 required by the interpolation estimates in the propagation region. The bounds from the stability analysis, however, are satisfied. This result is expected since the damped solutions are stable, but have no approximation capability.

6.3.4 Error estimates

Let $e^h := e - \eta \in \mathcal{V}^h$. We estimate e^h first

$$\begin{aligned} \frac{1}{\sqrt{2}}|||e^h|||^2_{GLS} &\leq \left|A_{GLS}(e^h, e^h)\right| \\ &= \left|A_{GLS}(e^h, e - \eta)\right| \\ &= \left|A_{GLS}(e^h, \eta)\right| \\ &= \left|a_{GLS}(e^h, \eta) + Re\, b_k(e^h, \eta) + i\, Im\, b_k(e^h, \eta)\right| \\ &= \left|\left\langle e^h, \eta\right\rangle_{GLS} + (1 + i)\, Im\, b_k(e^h, \eta)\right| \\ &\leq \left|\left\langle e^h, \eta\right\rangle_{GLS}\right| + \sqrt{2}\,\left|Im\, b_k(e^h, \eta)\right| \end{aligned}$$

$$\leq |||e^h|||_{GLS}\,|||\eta|||_{GLS} + \left(2\,Im\,b_k(e^h,e^h)\;Im\,b_k(\eta,\eta)\right)^{1/2}$$
$$\leq \left(1+\sqrt{2}\right)|||e^h|||_{GLS}\,|||\eta|||_{GLS} \tag{6.64}$$

In the above calculation we used the stability conditions (6.58) and (6.59) in line one, the consistency condition (6.49) in line three, and the Schwarz inequality in line seven. And so, by the triangle inequality, and the interpolation estimates (6.62) and (6.63)

$$|||e|||^2_{GLS} \leq \begin{cases} C_\phi h^{2l}, & |\alpha^h| < 1 \\ |\alpha^h|\,C_\phi h^{2l}, & |\alpha^h| \geq 1 \end{cases} \tag{6.65}$$

Remarks

1. The DtN term is essential for proving stability of the Neumann problem, and does not adversely affect the interpolation and error estimates.

2. Convergence rates of the Galerkin/least-squares method are optimal for all values of α^h. The error estimates (6.65) indicate convergence of the finite element solution at optimal rates in the H^1 and L_2 norms for $|\alpha^h| \geq 1$, and when waves are resolved ($|\alpha^h| < 1$) in the H^1 seminorm, which implies optimal rate of convergence in L_2 as well.

3. As expected, the error bound for *unresolved waves* in (6.65) indicates deterioration of the finite element solution with growth in wave number or decay rate. Nevertheless, optimal convergence rate with mesh refinement is preserved.

6.4 Numerical Results

Numerical examples of problems that can be reduced to one dimension were employed in previous chapters as a design tool and, in conjunction with the convergence proof, as a means to verify the generality of the finite element formulations proposed. In the following we consider additional numerical examples of increasing complexity to further validate these methods. The examples are selected so that either analytical solutions or an intuitive understanding of the behavior of solutions are available, in order to evaluate the quality of the computed solutions.

6.4.1 Plane-wave propagation in a waveguide

Consider the problem of finding the solution $\phi : \bar{\Omega} = \{(x,y) : 0 \leq x \leq L_x, 0 \leq y \leq L_y\} \rightarrow \mathbb{R}$ within a waveguide:

$$(\nabla^2 + k^2)\phi(x,y) = 0 \qquad \text{in } \Omega \tag{6.66}$$
$$\phi(0,y) = g_0, \qquad \phi(L_x,y) = 0 \tag{6.67}$$
$$\phi_{,y}(x,0) = \phi_{,y}(x,L_y) = 0 \tag{6.68}$$

This example illustrates that for problems where the direction of wave propagation is known *a priori*, in this case along the x-axis, the optimum GLS parameter τ can be

calculated from (6.22). With the computational domain discretized with a uniform mesh of equally spaced bilinear finite elements, it can be shown that the GLS nodal solution to this problem has the same form as the analytical solution but with the physical wavenumber k replaced with a numerical wavenumber k^h. Since this problem is an example of a plane-wave solution directed along x-direction mesh lines, the problem essentially is one-dimensional. In this special case the GLS method can be designed to achieve nodal exactness (superconvergence) by choosing the optimal GLS parameter τ_0 such that exact phase is obtained; that is $k^h = k$.

Now consider this same problem but now with the mesh rotated at 45 degrees relative to the rectangular boundaries, see Figure 6.15. For this mesh and loading, the greatest accuracy is obtained by choosing τ such that $\theta_o = 45$ in (6.22) since the mesh lines are rotated by 45 degrees to the direction of propagation. The GLS solution to this problem is illustrated in Figure 6.16. For comparison, the Galerkin and GLS solutions using τ_{45}; exact for waves directed along $\theta = 45$ relative to mesh lines, and τ_0 and $\tau_{22.5}$; exact for waves directed along $\theta = 0$ and $\theta = 22.5$ are also shown. From this result we observe that the GLS solution with τ_{45} is very close to the nodal interpolate of the exact solution. The solution is not perfectly nodally exact for this mesh due to the presence of linear triangular elements used near the boundaries. Results for the alternative GLS parameter $\tau_{22.5}$ also exhibit significantly improved phase accuracy when compared to Galerkin. The solution using the one-dimensional τ_0 shows no improvement in accuracy when compared to Galerkin.

6.4.2 Green's function for a rectangular domain

Consider the problem of finding the Green's function $\phi : \bar{\Omega} \rightarrow \mathbb{R}$ within a square domain:

$$(\nabla^2 + k^2)\phi(x,y) = -\delta(x - x_0, y - y_0) \qquad \text{in } \Omega \tag{6.69}$$

$$\phi(0,y) = \phi(L,y) = \phi(x,0) = \phi(x,L) = 0 \tag{6.70}$$

where L is the side length. The solution to this problem is composed of a series of reflected waves which give rise to complicated standing wave patterns, see [152].

This problem is numerically solved by the Galerkin/Least-Squares method using a uniform mesh of 20×20 bilinear quadrilateral elements. All calculations are performed with 2×2 Gauss integration with $kL = 5\pi/3$. The source is located in the upper right quadrant $(x_0, y_0) = (0.8L, 0.8L)$. In Figure 6.17 the contours of the exact series solution interpolated with the mesh employed is illustrated. The solution profile for a cut located at $y = 0.2L$ is given in Figure 6.18. The L_2 norm of the error $||e||$ for the Galerkin and GLS solutions using the mesh parameters τ_0 and $\tau_{22.5}$ is computed as:

$$\begin{aligned} \text{Galerkin} &= 0.691 \\ \text{GLS}(\tau_0) &= 0.240 \\ \text{GLS}(\tau_{22.5}) &= 0.148 \end{aligned}$$

Results of this numerical example indicate that the additional least-squares operator with the family of mesh parameters τ defined in (6.22) improves the accuracy of the

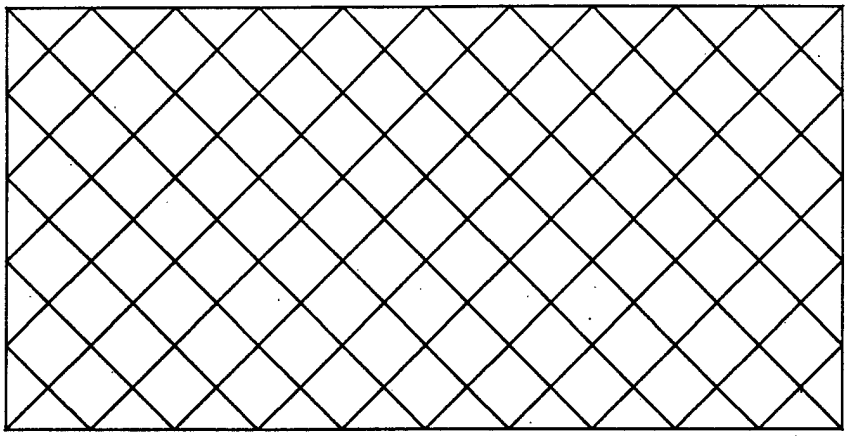

Figure 6.15: Rotated finite element mesh of linear quadrilateral elements and linear triangular elements for Dirichlet waveguide problem.

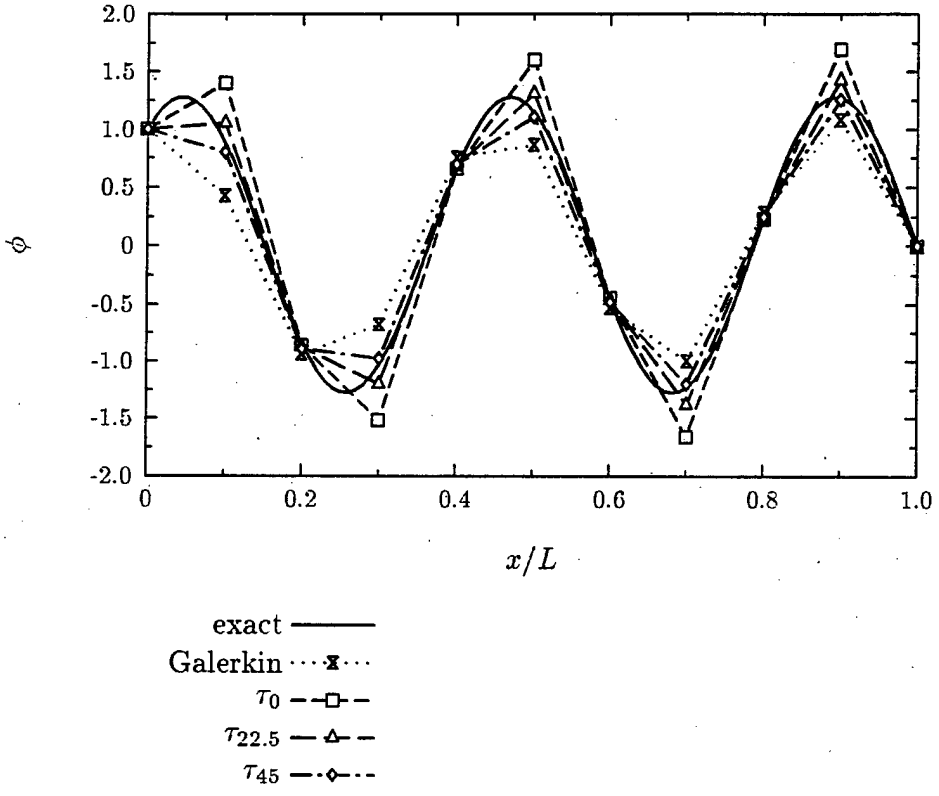

Figure 6.16: Waveguide problem with rotated mesh and plane-wave solution directed along x-axis; $kh = \pi/3$, six elements per wavelength.

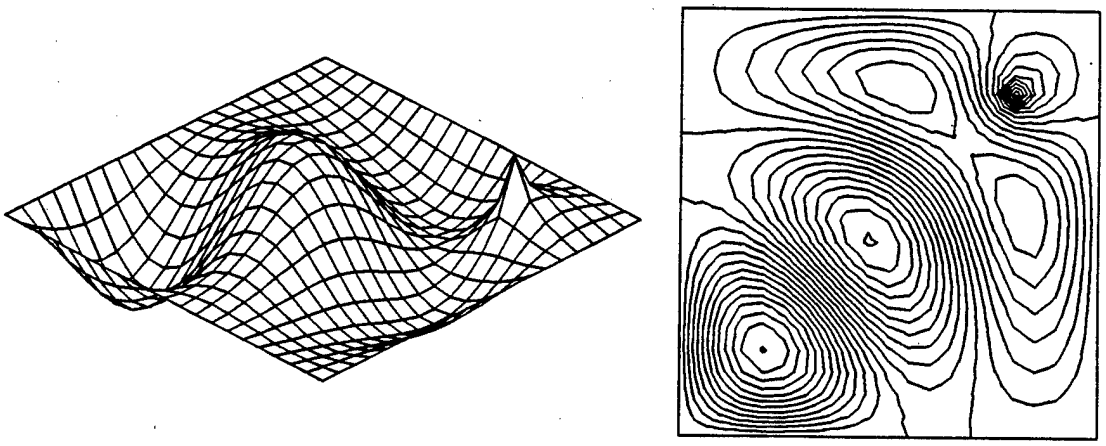

Figure 6.17: Contours for point source located in upper right quadrant of a uniform mesh of (20×20) bilinear elements, at $kL = 5\pi/3$.

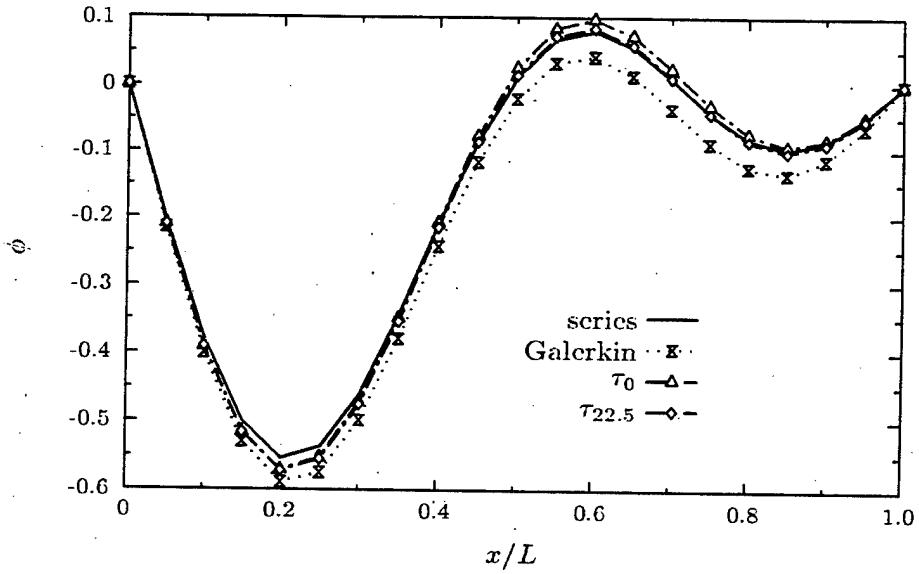

Figure 6.18: Point source located in upper right quadrant: Solution profile along x–axis for fixed $y/L = 0.2$

Galerkin solution. However for this problem where waves are directed in arbitrary directions in $\mathbf{R}^2$, use of the GLS parameter $\tau_{22.5}$ is more accurate than the use of τ_0 as predicted from the two-dimensional Fourier analysis. These results substantiate the conclusions drawn earlier: If the predominant direction θ, is known *a priori*, then the optimal mesh parameter can be calculated from (6.22). However, for general problems where waves are directed in arbitrary directions in $\mathbf{R}^2$, the GLS parameter $\tau_{22.5}$ gives the most accurate solution.

6.4.3 Acoustic radiation from a circular cylinder

In this example we consider the problem of non-uniform radiation from a rigid infinite cylinder of radius a. By increasing the circumferential harmonic loading on the surface of the cylinder, the response of individual modes on the performance of the numerical solution is examined. The position of the truncation boundary is set at $R = 2a$ where the exact DtN non-reflecting boundary condition is applied. The resulting computational domain is discretized by 3×32 bilinear quadrilateral elements (Figure 3.3). The geometrically non-dimensionalized wavenumber is set at $ka = \pi$. With the finite element mesh employed, this value corresponds to a resolution of six elements per wavelength in the radial direction.

For the first harmonic (breathing mode $n = 0$), the exact solution is a simple cylindrical wave which has the character of a radially decaying plane-wave. For the radially uniform mesh employed, this problem reduces to a one dimensional problem with radial coordinate r. Taking h to be the element length in the r-direction, Harari and Hughes [60] have shown that the GLS parameter τ_0 is optimal in this case.

In [152], the higher-order circumferential harmonics $n = 1$ through $n = 4$ were investigated in order to further validate the accuracy of the GLS method for more complex non-uniform radiation patterns. Figure 6.19 shows a summary of these results as a profile of the solution evaluated on the DtN boundary $r = R$. The GLS solution was calculated using both τ_0 and $\tau_{22.5}$ defined previously.

For mode $n = 1$, the improvement of the GLS solutions in comparison to the Galerkin solution is significant. We also observe that in this case, τ_0 performs better than $\tau_{22.5}$. As the circumferential mode is increased to $n = 2$, the improvement in the GLS solution is again significant, however in this case, the GLS solution using either τ_0 or $\tau_{22.5}$ are nearly identical. For mode $n = 3$, the improvement of the GLS solutions in comparison to the Galerkin solution is again clearly shown. However, in this case the use of $\tau_{22.5}$ gives the most accurate solution and is barely distinguishable from the exact solution. Results for mode $n = 4$ are given in [152].

The results of this study indicate that for this particular problem, for low modes $n = 0, 1$, the radiated energy of the cylindrical waves are best resolved by the GLS parameter τ_0, designed to improve dispersion errors for plane-waves directed along radial rays, while for higher modes $n = 3, 4$, the alternative GLS parameter $\tau_{22.5}$ designed for arbitrary directional wave vectors performs better. In more general settings where the radiation pattern is more complex and for unstructured meshes, it is expected that $\tau_{22.5}$ will give the best results.

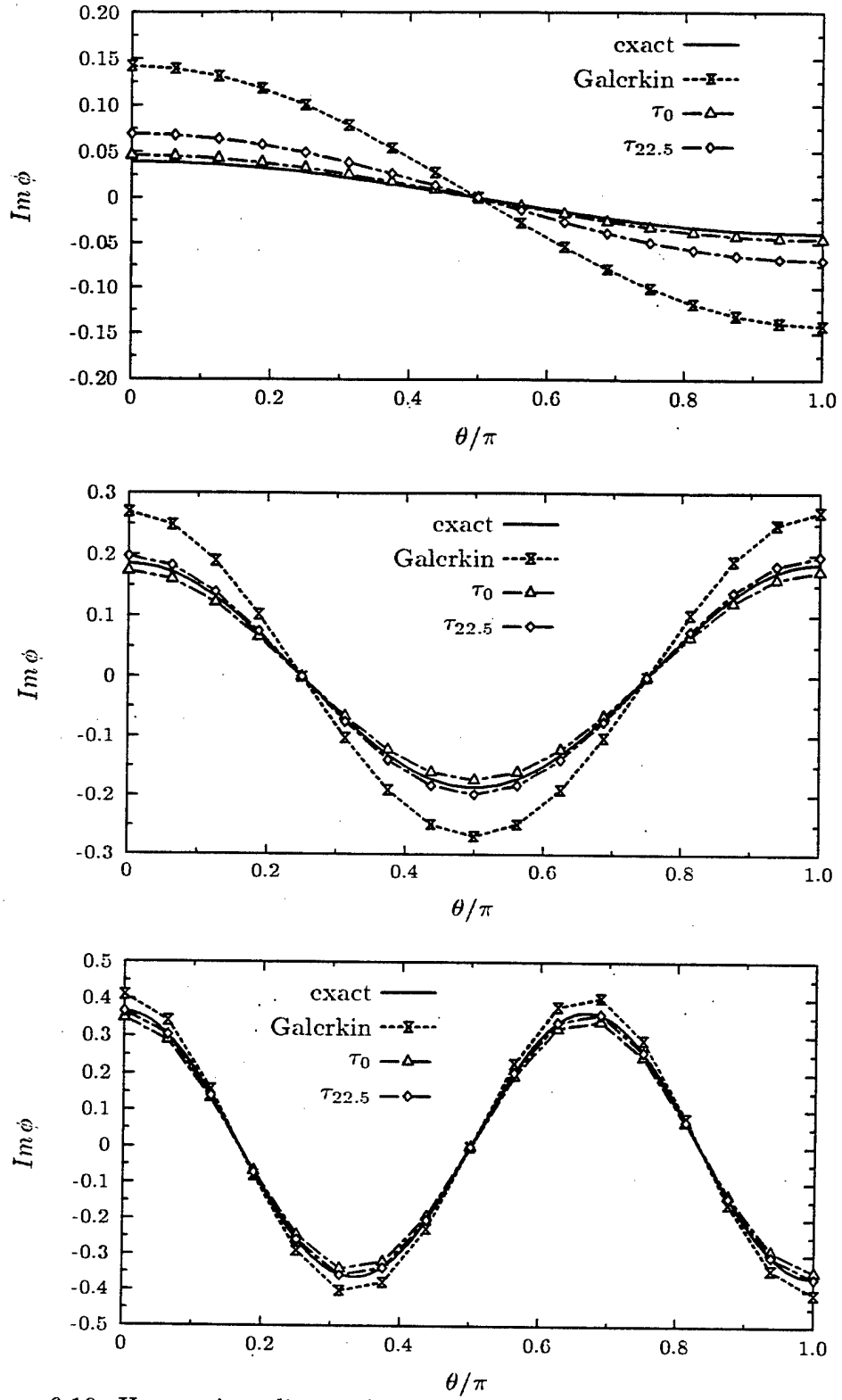

Figure 6.19: Harmonic radiation from a cylinder with $ka = \pi$. Solution plotted along the truncation boundary $R = 2a$. From top to bottom, mode $n = 1, 2, 3$

6.4.4 Radiation from an element of a cylinder

In all of the following examples the GLS solution employs τ_0 based on the analysis in Section 5.2. To solve more complicated problems we consider the non-uniform radiation from a rigid infinite circular cylinder with a constant inhomogeneous value on an arc ($-\alpha < \theta < \alpha$) and vanishing elsewhere. The normalized analytical solution to this problem for a cylinder of radius a is

$$\phi = \frac{2}{\pi} \sum_{n=0}^{\infty}{}' \frac{\sin n\alpha}{n} \frac{H_n^{(1)}(kr)}{H_n^{(1)}(ka)} \cos n\theta \tag{6.71}$$

For low wave numbers this solution is relatively uniform in the circumferential direction. The directionality of the solution grows as the wave number is increased, and the solution becomes attenuated at the side of the cylinder opposite the radiating element.

The properties and discretization are unchanged from the previous problem considered (Fig. 3.3). We select $\alpha = 5\pi/32$ and employ 8 terms in the DtN kernel. Figure 6.20 shows the real part of the analytical solution, nodally interpolated by the mesh employed. The low-amplitude oscillations in the vicinity of the wet surface are merely a product of the series representation of the discontinuity in the boundary condition, and are not relevant to the validation of the numerical results. The real parts of the Galerkin and Galerkin/least-squares solutions are presented in Figs. 6.21 and 6.22, respectively, in comparison to the series solution which is denoted by the dotted contours. Again, both numerical solutions capture the essential physics of the problem, but their individual performance is difficult to evaluate from the contour plots. Figure 6.23 depicts the imaginary part of the solutions evaluated along the artificial boundary. The improvement of the Galerkin/least-squares solution in comparison to the Galerkin solution is striking in this case. Recall the impact of numerical accuracy on the artificial boundary on the quality of far-field solutions obtained by the DtN method.

6.4.5 Scattering of a plane wave from a cylinder

The difference between an undisturbed wave and the acoustic field generated when the wave encounters an obstacle is called a scattered wave. In the typical range of acoustic phenomena the scattered wave usually does not destructively interfere with the incident wave, allowing their complete separation. As an example we compute the scattering, by a cylinder of radius a, of a plane wave traveling along the positive x axis ($\theta = 0$) in a direction perpendicular to the cylinder's axis. The normalized analytical solution to this problem is

$$\phi = -2 \sum_{n=0}^{\infty}{}' i^n \frac{\eta J_n(ka) + J_n'(ka)}{\eta H_n^{(1)}(ka) + H_n^{(1)\prime}(ka)} H_n^{(1)}(kr) \cos n\theta \tag{6.72}$$

where η is related to the acoustic impedance of the cylinder. Again, the directionality of the response increases with wave number, and the distribution becomes more complicated.

Figure 6.20: Radiation from an element of a cylinder of radius a, $R = 2a$, $ka = \pi$, nodal interpolation of the series solution (6.71).

The properties and discretization are retained from the previous problems considered (Fig. 3.3). We select a hard boundary condition ($\eta = 0$) on the wet surface to represent a rigid solid, and again employ 8 terms in the DtN kernel. Figure 6.24 shows the real part of the analytical solution, nodally interpolated by the mesh employed. The real parts of the Galerkin and Galerkin/least-squares solutions are presented in Figs. 6.25 and 6.26, respectively, in comparison to the series solution which is denoted by the dotted contours. Again, both numerical solutions represent the expected physical behavior of the solution, but the Galerkin/least-squares solution is clearly superior and is barely distinguishable from the series solution in most of the domain. Figure 6.27 depicts the imaginary part of the solutions evaluated along the artificial boundary. The improvement of the Galerkin/least-squares solution in comparison to the Galerkin solution is again evident. Recall that the accuracy of numerical solutions on the artificial boundary determines the quality in which the DtN method represents the far field, which is particularly significant in scattering problems.

6.4.6 Decay in a unit square with a uniform source distribution

The configuration of this example, which has a decaying exact solution, is taken from Franca and Dutra do Carmo [34]. The domain is a unit square discretized by a 20×20 mesh of bilinear elements. Homogeneous Dirichlet boundary conditions are imposed

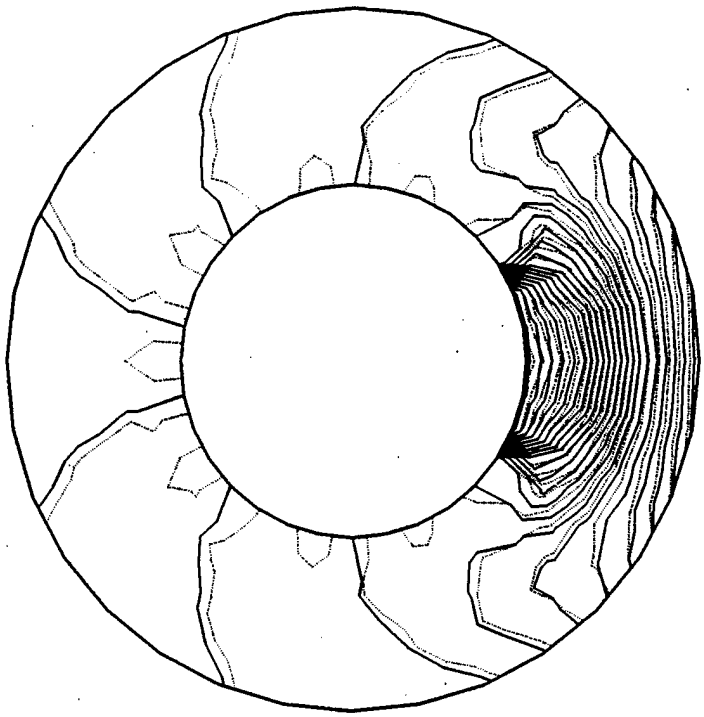

Figure 6.21: Radiation from an element of a cylinder of radius a, $R = 2a$, $ka = \pi$, Galerkin solution (dotted contours denote series solution).

on two adjacent sides and the function is required to take on the value of unity on the remaining sides. There is a uniform source distribution $f = 10^8$ and the decay rate is $k^2 = -10^8$. These values are selected so that the exact solution is essentially uniform throughout most of the domain, decaying sharply in thin boundary layers near the boundaries with homogeneous boundary conditions. Figure 6.28 shows an elevation plot of the Galerkin solution to this problem, with the expected spurious oscillations in the neighborhood of the boundary layer. Again, this is an indication of insufficient resolution, and would improve with mesh refinement. These oscillations are absent in the Galerkin/least-squares solution, Fig. 6.29, which is identical to the Galerkin/gradient least-squares solution shown in [34], as predicted. This solution captures the expected behavior of the exact solution.

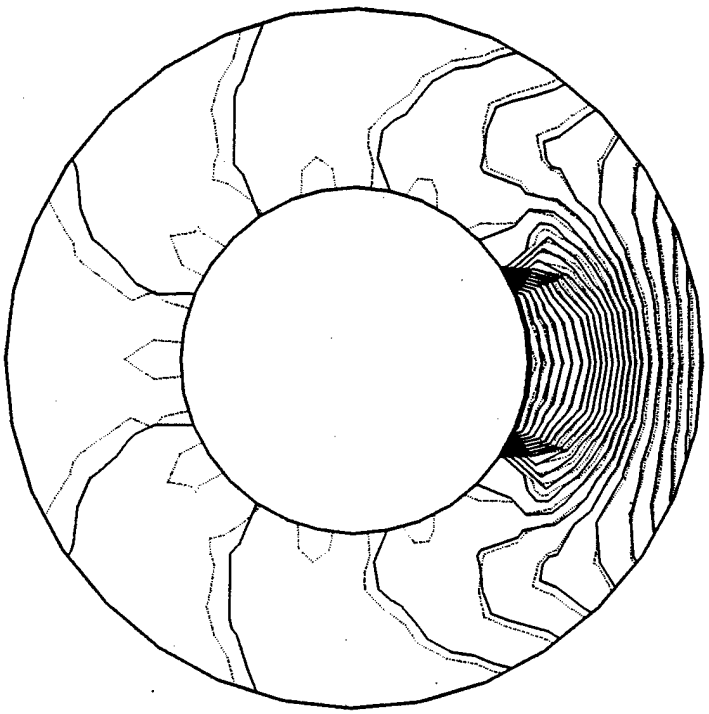

Figure 6.22: Radiation from an element of a cylinder of radius a, $R = 2a$, $ka = \pi$, Galerkin/least-squares solution (dotted contours denote series solution).

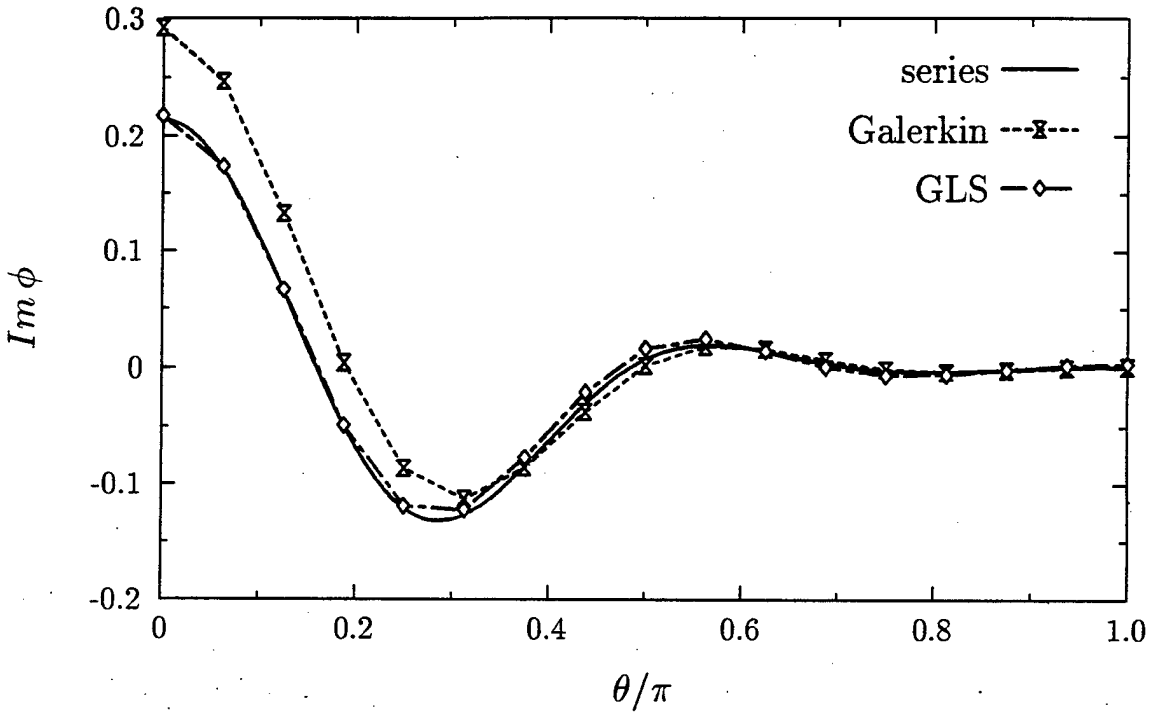

Figure 6.23: Radiation from an element of a cylinder of radius a, $R = 2a$, $ka = \pi$, along the artificial boundary $R = 2a$.

Figure 6.24: Scattering of a plane wave (at $\theta = 0$) from a cylinder of radius a, $R = 2a$, $ka = \pi$, nodal interpolation of the series solution (6.72).

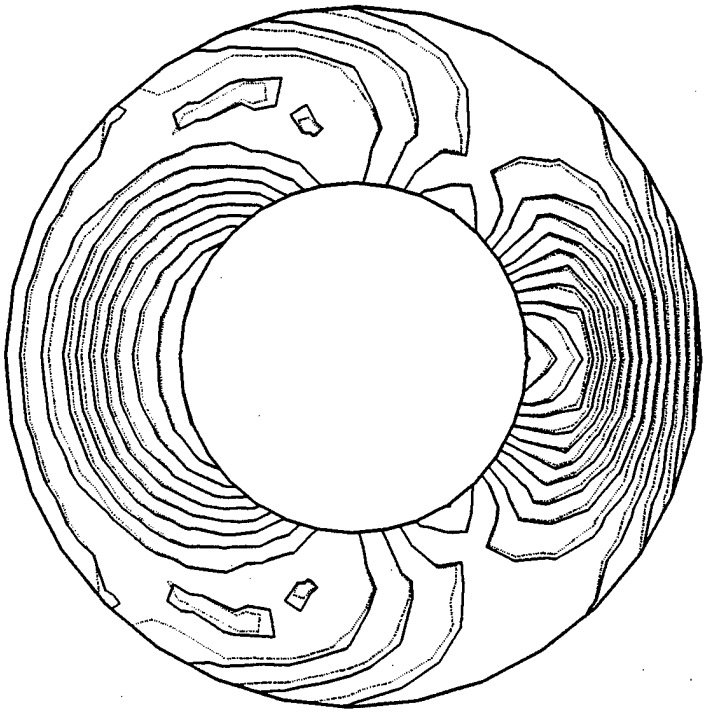

Figure 6.25: Scattering of a plane wave (at $\theta = 0$) from a cylinder of radius a, $R = 2a$, $ka = \pi$, Galerkin solution (dotted contours denote series solution).

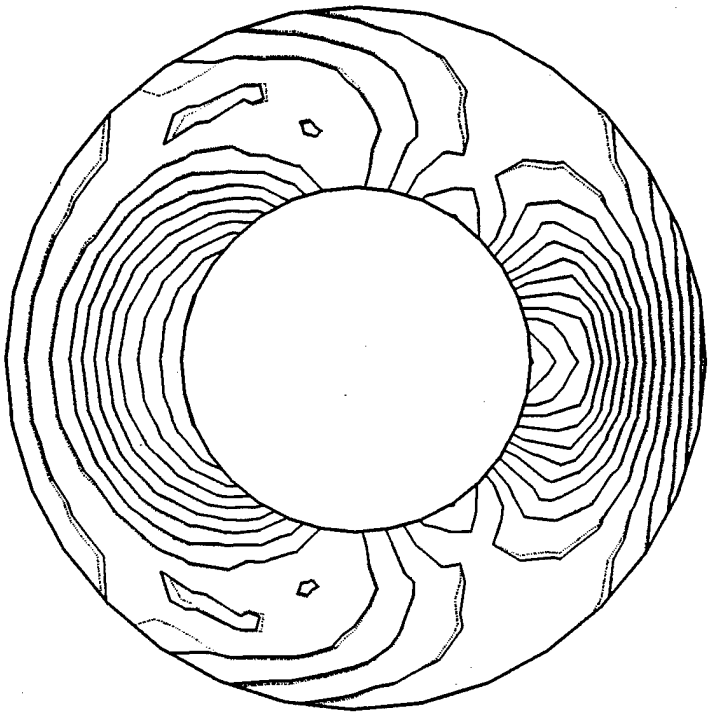

Figure 6.26: Scattering of a plane wave (at $\theta = 0$) from a cylinder of radius a, $R = 2a$, $ka = \pi$, Galerkin/least-squares solution (dotted contours denote series solution).

Figure 6.27: Scattering of a plane wave (at $\theta = 0$) from a cylinder of radius a, $R = 2a$, $ka = \pi$, along the artificial boundary $R = 2a$.

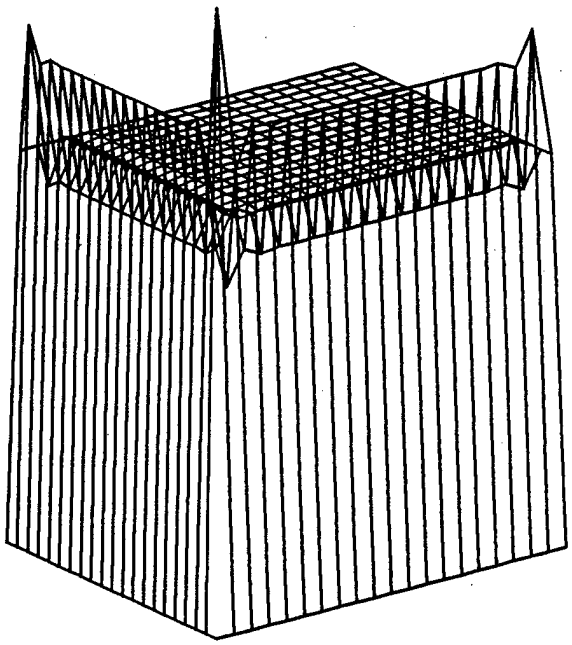

Figure 6.28: Galerkin solution to a Dirichlet problem with a decaying exact solution.

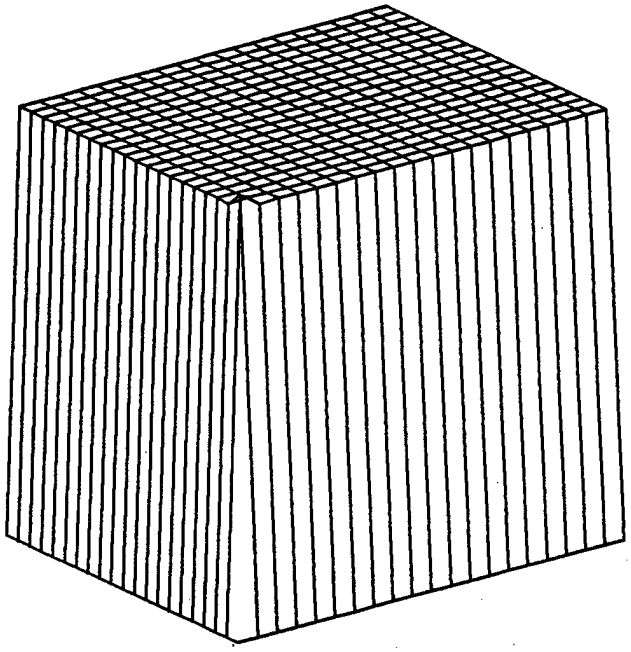

Figure 6.29: Galerkin/least-squares solution to a Dirichlet problem with a decaying exact solution.

Chapter 7

The Cost of Computation

Cost-effectiveness of numerical schemes is a primary consideration in method design, since it determines both the economics of computation and the limit of problem-solving capabilities on existing computer technology. The demand for large-scale problem-solving capabilities is growing with increasing interest in the numerical modeling of realistic configurations, driving the development of sophisticated algorithms that are amenable to efficient implementation on modern vector and parallel platforms. In this study we investigate the computational cost of obtaining solutions to problems of time-harmonic acoustics by the boundary element and finite element methods. In order to arrive at comprehensive conclusions, a set of representative problems in both bounded and unbounded domains are examined. The results obtained apply directly to any class of problems with complex scalar dependent variables, defined over similar configurations, and can easily be specialized to real variables and/or extended to problems that are governed by systems of equations.

We concentrate on the cost of solving the linear algebraic systems of n_{eq} equations

$$\boldsymbol{A}\boldsymbol{x} = \boldsymbol{b} \tag{7.1}$$

that arise in discretizations employing linear elements. Problems are parameterized by n, a typical number of elements, and quantities pertinent to the computation are expressed in terms of this parameter. Computational cost for a given problem size may then be discussed in terms of the *order* of n and its coefficient, and boundary element and finite element techniques are thus compared.

The choice of linear elements as the basis for comparison is motivated by convenience. Higher-order interpolation favors boundary element methods since the ensuing equations are always fully coupled, the order of interpolation notwithstanding, whereas the bandedness of finite element matrices is adversely effected by higher-order elements. Nevertheless, the results obtained by employing linear elements are applicable to our interests, which are primarily in conclusions of a general nature, in establishing the feasibility of employing the two methods, rather than pinpointing the crossover at which one gains an advantage over the other for specific cases. Higher-order elements may also improve some aspects of the solution, but considerations of accuracy are not addressed in this study. The prevalent opinion among practitioners of boundary element methods appears to be that for comparable levels of discretization (when the boundary element mesh is the restriction of the finite element mesh to

the boundary), boundary element methods will provide more accurate solutions than finite element methods. We have been unsuccessful in locating references to substantiate this claim, and on the other hand have found studies performed in the boundary element community indicating that the accuracy of the two methods is comparable ([24] and [110]).

The strategies for solving systems of coupled equations fall into two main classes: direct methods and iterative methods. Direct methods, which are based on Gaussian elimination, are more prevalent in commercial software and better understood theoretically. These procedures are extremely reliable, and provide an *a priori* estimate of the computational effort required, but the cost grows rapidly with the number of equations, restricting the problem size for which direct methods are economical. Investigation of iterative solution techniques is currently on the rise. The performance of these methods varies widely, and is particularly sensitive to the conditioning of the equations, but, overall, iterative algorithms are very efficient for large-scale computation, most notedly in parallel computational environments. In addition to comparing boundary element and finite element methods within the context of each solution procedure, we examine the relative performance of the two solution techniques. Unlike many conventional numerical applications, in which the cost of forming the discrete equations is small in comparison to the cost of solving the linear system, in many of the cases considered herein *equation formation is not a negligible component of the computation*, especially when considering iterative solution methods for large-scale problems. The greater part of this work concerns these three topics: direct solvers, iterative solvers and equation formation

The work of scientific computation is measured in *flops*, floating-point operations. In the following we employ the traditional definition of a flop given in [45, p. 32] and [69, p. 642] as approximately the work required to execute $s := s + x_i y_j$, i.e., a multiplication, an addition and some bookkeeping. This convenient definition suffices for the comparative study pursued herein, but is inappropriate as an absolute measure on modern vector and parallel platforms in which an individual addition or multiplication is considered to constitute a flop [31, pp. 42–45]. Storage requirements are measured in words.

In Section 7.1 computations attributes of boundary element and finite element methods are presented. Direct solution techniques are reviewed in Section 7.2, and the cost of employing such techniques to solve the equations arising from boundary element and finite element analyses of a wide range of geometric configurations is evaluated and compared. This study is repeated for iterative solvers in Section 7.3, employing the GMRES procedure as a representative technique. In Section 7.4 the two solution strategies are compared, and the cost of equation formation is examined.

7.1 Computational Attributes of Numerical Methods

The comparison of boundary-based computation to domain discretization leads to interesting issues in terms of the economics of computation. The advantage in terms of

the effort of forming and solving the algebraic equations that the former might intuitively be expected to gain, due to its fewer number of equations, is counterbalanced by the favorable structure of the matrices arising in the latter. The groundwork for a detailed study is laid out in the section by examining the properties of the systems of equations associated with the two types of computational methods.

7.1.1 Boundary element formulations

The use of boundary element methods (e.g., [20, 101]) for computing solutions to linear, homogeneous, isotropic problems governed by the homogeneous Helmholtz equation is wide-spread (see, e.g., the survey in [137]). Based on Helmholtz integral representations, and hence requiring only surface discretization, boundary formulations appear to be well-suited for problems of acoustics, which are often defined over unbounded domains. Surface discretization leads to an undisputed advantage over domain-based methods in the effort (both human and computational) required by the mesh-generation portion of model preparation. The ensuing computational effort associated with the algebraic equations is studied in detail and compared in Sections 7.2 and 7.3 in the context of direct and iterative solutions strategies, respectively. Numerical methods that are based directly on surface Helmholtz equations of exterior problems, evaluated at physical boundaries, are known to produce discrete equations that are ill-conditioned in the vicinity of characteristic wave numbers [22]. We consider the Burton-Miller approach [19] for generating boundary element formulations that theoretically preclude non-unique solutions. (Other notable attempts at alleviating this difficulty are the CHIEF method [130], and the use of modified Green functions [95].) The integration of the hyper-singular kernels that arise in this scheme is addressed by the regularized version of this formulation. Alternative remedies have been proposed, such as isolating problematic terms in the integrand by means of a Taylor series expansion and employing Stokes' theorem to remove the hypersingular kernels [103] and applied to Burton-Miller formulations for problems of time-harmonic acoustics [107].

The arrays in (7.1) for boundary element implementations are $\boldsymbol{A} \in \mathbb{C}^{n_{eq} \times n_{eq}}$, a full and nonsymmetric matrix, and $\boldsymbol{b} \in \mathbb{C}^{n}_{eq}$. The computational advantage that could be gained by boundary discretization, giving rise to relatively small systems of equations, is offset to a degree by the fact that the equations are fully coupled. A major thrust of this study is to characterize the extent of this offset. Furthermore, formation of the linear equations may be a significant portion of obtaining solutions by boundary element techniques. This is mainly due to implementational issues such as integration along non-smooth boundaries. The impact of equation formation may become considerably higher when a Burton-Miller approach to boundary element formulation is used, and can overwhelm all other aspects of the computation for the regularized version of that approach ([6], see Section 7.4). Alternatives to the regularized Burton-Miller scheme that do not contain hyper-singular integrals [107] may alleviate this difficulty.

Iterative solvers are notoriously sensitive to ill conditioning of the linear equations, emphasizing the importance of this facet of the algebraic problem. Loss of uniqueness

of solutions of the continuous formulation will manifest itself as poor conditioning of the discrete equations. This is evident in the conditioning of the coupled boundary element equations reported in [46], for the scattering from an elastic aluminum sphere of radius a immersed in water, in the geometrically nondimensionalized wave number range $1 \leq ka \leq 7$, where k is the (physical) wave number. The condition number rises sharply in the vicinity of the characteristic wave numbers of the sphere. These results are presented in the 1-norm, which is equivalent to the 2-norm that is commonly used, and are normalized by the condition number at $ka = 1$, which was about 40, and scaled by the shear modulus of the solid.

7.1.2 Finite element formulations

Finite element techniques are a general-purpose computational tool (not restricted to linear, homogeneous or isotropic problems) used in a wide variety of applications. These methods are being increasingly employed for problems of acoustics and structural acoustics, e.g., [2, 8, 117, 123], as well as being presented herein. Traditional finite element formulations can not be directly applied to problems in unbounded domains. Infinite elements [17] and a sequence of local boundary operators [15] are examples of means that have been suggested to circumvent this difficulty. In this study, we consider finite element techniques that utilize the DtN methodology introduced by Givoli and Keller [41, 98] for constructing boundary conditions on an artificial boundary (Fig. 2.1) as presented in Chapter 2. It is shown in Chapter 3 that the DtN boundary condition precludes singular behavior in finite element solutions for problems in exterior domains (recall, the exact solution is unique). The DtN operator imposes an *exact* impedance condition on the artificial boundary, enabling the development of finite element methods that converge with mesh refinement for *fixed* computational domains.

Wave resolution requirements in finite element formulations for problems of acoustics are relaxed in Chapter 5 by the Galerkin/least-squares (GLS) methodology. The resulting finite element models are accurate to a minimum of four linear elements per wave (the limit of approximability of such physical features), and exhibit strong damping of phenomena that are insufficiently resolved. Evanescent waves are also well represented by these models. A specialization of this technique is particularly appropriate for exterior problems which are meshed by a single layer of elements, shown in some of the examples that follow.

For interior problems $\boldsymbol{A} \in \mathbb{R}^{n_{eq} \times n_{eq}}$ is banded (with half-bandwidth b_w) and symmetric, as in traditional finite element implementations. Employing a DtN boundary condition for exterior problems has significant computational ramifications. Consider an external artificial boundary with $n_b < n_{eq}$ nodes. The coefficient matrix $\boldsymbol{A}$ above can be written in partitioned form, separating nodes on the external boundary

$$\boldsymbol{A} = \begin{bmatrix} \boldsymbol{A}_{11} & \boldsymbol{A}_{12} \\ \boldsymbol{A}_{21} & \boldsymbol{A}_{22} \end{bmatrix} \tag{7.2}$$

where $\boldsymbol{A}_{12} = \boldsymbol{A}_{21}^T$. The coefficient matrix for the exterior problem with a DtN boundary condition, which couples all of the equations on the artificial boundary, takes the

form

$$\boldsymbol{A} = \begin{bmatrix} \boldsymbol{A}_{11} & \boldsymbol{A}_{12} \\ \boldsymbol{A}_{21} & \boldsymbol{A}_{22} + \boldsymbol{A}_{DtN} \end{bmatrix} \tag{7.3}$$

where the DtN contribution $\boldsymbol{A}_{DtN} \in \mathbb{C}^{n_b \times n_b}$ is full and symmetric. If $n_b \ll n_{eq}$, the node numbering can often be ordered so as to maintain the underlying bandwidth (see [98]). Unfortunately, this is not always possible, and, as a matter of fact, is not the case in any of the configurations considered herein. As well as potentially degrading the bandwidth of the linear equations, the DtN operator consists of kernels that are similar in nature to those found in boundary element methods. The cost of equation formation might thus become comparable to the cost of solving the linear system. In finite element implementations for interior problems formation of the discrete equations is a negligible part of the computation. This issue will be discussed further in Section 7.4. As in the case of boundary element implementations, $\boldsymbol{b} \in \mathbb{C}^n_{eq}$.

The conditioning of finite element models for time-harmonic acoustics was examined in [59]. The Galerkin/least-squares equations are slightly better conditioned the the Galerkin equations, influencing the performance of iterative solution techniques.

7.2 Direct Solution Techniques

The solution to linear systems of coupled equations is currently most often obtained by direct methods, algorithms that employ Gaussian elimination procedures to essentially invert the coefficient matrix. The popularity of these schemes can be attributed to their robust performance, relatively simple implementation and their predictability in cost requirements, but they are not cost-effective in large-scale computation.

Typically, the first step in solving (7.1) for a general, nonsingular $\boldsymbol{A} \in \mathbb{R}^{n_{eq} \times n_{eq}}$ (see [45, pp. 53–58]) is to *factorize* $\boldsymbol{A}$ into lower and upper triangular matrices, $\boldsymbol{L}$ and $\boldsymbol{U}$, respectively,

$$\boldsymbol{A} = \boldsymbol{L}\boldsymbol{U} \qquad n^3_{eq}/3 \text{ flops} \tag{7.4}$$

The solution is then obtained by a *backsolve*, namely

$$\boldsymbol{L}\boldsymbol{y} = \boldsymbol{b} \qquad \text{forward reduction, } n^2_{eq}/2 \text{ flops} \tag{7.5}$$

$$\boldsymbol{U}\boldsymbol{x} = \boldsymbol{y} \qquad \text{back-substitution, } n^2_{eq}/2 \text{ flops} \tag{7.6}$$

totaling n^2_{eq} flops. There are n^2_{eq} words of storage required.
Remark: For complex arithmetic, operation counts are increased by a factor of four, and storage by two.

In finite element analysis the matrices have special structure which may be exploited to economize the computation. There are two main approaches to implementing direct methods in this context. An active column solver [154] assembles the matrix in a compact data structure, prior to factorization, taking full advantage of symmetry and sparseness of the array. In a frontal method [83] only the coefficients needed for the reduction of a particular equation are assembled, and the equation is immediately eliminated. The number of operations for the two approaches is the

same, but frontal solvers, which typically require less core memory, are inferior to column solvers for large-scale problems, in particular on vector platforms [142]. Frontal techniques are also inappropriate for configurations in which there is a relatively high degree of coupling such as models of exterior problems which are dominated by the DtN portion. In this study we consider the active column implementation of finite element methods (b_w then denotes the *mean* half-bandwidth) for comparison with boundary element techniques.

More efficient, special-purpose algorithms are thus used when $\boldsymbol{A}$ is banded and symmetric ([45, pp. 93–97] and [69, pp. 635–643]). Factorization is

$$\boldsymbol{A} = \boldsymbol{U}^T\boldsymbol{D}\boldsymbol{U} \qquad n_{eq}b_w^2/2 - b_w^3/3 \text{ flops} \tag{7.7}$$

where $\boldsymbol{D}$ is a diagonal matrix, and the appropriate backsolve procedure

$$\boldsymbol{U}^T\boldsymbol{z} = \boldsymbol{b} \qquad \text{forward reduction, } n_{eq}b_w - b_w^2/2 \text{ flops} \tag{7.8}$$

$$\boldsymbol{D}\boldsymbol{y} = \boldsymbol{z} \qquad \text{diagonal scaling, } n_{eq} \text{ flops} \tag{7.9}$$

$$\boldsymbol{U}\boldsymbol{x} = \boldsymbol{y} \qquad \text{back-substitution, } n_{eq}b_w - b_w^2/2 \text{ flops} \tag{7.10}$$

requires a total of $2n_{eq}b_w - b_w^2$ flops. The storage required is $n_{eq}b_w$ words.
Remarks

1. These are asymptotic cost estimates, assuming $n_{eq} \gg 1$ and $b_w \gg 1$.
2. In traditional finite element implementations $n_{eq} \gg b_w$, and thus factorization requires $n_{eq}b_w^2/2$ flops, and $2n_{eq}b_w$ flops are needed for the backsolve portion. When using a DtN boundary condition, however, the higher-order b_w terms may become significant.

7.2.1 Interior problems

We first consider boundary-value problems of acoustics defined over interior domains, bounded externally by a physical boundary. Such problems exhibit resonance at countably infinite discrete wave numbers. The equations that emanate from numerical methods should be well-conditioned at intermediate values.

The economic performance of direct solvers for boundary element and finite element methods applied to the configurations examined in this section was studied by Bettess [18]. The following results differ somewhat in that the equations of time-harmonic acoustics are considered, engendering boundary element equations with complex coefficients. Nevertheless, the conclusions presented at the end of this section are in agreement with those drawn in [18].

Two configurations are considered, each with n elements per side. Figure 7.1 shows the first example, a square domain discretized by a mesh of $n \times n$ elements. The second configuration is its three-dimensional analog (Fig. 7.2). We are interested in evaluating method performance on large-scale problems and therefore consider $n \gg 1$.

Figure 7.1: A square domain discretized by a $n \times n$ mesh.

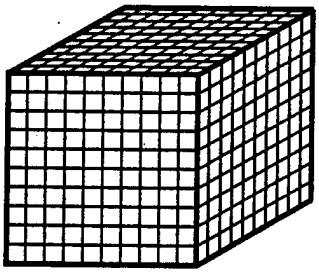

Figure 7.2: A cube discretized by a $n \times n \times n$ mesh.

Table 7.1: Cost of directly solving boundary element equations for interior problems shown in Figs. 7.1 and 7.2 (all operations are in complex arithmetic).

Mesh	No. of equations	Factorization [Flops]	Backsolve [Flops]	Storage [words]
	n_{eq}	$4n_{eq}^3/3$	$4n_{eq}^2$	$2n_{eq}^2$
$n \times n$	$4n$	$256n^3/3$	$64n^2$	$32n^2$
$n \times n \times n$	$6n^2$	$288n^6$	$144n^4$	$72n^4$

Table 7.2: Cost of directly solving finite element equations for interior problems shown in Figs. 7.1 and 7.2 (all operations are in complex arithmetic).

Mesh	No. of equations	Half-bandwidth	Factorization [Flops]	Backsolve [Flops]	Storage [words]
	n_{eq}	b_w	$n_{eq}b_w^2/2$	$8n_{eq}b_w$	$n_{eq}b_w$
$n \times n$	n^2	n	$n^4/2$	$8n^3$	n^3
$n \times n \times n$	n^3	n^2	$n^7/2$	$8n^5$	n^5

Recall that boundary element methods give rise to systems of equations in which the coefficients, as well as the unknowns and the prescribed data, are complex. This fact is reflected in Table 7.1, which shows the cost entailed in directly solving these equations.

Due to phase lag in Galerkin finite element methods, resonance adversely effects the results in the *vicinity* of characteristic wave numbers, causing amplitude modulation. This was demonstrated in [57], along with superior performance of a Galerkin/least-squares method. Interior problems are suitable for traditional finite element implementations (without a DtN procedure). The left-hand side coefficients are therefore real, and only the backsolve procedure need take into account complex arithmetic, as shown in Table 7.2.

It is immediately evident that the anticipation that boundary element methods uniformly entail less cost due to the smaller number of equations involved is a misconception. As a rule (for this type of problems), the order of the cost is indeed lower for boundary elements. The coefficient, however, is significantly higher. This leads to finite elements being more cost-effective for relatively small problems, and boundary elements being more cost-effective for larger problems. Table 7.3 indicates the number of elements per side at which the costs of the two methods are equal for the two configurations considered. The magnitude of the problem that must be considered before boundary element methods exhibit computational benefits is indeed quite large, in particular in three dimensions, both from the point of view of computations and that of storage requirements.

Remark: The crossover for the three-dimensional mesh ($n = 576$) is equivalent to 1,990,656 (fully coupled) boundary element equations. This is clearly beyond the range of capabilities of direct solvers in current computer technology, indicating that

Table 7.3: Crossover for direct methods on interior problems shown in Figs. 7.1 and 7.2 (value of n, number of elements per side, at which costs are equal).

Mesh	Factorization	Backsolve	Storage
$n \times n$	171	8	32
$n \times n \times n$	576	18	72

for many practical configurations the use of direct solution techniques for interior problems is more cost-effective with finite elements.

7.2.2 Exterior problems

We now direct our attention to exterior domains, bounded internally by a physical body. As previously noted, the exact solution is unique, in contrast to interior problems. Problems with simple interior boundaries, that allow uniform discretization, are treated separately from those with more intricate geometric features on the physical boundaries, that require gradual refinement of finite element meshes. In the following all operation counts correspond to complex arithmetic.

Uniform discretizations

We first consider counterparts to the interior examples that were discussed above. Figure 7.3 shows a square body with n elements per side, and its three-dimensional analog in the form of a cube discretized by a mesh of $n \times n \times 6$ elements (not shown) is considered as well. Boundary element discretizations are unchanged from the ones employed to model interior problems. Operation counts, Table 7.4, are also identical to interior problems, cf. Table 7.1. We have already noted the failure of surface Helmholtz equations evaluated at physical boundaries at characteristic wave numbers. In practical terms this translates to a restriction of the applicability of these methods to problems with low wave numbers, unless an appropriate modification to the basic formulation, such as the Burton-Miller approach, is employed. We have mentioned other remedies for this limitation, but the clustering of characteristic wave numbers in the higher range and for elongated geometries greatly reduces their reliability. A value that is often employed by numerical analysts is $kA < \pi$ (in three dimensions), where A is the radius of the circumscribing sphere.

The finite element meshes employ a single layer of elements with a DtN boundary in the form of a d-dimensional sphere (e.g., Fig. 7.3), where $d = 2$ or 3 is the number of space dimensions. As previously noted, there is a version of the Galerkin/least-squares method in [57] that is particularly appropriate for such meshes. Table 7.5 shows the operation counts for finite elements. In these examples the non-localness of the DtN boundary condition effects the bandwidth significantly. Without the DtN boundary condition, the bandwidth would be of one order lower than that of the number of equations (Table 7.2). With the DtN boundary condition, the bandwidth is of an order *equal* to the order of the number of equations, namely, for one layer of

Figure 7.3: The computational domain exterior to a square discretized by n elements per side.

Table 7.4: Cost of directly solving boundary element equations for exterior problems with uniform discretizations, e.g., see Fig. 7.3.

Mesh	No. of equations	Factorization [Flops]	Backsolve [Flops]	Storage [words]
	n_{eq}	$4n_{eq}^3/3$	$4n_{eq}^2$	$2n_{eq}^2$
$n \times 4$	$4n$	$256n^3/3$	$64n^2$	$32n^2$
$n \times n \times 6$	$6n^2$	$288n^6$	$144n^4$	$72n^4$

Table 7.5: Cost of directly solving finite element equations for exterior problems with uniform discretizations, e.g., see Fig. 7.3.

Mesh	No. of equations	Half-bandwidth	Factorization [Flops]	Backsolve [Flops]	Storage [words]
	n_{eq}	b_w	$2n_{eq}b_w^2 - 4b_w^3/3$	$8n_{eq}b_w - 4b_w^2$	$2n_{eq}b_w$
$n \times 4$	$8n$	$2n$	$160n^3/3$	$112n^2$	$32n^2$
$n \times n \times 6$	$12n^2$	$3n^2$	$180n^6$	$252n^4$	$72n^4$

elements $b_w = n_{eq}/4$, see Table 7.5. Higher-order b_w terms are therefore kept in the operation counts. Nevertheless, the factorization costs are of the same asymptotic order as boundary elements, with *lower* constants for one layer of elements. There is no crossover because *finite elements are less costly for these configurations on any size mesh*. This is easily explained by the fact that the factorization of the finite element equations is dominated by the DtN portion, which is equal in size to the boundary element problem, but symmetrical. (The backsolve procedure is uniformly more expensive on these problems for finite element equations, but this portion of the calculation is relatively insignificant. Storage requirements of the two methods are identical.) Furthermore, the resulting finite element wave number limitation

$$kA < \frac{\pi}{\sqrt{d}-1} \approx \begin{cases} 7.58, & d=2 \\ 4.29, & d=3 \end{cases} \tag{7.11}$$

is less restrictive than for boundary elements. This value is based on a minimum resolution of four elements per wave, obtained in Chapter 5 with the Galerkin/least-squares methodology.

Remark: The situation is unchanged when considering boundary element models of more regular physical objects such as cross sections of circular cylinders (Fig. 7.4) and spheres. The operation counts and storage requirements are identical to those of squares and cubes, respectively, for the same number of elements, and the wave number restriction, which is inherent to the formulation, is still the same. For finite elements the solution cost is also unchanged, but the wave number restriction, which was a consequence of the geometry, is lifted. The same is true for an ellipsoid of revolution (Fig. 7.5), which requires the introduction of a non-spherical DtN boundary. This is achieved by employing fundamental solutions in elliptic coordinates [53].

The wave number restriction of boundary elements is in terms of a *geometrically* non-dimensionalized wave number, and hence can not be relaxed except via a modification of the method such as the Burton-Miller approach, engendering significant additional computation. In contrast, finite element models are restricted by wave resolution, i.e., a *numerically* nondimensionalized wave number. The range of applicability of these models can be extended simply by mesh refinement, with the obvious consequence of higher cost. An example of this tradeoff is shown in Table 7.6, in which meshes with two layers of elements are considered, increasing the upper bounds on the allowable wave number in (7.11) by a factor of two.

In summary, for exterior problems with uniform discretizations, it is less costly to

Figure 7.4: The computational domain exterior to a circular cylinder or a sphere.

Figure 7.5: The computational domain exterior to an ellipsoid of revolution.

Table 7.6: Cost of directly solving finite element equations with a double wave number range for exterior problems with uniform discretizations, by employing meshes with two layers of elements.

Mesh	No. of equations	Half-bandwidth	Factorization [Flops]	Backsolve [Flops]	Storage [words]
	n_{eq}	b_w	$2n_{eq}b_w^2 - 4b_w^3/3$	$8n_{eq}b_w - 4b_w^2$	$2n_{eq}b_w$
$2n \times 4$	$12n$	$8n/3$	$11776n^3/81$	$2048n^2/9$	$64n^2$
$2n \times n \times 6$	$18n^2$	$4n^2$	$1472n^6/3$	$512n^4$	$144n^4$

Table 7.7: Cost of directly solving boundary element equations for exterior problems with gradually refined discretizations shown in Figs. 7.6 and 7.7.

Mesh	No. of equations	Factorization [Flops]	Backsolve [Flops]	Storage [words]
	n_{eq}	$4n_{eq}^3/3$	$4n_{eq}^2$	$2n_{eq}^2$
$n \times 1$	$11n/9$	$5324n^3/2187$	$484n^2/81$	$242n^2/81$
$n \times 3n \times 1$	$5(7n/9)^2$	$500(7n/9)^6/3$	$100(7n/9)^4$	$50(7n/9)^4$

employ direct solvers with single-layer finite element meshes than boundary element models. Furthermore, the wave number restriction on finite elements is less severe, and can easily be relaxed by mesh refinement.

Gradually refined discretizations

We next consider physical boundaries with more elaborate geometric features. A two-dimensional example is a circle with a thin protrusion, of length approximately a third of the diameter of the circle (Fig. 7.6). This configuration is discretized with n elements around the circumference of the circle. We accounted for gradual refinement of the finite element mesh around the protrusion. Figure 7.7 depicts a slender ellipsoid of revolution, with length-to-diameter ratio of ten-to-one. It also contains a thin protrusion, of length approximately a third of the diameter. The two-dimensional configuration can be thought of as a cross section through the middle of this model. The mesh, again, contains n elements around the circular circumference, and gradual refinement of the finite element mesh is accounted for. Table 7.7 shows the operation counts and storage requirements for solving the equations associated with boundary elements. The same type of wave number restriction as before applies to these solutions.

The costs of solving the finite element equations are shown in Table 7.8. These expressions are more complicated than in previous examples because of the internal mesh grading. Upon examination of the coefficients it becomes apparent that the bandwidth varies from being of the same order as the number of equations for relatively small meshes, to one order lower than the number of equations for larger meshes. This occurs because the mesh on the DtN boundary need not resolve geo-

Figure 7.6: The computational domain exterior to a circle with a thin protrusion.

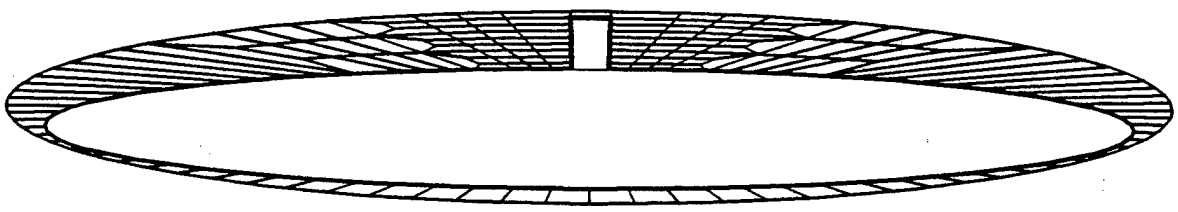

Figure 7.7: The computational domain exterior to a slender ellipsoid of revolution with a thin protrusion.

Table 7.8: Cost of directly solving finite element equations for exterior problems with gradually refined discretizations shown in Figs. 7.6 and 7.7 (the coefficients are: $\beta_2 = (180+n)/81$, $\gamma_2 = \frac{729+10n}{9(180+n)}$, $\beta_3 = (13176+5n)/2187$, $\gamma_3 = \frac{1062882+815n}{54(13176+5n)}$).

Mesh	No. of equations	Half-bandwidth	Factorization [Flops]	Backsolve [Flops]	Storage [words]
	n_{eq}	b_w	$2n_{eq}b_w^2 - 4b_w^3/3$	$8n_{eq}b_w - 4b_w^2$	$2n_{eq}b_w$
$n \times 1$	$\beta_2 n$	$\gamma_2 n$	$2\gamma_2^2(3\beta_2 - 2\gamma_2)n^3/3$	$4\gamma_2(2\beta_2 - \gamma_2)n^2$	$2\beta_2\gamma_2 n^2$
$n \times 3n \times 1$	$\beta_3 n^2$	$\gamma_3 n^2$	$2\gamma_3^2(3\beta_3 - 2\gamma_3)n^6/3$	$4\gamma_3(2\beta_3 - \gamma_3)n^4$	$2\beta_3\gamma_3 n^4$

Table 7.9: Crossover for direct methods on exterior problems with gradually refined discretizations shown in Figs. 7.6 and 7.7 (value of n, number of elements around the circular circumference, at which costs are equal).

Mesh	Factorization	Backsolve	Storage
$n \times 1$	83	—	36
$n \times 3n \times 1$	522	—	22

metric details of the physical boundary. On coarser meshes, the number of nodes on the physical boundary is close to the number on the DtN boundary, and hence the coupling of the DtN operator significantly impacts the bandwidth as in the exterior problems with uniform discretizations. The higher-order b_w terms are therefore not neglected in Table 7.8. However, as the mesh is refined, the number of nodes on the interior boundary increases at a faster rate than on the exterior boundary, diminishing the influence of the DtN coupling, and progressively approaching the tendencies seen in the interior problems, where the DtN operator was not present.

In order to interpret the costs of the finite element analysis and compare them to boundary elements it is convenient to examine asymptotic values of the expressions in Table 7.8. Consider the cost of the two-dimensional $(n \times 1)$ mesh. Factorization of the finite element equations on smaller meshes tends to approximately $0.78n^3$ flops, i.e., the same order of the corresponding cost for boundary elements (Table 7.7), but with a smaller constant, and hence a lower cost. In the limit of very large meshes, this cost tends to $0.031n^4$ flops, one order higher than boundary elements, indicating that there will be an intermediate mesh for which the two costs will be equal. Indeed, this occurs with 83 elements around the circumference of the circle (Table 7.9). The situation is similar for factorization of the three-dimensional case. As in the exterior problems with uniform discretizations, the backsolve costs for finite elements are always higher (see Table 7.9), but these costs are negligible in comparison to factorization. For these problems boundary elements require less storage from relatively small size meshes.
Remark: The crossover for the three-dimensional mesh of 522 elements around the circular circumference is equivalent to 824,180 boundary element equations. In a coupled problem with a structure this will by scaled by a factor of six, leading to over 5,000,000 equations. As in the case of interior problems, this is well beyond the

current scope of application of direct solution technology. To summarize the results so far, in the range of problem sizes that is applicable for direct solvers, finite element methods are overall more cost-effective, except for larger storage requirements in some exterior problems that require gradual mesh refinement.

7.3 Iterative Solution Techniques

It is well-known, and corroborated by results of the previous section, that the cost of direct methods for the solution of coupled linear equations grows rapidly with problem size, both in operation counts and in storage requirements. Traditional direct solvers are thus rendered inapplicable to large-scale models of realistic configurations, in which the computational community is becoming increasingly interested. Such problems have motivated the resurgence of alternative solution strategies based on iterative algorithms, for which asymptotic growth rates of cost can be significantly lower than those of direct methods. In general, these are procedures for deriving successively improved approximations to the solution of the linear algebraic problem (7.1), by means of a sequence of updates of an initial approximation. Iterative schemes are being adopted for the solution of both boundary element and finite element equations in a variety of applications, including acoustics [6], solid and structural mechanics [31], the compressible Euler and Navier-Stokes equations [135] and the Stokes problem [138]. Interest in these methods is currently growing as they are proving to be particularly well-suited for implementation in parallel-processing environments.

In contrast to direct methods, the performance of iterative solvers is highly problem-dependent and the convergence of some schemes may deteriorate severely under certain conditions, hindering the advance determination of execution-time requirements. For the purposes of analyzing method performance, the lack of capability to predict the number of iterations required for the approximate solution to converge to within a given tolerance of the exact solution motivates the parameterization of equation solving costs by the number of iterations. A concrete comparison of boundary element and finite element methods is then possible in terms of *costs per iteration*, which are easily evaluated.

The field of iterative solvers for linear systems is pervaded with a profusion of algorithmic issues of a problem-specific nature, that have significant impact on the number of iterations required to solve the equations. We address these issues only in a qualitative manner. It is well-known, and can also be shown theoretically, that the convergence of iterative techniques is highly dependent on the conditioning of the equations. This fact favors finite element formulations, which are quite well conditioned, in contrast to the potentially extreme ill conditioning of boundary element equations in the vicinity of characteristic frequencies (see Section 7.1). On the other hand, numerical experience indicates that convergence may improve with an increasing degree of coupling of the system of equations, which is the case for boundary element methods. We conjecture that, by and large, finite element equations converge more rapidly, but a significant amount of numerical experimentation is required to

settle this issue.

Remark: The sensitivity of iterative solvers to the conditioning of the system of equations is often addressed by preconditioning and scaling, which can lead to substantial improvement in convergence rates. There are many approaches to preconditioning and most practical implementations do employ one version or another, or a combination of several. However, in focusing on cost per iteration, there is no need to include these techniques in the solution algorithms on which we base our comparisons, thereby simplifying the presentation considerably.

Of the myriad iterative procedures available for computation, the choice of which to use as a base for the cost comparison is limited by the nonsymmetry of the systems that arise in boundary element equations. Earlier references regarding the iterative solution of boundary element equations of acoustics propose employing classical schemes such as Jacobi and Gauss-Seidel, as well as certain special-purpose methods (see, e.g., [20, pp. 31–37]). In [6], versions of multi-grid methods are employed to solve the boundary element equations that emanate from the regularized Burton-Miller formulation. We are not interested in investigating multi-grid schemes in this study because fundamental issues regarding the performance of iterative solvers become blurred in the context of these methods. Among the more sophisticated and modern iterative algorithms that are both cost-effective and robust, without requiring *a priori* estimates of eigenvalues, and that may be employed for nonsymmetric systems, two appear to be appropriate for large-scale problems of acoustics: generalized conjugate gradient and generalized minimal residual. Generalized conjugate gradients [9, 155] are a family of extensions of the ubiquitous conjugate gradient algorithm to nonsymmetric matrices. Similarly, the generalized minimal residual procedure (GMRES), introduced by Saad and Schultz [127], is analogous to the Lanczos method for nonsymmetric systems. While the generalized conjugate gradient approach is the simpler of the two conceptually, and is particularly easy to implement for programmers who are familiar with conjugate gradients, it can be shown that the GMRES method is less sensitive numerically, and more cost-effective in both operations and storage [127]. The following cost comparison of boundary element and finite element methods is therefore performed on the basis of the GMRES algorithm. In order to highlight the computational effort required to iteratively solve smaller, full systems of equations as compared to larger, sparse systems, we examine a rudimentary implementation of the procedure that is employed in practice.

An outline of GMRES for solving (7.1) for a nonsymmetric, positive semidefinite matrix $\boldsymbol{A} \in \mathbb{R}^{n_{eq} \times n_{eq}}$ is presented in the following. (A general reference for the review of specific procedures and nomenclature utilized in this algorithm is [45].) Consider an approximate solution of the form $\boldsymbol{x}_0 + \boldsymbol{z}$, where $\boldsymbol{x}_0$ is an initial approximation and $\boldsymbol{z}$ is a member of the k-dimensional Krylov space, $\mathcal{K}_k = \text{span}\{\boldsymbol{r}_0, \boldsymbol{A}\boldsymbol{r}_0, \boldsymbol{A}^2\boldsymbol{r}_0, \cdots, \boldsymbol{A}^{k-1}\boldsymbol{r}_0\}$, expressed in terms of the initial residual $\boldsymbol{r}_0 = \boldsymbol{b} - \boldsymbol{A}\boldsymbol{x}_0$. (In accordance with conventional usage, k here denotes the dimension of the Krylov space; subsequent distinction from the wave number will be clear from the context.)

Remark: In the low wave number case, a solution to the boundary-value problem for the Laplace equation (if available) may serve as an appropriate initial approximation. As long as the boundary conditions are not entirely of the Neumann type this solution

is well conditioned.

An approximate solution of the linear system of equations (7.1) is sought by considering a least-squares problem of size k in terms of the 2-norm of the residual

$$\min_{\boldsymbol{z}\in\mathcal{K}_k} \|\boldsymbol{b} - \boldsymbol{A}(\boldsymbol{x}_0 + \boldsymbol{z})\| \tag{7.12}$$

Consider the matrix $\boldsymbol{U}_k = [\boldsymbol{u}_1, \boldsymbol{u}_2, \cdots, \boldsymbol{u}_k]$, where the columns form a basis of $\mathcal{K}_k$. The representation $\boldsymbol{z} = \boldsymbol{U}_k\boldsymbol{y}$ gives rise to an equivalent minimization problem in terms of $\boldsymbol{y}$, the k scalar coefficients of the linear combination, namely

$$\min_{\boldsymbol{y}\in\mathbb{R}^k} \|\boldsymbol{r}_0 - \boldsymbol{A}\boldsymbol{U}_k\boldsymbol{y}\| \tag{7.13}$$

If $\boldsymbol{U}_k$ is an orthonormal basis, then the problem can be written in terms of a Hessenberg matrix, offering significant computational advantage. The Hessenberg matrix is triangularized by the Q-R algorithm, employing Givens rotations, to convert the minimization problem to a back-substitution process. The residual norm is updated at every iteration at no extra cost, providing a stopping criterion without explicitly updating the solution. The costs of the Q-R factorization of a Hessenberg matrix, the back-substitution, as well as updating the solution at the end of the iterative procedure are negligible.

We now examine the cost per iteration of performing k iterations (see discussion in [127]). These are asymptotic cost estimates, assuming $n_{eq} \gg k \gg 1$. The first step in each iteration is to form the Krylov vector, which consists of an $\boldsymbol{Au}$ *product*

$$\boldsymbol{u}_{k+1} = \boldsymbol{A}\boldsymbol{u}_k \qquad n_{eq}^2 \text{ flops} \tag{7.14}$$

The vector is *orthonormalized* with respect to the existing basis of the Krylov space by the modified Gram-Schmidt procedure, requiring kn_{eq} flops. The storage required is n_{eq}^2 words (for the full matrix, as is the case for direct solution procedures; the additional kn_{eq} words required to store the Krylov vectors are neglected in this asymptotic estimate). Recall that for complex arithmetic, operation counts are increased by a factor of four, and storage by two.

The matrix $\boldsymbol{A}$ need not be assembled since it is never operated upon directly in an iterative procedure. This fact offers no advantage for the fully-coupled equations that arise in boundary element methods, which is certainly a hindrance to efficient implementation in parallel-processing environments. In typical finite element applications, on the other hand, where $\boldsymbol{A}$ is sparse, this feature may be exploited by storing the matrix in element files (see, e.g., [31, pp. 32–33] and [135]). The computational effort will then also depend on n_{el}, the number of elements employed, and n_{en}, the number of element nodes. For linear elements in two dimensions $n_{en} = 4$, and in three dimensions $n_{en} = 8$. The DtN contribution, however, is coupled, and must therefore be stored as a full matrix $\boldsymbol{A}_{DtN}$, see (7.3). The $\boldsymbol{Au}$ product then requires $2n_{el}n_{en}^2 + 4n_b^2$ flops. The orthonormalization procedure is not effected by the element data structure. The kn_{eq} words of storage for the Krylov vectors are no longer negligible, and the storage requirement is thus $n_{el}n_{en}^2 + 2(n_b^2 + kn_{eq})$ words. These estimates take into account all complex arithmetic required, i.e., operations and storage involving the DtN contribution and the Krylov vectors.

Remarks

1. It is evident that the computational cost increases with k, the number of iterations, even on a per iteration basis. In practical implementation of many iterative schemes, including the GMRES procedure, this difficulty is overcome by restarting the calculation after a predetermined number of steps (usually based on numerical experience). A restarted algorithm also alleviates loss of orthogonality that emanates from accumulation of error due to finite precision arithmetic. We choose not to encumber our analysis with this option since it has little impact on the comparison of the two methods considered, other than to limit the number of iterations that are employed in practice. When a restart option is activated, k can be thought of as the number of steps allowed before the calculation is restarted, and the costs per iteration shown in the following are good estimates of those obtained in practice.

2. Potential cost savings in the operations and storage required for the $\boldsymbol{Au}$ product can be realized by employing a "matrix-free" implementation, i.e., by performing the multiplication prior to the integration which leads to the formation of $\boldsymbol{A}$ (see [86] and references therein). This procedure is particularly advantageous in cases that require several matrix multiplications to form $\boldsymbol{A}$, such as the regularized Burton-Miller formulation [6]. The drawback of this approach for comparison purposes is that the effects of solving the equations become confounded with those of equation formation. Furthermore, if equation formation is significant, as it is in many of the cases considered in this study, this may not be a cost-effective alternative. Employing this idea in practical situations merits further study, but is beyond the scope of this work.

The example problems that tested the performance of direct methods in Section 7.2 are now revisited and examined in the context of iterative solvers.

7.3.1 Interior problems

As in the study of direct methods, problems defined over interior domains bounded externally by a physical boundary, Figs. 7.1 and 7.2, are first considered. The numerical difficulties induced by the existence of resonant wave numbers of exact solutions to these problems are exacerbated in the context of iterative solvers, underscoring the importance of well-conditioned discrete equations at intermediate values. Table 7.10 shows the cost incurred by iteratively solving the boundary element equations, reflecting the fact that this formulation is entirely in terms of complex arithmetic.

A DtN procedure is not required for finite element models of interior problems ($n_b = 0$). The matrix $\boldsymbol{A}$ is therefore real, as shown in Table 7.11.

Remark: For large problems, when $n_{eq} \gg k$, considerable savings over direct solvers are immediately evident, in particular in three dimensions, cf. Tables 7.1 and 7.2.

Table 7.10: Cost per iteration of k iterations for solving boundary element equations for interior problems shown in Figs. 7.1 and 7.2.

Mesh	No. of equations	$\boldsymbol{Au}$ product [Flops]	Orthonormalization [Flops]	Storage [words]
	n_{eq}	$4n_{eq}^3/3$	$4kn_{eq}$	$2n_{eq}^2$
$n \times n$	$4n$	$64n^2$	$16kn$	$32n^2$
$n \times n \times n$	$6n^2$	$144n^4$	$24kn^2$	$72n^4$

Table 7.11: Cost per iteration of k iterations for solving finite element equations for interior problems shown in Figs. 7.1 and 7.2 (in two dimensions $n_{en} = 4$, and in three dimensions $n_{en} = 8$).

Mesh	No. of equations	No. of elements	$\boldsymbol{Au}$ product [Flops]	Orthonormalization [Flops]	Storage [words]
	n_{eq}	n_{el}	$2n_{el}n_{en}^2$	$4kn_{eq}$	$n_{el}n_{en}^2 + 2kn_{eq}$
$n \times n$	n^2	n^2	$32n^2$	$4kn^2$	$2n^2(8+k)$
$n \times n \times n$	n^3	n^3	$128n^3$	$4kn^3$	$2n^3(32+k)$

Crossover: For the two-dimensional $n \times n$ mesh, if the solution is obtained in $k \leq 8$ iterations the cost in operation counts of utilizing finite elements is less than that of a boundary element method on any size mesh. If more iterations are performed, a crossover occurs at $n = 4k/(k-8)$, after which finite elements become more costly. *In the three-dimensional case, the cost per iteration of k iterations for solving the finite element equations is less than that of boundary elements for any number of iterations on a mesh of any size.*

7.3.2 Exterior problems

As in the examination of direct methods, we next investigate exterior domains, bounded internally by a physical body, for which the exact solution is unique.

Uniform discretizations

We again examine d-dimensional cubes (with d-dimensional spherical DtN boundaries in the case of finite elements), e.g., Fig. 7.3, as counterparts of the interior examples. Recall that no modification from the interior problems is made in discretizations employed by boundary elements, and hence the costs in Table 7.12 are identical to those in Table 7.10. The practical ramifications of the geometrical wave number restriction on boundary element implementations are more severe than those stated in the study of direct methods due to the deterioration of equation conditioning in the vicinity of characteristic wave numbers.

Recall that finite element models of exterior problems that employ DtN boundary conditions inherit the uniqueness of the exact solution. In these examples the DtN

Table 7.12: Cost per iteration of k iterations for solving boundary element equations for exterior problems with uniform discretizations. e.g., see Fig. 7.3.

Mesh	No. of equations	$\boldsymbol{Au}$ product [Flops]	Orthonormalization [Flops]	Storage [words]
	n_{eq}	$4n_{eq}^3/3$	$4kn_{eq}$	$2n_{eq}^2$
$n \times 4$	$4n$	$64n^2$	$16kn$	$32n^2$
$n \times n \times 6$	$6n^2$	$144n^4$	$24kn^2$	$72n^4$

Table 7.13: Cost per iteration of k iterations for solving finite element equations for exterior problems with uniform discretizations, e.g., see Fig. 7.3.

Mesh	No. of equations	DtN equations	$\boldsymbol{Au}$ product [Flops]	Orthonormalization [Flops]	Storage [words]
	n_{eq}	n_b	$4n_b^2$	$4kn_{eq}$	$2n_b^2$
$n \times 4$	$8n$	$4n$	$64n^2$	$32kn$	$32n^2$
$n \times n \times 6$	$12n^2$	$6n^2$	$144n^4$	$48kn^2$	$72n^4$

contribution dominates the operation count of the $\boldsymbol{Au}$ product as well as the storage requirements (see Table 7.13, in which the non-DtN portions are neglected). Since the DtN portion of the coefficient matrix is full and complex, and since the number of DtN equations is equal to the number of boundary element equations, the computational effort will be approximately equal for the two methods in these examples. (The solution obtained by finite elements will be more costly by a negligible amount.) The finite element wave number limitation (7.11), which emanates from the need to obtain sufficient *numerical* wave resolution, is less restrictive than for boundary elements, and is removed for more regular physical objects (Figs. 7.3 and 7.4) that require identical costs. The tradeoff of relaxing the finite element numerically nondimensionalized wave number limitation by mesh refinement at added computational cost (cf. Table 7.6), which is impossible with the basic boundary integral equation, in which the limitation is in terms of a geometrically nondimensionalized wave number, is applicable to iterative solvers as well.

Gradually refined discretizations

As in the study of direct methods, we now examine physical boundaries with more elaborate geometric features, Figs. 7.6 and 7.7, in which gradual refinement of the finite element mesh is considered. Table 7.14 shows the operation counts and storage requirements for solving the equations associated with boundary elements.

The costs of solving the finite element equations are shown in Table 7.15. As in Table 7.8, the internal mesh grading gives rise to expressions that are relatively complicated. As in the previous examples, the number of equations and the number of elements are of the same order. The number of nodes on the artificial boundary, n_b, varies from being of the same order as the number of equations for relatively small

Table 7.14: Cost per iteration of k iterations for solving boundary element equations for exterior problems with gradually refined discretizations shown in Figs. 7.6 and 7.7.

Mesh	No. of equations	$\boldsymbol{Au}$ product [Flops]	Orthonormalization [Flops]	Storage [words]
	n_{eq}	$4n_{eq}^2$	$4kn_{eq}$	$2n_{eq}^2$
$n \times 1$	$11n/9$	$484n^2/81$	$44kn/9$	$242n^2/81$
$n \times 3n \times 1$	$245n^2/81$	$240100n^4/6561$	$980kn^2/81$	$120050n^4/6561$

Table 7.15: Cost per iteration of k iterations for solving finite element equations for exterior problems with gradually refined discretizations shown in Figs. 7.6 and 7.7 (in two dimensions $n_{en} = 4$, and in three dimensions $n_{en} = 8$; the coefficients are: $\beta_2 = (180 + n)/81$, $\delta_2 = (162 + n)/162$, $\beta_3 = (13176 + 5n)/2187$, $\delta_3 = (13122 + 5n)/4374$).

Mesh	No. of eqns.	DtN eqns.	No. of elems.	$\boldsymbol{Au}$ product [Flops]	Ortho. [Flops]	Storage [words]
	n_{eq}	n_b	n_{el}	$2n_{el}n_{en}^2 + 4n_b^2$	$4kn_{eq}$	$n_{el}n_{en}^2 + 2(n_b^2 + kn_{eq})$
$n \times 1$	$\beta_2 n$	n	$\delta_2 n$	$4n(8\delta_2 + n)$	$4\beta_2 kn$	$2n(8\delta_2 + \beta_2 k + n)$
$n \times 3n \times 1$	$\beta_3 n^2$	$3n^2$	$\delta_3 n^2$	$4n^2(32\delta_3 + 9n^2)$	$4\beta_3 kn^2$	$2n^2(32\delta_3 + \beta_3 k + 9n^2)$

meshes, to one order lower than the number of equations for larger meshes. This occurs because the mesh on the DtN boundary need not resolve geometric details of the physical boundary. On coarser meshes, the number of nodes on the physical boundary is close to the number on the artificial boundary, and hence the coupling of the DtN operator significantly impacts the computation of the $\boldsymbol{Au}$ product and the storage requirements, as in the exterior problems with uniform discretizations. However, as the mesh is refined, the number of nodes on the interior boundary increases much faster than on the exterior boundary, diminishing the influence of the DtN coupling, and tending towards the kind of behavior seen in the interior problems, where the DtN operator was not present.

The expressions in Tables 7.14 and 7.15 indicate a reversal in the trend observed before. The interaction between the effects of the coupling of the DtN operator and the grading of the internal mesh actually allow finite element formulations to gain a computational edge for *larger* problems, whereas boundary elements will be less costly per iteration for smaller problems. Recall that it is the solution of larger problems that motivated the consideration of iterative techniques. For the two-dimensional $(n \times 1)$ mesh, there is a crossover if $k < 36$

$$n = \begin{cases} \dfrac{648 + 81k}{36 - k}, & \text{Operations} \\ \dfrac{648 + 180k}{36 - k}, & \text{Storage} \end{cases} \tag{7.15}$$

after which finite elements become economical. (In the three-dimensional case there is a crossover for any number of iterations, but the expressions are cumbersome and

Table 7.16: Crossover for *five iterations* on exterior problems with gradually refined discretizations shown in Figs. 7.6 and 7.7 (value of n, number of elements around the circular circumference, at which costs are equal).

Mesh	Operations	Storage
$n \times 1$	34	50
$n \times 3n \times 1$	27	29

Table 7.17: Crossover for *30 iterations* on exterior problems with gradually refined discretizations shown in Figs. 7.6 and 7.7 (value of n, number of elements around the circular circumference, at which costs are equal).

Mesh	Operations	Storage
$n \times 1$	513	1008
$n \times 3n \times 1$	36	43

hence not presented here.) Boundary elements are more cost-effective on all size two-dimensional problems in the configuration shown in Fig. 7.6 if the number of iterations is larger than 36, but there is little likelihood that this will occur in practice. Typically, the calculation will be restarted after a much smaller amount of iterations, often in the vicinity of ten. Numerical values of the crossover for five iterations, also representative of the cost with restarts approximately every ten iterations, are shown in Table 7.16. An example of the crossover in the unlikely event of using a large number of iterations, in this case 30, is shown in Table 7.17.

Remark: The crossover for operation counts on the three-dimensional mesh with five iterations of 27 elements around the circular circumference is equivalent to approximately 2,200 boundary element equations. Problems of this size are still within the range of applicability of direct methods. An iterative procedure will be effective on larger problems, for which the finite element equations are more cost-effective.

In summary of the comparison of the iterative solution of boundary element and finite element equations, finite element methods appear to be overall more economical per iteration in the range of problem sizes that is applicable for iterative solvers, and in the range of number of iterations that will be encountered in typical practical implementations of iterative schemes.

7.4 Evaluation of Solution Strategies and Set-up Costs

Up to this point our attention has focused on the computational effort required to solve the systems of equations emanating from boundary element and finite element methods, by means of either direct or iterative procedures. We now examine two other issues that effect the economics of computational acoustics: a comparison of

Table 7.18: Crossover for solving boundary element equations of interior problems shown in Figs. 7.1 and 7.2 (value of k, number of iterations, at which costs are equal).

Mesh	Operations	Storage
$n \times n$	$4(\sqrt{5}/3 - 1)n$	equal
$n \times n \times n$	$2(\sqrt{15} - 3)n^2$	equal

Table 7.19: Crossover for solving finite element equations of interior problems shown in Figs. 7.1 and 7.2 (value of k, number of iterations, at which costs are equal).

Mesh	Operations	Storage
$n \times n$	$\sqrt{64 + n^2/4} - 8$	$n/2 - 8$
$n \times n \times n$	$\sqrt{1024 + n^4/4} - 32$	$n^2/2 - 32$

the cost-effectiveness of the two solution strategies, and an evaluation of the effort required to form the equations, which is non-negligible for many of these problems.

7.4.1 Comparison of direct and iterative procedures

In considering solution strategies, conventional wisdom postulates the cost-effectiveness of direct methods for relatively small problems and of iterative procedures for larger problems. We wish to determine the problem size at which it is economical to transfer from one solution technique to the other. Since the number of iterations required for convergence cannot be accurately predicted, a comparison can be made only in terms of problem size relative to the number of iterations, rather than absolute problem size.

Interior problems

The number of iterations, expressed in terms of number of elements per side, at which the costs of directly solving boundary element equations for interior problems are equal to obtaining a solution iteratively are presented in Table 7.18. These results are obtained by comparing Tables 7.1 and 7.10. In both cases, the crossover is approximately equal to the number of equations.

The crossover for finite elements, obtained from Tables 7.2 and 7.11, is shown in Table 7.19. In general it is of the order of the bandwidth.

Exterior problems with uniform discretizations

The crossover for boundary elements is identical to that obtained for interior problems (Table 7.18), since both the direct costs (Table 7.4) and the iterative costs (Table 7.12) for the exterior problems are equal to the corresponding costs for interior problems. For the finite element equations, comparing Tables 7.5 and 7.5 yields a crossover that

Table 7.20: Crossover for solving finite element equations of exterior problems with uniform discretizations, e.g., see Fig. 7.3 (value of k, number of iterations, at which costs are equal).

Mesh	Operations	Storage
$n \times 4$	$(\sqrt{22/3} - 2)n$	equal
$n \times n \times 6$	$(\sqrt{33/2} - 3)n^2$	equal

Table 7.21: Crossover for solving boundary element equations of exterior problems with gradually refined discretizations shown in Figs. 7.6 and 7.7 (value of k, number of iterations, at which costs are equal).

Mesh	Operations	Storage
$n \times 1$	$(\sqrt{605/243} - 11/9)n$	equal
$n \times 3n \times 1$	$(\sqrt{5/3} - 1)n^2$	equal

is still of the order of the bandwidth, see Table 7.20, even though the number of equations is much lower than for the corresponding interior problems, since the DtN portion dominates the computation.

Exterior problems with gradually refined discretizations

The results for boundary element equations for these problems, presented in Table 7.21, continue the trend observed previously, that the crossover is of the order of the number of equations.

The expressions for the crossover of finite element equations for these problems, from Tables 7.8 and 7.15, are quite cumbersome and hence not presented. For both cases, the crossover is of order n (for operations and storage), in contrast to the previous examples.

Employing an efficient iterative scheme, such as GMRES with scaling and preconditioning, we expect the number of iterations required for the solution of well-conditioned equations to be much less than n. Taking into account this observation, the results of this section indicate that iterative solution strategies can be more cost-effective on all configurations of practical interest. Nevertheless, direct solvers maintain their appeal in the range of relatively small problems, not by economic considerations but rather due to their robustness and predictability.

7.4.2 Equation formation

We wish to evaluate the expense of the left-hand side formation which, unlike many conventional numerical applications, is significant in most of the cases considered here. This is due to the costly kernel evaluation associated with boundary element methods and DtN operators, effecting cases of finite element analysis with substantial DtN

contributions. As a result, the number of operations required for equation formation can be of the same order as for the iterative solution. We use as reference recent results for Burton-Miller boundary element formulations presented in [6]. Evaluation is based on numerical experiments rather than on theoretical operation counts, with the caveat that results are subject to quality of implementation (which should be examined) and hence subjective.

The configurations considered are fully described in [6]. Essentially, there are two three-dimensional cases: a unit sphere and right circular cylinder with height-to-radius ratio of two, each discretized by 448 linear triangular boundary elements. The number of equations is approximately $n_{eq} = 225$. The cost of equation formation is $O(n_{eq}^2)$ and we estimate the constant based on CPU timings given in [6]. First the machine speed must be estimated. The direct solution time is 920 CPU seconds, and since the number of operations required is $4n_{eq}^3/3$, the Prime 750 that is employed is computing at about 0.0165 Mflops/second. This is a reasonable flop rate for that machine, indicating that the implementation is fairly efficient. The constants in the cost of equation formation may now be estimated. Set-up time for the Burton-Miller formulation is 600 CPU seconds, corresponding to about 9.9 million flops, or $196n_{eq}^2$. Forming the regularized Burton-Miller equations for direct solution requires 7000 CPU seconds, more than *20 times* greater than the original Burton-Miller formulation, corresponding to about 116 million flops, or $2283n_{eq}^2$. Set-up time of regularized Burton-Miller for iterative solvers is 940 CPU seconds, corresponding to about 15.5 million flops, or $307n_{eq}^2$. The matrix multiplications required for forming $\boldsymbol{A}$ in the regularized Burton-Miller formulation are replaced by a sequence of matrix-vector products in iterative procedures (since $\boldsymbol{A}$ is not operated upon directly), accounting for the difference between the latter two costs. However, this gives rise to several matrix-vector multiplications in each iteration, as opposed to the single product that was assumed in Section 7.3, as well as significantly increased storage requirements, and the costs presented therein would therefore have to be modified for this formulation. We estimate the set-up time for the DtN operator to be one half of direct boundary element methods (due to symmetry of the DtN formulation), which is about half the Burton-Miller set-up time, i.e., $50n_b^2$ is used. The cost of formulating the finite element equations is dominated by the DtN portion. Since n_b, the number of nodes on the artificial boundary, is no larger than the number of boundary element equations for a given configuration, and is much less for more intricate physical boundaries, *the set-up costs for finite elements will always be lower than boundary elements*, possibly to a great extent.

We now compare the cost of equation formation to that of obtaining solutions for the examples considered previously. As before we start with direct solution strategies. An example of formation costs, the case of boundary element equations for the direct solution of interior problems is presented in Table 7.22. (The costs of forming boundary element equations for the direct solution of the exterior problems with uniform discretizations previously considered are identical to those of corresponding interior problems.) The costs of forming boundary element equations for direct solution are

Table 7.22: Cost of forming boundary element equations for direct solution of interior problems shown in Figs. 7.1 and 7.2.

Mesh	No. of equations	Burton-Miller	Regularized Burton-Miller	Factorization
	n_{eq}	$196n_{eq}^2$	$2283n_{eq}^2$	$4n_{eq}^3/3$
$n \times n$	$4n$	$3136n^2$	$36528n^2$	$256n^3/3$
$n \times n \times n$	$6n^2$	$7056n^4$	$82188n^4$	$288n^6$

equal to the factorization costs at

$$n_{eq} = \begin{cases} 147, & \text{Burton-Miller} \\ 1712, & \text{Regularized Burton-Miller} \end{cases} \tag{7.16}$$

for all problems, and for smaller problems set-up costs actually dominate the computation.

The cost of forming finite element equations to interior problems is negligible since a DtN operator is not required. The cost for exterior problems is no longer negligible, and for problems with uniform discretizations (e.g., Fig. 7.3) equals the factorization cost at $n_{eq} = 120$. For the exterior problems with gradually refined discretizations a cost of equation formation of $50n_b^2$ equals that of factorization at

$$n_{eq} = \begin{cases} 93, & n \times 1 \text{ mesh} \\ 151, & n \times 3n \times 1 \text{ mesh} \end{cases} \tag{7.17}$$

but this may be an underestimation due to additional expenses entailed by employing elliptical artificial boundaries. In general, these results show that equation formation is a significant portion of the cost of directly obtaining solutions to problems of practical interest only in the case of the regularized Burton-Miller formulation.

Remark: An attractive alternative to this formulation has recently been reported in [107]. In this work a Burton-Miller approach is employed to obtain a formulation in which no hyper-singular kernels are integrated, by use of certain integral identities. The cost of evaluating the integrals and obtaining the discrete equations is thus greatly reduced. Nevertheless, some implementational difficulties persist, such as the need to employ C^1 elements.

When iterative strategies are considered the relative cost of equation formation increases significantly. Recall the an $\boldsymbol{Au}$ product in boundary element formulations required $4n_{eq}^2$ flops per iteration, in comparison to $196n_{eq}^2$ flops required to form the Burton-Miller equations, i.e., the cost of equation formation is equal to almost *50 iterations* of $\boldsymbol{Au}$ products. As mentioned previously, the regularized formulation requires 50% more operations to set up the equations, and also significantly increases the cost per iteration of solving the equations. Similar results, if not quite as drastic, are obtained for finite elements. For exterior problems an $\boldsymbol{Au}$ product required $4n_b^2$ flops per iteration, or more (as in the case of gradually refined discretizations), in comparison to $50n_b^2$ flops required to form the equations.

In summary, this study clearly demonstrates that finite element methods are economically competitive with boundary element methods for obtaining solutions to problems of time-harmonic acoustics. Despite the fact that boundary elements need less equations to discretize the same physical problem, the structure possessed by the finite element equations often leads to an overall computational advantage. For both direct and iterative solution techniques, finite element methods for the examples studied herein are more economical in most of the range of problem size on which either solver is applicable. Comparing the two solution strategies demonstrates that efficient implementation of iterative techniques has the potential of being more cost-effective for all problems of interest, as long as the equations are well-conditioned, motivating wider acceptance of iterative strategies. This work indicates that unlike many traditional numerical applications, set-up costs may constitute a significant portion of the computational expense, pointing to opportunities for considerable savings by addressing these issues alongside economizing equation-solving strategies.

Chapter 8

Iterative Solution Methods for Large-scale Problems

In this chapter we consider efficient methods for the solution of large-scale matrix problems that arise from finite element methods for structural acoustics. We focus on iterative solution methods that are applicable over a wide range of frequencies, and characterize the robustness and efficiency of several algorithms for problems in acoustics. We also examine special techniques to enhance the performance of these solution strategies for analysis at high frequencies. Results from a number of numerical tests on both sequential and parallel computers are presented to highlight the performance of methods considered.

Finite element methods are capable of modeling problems of structural acoustics at arbitrarily high wavenumbers providing that an appropriate level of mesh refinement is employed. For analyses at high wavenumbers, the necessary refinement may lead to a large system of equations which needs to be solved efficiently and accurately. Direct solution techniques become expensive for solving large systems of linear equations due to excessive growth in computational and storage requirements. Iterative solution strategies are an attractive alternative in these situations. Unlike direct methods, characteristic computational kernels associated with iterative solution methods parallelize very efficiently, making them even more attractive for use on modern vector and parallel computers.

Gradient-type iterative methods, which are based on working with sequences of orthogonal vectors, are amongst the most effective iterative procedures for solving large sparse linear systems and can also be very attractive for large dense matrix problems. The effectiveness of an iterative method is dependent on its rate of convergence and the costs involved in performing each iteration. Convergence of gradient-type methods is closely related to spectral properties of the coefficient matrix and often preconditioners are employed to make the spectrum more favorable to faster convergence. Generally, the success of an iterative method depends on the availability of a good preconditioner and preconditioners are often observed to be problem dependent. An important part of efficient parallelization of iterative methods is the development of effective preconditioners that are amenable to parallelization.

For certain special problems, such as those arising from smooth differential operators on regular domains discretized with equi-spaced grid points, special direct or

iterative methods such as fast poisson solvers, multigrid or other methods may be effective. However, in the context of adaptive solution of coupled acoustics problems on unstructured grids most of these methods become inapplicable and hence they are not considered here.

8.1 Iterative Solvers for Indefinite Systems

For solving Hermitian positive definite (HPD) systems the classical Conjugate Gradient (CG) algorithm [65] is amongst the most effective iterative methods because of its low work and storage requirements per iteration and good convergence properties. However, problems in acoustics discretized using finite element or boundary element methods give rise to non-Hermitian indefinite systems. In such cases a good choice of an iterative method is not so clear and various approaches exist. For a nonsingular matrix A, the normal equations given as $A^H Ax = A^H b$ are HPD and can be solved using preconditioned CG method. We denote this approach by CGNR. This approach, in fact, is not practical because the normal equations have a condition number which is square of the condition number of the original system and this typically leads to unacceptable convergence rates [14].

Amongst the more recent gradient-type algorithms for non-Hermitian problems there are essentially two different approaches. One approach is based on explicitly computing and storing a sequences of orthogonal vectors, $V_n = \{v_1, v_2, ..., v_n\}$, that can be combined using a least-squares solve to generate iterates that have minimal residual in the subspace spanned by V_n; this leads to the Generalized Minimal Residual method (GMRES) [127]. Due to the requirement to store the entire sequence of vectors the GMRES method becomes expensive. Restarted versions of the method are used in practice to limit storage and computation costs. However, convergence of the restarted algorithm is often slow and also sensitive to the number of orthogonal vectors stored.

The other approach involves using the unsymmetric Lanczos process to generate two sequence of vectors that satisfy a bi-orthogonality condition. The method of Bi-Conjugate Gradients (BiCG) is based on using these vectors to obtain iterates by enforcing a Galerkin-type condition on the residuals [32]. The advantage of such an approach is that, unlike GMRES, only a limited amount of work and storage is needed per iteration. However, the residuals of BiCG iterates display irregular convergence and the method can sometimes experience numerical breakdowns [32]. Recently, Freund and Nachtigal [39] have proposed a new approach, the Quasi-Minimal Residual method (QMR) which applies a least-squares solve and update to the BiCG residuals, thereby smoothing out the irregular convergence behavior of BiCG. A special implementation of QMR (with "look ahead") also eliminates any sources of possible breakdown in the BiCG approach.

Before selecting an iterative method, it is important to characterize matrix problems that arise in finite element methods for acoustics. In the case of interior problems, finite element discretizations lead to real symmetric but indefinite matrices. For such systems the MINRES and SYMMLQ methods [119] are applicable. These methods

are somewhat restrictive as they allow the use of only positive definite preconditioners. At wavenumbers close to the square-root of the eigenvalues of the discrete Laplacian operator, the conditioning of the interior problems deteriorates considerably. In such cases preconditioning becomes essential. Since QMR allows the use of nonsingular indefinite matrices as preconditioners it is more effective for such problems. The general QMR method can be particularized to the symmetric indefinite case thereby reducing its work and storage costs to a level similar to those associated with MINRES and SYMMLQ [38].

For exterior problems the introduction of radiation boundary conditions changes the fundamental nature of the matrix problem. The matrix contribution of the non-local DtN radiation condition, A_{DtN}, is fully populated and complex-symmetric i.e. $A_{DtN} = A_{DtN}^T$. Exploiting complex-symmetry in non-Hermitian systems is crucial for Lanczos based iterative methods because it reduces the storage and computational requirements to half of those needed for solving general non-Hermitian systems. A comparison of number of operations and storage required at the k-th iteration for solving exterior problems is summarized in Table 8.1.

Table 8.1: Computation and storage (in words) costs for solving complex-symmetric systems of size n×n. Computation costs are in terms of number of inner products, vector updates, matrix-vector products and transpose products required in the k-th iteration.

Iterative Method	Operations per Iteration			Storage
	$x^T y$	$\alpha x + y$	Ap^k,$A^T p^k$	Required
CGNR	2	3	1,1	4n
GMRES	k+1	k+1	1,0	(k+5)n
BiCG	2	3	1,0	4n
QMR	2	4	1,0	5n

A significant impact of exploiting complex-symmetry is that QMR and BiCG do not need to compute a transpose product $A^T p^k$, which is required in the case of non-Hermitian versions of these algorithms. The above comparison indicates that, unless less $k \leq 2$, BiCG and QMR are more efficient than GMRES in terms of storage and computing costs per iteration. In contrast to finite element equations which are complex-symmetric, boundary element methods lead to non-Hermitian matrices. In that situation BiCG and QMR algorithms may lose the above advantage.

8.2 Performance of Iterative Solvers

In this section the convergence characteristics of various iterative solvers for some typical acoustics problems in interior and exterior domains are studied. Numerical results demonstrate the robustness and superior convergence properties of QMR for solving such problems. No preconditioning is used in Examples 1-4. The effects of preconditioning are discussed in the next section.

Example 1. An interior Dirichlet problem.

Consider the solution of Helmholtz equation on a square domain of unit side, $a = 1$, with homogeneous Dirichlet boundary conditions on all edges. A source distribution of unit intensity in the domain is taken as the forcing function. The domain is discretized using bilinear GLS finite elements with 80 elements along each edge, such that frequencies examined are well within the resolution limit. The symmetric-indefinite QMR algorithm is employed and iterations are stopped when the relative residual norm satisfies $\frac{\|r_n\|_2}{\|r_0\|_2} \leq 10^{-7}$.

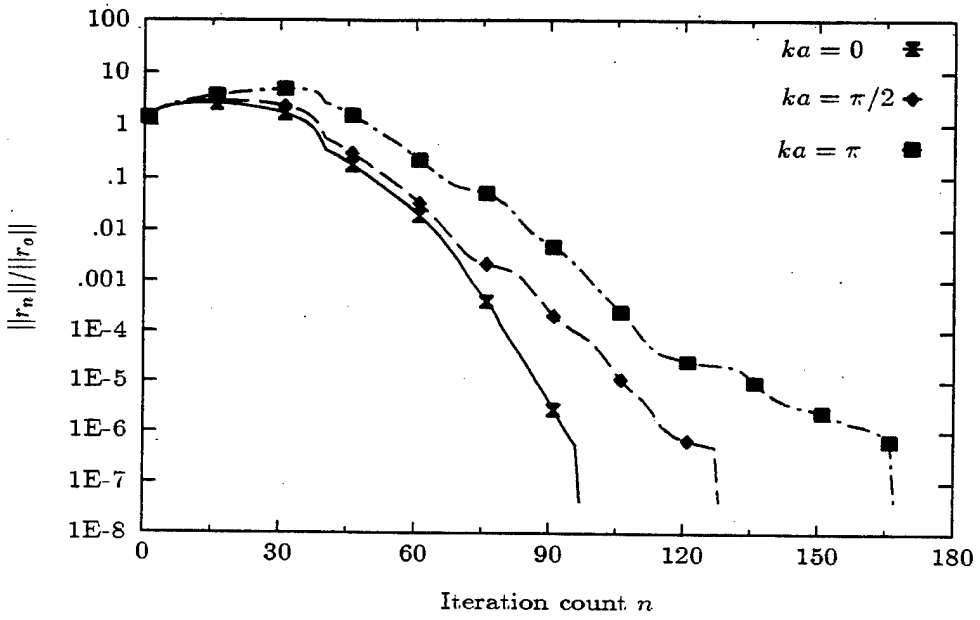

Figure 8.1: Convergence curves for interior problem at $ka = 0, \pi/2$ and π.

Convergence curves for various frequencies of analysis (see Fig. 8.1) illustrate that QMR displays smooth convergence behavior with almost monotonically decreasing residuals. As the frequency of analysis is increased from $ka = 0$ to π the total number of iterations required for convergence also increase steadily. This indicates a decreasing rate of convergence of the iterative solution method as the matrix problem becomes more indefinite. Such behavior is also observed in solving exterior problems as we will see in Example 4.

Next, we compare the performance of CGNR, BiCG, QMR and GMRES(m) algorithms for some typical exterior problems of radiation and scattering. GMRES(m) denotes the restarted GMRES algorithm with a maximum of m iterations before each restart. Different values of the parameter m are chosen in order to study its effect on the rate of convergence.

Example 2. Two-dimensional radiation from a rigid infinite cylinder.

Consider a rigid infinite cylinder of radius a submerged in an infinite acoustic fluid. The DtN radiation boundary is applied, at radius $r = 2a$, to obtain a finite computational domain given by $a \leq r \leq 2a$ and $0 \leq \theta \leq 2\pi$. This computational domain is discretized with a uniform mesh which has 20 radial and 64 circumferential bilinear

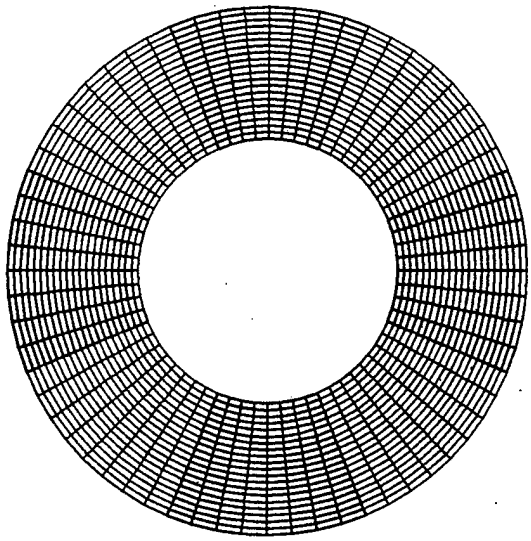

Figure 8.2: Finite element mesh consisting of 1280 bilinear elements for radiation and scattering problems studied in Examples 2-4.

elements, Fig. 8.2. Dirichlet boundary conditions corresponding to uniform radiation in the zeroth and fourth circumferential modes are prescribed on the wet surface of the cylinder. The two problems are solved for a non-dimensional wavenumber of $ka = \pi$.

Figure 8.3 shows the convergence characteristics of a number of solution methods for analysis of the zeroth harmonic radiation pattern. Iterative methods based on the Lanczos process, BiCG and QMR, display superlinear convergence and require only 20 iterations to converge, to a tolerance of 10^{-5}, which is exactly the number of distinct eigenvalues of the coefficient matrix. Performance of GMRES(5) and GMRES(15) iterations indicate loss of superlinear convergence behavior due to frequent restarts. However, convergence of the GMRES algorithm without any restarts is as fast as BiCG and QMR. These results indicate a strong dependence of the rate of convergence of GMRES on the choice of restart parameter m. Similar conclusions hold for analysis of the fourth harmonic radiation pattern, as shown in Fig. 8.4.

Example 3. Two-dimensional radiation from panel of a rigid infinite cylinder.

The case of non-uniform radiation due to vibrations of a panel of the rigid cylinder is a more complex numerical problem due the presence of an infinite number of modes in the solution. We consider the same geometry and discretization as in Example 2. The boundary condition on the wet surface consists of unit Dirichlet data specified on the sector $-\pi/12 \leq \theta \leq \pi/12$ and homogeneous Dirichlet data on the remaining part. Convergence curves in Figure 8.5 show that BiCG residuals exhibit some oscillatory behavior while QMR has a smooth and almost monotonic convergence behavior. The convergence of restarted GMRES iterations, GMRES(5) and GMRES(20), is much slower than QMR. Since the solution consists of a very large number of modes, the choice of parameter m at which convergence of GMRES becomes acceptable may require a prohibitive amount of storage for such classes of problems.

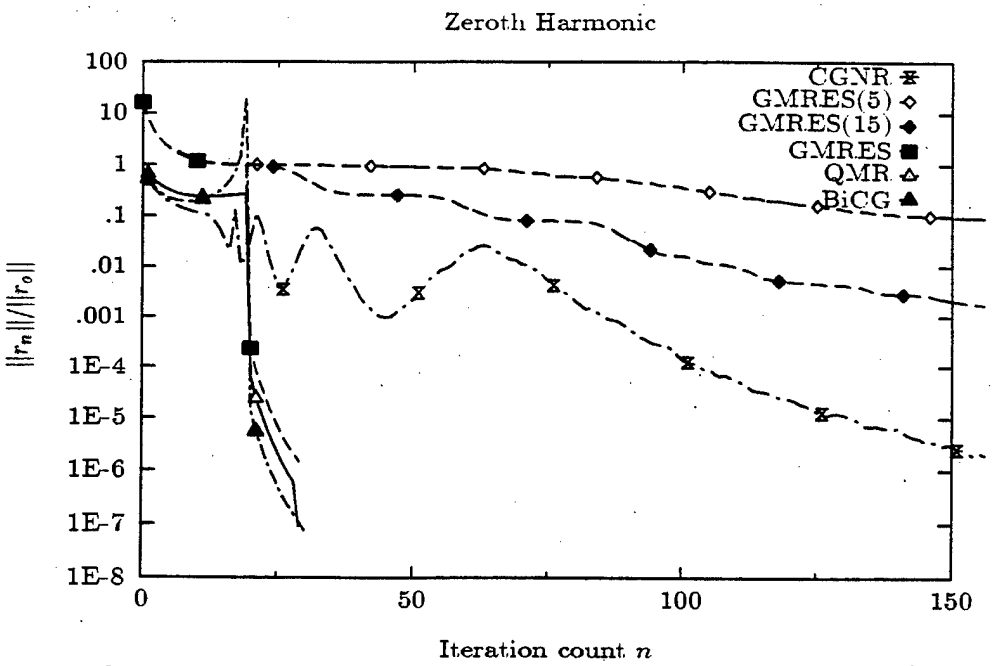

Figure 8.3: Convergence curves for radiation from rigid cylinder in 0^{th} harmonic, $ka = \pi$.

Example 4. Plane wave scattering off a rigid infinite cylinder in two dimensions.

The scattering of plane waves from a rigid cylinder leads to boundary value problems with purely Neumann boundary conditions. We characterize convergence for such problems using the same geometry and discretization as used in Example 2. For this case, the normal derivative of the incident field is prescribed as Neumann data on the wet surface of the cylinder. Results for analysis at $ka = \pi$ are presented in Figure 8.6. Observe that BiCG residuals suffer rapid fluctuations, whereas the convergence behavior of QMR remains smooth. The restarted GMRES and the CGNR methods are once again not competitive with QMR.

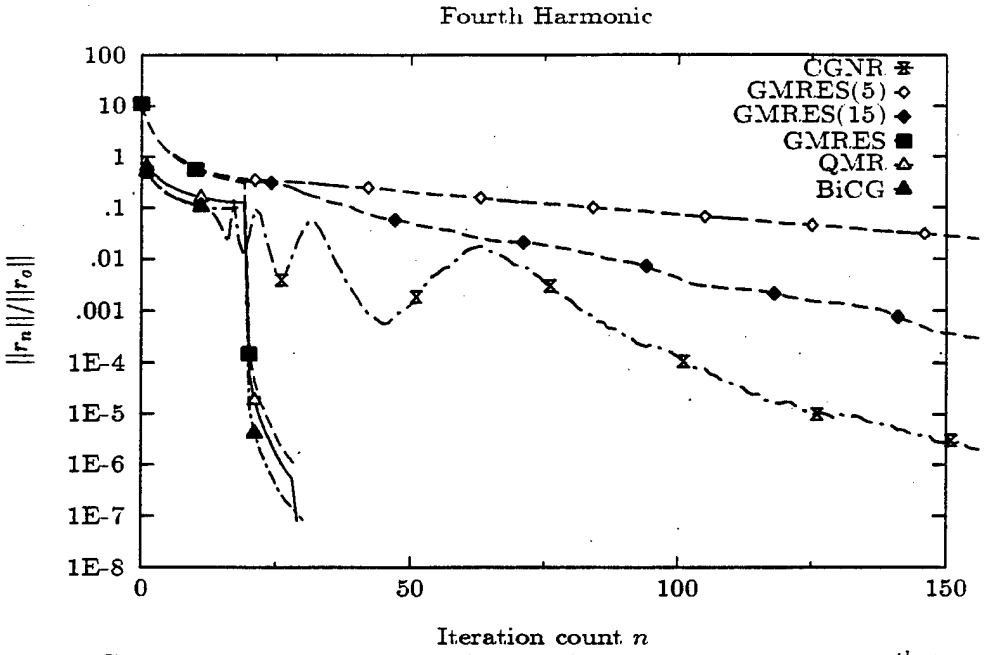

Figure 8.4: Convergence curves for radiation from rigid cylinder in 4^{th} harmonic, $ka = \pi$

In order to examine the effect of frequency, the scattering problem is reanalyzed with plane waves incident at higher frequencies. As frequency is increased, the eigenspectrum of the coefficient matrix shifts towards the left half of the complex plane resulting in a larger number of eigenvalues that have negative real components. Numerical results corresponding to analysis over $ka = \pi$ to 4π are shown in Fig. 8.7 and indicate that convergence of QMR deteriorates under these circumstances. A more refined mesh with 9000 bilinear elements was used in this case to achieve an appropriate level of resolution at $ka = 4\pi$. The requirement to employ finer meshes at increasing frequencies leads to a decline in conditioning of the coefficient matrix which further slows convergence (compare curves for $ka = \pi$ in Fig. 8.6 and 8.7). These results motivate the need for effective preconditioning, especially for analyses at higher frequencies.

8.3 Preconditioning for the Helmholtz Operator

Convergence of gradient-type methods depends on the condition number of the coefficient matrix A and the distribution of its eigenvalues. To improve convergence of such methods, a preconditioner M is employed such that $M^{-1}A$ is better conditioned, and linear systems with coefficient matrix M are easy to solve. The construction of preconditioners that simultaneously satisfy these two criterion and which are also suitable for implementation on parallel computers is often difficult.

We first consider some common preconditioning methods:

1. The diagonal preconditioner, $M_D = \text{diag}(A)$, is the simplest preconditioner.

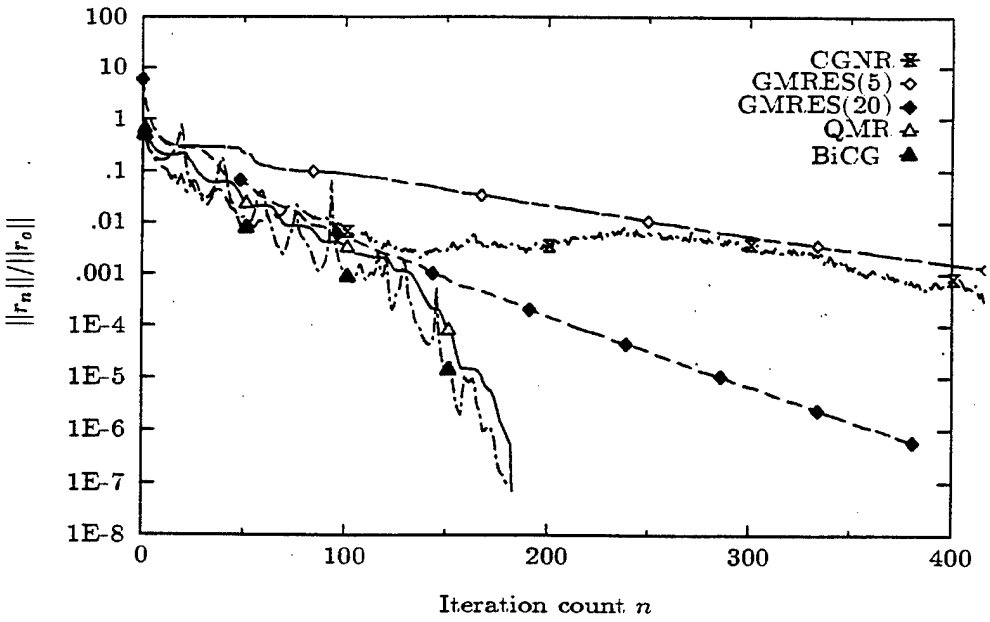

Figure 8.5: Convergence curves for radiation from panel of rigid cylinder.

2. The SSOR preconditioner is given by $M_{SSOR} = (D + \omega L)D^{-1}(D + \omega U)$, where $A = L + D + U$, and ω is a design parameter.

3. Incomplete Cholesky factorization preconditioners [113] which are based on approximate factorizations of A in order to limit the amount of fill-ins.

Although preconditioners based on incomplete factorization are quite effective in reducing the number of iterations, significant computational effort is required to initially construct them. Moreover, both the construction and the application phases of these preconditioners parallelize poorly on massively parallel computers, such as the Maspar MP-1 or the CM-2 [16], and as a result often only diagonal preconditioning is used in such cases. However, diagonal preconditioners are not effective for acoustics problems, providing little improvement in convergence rates.

For effective preconditioning of the Helmholtz operator we examine a novel approach which is based on an understanding of the properties of finite element approximations for second order elliptic differential operators. For finite element formulations arising from piecewise linear shape functions, it can be shown that the spectral condition number of a discrete second order elliptic operator grows as $\mathcal{O}(h^{-2})$. However, by using hierarchical basis functions [157] in place of nodal basis functions, the growth in condition number of the discrete system can be significantly reduced to $\mathcal{O}(\log h^{-1})^2$. This idea was exploited for developing preconditioners for the case of self-adjoint positive definite second order elliptic boundary value problems by Yserentant [157] and extended to the case of nonsymmetric operators that also satisfy the positivity condition [156].

However, the Helmholtz operator is not positive definite but satisfies a Gårding type inequality. For such problems convergence of Galerkin methods requires that

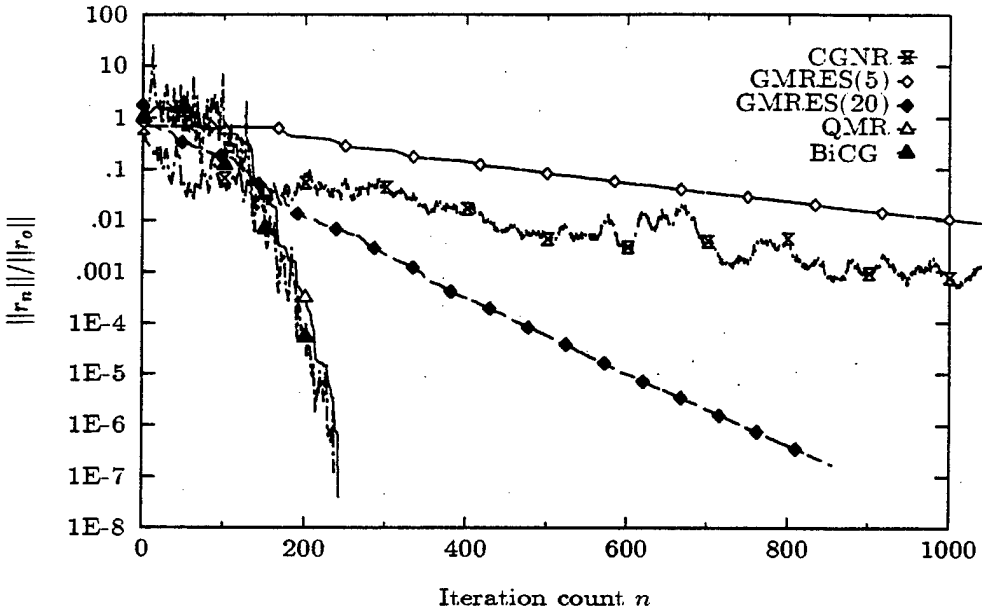

Figure 8.6: Convergence curves for plane wave scattering from rigid cylinder at $ka = \pi$.

the characteristic grid size of the mesh on which the problem is solved be less than some threshold value [129]. Under these circumstances, construction of hierarchical basis functions that preserve the approximation property of the chosen discretization while improving the conditioning of the discretization matrix is not assured. We show through numerical experimentation that the hierarchical basis formulation can also be applied profitably for solving acoustics problems in both interior and exterior domains.

Hierarchical basis functions are associated with a multilevel splitting of the finite element mesh on which the problem is solved. Figure 8.8 illustrates a one-dimensional mesh with nodal basis consisting of piecewise linear functions and a splitting of the mesh into multiple levels. The hierarchical basis on such a splitting can be defined as follows: (1) basis functions at the coarsest level, Level 1, consist of the nodal basis functions, and (2) the hierarchical basis at any level j consists of nodal basis functions corresponding to nodes in that level which are not present in any of the coarser levels, together with the hierarchical basis for level j-1. This recursive definition leads to a set of basis functions which are complete and unique, and also provide the desired improvement in conditioning of the discrete operator.

Hierarchical basis functions do not possess compact support which is characteristic of nodal basis functions. Therefore coefficient matrices based on hierarchical basis, A_H, are likely to be much less sparse than the nodal matrices A_N. However, the explicit computation of A_H can be avoided by using a transformation which maps the hierarchical basis representation of a function to its nodal representation. This transformation can be used in a special way, as described below, to construct a preconditioner.

Let $u(x)$ be a function approximated on a given grid of n unknowns (or degrees

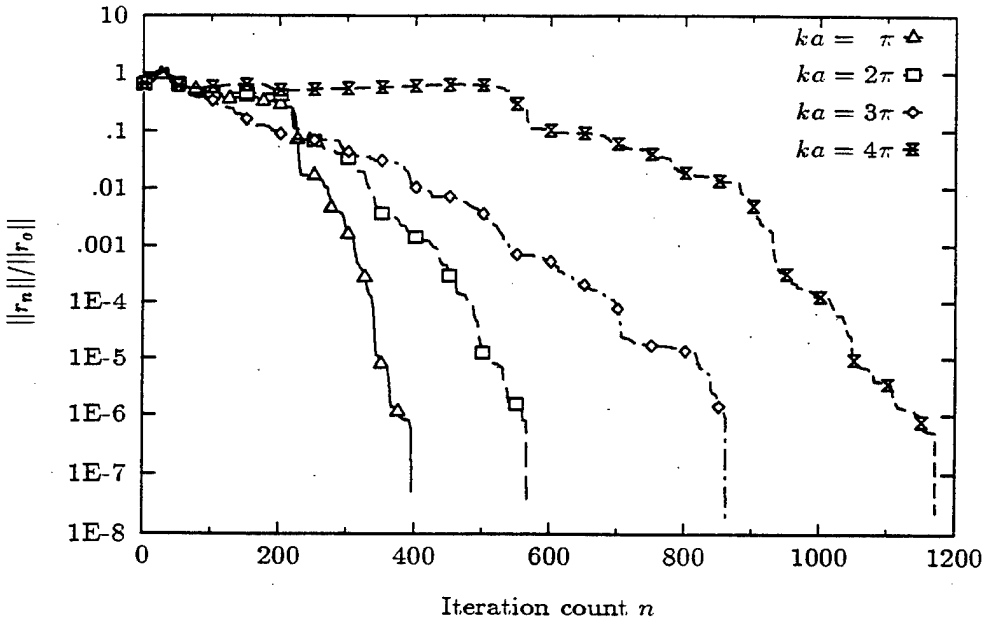

Figure 8.7: Convergence curves for scattering from rigid circular cylinder using a finer mesh with 9000 bilinear elements, $ka = \pi, 2\pi, 3\pi, 4\pi$.

of freedom) using nodal, ϕ_i^N, and hierarchical basis functions, ϕ_i^H, as follows:

$$u(x) = \sum_{i=1}^{n} z_i^N \phi_i^N$$

$$u(x) = \sum_{i=1}^{n} z_i^H \phi_i^H$$

Let $z_N = \{z_1^N, z_2^N, ..., z_n^N\}$, be the vector of coefficients in the nodal basis, and $z_H = \{z_1^H, z_2^H, ..., z_n^H\}$ in the hierarchical basis. Let S be the linear transformation such that $z_N = Sz_H$. Then it can be shown [157] that $A_H = S^T A_N S$.

Now consider solving the finite element equations, $A_N x_N = b_N$, arising from the nodal basis representation. Let this system be preconditioned using the matrix $M = M_L M_R$ in the following way,

$$M_L^{-1} A_N M_R^{-1} M_R x_N = M_L^{-1} b_N.$$

In this form, matrices M_L and M_R are the left and right preconditioners respectively. If we choose $M_L^{-1} = S^T$ and $M_R^{-1} = S$ then the preconditioned matrix becomes $S^T A_N S$. In this way the hierarchical basis preconditioner, $M_{HB} = (SS^T)^{-1}$, transforms A_N to A_H. Frequently, it is advantageous to combine diagonal scaling with M_{HB}, so that $M_{HBDS}^{-1} = SD^{-1}S^T$ [48].

To save storage and computation costs, the matrices S and S^T are not computed explicitly but their product with a vector is obtained using neighbor-neighbor connectivity data between successive levels of the hierarchical basis grids [157]. This involves only limited amount of additional storage of $\mathcal{O}(n)$ integer words and $\mathcal{O}(n)$

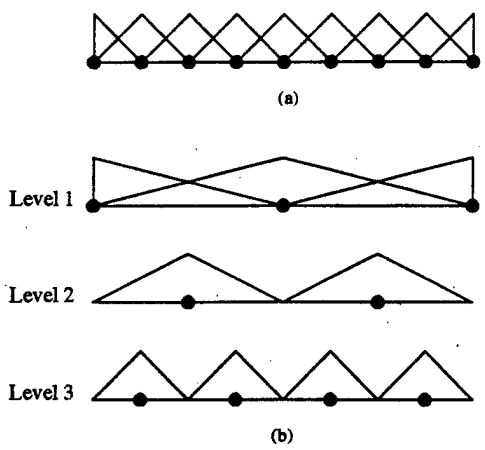

Figure 8.8: (a) Nodal basis associated with a 1-D mesh; (b) A multilevel splitting of the mesh and hierarchical basis functions associated with this splitting.

computations. Moreover, these computations can be done in j data parallel steps on a massively parallel machine, where j is the total number of levels in the multilevel splitting.

It is also noteworthy that the preconditioners M_{HB} and M_{HBDS} are not based on a "splitting" or "factorization" of the coefficient matrix and hence do not explicitly require the matrix A_N. Iterative solution strategies on massively parallel computers often employ "matrix-free" approaches [86] to fully exploit the high degree of data parallelism intrinsic in finite element computations. In such cases, the coefficient matrix A is never explicitly formed and due to this usual preconditioners entail significant storage and computational overheads. However, matrix-free iterative strategies can very naturally be combined with the hierarchical basis preconditioner to achieve highly efficient data parallel iterative solution algorithms suitable for contemporary parallel computers. We have exploited these characteristics of the preconditioning algorithm in our data parallel structural acoustics code developed on the Maspar MP-1.

Numerical Results

Results from a number of numerical tests are presented to demonstrate the effectiveness of the hierarchical basis preconditioner on both serial and parallel computing platforms, and characterize conditions under which the preconditioner is most effective. Preconditioned QMR algorithms are used for iterative solution of all matrix problems considered here.

Example 5. An interior Dirichlet problem.

We consider the interior square domain problem introduced in Example 1. The problem is solved on a uniform grid of 6400 elements, with 80 elements along each edge. The multilevel splitting associated with this mesh consists of 5 levels with the coarsest level consisting of 5 elements per edge. Intermediate levels are obtained through repeated uniform refinement of the coarsest mesh.

Table 8.2 shows a comparison of the number of iterations required for convergence

Table 8.2: Number of iterations to convergence for the interior problem.

Wavenumber ka	0	$\pi/6$	$2\pi/6$	$3\pi/6$	$4\pi/6$	$5\pi/6$	π
M_I	97	114	117	128	138	158	167
M_D	97	114	117	128	138	158	167
M_{SSOR}	55	56	56	60	66	70	72
M_{HBDS}	38	39	40	40	40	42	42

to a tolerance of 10^{-7} using various preconditioners. We denote the unpreconditioned algorithm by $M_I = I$, where I is the identity matrix. Observe that for any given frequency, diagonal preconditioning is totally ineffective whereas hierarchical basis method gives the lowest iteration count. As the frequency of analysis is increased, the iteration counts for M_{HBDS} show only a slight increase.

To further examine the effect of increasing frequency and decreasing mesh size on convergence, we study a problem of practical interest namely the scattering of plane waves from an elongated body in an exterior domain.

Example 6. Two-dimensional plane wave scattering.

Consider the scattering of plane waves from a rigid cylinder with conical-to-spherical end caps and a large length to diameter ratio, $l/d = 8.0$ (see Fig. 8.9). The DtN radiation condition is applied at radius $R = l$. We consider incoming plane waves to be incident along the length of the cylinder and study 3 different wavenumber cases, $kd = \pi/6, \pi/2, \pi$.

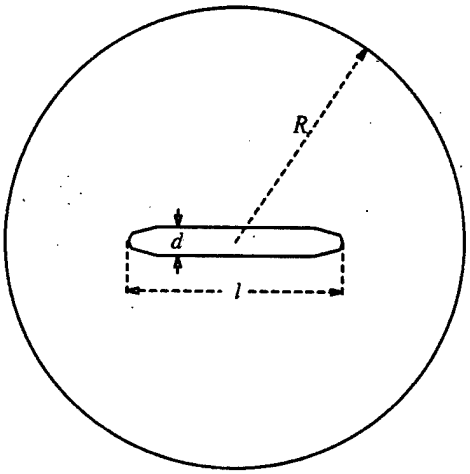

Figure 8.9: Plane wave scattering by cylinder with end caps in 2D.

The effect of mesh refinement is examined first by choosing a constant frequency of analysis, $kd = \pi/6$, and solving the problem on four successively refined meshes. An initial coarse mesh of 3x16 elements (radial x circumferential elements) is used for constructing the hierarchical basis associated with all four meshes. Intermediate mesh levels are obtained by successive uniform refinement of this coarse mesh. Fig-

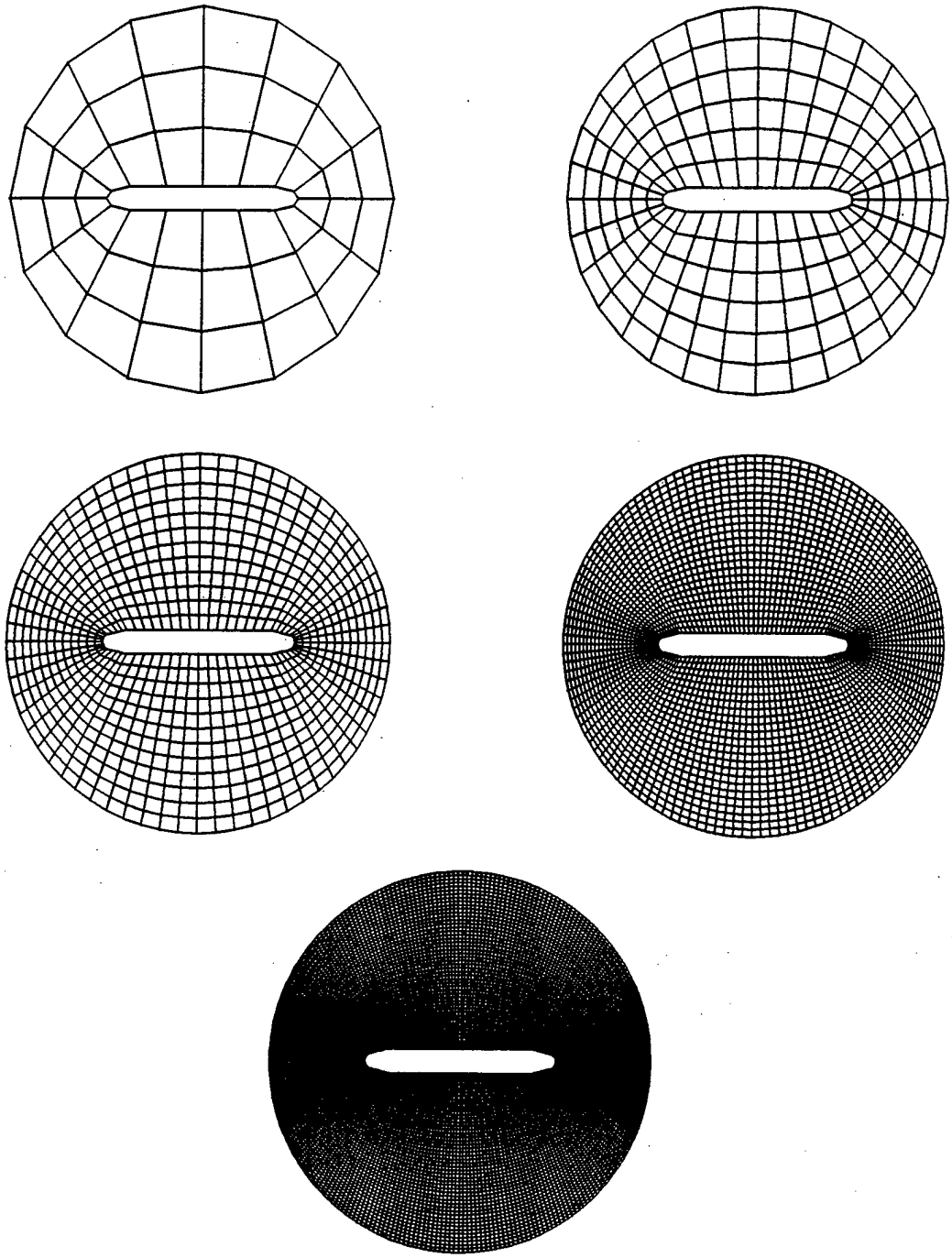

Figure 8.10: Multiple grid levels for the scattering example: Clockwise from top left are meshes with 64, 224, 3200, 12544 and 832 unknowns.

ure 8.10 shows meshes which are used as coarse, intermediate or finest grid levels in the following numerical tests.

Table 8.3: Number of iterations for convergence to 10^{-7} for plane wave scattering, $kd = \pi/6$.

Mesh	Unknowns	kd	M_I	M_D	M_{SSOR}	HB Levels	M_{HBDS}
12 x 64	832	$\pi/6$	124	116	57	3	56
24 x 128	3200		286	244	105	4	70
48 x 256	12544		592	468	197	5	83
96 x 512	49664		1372	1083	-	6	102

Table 8.4: Elapsed time (in seconds) for computing matrix-vector product and for preconditioning in each iteration of QMR on a Sun SPARCstation10.

Mesh	Unknowns	Matvec	M_D	M_{SSOR}	M_{HBDS}
12 x 64	832	0.34	0.001	0.51	0.03
24 x 128	3200	3.8	0.01	5.4	0.09
48 x 256	12544	50.7	0.6	71.0	0.73

Table 8.3 summarizes the number of iterations required for convergence to a tolerance of 10^{-7} using various preconditioners. Observe that the unpreconditioned algorithm suffers substantial deterioration in iteration count with decreasing mesh size and use of M_D yields little improvement. The hierarchical basis method is most effective in reducing total number of iterations. Although M_{SSOR} is competitive in reducing iteration counts, it requires significantly more computations and is therefore much more expensive than M_{HBDS}, see Table 8.4. A comparison of actual preconditioning times illustrates the superiority of M_{HBDS} on both serial and parallel platforms (Table 8.4 and 8.5).

Next, we study the effect of increase in frequency on performance of the hierarchical basis preconditioner. Table 8.6 shows the number of iterations to converge as

Table 8.5: Elapsed time (in seconds) for computing matrix-vector product and for preconditioning in each iteration of QMR on a Maspar MP-1 with 8192 processors.

Mesh	Unknowns	Matvec	M_D	M_{HBDS}
24 x 128	3200	0.098	0.023	0.15
48 x 256	12544	0.219	0.048	0.270
96 x 512	49664	0.640	0.125	0.990

Table 8.6: Number of iterations for convergence to 10^{-7} for plane wave scattering at $kd = \pi/2, \pi$.

Mesh	Unknowns	kd	M_I	M_D	M_{SSOR}	Coarse Mesh	HB Levels	M_{HBDS}
12 x 64	832	$\pi/2$	211	205	117	6 x 32	2	143
24 x 128	3200		465	451	201		3	162
48 x 256	12544		1023	876	334		4	187
96 x 512	49664		2338	1844	-		5	214
24 x 128	3200	π	724	715	418	12 x 64	2	469
48 x 256	12544		1533	1377	587		3	506
96 x 512	49664		3452	2972	-		4	564

Table 8.7: Effect of combining HB transformations with a coarse level solve on the number of iterations to converge.

Mesh	Unknowns	kd	Coarse Mesh	HB Levels	M_{HBDS}	M_{HBCS}
24 x 128	3200	$\pi/6$	3 x 16	4	70	62
48 x 256	12544			5	83	78
96 x 512	49664			6	102	96
24 x 128	3200	$\pi/2$	6 x 32	3	162	84
48 x 256	12544			4	187	109
96 x 512	49664			5	214	134
24 x 128	3200	π	12 x 64	2	469	96
48 x 256	12544			3	506	143
96 x 512	49664			4	564	175

the wavenumber is increased to $kd = \pi/2$ and then π. The performance of M_{HBDS} remains quite favorable as the wavenumber increases. However, notice that a different coarse mesh is chosen as the frequency is increased. This is due to the necessity to maintain the approximation property of the associated hierarchical basis functions. A decrease in size of the coarse mesh results in some increase in the number of iterations required for convergence.

To counter the effect of conditioning associated with nodal basis representation of the coarse initial mesh, we form the preconditioner $M_{HBCS}^{-1} = S(LL^T)^{-1}S^T$, where the action of $(LL^T)^{-1}$ represents an approximate solution of the coarse level unknowns. This preconditioner leads to a distinct reduction in iteration counts as the coarse mesh size decreases, see Table 8.7. However, the coarse solution procedure lacks parallelism and a reduction in iterations may not necessarily reduce actual computation times. Further work is needed to investigate efficient means of accelerating this step.

Selection of multiple levels

An important ingredient in the success of the hierarchical basis preconditioners is the choice of a multilevel splitting associated with the finite element mesh on which

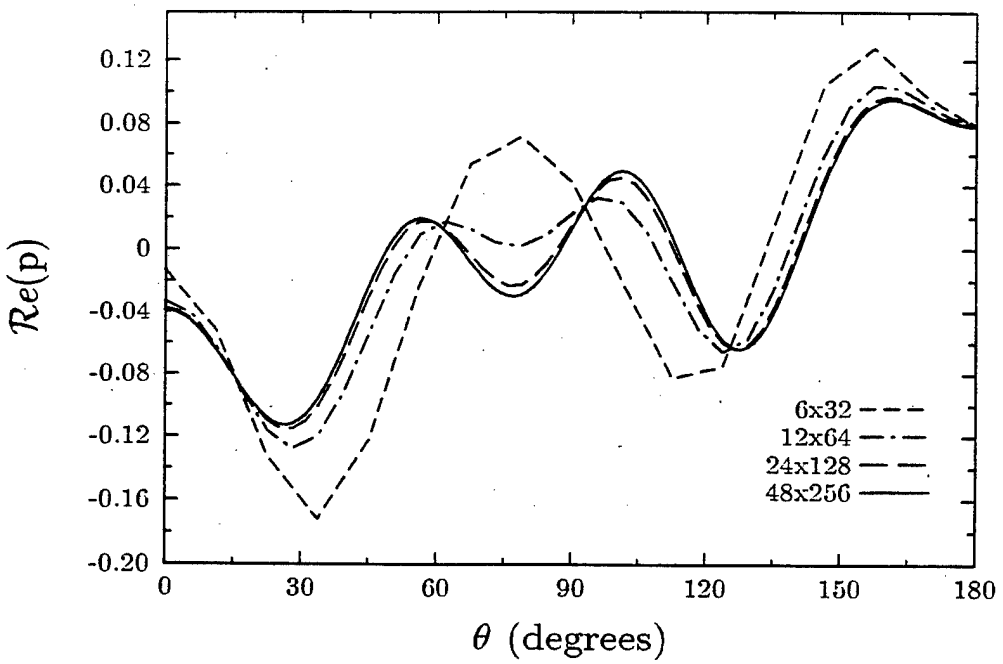

Figure 8.11: Scattered pressure field at radiation boundary with different discretizations at $kd = \pi/2$.

the problem needs to be solved. For indefinite problems it is essential that the coarse mesh size be sufficiently small in order to maintain the approximation property of basis functions. Results of numerical tests reveal that a coarse mesh with a resolution of $kh_c \leq \pi$ (h_c is the characteristic size of the coarse mesh), which corresponds to just two elements per wavelength, performs very well. Standard guidelines for creating discretizations on which the problem should be solved suggest using at least ten elements per wavelength or $kh \leq 0.6$ where h is characteristic size of the finest mesh on which the problem is solved. Figure 8.11 shows the resolution of acoustic pressure on the DtN boundary by employing successively refined meshes for the scattering example at $kd = \pi/2$. The resolution capabilities of different meshes clearly indicates that sufficient opportunity exists to construct intermediate levels of meshes between a coarse level that satisfies the condition $kh_c \leq \pi$ and the finest level of discretization required for sufficient accuracy.

The nested family of grids required for forming the preconditioner can be constructed through uniform or adaptive refinement of an initial mesh. This process can be integrated with multiple frequency analyses in such a way that as frequency increases the coarsest mesh is updated by combining initial few mesh levels and the additional grid points needed for resolution are obtained from adaptive refinement based on *a-posteriori* error estimates.

Numerical results presented in this chapter demonstrate the superiority of QMR over other gradient-type iterative methods for solving problems in acoustics. The hierarchical basis preconditioner, based on a careful selection of the associated multilevel splitting, and employed in conjunction with QMR results in a very efficient iterative strategy for solving large-scale acoustics problems on massively parallel computers. Current results are based on the effectiveness of these algorithms for uncoupled prob-

lems in two-dimensions. It is expected that the iterative solver and the proposed preconditioner will also prove effective for the coupled problem. Extension to three-dimensional problems needs further investigation.

Chapter 9

A Posteriori Error Estimation and Adaptivity

It was shown in Chapter 5 that the Galerkin method provides good phase and amplitude accuracy as long as the mesh is fine enough with respect to the wave number. However, "fine enough" is often too expensive for adequate resolution, even for moderate wave numbers. This motivated development of the Galerkin Least-Squares (GLS) method for the Helmholtz equation, which provides accuracy and stability with fewer mesh points. Results verifying this assertion for various model problems were shown in Chapter 6.

A second mechanism for enhancing accuracy is *adaptivity*, and is the subject of this chapter. Adaptivity involves distributing mesh degrees of freedom as efficiently as possible, i.e., placing more nodes where solution errors are large and fewer nodes where errors are small. The effect is a reduced problem size for a given level of accuracy. This can be accomplished by locally changing the element size (h-refinement), spectral order of the finite element shape functions (p-refinement), or a combination thereof (hp-refinement). Here we consider only h-refinement. The focus of adaptivity is on technologies occurring outside the finite element solver. These include mesh generation (or some way to locally refine the mesh), a posteriori error estimation, and an adaptive strategy.

Adaptivity works essentially as follows: A spatial error distribution is computed from the finite element solution, using the a posteriori error estimator. The adaptive strategy computes a new mesh size distribution from the estimated error, and the mesh generator uses this information to construct a new, or adaptive mesh, on which an improved finite element solution can be obtained. This process repeats until some criterion for convergence is met. For mesh generation we use an advancing front code written by Jaime Peraire; the advancing front method is described in [122]. The a posteriori error estimator and adaptive strategy were derived specifically for the Helmholtz equation and are presented herein.

In Section 9.1 we present the error estimator, adaptive strategy and numerical results for the Galerkin method. Of particular interest is the effect of adaptivity in combination with GLS; this is examined in Section 9.2. In Section 9.3 the role of adaptivity in reducing the cost of computation is addressed. The numerical examples throughout this chapter involve the problem of non-uniform radiation from a rigid

infinite circular cylinder, which was also used in Chapter 6 to show GLS computations.

9.1 Adaptivity for the Galerkin Formulation

The purpose of the a posteriori error estimator is to provide a local estimate, or indication of, the solution error $e = \phi^h - \phi$ in some norm. The choice of norm is restricted somewhat because the Helmholtz operator is not positive-definite; thus an energy norm does not exist. Therefore a posteriori error estimators which measure error in an energy norm or otherwise assume positive-definiteness [4, 5, 10, 11, 99] cannot be applied in a straightforward manner. Hsiao, et al [67] derive a residual-based a posteriori error estimator for the boundary integral equations, utilizing the natural norms of the operator and the solution. In particular, the residual measured in the $H^{1/2}$ norm approximates the error in the $H^{-1/2}$ norm. Computation of the residual in the L_2 norm results in *underestimation* of the error (in the $H^{-1/2}$ norm).

The error estimator we present for the Helmholtz equation was derived using a recipe developed by Johnson, et al, in the context of model elliptic and advection-diffusion equations (see, for example, [92, 90]). The error estimator does not assume positive-definiteness of the operator, and provides an upper bound on the L_2 norm of the error. It is also residual-based, making it easily applicable to general unstructured meshes. The error bound is given by

$$\|e\| \leq C_1 \left[\|h^2 r^h\|_{L_2(\tilde{\Omega})} + \|h^2 R^h\|_{L_2(\tilde{\Omega})} \right] \tag{9.1}$$

where C_1 is a constant, h is a measure of element length, and r^h and R^h are residuals. The subscript $L_2(\tilde{\Omega})$ denotes integration over element interiors. Details of the derivation of (9.1) appear in [140]. An important assumption here is that ϕ^h was obtained using the *Galerkin* method. The first term on the right hand side of (9.1) is the error contribution from element interiors, and the second term is the error contribution from element boundaries (which is assigned a constant value over each element interior for the purpose of computing the norm).

The residual on element interiors, r^h, is given by

$$r^h = f + \nabla^2 \phi^h + k^2 \phi^h \tag{9.2}$$

The element boundary residual, R^h, is defined as

$$R^h|_K = \max_{S \subset \partial K} \max_S (|r_2^h|) \tag{9.3}$$

where

$$h_K r_2^h(\phi^h) = \begin{cases} \frac{1}{2}[\![\phi^h_{,n_S}]\!] & \text{on } S \subset \partial K_{\text{int}} \\ \phi^h_{,n} - ikh & \text{on } S \subset \Gamma_h \\ \phi^h_{,n} - (-M\phi^h) & \text{on } S \subset \partial B_R \\ 0 & \text{on } S \subset \Gamma_g \end{cases} \tag{9.4}$$

In two dimensions, S denotes an element edge and ∂K_{int} denotes an interior mesh edge belonging to element K. In words, (9.3) states that R^h on element K is the

maximum value of the boundary residual, r_2^h, over all the edges (i.e., the boundary) of the element. The boundary residual involves a jump in the normal derivative of ϕ^h across interior edges, which emanates from the use of C^0-continuous shape functions. In addition, (9.4) naturally encompasses the DtN boundary condition on ∂B_R. It is assumed that on Γ_g the given data is exactly representable by the finite element functions, i.e., $g \in V^h$.

The a posteriori estimate of the solution error, by itself, is not enough information for an adaptive analysis to be performed. An additional step, which we refer to as the *adaptive strategy*, is necessary to translate the estimated error into requirements for an improved, or adaptive, mesh. The adaptive mesh is not generated in this step; the sole purpose of the adaptive strategy is to obtain a new element size distribution (in the case of h-refinement) for the adaptive mesh, given the estimated error on the current mesh.

For adaptivity we require an estimate of the error *distribution*, not an absolute value of the error. We therefore choose to ignore the constant C_1 appearing in (9.1) by absorbing it into the left hand side. This changes the error magnitude but not the relative error distribution. The scaled error, denoted by $\bar{e}$, is given by

$$\bar{e} \stackrel{\text{def}}{=} \|h^2 r^h\|_{L_2(\tilde{\Omega})} + \|h^2 R^h\|_{L_2(\tilde{\Omega})} \tag{9.5}$$

where

$$\frac{\|e\|}{C_1} \leq \bar{e}$$

The error estimate (9.5) is in terms of a *global* norm. We wish to use this error estimate to define a new element size distribution, which constitutes the specification of element sizes *locally*. It is therefore necessary to extract local error information from the global error bound, which is accomplished by extracting (approximately) an element contribution to the error estimate. The estimated error in element K is given by

$$\bar{e}_K \stackrel{\text{def}}{=} \left[\|h_K^2 r_K^h\|_{\tilde{\Omega}_K}^2 + \|h_K^2 R_K^h\|_{\Omega_K}^2\right]^{1/2} \tag{9.6}$$

We choose an adaptive strategy which equidistributes the error in each element of the new mesh. That is, we must specify a new element size distribution such that $\bar{e}_K$ in the adaptive mesh solution is the same in each element K of that mesh. The new element size is denoted by h_{new} and is specified as a function of the spatial location $\boldsymbol{x}_K$. In terms of $\bar{e}_K$, h_K, and a user-input element error tolerance $\bar{e}_{\text{tol}}$ (which is the target element error for the new mesh), h_{new} is given by

$$h_{\text{new}}(\boldsymbol{x}_K) = \left(\frac{\bar{e}_{\text{tol}}}{\bar{e}_K}\right)^{1/3} h_K \tag{9.7}$$

This refinement scheme is derived from heuristics, based on the dependence of $\bar{e}_K$ on h_K. Details are provided in [140].

In practice, h_{new} is computed for all K and stored at the nodes. The advancing front mesh generator [122] then interpolates h_{new} from the current mesh in producing the new, adaptive mesh. This process entails *global* mesh regeneration for each adaptive mesh. The meshes consist of linear triangles.

The goal of adaptivity is to drive the solution error down to a given tolerance in an optimal manner. A complete adaptive solution consists of a sequence of three to five meshes, usually starting from a relatively coarse uniform mesh. Trying to achieve the error tolerance in a single adaptive step would result in over-refinement, since the error on the initial mesh tends to be spread out over the larger elements. A conservative strategy which grossly under-refines would likewise be inefficient, requiring too many meshes for sufficient resolution.

The numerical example we present is the problem of non-uniform radiation from a rigid infinite circular cylinder, with a nondimensional wave number $ka = 2\pi$ (a is the radius of the cylinder). Solutions are obtained using the Galerkin method. Dirichlet boundary conditions are applied to the cylinder surface; the portion $-5\pi/32 < \alpha < +5\pi/32$ is assigned a unit value, while the remaining portion is assigned a homogeneous value. The DtN boundary is located at $R = 2a$.

The solution was computed on a sequence of five meshes. Fig. 9.1 shows the real part of the solution along with the corresponding mesh, for the first, third and fifth meshes. The computation begins with a coarse uniform mesh, while the subsequent adaptive meshes were obtained by gradually decreasing the element error tolerance, $\bar{e}_{\text{tol}}$. The solution becomes highly attenuated to the left of the cylinder, and the error estimator records a very small error there. This is reflected in the third mesh, as the adaptive strategy computes a large element size. The refinement capturing the radiated wave is also evident in the third mesh. This problem contains highly localized features, namely the discontinuities in the boundary values at $\alpha = \pm 5\pi/32$. It can be seen in the fifth mesh that they are efficiently captured. A high degree of refinement exists at the discontinuities, and a lesser degree of refinement resolves the radiated wave. The mesh gradually coarsens towards the left side of the cylinder, efficiently adapting to the attenuating solution.[1]

Fig. 9.2 shows the final adaptive mesh and a uniform mesh with nearly the same number of elements. Alongside the full mesh is an enlargement of the region near the upper boundary condition discontinuity. The elements in the uniform mesh are extremely large in this region compared to the adaptive mesh, leading to a relatively poor resolution of the discontinuity. This contributes to a global error ($\|e\| = 3.8\%$) over three times greater than that in the adaptive mesh ($\|e\| = 1.2\%$). The percent error is defined as $\|e\|/\|\phi\| \times 100$.

Convergence with increasing number of elements is shown in Fig. 9.3, comparing the adaptive and uniform mesh (exact) errors for the entire sequence of mesh refinements. Recall the analytical solution is given by (6.71); the number of elements in the mesh is denoted by n_{el}. To get an idea of required mesh sizes for further decreases in error, linear fits of the convergence data are also shown. The slopes of these lines, indicated in the figure, show that the convergence rate of adaptive refinement is roughly the same as the convergence rate of uniform refinement. It is easily seen that the uniform mesh requires a much larger number of elements to achieve a given

[1]Note the boundary condition $g \notin V^h$, which violates the assumption in (9.4). Nonetheless, as seen in foregoing results, the error estimator has enough robustness to adapt to the boundary discontinuities. As the mesh is refined, the approximation of g improves.

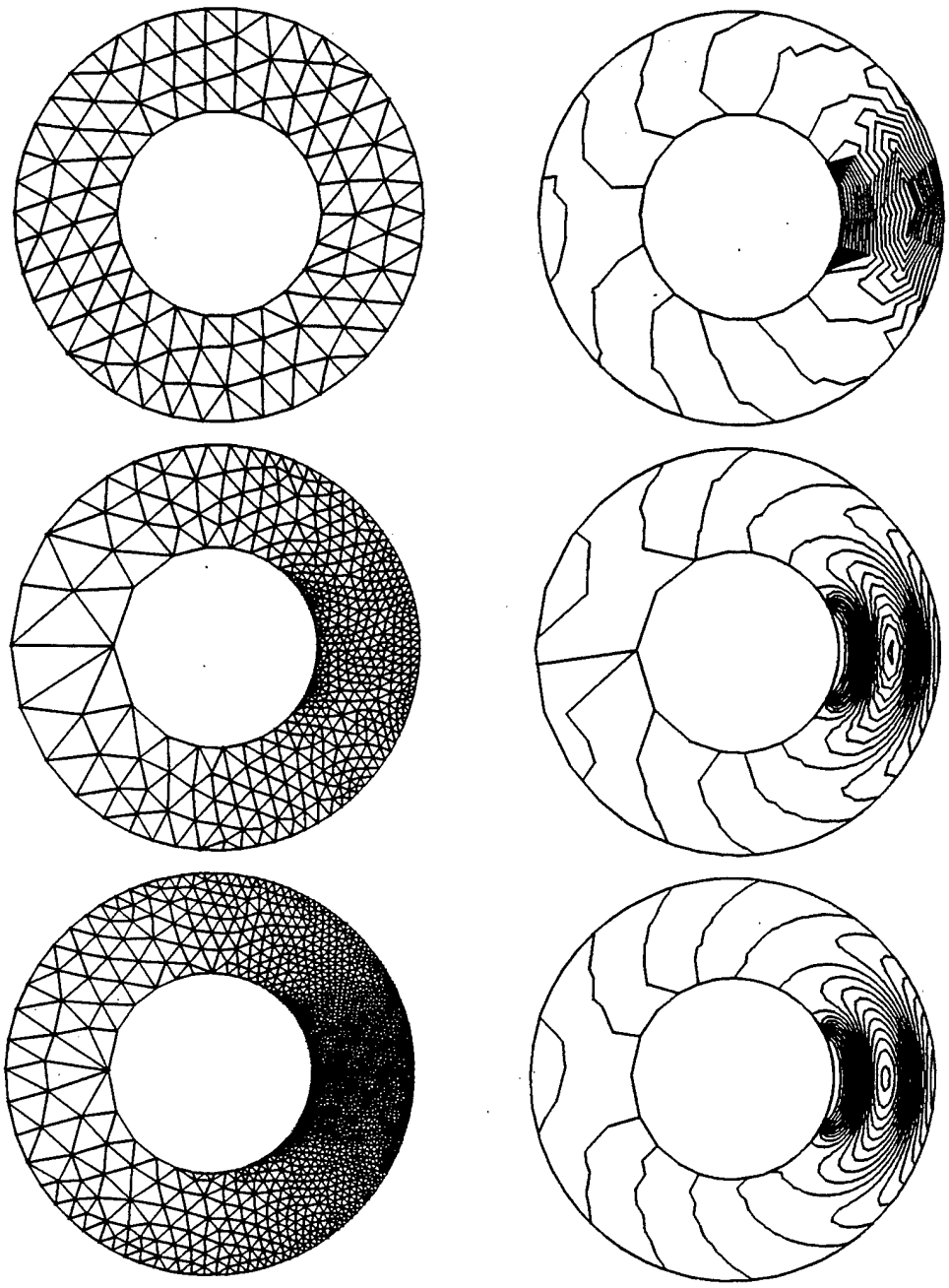

Figure 9.1: Real part of solution along with corresponding mesh, showing the initial mesh (184 elements, 124 nodes), third mesh (797 elements, 458 nodes) and final (fifth) mesh (2791 elements, 1521 nodes) of the adaptive sequence.

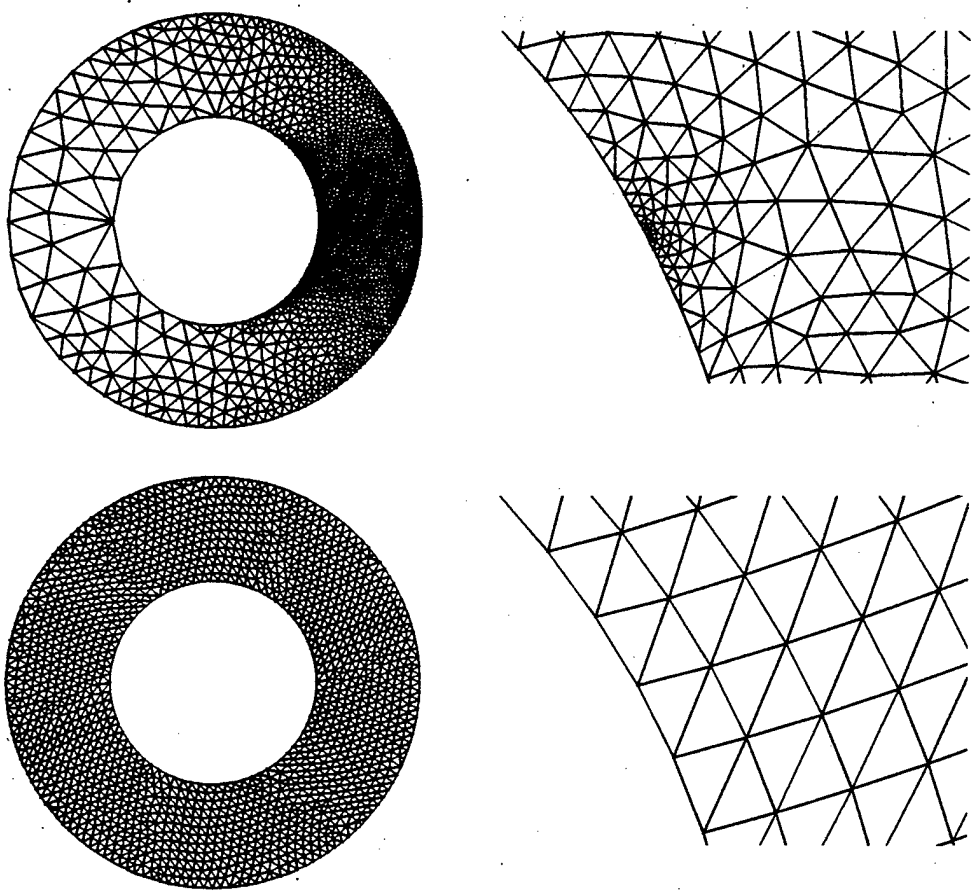

Figure 9.2: Final adaptive mesh (fifth mesh in adaptive sequence; 2791 elements, $\|e\| = 1.2\%$) and uniform mesh (2792 elements, $\|e\| = 3.8\%$), along with detailed view of meshes in region of upper boundary condition discontinuity.

error tolerance, compared to the required adaptive mesh size. For example, to attain $\|e\| = 1\%$ requires just under 4,000 elements in the adaptive mesh, but over 13,000 elements in the uniform mesh.

Remarks:

1. Convergence studies are often presented in terms of the mesh parameter, or element size, h, as it asymptotically approaches zero. The definition of h becomes confusing, however, in adaptive meshes where h can vary considerably throughout the mesh and approach zero at different rates. For this reason it is more convenient to present convergence studies in terms of n_{el}. An intuitive conversion from n_{el} to h can be made for uniform mesh convergence. In two dimensions, n_{el} is proportional to $1/h^2$. Therefore, the slope of -0.91 indicated in Fig. 9.4 roughly translates to a slope of $+2$ if $\|e\|$ is plotted versus h. In other words, the error decreases as the square of h, which is the optimal rate of convergence for the Galerkin method. Since the slope of $\|e\|$ vs. n_{el} for adaptive refinement is -0.93, it is concluded that optimal convergence is also obtained in this case. The effect of adaptivity then is to reduce the constant of proportionality between solution error and problem size.

2. For computing the exact error, 200 terms were used in the series given by (6.71). This provided a reasonable approximation of the discontinuities on the wet surface at $\alpha = \pm 5\pi/32$, where the series converges to the average value $\phi = 0.5$ (note that the term "discontinuities" is used loosely — the truncated series representation of them is actually smooth but very steep). To provide consistency and meaning to the term "exact error", the truncated series solution was used as the Dirichlet boundary condition. In addition, a node was fixed at each discontinuity and assigned a value $\phi^h = 0.5$. This was found to be critical when the mesh is refined enough for the overall error to be dominated by the error at the discontinuities. The effect of not fixing nodes there is discussed in [140].

3. Note that the boundary condition $g \notin V^h$, which violates the assumption in (9.4). Nonetheless, as seen in foregoing results, the error estimator has enough robustness to adapt to the boundary solution. As the mesh is refined, the approximation of g improves. With respect to the analytically discontinuous problem, i.e., the problem described by computing an infinite number of terms in the analytical solution, the only error incurred by the piecewise linear representation of g would be at the two discontinuities. With respect to the truncated series form of the analytical solution, additional error (assumed to be small) is incurred away from the "discontinuities".

9.2 Adaptivity for the GLS Formulation

The Galerkin Least-Squares (GLS) method was presented in Chapter 4, and numerical examples using GLS on a coarse uniform mesh were presented in Chapter 6. Recall

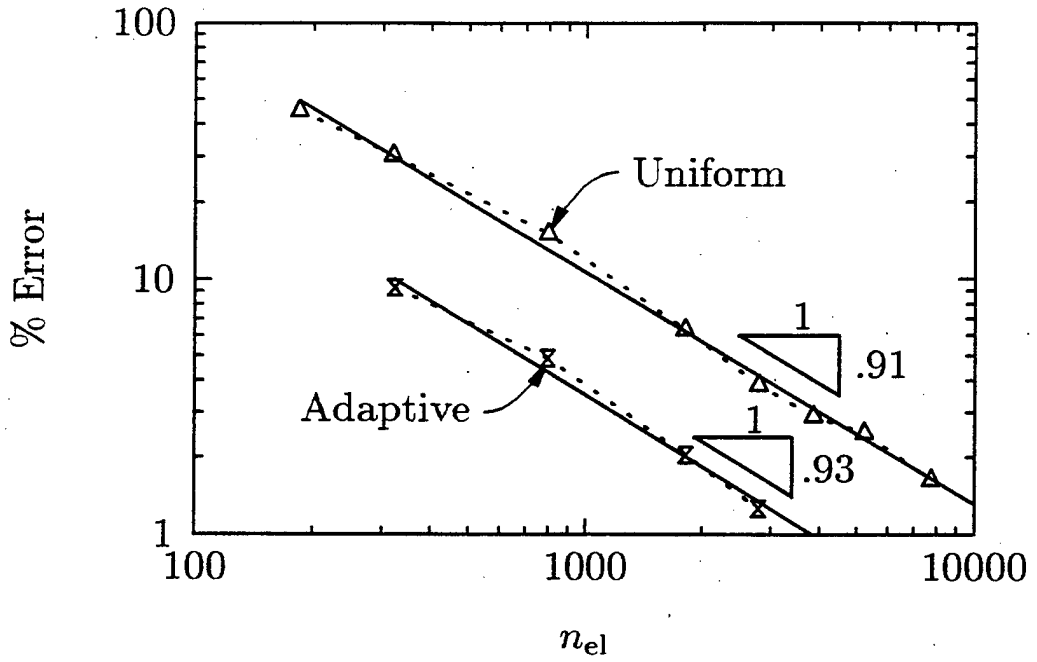

Figure 9.3: Exact error vs. number of elements in mesh. The solid lines are curve fits of the data.

that GLS is essentially the Galerkin formulation with a residual-based stabilization term added. With proper design of the parameter τ (see Section 5.2), GLS provides enhanced accuracy with fewer mesh points. In addition to how the GLS results compare to those using Galerkin, of interest is how GLS supplements adaptivity in enhancing computational efficiency.

An important assumption in the derivation of the a posteriori error estimate (9.1) is that the solution ϕ^h is obtained by the Galerkin method. The derivation can be repeated for the GLS method, which results in the following a posteriori error bound:

$$\|e\| \leq C_1 \left[\|h^2 r^h\|_{L_2(\tilde{\Omega})} + \|h^2 R^h\|_{L_2(\tilde{\Omega})} \right] + C_2 \|h^2 r^h\|_{L_2(\tilde{\Omega})} \tag{9.8}$$

where C_1 is the same constant appearing in (9.1) and C_2 is a new constant. Thus (9.8) is equal to the Galerkin bound (9.1) plus an additional contribution due to the error on element interiors. Recall r^h is the residual on element interiors, given by (9.2); R^h is the residual on element boundaries, given by (9.3); h is a measure of element length; and $L_2(\tilde{\Omega})$ denotes integration over element interiors. The derivation of (9.8) includes an assumption on the specific form of the GLS parameter τ; details of the derivation appear in [140].

For the GLS adaptive strategy, we simply use the Galerkin adaptive strategy given by (9.7). This can be justified by rearranging (9.8) to get

$$\|e\| \leq (C_1 + C_2) \|h^2 r^h\|_{L_2(\tilde{\Omega})} + C_1 \|h^2 R^h\|_{L_2(\tilde{\Omega})} \tag{9.9}$$

In the previous section we divided (9.1) through by C_1 to get an expression for the Galerkin scaled error $\bar{e}$ (see (9.5)). Although such a scaling cannot be exactly carried

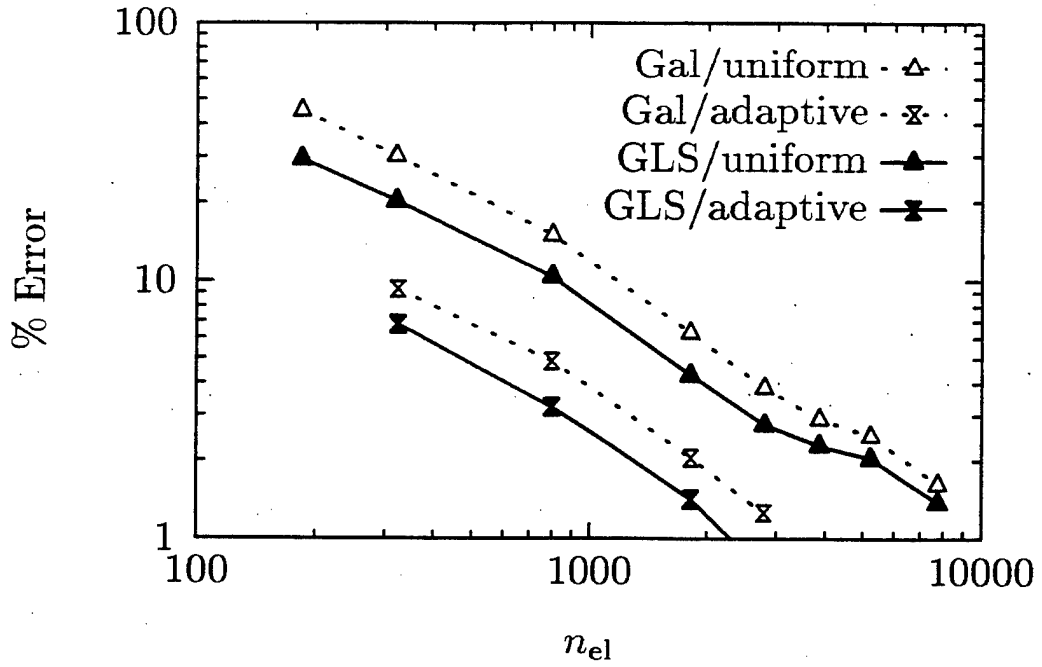

Figure 9.4: Exact error vs. number of elements in mesh.

out here, we can *approximate* $\bar{e}$ by effectively ignoring the contribution from C_2 in (9.9), resulting in

$$\bar{e} \stackrel{\text{def}}{=} \|h^2 r^h\|_{L_2(\tilde{\Omega})} + \|h^2 R^h\|_{L_2(\tilde{\Omega})} \tag{9.10}$$

which is the same expression as (9.5). This result then leads to the adaptive strategy (9.7).

Remark: This does not imply that the estimated error distribution is the same for GLS and Galerkin. Note that the error distribution is a function of the residual, which in general may be different for the GLS solution. This is discussed in more detail later in this section.

We now present convergence studies to show the effect of GLS and adaptivity, together and separately. As in the previous section, the problem is that of non-uniform radiation from a rigid infinite circular cylinder, with a nondimensional wave number $ka = 2\pi$. The GLS solution employs τ_0 based on the analysis in Section 5.2. Shown in Fig. 9.4 is the exact error as a function of n_{el}, for GLS with both uniform and adaptive refinement, as well as Galerkin with both uniform and adaptive refinement. The Galerkin convergence curves are the same ones that were presented in Fig. 9.3, and are included here for comparison with GLS convergence. We consider first the GLS convergence with uniform mesh refinement, and hereafter refer to it as GLS/uniform (analogous notation is used for the other cases). As expected, the GLS/uniform curve lies below the Galerkin/uniform curve, indicating improved accuracy using GLS.

The convergence of GLS (on uniform meshes) is now compared to that of (Galerkin) adaptive refinement. Referring again to Fig. 9.4, the GLS/uniform convergence curve lies above the Galerkin/adaptive curve, indicating (at least for this problem) that adaptivity results in higher computational efficiencies relative to GLS. Finally, adap-

tivity is combined with GLS to produce the greatest gains in efficiency: this is shown by the GLS/adaptive curve in Fig 9.4. It is seen that adaptivity and GLS are complementary in that their effects are additive. It is also evident that the convergence rates of GLS mirror those of Galerkin.

Remark: Recall that adaptive calculations also require error estimation, implementation of the adaptive strategy, etc., which are not accounted for here. These costs, although individually small, may accumulate to have the effect of decreasing the net efficiency of adaptivity. It should be realized that for very large problems (particularly in three dimensions), where a sufficiently fine uniform mesh may be impossible to generate (due to limited time and/or computer storage), adaptivity may be *necessary* to obtain any reasonable level of accuracy. In this sense adaptivity allows problems to be solved which would otherwise not be possible.

The preceding conclusions are based on analysis of the *exact* error, which is shown in Fig. 9.4. We now focus on the *estimated* error. Fig. 9.5 repeats the convergence study of Fig. 9.4, this time showing the estimated error as a function of mesh refinement. The estimated error $\bar{e}$ is given by the right-hand side of (9.5), and represents the *scaled* error. We thus examine only relative magnitudes of $\bar{e}$. It is immediately evident from Fig. 9.5 that $\bar{e}_{\text{GLS}}$ is nearly identical to $\bar{e}_{\text{Galerkin}}$, for both uniform refinement (top curve) and adaptive refinement (bottom curve). This is in contrast to the conclusions of Fig. 9.4, where GLS significantly improves upon the accuracy of Galerkin. Since $\bar{e}$ is essentially a function of the residual, it must be concluded here that the GLS residual is nearly identical to the Galerkin residual, even when the two solutions are different.

The convergence rates with respect to the estimated error (indicated by the slopes shown in Fig. 9.5) are about 20% higher than the exact convergence rates (Fig. 9.4). It is likely that on coarser meshes the error estimator is less accurate by overpredicting the error to a greater extent (e.g., by lumping large residuals on element edges onto coarse elements, artificially spreading the area over which these errors influence), leading to a larger slope.

From these results we can draw conclusions regarding the absolute value of the estimated GLS error. Computation of the absolute error entails including the heretofore ignored parameters $C_{\ldots}$'s appearing in the estimated error expressions. Comparing the GLS error expression (9.9) to the Galerkin error expression (9.1), it is clear that the estimated GLS error will be larger than the estimated Galerkin error since

$$C_1 + C_2 > C_1$$

The overprediction of the GLS error estimator is actually greater upon noting, as discussed above, that the exact GLS error is lower than the exact Galerkin error.

A common measure of the absolute accuracy of error estimators is the global *effectivity index*, θ, given by

$$\theta = \frac{\|e\|_{\text{est}}}{\|e\|_{\text{exact}}} \tag{9.11}$$

Thus θ_{GLS} is larger than θ_{Galerkin}, since for GLS the numerator is larger and the denominator is smaller than the corresponding Galerkin values. Computations of C_1

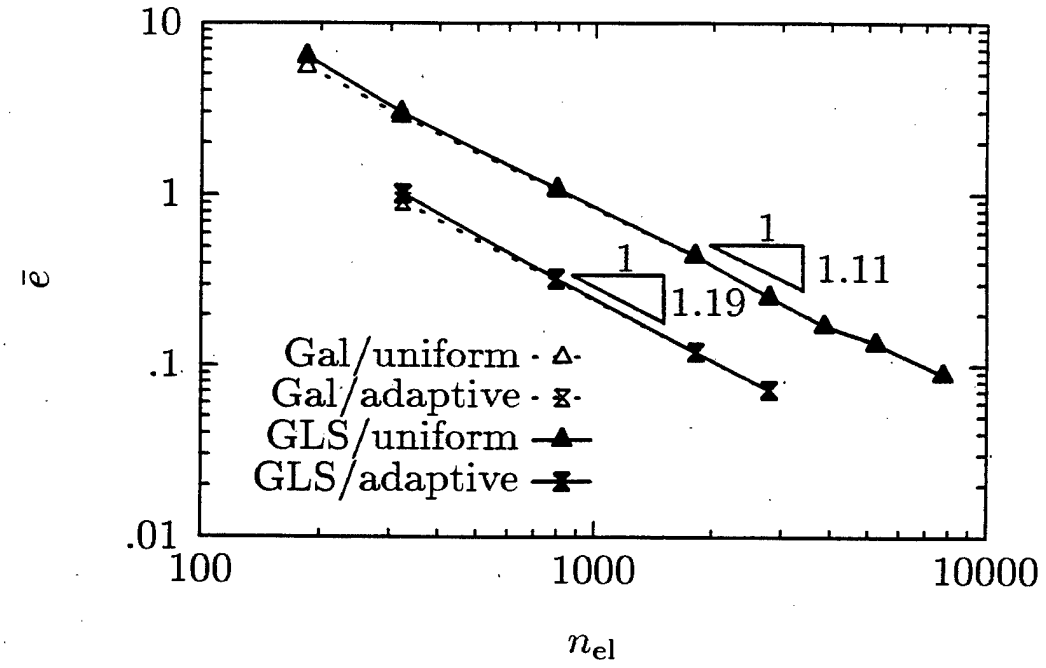

Figure 9.5: (Scaled) estimated error vs. number of elements in mesh.

and C_2, as well as θ, are given in [140].

Remark: Note that θ involves global quantities and does not measure the accuracy of the error distribution, which is the information required for adaptivity. A more useful measure for adaptivity is the *local*, or elementwise, effectivity index. See, for example, [118].

9.3 Cost Studies for Adaptivity

As mentioned in Remark 1 at the end of Section 9.1, using n_{el} as a basis of comparison for convergence studies is convenient since this information is readily available and doesn't depend on how the element sizes are distributed in the mesh. We wish now to move beyond the use of n_{el} and relate it to the underlying issue, which is the actual cost of computation. In particular, the connection between n_{el} and cost, of both computation and storage, will be established. This will provide a more meaningful framework for demonstrating the efficiency of adaptivity. We focus again on the problem of non-uniform radiation from a rigid infinite circular cylinder, with $ka = 2\pi$.

The costs of solving the linear system of equations, $\boldsymbol{Ax} = \boldsymbol{b}$, were outlined in Chapter 7. The results presented in Sections 9.1 and 9.2 were obtained using an active column direct solver; therefore, the solution costs will be analyzed only in the context of a direct solver. For the two-dimensional problems such as those presented here, which are not very large, a direct solver is relatively inexpensive. For very large problems, especially those in three dimensions, a direct solver would necessarily give way to a more efficient iterative solver. As shown in Chapter 7, the operation count of a direct solver grows much more rapidly with problem size. Nonetheless it is useful

to study direct solver costs even for large problems, for two reasons: A problem size can be identified in which a direct solver would become prohibitively expensive, based on the speed and memory of available computers; and qualitative assessments can be made of the cost efficiency of adaptivity for any level of solution accuracy.

In the following we carry out these assessments based on theoretical operation counts and storage requirements given in Chapter 7 for the direct solver. It is assumed that the direct solve step dominates the total cost, and that equation formation, overhead, etc., are comparatively inexpensive. This assumption will be further discussed later. The direct solve consists of two main components — the *factorization* of $\boldsymbol{A}$ followed by a *backsolve* procedure. The factorization of $\boldsymbol{A}$ dominates the direct solve cost. In terms of the number of equations, n_{eq}, and the mean half-bandwidth of $\boldsymbol{A}$, b_w, the factorization cost (i.e., the number of operations in the factorization step) is given by

$$\frac{1}{2}n_{\text{eq}}b_w^2 - \frac{1}{3}b_w^3$$

The unit of measurement here is the *flop*, or floating point operation. The cost of the backsolve step, again in flops, is

$$2n_{\text{eq}}b_w - b_w^2$$

The storage cost, measured in *words*, is given by

$$n_{\text{eq}}b_w$$

See Chapter 7 for a more complete discussion of these terms and expressions.

Recall the objective is to obtain the the computation and storage costs in terms of the number of elements in the mesh, n_{el}. For a mesh of linear triangles with one degree-of-freedom per node, which is the type of mesh used in Sections 9.1 and 9.2,

$$n_{\text{eq}} \approx \frac{n_{\text{el}}}{2}$$

Thus the computation cost and storage cost can be stated *approximately* in terms of n_{el} as

$$\text{Computation cost } (\textit{flops}): \quad \overbrace{\frac{1}{4}n_{\text{el}}b_w^2 - \frac{1}{3}b_w^3}^{\text{factorization}} + \overbrace{n_{\text{el}}b_w - b_w^2}^{\text{backsolve}} \tag{9.12}$$

$$\text{Storage cost } (\textit{words}): \quad \tfrac{1}{2}n_{\text{el}}b_w \tag{9.13}$$

For large problem sizes the factorization component dominates the computation cost. It is obvious that the bandwidth plays an important role and should be minimized. In the limit $b_w = n_{\text{eq}}$, which indicates a full matrix, the computation cost is $n_{\text{eq}}^3/6 + n_{\text{eq}}^2 \approx n_{\text{el}}^3/48 + n_{\text{el}}^2/4$ and the storage cost is $n_{\text{eq}}^2 \approx n_{\text{el}}^2/4$.

The bandwidths for exterior acoustics problems using the fully coupled DtN boundary condition are large enough such that the second term in (9.12) must be retained. For the computations in this work the bandwidth is optimized using the

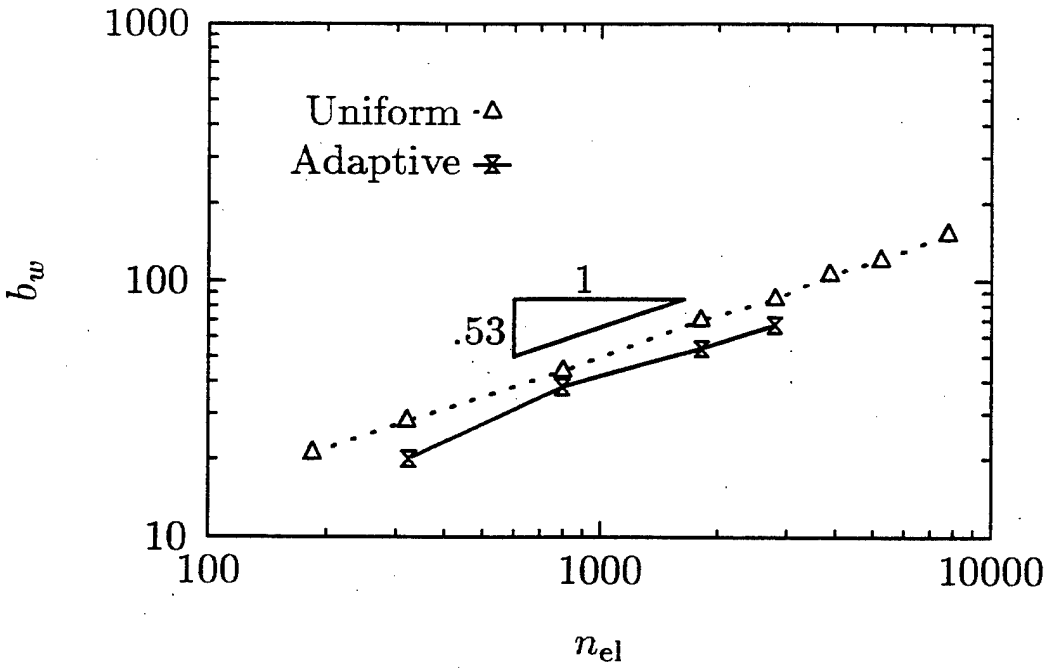

Figure 9.6: Mean half-bandwidth of the coefficient matrix vs. number of elements in the mesh.

reverse Cuthill-McKee algorithm. The optimized half-bandwidth is shown as a function of n_{el} in Fig. 9.6. Notice that smaller bandwidths are obtained for the adaptive meshes, which is partially due to the fact that the adaptive meshes have fewer nodes on the DtN boundary.

Cost comparisons are now presented for the problem of non-uniform radiation from a rigid infinite circular cylinder, with $ka = 2\pi$. The cost of computation is examined in Fig. 9.7, which shows convergence curves for the Galerkin/uniform and Galerkin/adaptive cases with respect to the computation time. The data points are measured times on a Sun Sparcstation 10 and include the total time of the solve step as well as the time required for equation formation. The solid lines are the theoretical values based on the above analysis of the direct solve cost.[2] The first thing to note about the results is that the theory does not match the data until the computation time, or, equivalently, the problem size, is sufficiently large. The theoretical costs are asymptotic cost estimates and assume $n_{\mathrm{eq}} \gg 1$ and $b_w \gg 1$; for the coarser meshes these assumptions do not hold, indicating that the costs of equation formation and any overhead within the direct solve step are significant. However, for larger problem sizes (corresponding roughly to $n_{\mathrm{el}} \geq 2800$, and $b_w \geq 67$ (adaptive) or $b_w \geq 85$ (uniform)) the direct solve is seen to sufficiently dominate the total cost.

The gain in computational efficiency engendered through adaptivity is greater

[2]It was necessary to convert the unit of theoretical cost from flops to seconds, which can be accomplished by knowing the actual speed of the computer. Estimates were made by dividing the theoretical number of operations of the direct solve step by the measured time of this step. A value of approximately 0.37 Mflops/sec (on a Sun Sparcstation 10) was obtained using the largest meshes available, and this value was used to obtain the theoretical curves in Fig. 9.7.

when considering computational cost (compare Fig. 9.7 to Fig. 9.1). Recall from Fig. 9.1, for example, that an error of one percent requires roughly 4,000 elements and 13,000 elements, respectively, for the adaptive and uniform refinements (these are the Galerkin solutions). The corresponding computation times, from Fig. 9.7, are approximately 20 seconds and 400 seconds. In other words, *the uniform mesh requires just over three times more elements than the adaptive mesh, but the computation takes twenty times longer*! This difference can be attributed to the smaller bandwidths associated with the adaptive meshes (see Fig. 9.6), as well as the functional dependence of computation cost on n_{el} and b_w. The rate of convergence with respect to computation cost is half the rate with respect to n_{el}, as indicated by the slopes of the curves in Fig. 9.7. This is easily shown algebraically: From Figs. 9.1 and 9.6, respectively (for uniform refinement), $\|e\| \propto n_{\text{el}}^{.91}$ and $b_w \propto n_{\text{el}}^{.53}$. For large n_{el}, the leading term in (9.12) dominates. Denoting the computation cost as C_{comp},

$$\begin{aligned} C_{\text{comp}} &\approx c_1\, n_{\text{el}} b_w^2 \\ &= c_2\, n_{\text{el}} (n_{\text{el}}^{.53})^2 \\ &= c_2\, n_{\text{el}}^{2.06} \end{aligned}$$

or

$$n_{\text{el}} = c_3\, C_{\text{comp}}^{.49}$$

Thus

$$\begin{aligned} \|e\| &= c_4\, n_{\text{el}}^{.91} \qquad \text{(continued)} \\ &= c_5\, (C_{\text{comp}}^{.49})^{.91} \\ &= c_5\, C_{\text{comp}}^{.45} \end{aligned}$$

where the c's represent constants. The results show that adaptivity reduces c_4 by a factor of three and c_5 by a factor of nearly four. That is, for a fixed number of elements, the adaptive computation is three times more accurate. Translated to a fixed computation time, the adaptive computation is nearly four times more accurate (this difference is due to the dependence of computation time on b_w, which (recall) depends on the type of refinement).

Computation times were also measured for the GLS runs, and are shown in Fig. 9.8. The Galerkin curves from the previous figure are repeated here for comparison. Recall Fig. 9.4 showed a significant computational advantage in terms of n_{el} using GLS, for both uniform and adaptive refinement. Similar conclusions can be drawn here. For example, a one percent error can be obtained in under ten seconds with GLS/adaptive, whereas roughly 400 seconds are required with Galerkin/uniform. *Thus the combination of GLS and adaptivity produces a speedup of a factor of 40, twice that of adaptivity alone.*

The two-dimensional computations shown herein are relatively fast, even on a workstation, because they are small (under 10,000 elements) and linear. In three dimensions the computation times will increase significantly, making the advantage of

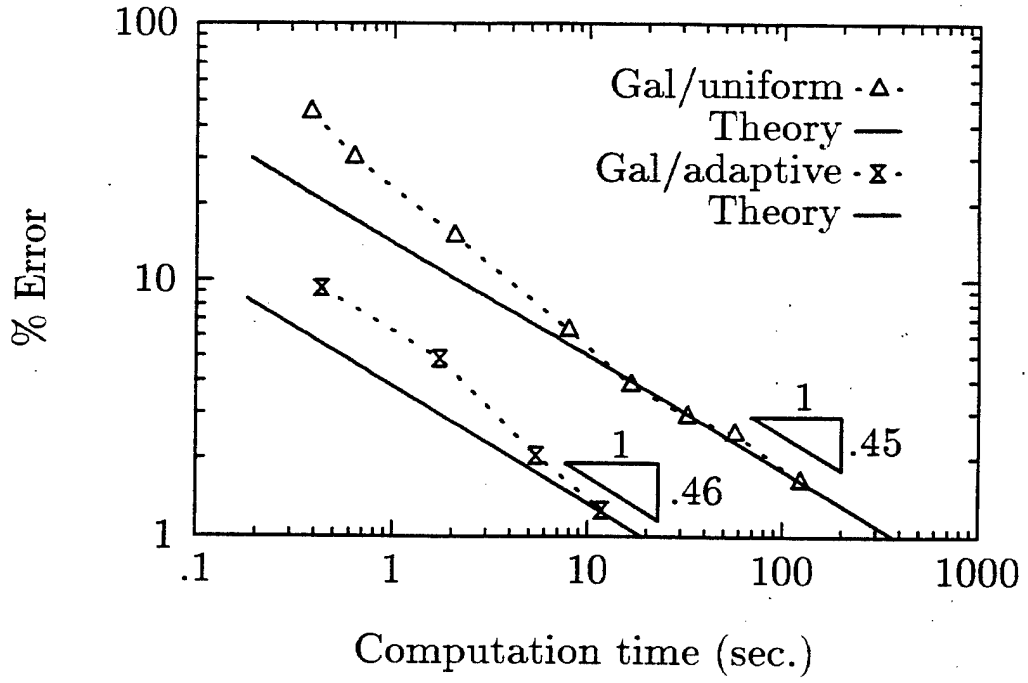

Figure 9.7: Exact error vs. computation time.

adaptivity much more pronounced, and very likely necessitating adaptivity or at least an iterative solver. In many cases it is the required computer storage, rather than the computation time, which motivates the need for adaptivity. This is particularly true when using a direct solver for linear problems on a workstation, where the computations can be performed rather quickly but the computer code requires most or all of the available memory on the machine. The storage estimate given by (9.13) represents minimum, asymptotic values, and requires efficient programming to actually realize. No attempt was made to achieve these estimates with our code; therefore, no data will be shown. The theoretical storage costs are shown (for Galerkin) in Fig. 9.9, and we assume that these hold for sufficiently large problem sizes. *Adaptivity results in a storage savings of a factor of more than eight.* The rate of storage increase with convergence is 0.60 (for both uniform and adaptive refinement), as indicated in the figure. This is shown algebraically as follows: Let C_{stor} denote the storage cost. From (9.13),

$$\begin{aligned} C_{\text{stor}} &= c_6\, n_{\text{el}} b_w \\ &= c_7\, n_{\text{el}}^{1.53} \end{aligned}$$

or

$$n_{\text{el}} = c_8\, C_{\text{stor}}^{.65}$$

Thus

$$\begin{aligned} \|e\| &= c_9\, n_{\text{el}}^{.91} \\ &= c_{10}\, (C_{\text{stor}}^{.65})^{.91} \\ &\approx c_{10}\, C_{\text{stor}}^{.60} \end{aligned}$$

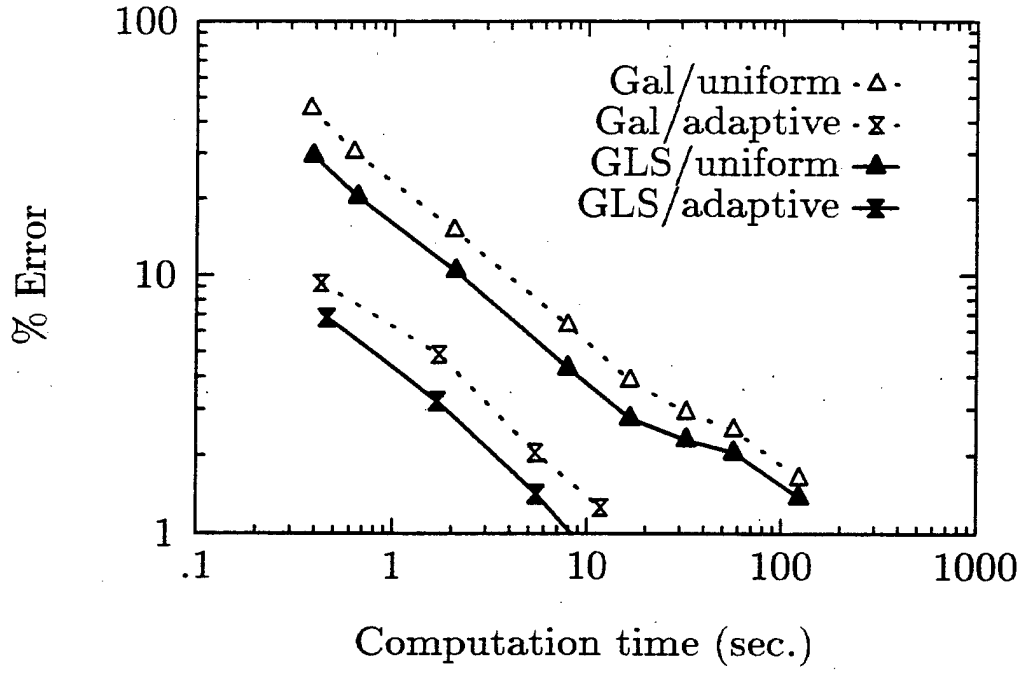

Figure 9.8: Exact error vs. computation time.

where the c's represent constants. The results show that adaptivity reduces c_{10} by a factor of approximately 3.5. That is, for a fixed amount of storage, the adaptive computation is 3.5 times more accurate.

Remark: These results apply to the non-uniform radiation problem with $ka = 2\pi$. For other problems it is expected that the trends would be similar, although specific cost savings from adaptivity depend on the presence and strength of local solution features.

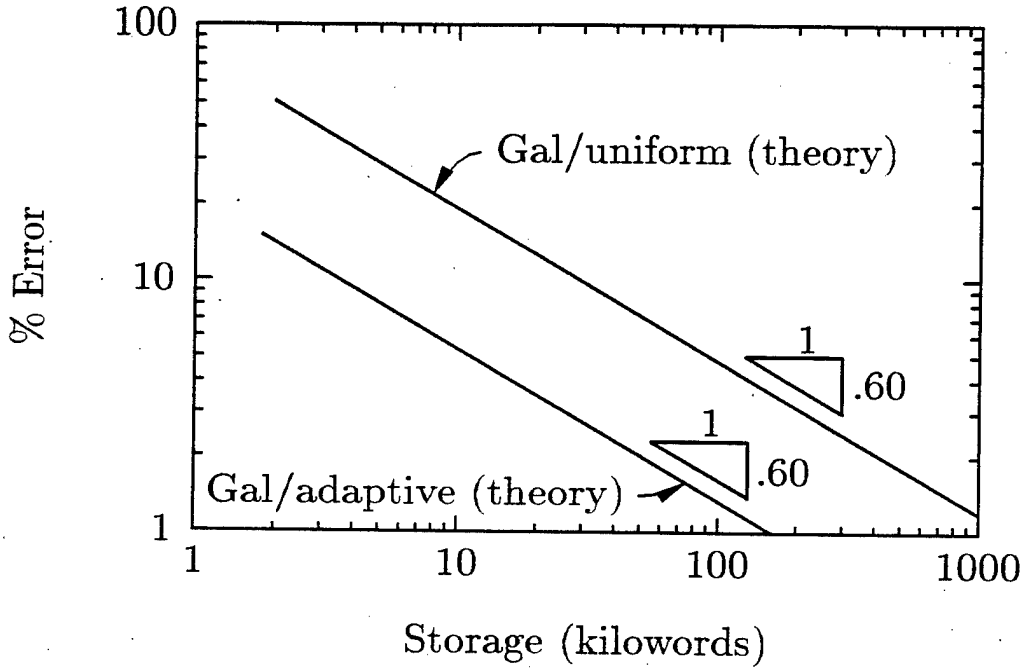

Figure 9.9: Exact error vs. theoretical storage requirement.

Chapter 10

Analysis and Method Design for Coupled Problems

A class of finite element methods, the Galerkin Generalized Least Squares methods, are developed and applied to model the steady-state response of *in vacuo* and fluid-loaded Timoshenko beams. These methods are discussed in greater detail in [49, 50, 52]. The goal of the new methods is to decrease the computational burden required to achieve a desired accuracy level at a particular frequency thereby enabling larger scale, higher frequency computations for a given platform. The results presented in this chapter are mainly drawn from [49, 50, 52].

The C^0 continuous Galerkin finite element formulation for Reissner-Mindlin plates and Timoshenko beams exhibit the deleterious effect of shear locking. Standard remedies, such as selective reduced integration, while rendering these formulations accurate for static problems, provide satisfactory results for wave propagation only for very small element size to wavelength ratios, placing an undue burden on the computations. Additionally, the standard approaches may engender spurious modes in plate models (see, e.g., [69] and [120]).

In order to improve the accuracy of the Galerkin method, Galerkin Generalized Least Squares (GGLS) techniques are applied to extend the usable frequency region for finite element models of Timoshenko beams. The general formalism for the application of this family of methods to the problem of modeling Timoshenko beams is presented. A new method is designed and implemented for a specific member of the GGLS, namely the Galerkin gradient Least Squares. The optimal design parameters for this GGLS method are obtained in closed form by considering the complex wave-number finite element dispersion relations. The parameters are chosen such that the finite element dispersion relations match the analytic dispersion relations. Also, the standard selective reduced integration approach and a modified version of selective reduced integration with mass lumping are shown to be GGLS methods. Other selections of the design parameters also are discussed. The optimal method results in a discretization requirement that is one-fifth that of selective reduced integration with a consistent mass matrix.

The design of finite element formulations for the static response of Timoshenko beams has been undertaken by Loula, *et al.* considering mixed Petrov-Galerkin finite elements [108]. Hughes and Franca developed mixed Reissner-Mindlin elements for

statics; it is in the Hughes and Franca paper that the seed of GGLS methods for structures exists as they add symmetric forms of the residuals of the equilibrium equations to the standard Galerkin equations in order to enhance accuracy [74].

The Galerkin Least Squares (GLS) technique has already been successfully applied to the finite element approximation to the Helmholtz equation, improving the accuracy for acoustics problems [56, 57] as well as structural acoustics problems [51]. In this chapter, optimal Galerkin Generalized Least Squares design parameters are obtained through the matching of analytic and finite element dispersion relations as in [50, 52]. This approach parallels the optimality criteria used by Harari and Hughes for the scalar Helmholtz equation [56, 57] and by Franca and do Carmo for the Galerkin gradient Least Squares method applied to the scalar advection diffusion equation [34].

With the improved beam formulation in hand, we move to developing more accurate methods for the fluid-structure interaction problem. New methods are designed by coupling the GGLS beam formulation to a GLS formulation for the acoustic medium. The superiority of these new methods is established through the complex wave-number dispersion analysis technique described in [51] as well as through numerical experiments [49]. The design of methods for the coupled problem provides a significant reduction in the discretization requirements allowing for computations at higher frequencies. GGLS methods for coupled systems had not been previously developed, other than in [49].

In this chapter, methods for the *in vacuo* response of beams are first presented. Numerical and analytic results for the method are then presented and compared to standard approaches. Methods for the coupled problem are presented next followed by results.

10.1 Galerkin/Generalized Least-squares Methods for Timoshenko Beams

10.1.1 Timoshenko beam equations

The coupled governing differential equations of motion for the steady-state response of the Timoshenko beam can be written in matrix form as:

$$\begin{bmatrix} -\kappa GA\frac{\partial^2}{\partial x^2} - \rho A\omega^2 & \kappa GA\frac{\partial}{\partial x} \\ -\kappa GA\frac{\partial}{\partial x} & \kappa GA - EI\frac{\partial^2}{\partial x^2} - \rho I\omega^2 \end{bmatrix} \begin{Bmatrix} w \\ \theta \end{Bmatrix} = \begin{Bmatrix} q \\ 0 \end{Bmatrix} \quad , \tag{10.1}$$

or,

$$\mathcal{L}_s \mathbf{u} = \mathbf{q} \tag{10.2}$$

where the definitions of the elements of the matrix differential operator $\mathcal{L}_s$ are obtained by inspection from (10.1) with $\mathbf{u}^T = \{w\ \theta\}$ and $\mathbf{q}^T = \{q\ 0\}$. The displacement vector is also subject to boundary conditions. The radian frequency of vibration is ω, the shear correction factor is κ, the shear modulus is G, the Young's modulus is E and the mass of the beam is ρ. The cross-sectional area of the beam is A and the moment of inertia is I.

10.1.2 Variational equations and Galerkin finite element formulation

Let the variational function spaces $\mathcal{S}_\alpha$ and $\mathcal{V}_\alpha$ both consist of continuous functions, $\alpha : \Omega \mapsto \mathbb{R}$, where $\Omega =]0, L[$, with square integrable first derivatives. The solution space, $\mathcal{S}_\alpha$, is the set of all such functions satisfying the essential boundary conditions. The weighting function space, $\mathcal{V}_\alpha$, is made up of functions whose value is zero where essential boundary conditions are specified. Define the weighting function vector as $\overline{\mathbf{u}} = \{\overline{w} \;\; \overline{\theta}\} \in \mathcal{V} \equiv \mathcal{V}_w \times \mathcal{V}_\theta$. The weak form of the problem is: given f and any boundary conditions, find $\mathbf{u} \in \mathcal{S} \equiv \mathcal{S}_w \times \mathcal{S}_\theta$ such that for all $\overline{\mathbf{u}} \in \mathcal{V}$

$$a^s(\overline{\mathbf{u}}, \mathbf{u}) = \mathrm{L}(\overline{\mathbf{u}}) \quad , \tag{10.3}$$

where

$$a^s(\overline{\mathbf{u}}, \mathbf{u}) := \int_0^L [(\frac{\partial \overline{w}}{\partial x} - \overline{\theta})\kappa GA(\frac{\partial w}{\partial x} - \theta) + \frac{\partial \overline{\theta}}{\partial x} EI \frac{\partial \theta}{\partial x} - \rho\omega^2(\overline{w}Aw + \overline{\theta}I\theta)]dx \quad , \tag{10.4}$$

and

$$\mathrm{L}(\overline{\mathbf{u}}) := (\overline{\mathbf{u}}, \mathbf{q}) + [\overline{w}\kappa GA(\frac{\partial w}{\partial x} - \theta)]\Big|_0^L - [EI\overline{\theta}\frac{\partial \theta}{\partial x}]\Big|_0^L \quad , \tag{10.5}$$

with

$$(\overline{\mathbf{u}}, \mathbf{q}) := \int_0^L \overline{\mathbf{u}} \cdot \mathbf{q} dx = \int_0^L \overline{\mathbf{u}}^T \mathbf{q} dx \quad . \tag{10.6}$$

Let the spaces $\mathcal{S}^h$ and $\mathcal{V}^h$ be the restriction of $\mathcal{S}$ and $\mathcal{V}$ to the space of piecewise polynomials of selected order. The Galerkin method is: given $\mathbf{q}$ and boundary conditions, find $\mathbf{u}^h \in \mathcal{S}^h$ such that for all $\overline{\mathbf{u}}^h \in \mathcal{V}^h$

$$a^s(\overline{\mathbf{u}}^h, \mathbf{u}^h) = \mathrm{L}(\overline{\mathbf{u}}^h) \quad . \tag{10.7}$$

A matrix problem of the following form results

$$[\mathbf{K} - \omega^2 \mathbf{M}]\mathbf{d} = \boldsymbol{f} \quad , \tag{10.8}$$

where $\mathbf{K}$, $\mathbf{M}$ and and $\boldsymbol{f}$ are the assembled stiffness matrix, mass matrix and force vector respectively. The vector of nodal displacements and rotations is given by $\mathbf{d}$. The element stiffness matrices are $\mathbf{k}^e$ and the element mass matrices are $\mathbf{m}^e$ (see e.g., [69]).

10.1.3 Galerkin/generalized least-squares finite element formulations for the Timoshenko beams

The Galerkin Generalized Least Squares (GGLS) formulation is an extension of the Galerkin Least Squares (GLS) technique along the lines of the Galerkin gradient Least Squares (G∇LS) method [34, 56, 57]. In the GLS technique, a term proportional to a weighted integral of the residual of the original differential equations is added to the standard Galerkin equations. The GGLS formulation differs from the GLS in that

the added term consists of a weighted integral of a differential operator acting on the residual. The GGLS method is to find $\mathbf{u}^h \in \mathcal{S}^h$ such that for all $\overline{\mathbf{u}}^h \in \mathcal{V}^h$

$$A_{GGLS}(\overline{\mathbf{u}}^h, \mathbf{u}^h) = \mathrm{L}_{GGLS}(\overline{\mathbf{u}}^h) \quad , \tag{10.9}$$

where

$$A_{GGLS}(\overline{\mathbf{u}}^h, \mathbf{u}^h) := a^s(\overline{\mathbf{u}}^h, \mathbf{u}^h) + \sum_{j=1}^{n_{LS}} (\mathbf{H}_j \mathcal{L}_s \overline{\mathbf{u}}^h, \mathbf{H}_j \mathcal{L}_s \mathbf{u}^h)_{\tilde{\Omega}} \quad , \tag{10.10}$$

and

$$(\mathbf{H}_j \mathcal{L}_s \overline{\mathbf{u}}^h, \mathbf{H}_j \mathcal{L}_s \mathbf{u}^h)_{\tilde{\Omega}} = \sum_{e=1}^{N-1} \int_{x_e}^{x_{e+1}} (\mathbf{H}_j \mathcal{L}_s \overline{\mathbf{u}}^h) \cdot (\mathbf{H}_j \mathcal{L}_s \mathbf{u}^h) dx \quad . \tag{10.11}$$

The matrix operator $\mathbf{H}_j$ is defined as

$$\mathbf{H}_j := \begin{bmatrix} \sqrt{\tau_{1j}} \frac{\partial^{n_j}}{\partial x^{n_j}} & 0 \\ 0 & \sqrt{\tau_{2j}} \frac{\partial^{m_j}}{\partial x^{m_j}} \end{bmatrix} \quad , \tag{10.12}$$

where τ_{1j} and τ_{2j} are design parameters to be determined, as are n_j and m_j. The number of least squares operators modifying the the variational equations is n_{LS}. The force contribution is

$$\mathrm{L}_{GGLS}(\overline{\mathbf{u}}^h) := \mathrm{L}(\overline{\mathbf{u}}^h) + \sum_{j=1}^{n_{LS}} (\mathbf{H}_j \mathcal{L}_s \overline{\mathbf{u}}^h, \mathbf{H}_j \mathbf{q})_{\tilde{\Omega}} \quad . \tag{10.13}$$

In general, the method will consist of fixing n_j, m_j and n_{LS} and choosing the values of the τ parameters judiciously. The τ's are element quantities, constant over the element but varying with element. The formalism of (10.9)–(10.13) represents a very flexible methodology and allows for very general modifications to the Galerkin equations. The use of $n_{LS} > 1$ has been studied recently by Harari [62] for the advection diffusion equation and this approach has great promise, especially for applications to Reissner-Mindlin plate elements. In the sequel, we will consider $n_{LS} = 1$ and drop the summation and subscript notation.

We consider the Galerkin gradient Least Squares (G∇LS) method where $n = m = 1$,

$$\mathbf{H}_{G\nabla LS} = \begin{bmatrix} \sqrt{\tau_1} \frac{\partial}{\partial x} & 0 \\ 0 & \sqrt{\tau_2} \frac{\partial}{\partial x} \end{bmatrix} \quad . \tag{10.14}$$

The additional force contribution arising from the least-squares addition comes from the τ_1 proportional terms only. Hence, if τ_1 is zero, there is no alteration to the consistent Galerkin force vector.

The GGLS method results in a matrix problem of the form:

$$[\mathbf{K} - \omega^2 \mathbf{M} + \tilde{\mathbf{K}}]\mathbf{d} = \mathbf{Z}\mathbf{d} = \tilde{\boldsymbol{f}} \quad , \tag{10.15}$$

where $\tilde{\mathbf{K}}$ is the GGLS contribution to the stiffness matrix assembled from the element GGLS contributions, $\tilde{\mathbf{k}}^e$. The assembled force vector, $\tilde{\boldsymbol{f}}$, includes any contributions from the GGLS formulation through (10.13). The dynamic stiffness matrix, $\mathbf{Z}$, is the assembly of the element dynamic stiffness matrices:

$$\mathbf{z}^e = \mathbf{k}^e - \omega^2 \mathbf{m}^e + \tilde{\mathbf{k}}^e \quad . \tag{10.16}$$

Let $z_{j\ell} = [\mathbf{z}^e]_{j\ell}$, $j\ell$th element of $\mathbf{z}^e$.

10.2 New Timoshenko Beam Elements Using Linear Interpolants

In this study, the G∇LS version of the GGLS is applied to a linear finite element interpolation of the Timoshenko beam equations. While other formulations, such as the GLS method, were examined, the G∇LS was found to yield most directly successful results for linear interpolants. The G∇LS gives control over the dominant error terms. In this section, the specific form of the G∇LS is presented along with optimal design parameters that yield zero dispersion error and suboptimal design parameters that yield selective reduced integration (SRI) and SRI with mass lumping. To our knowledge, this presentation is the first to link a mass lumping method with a consistent finite element method.

10.2.1 G∇LS with linear interpolants

For linear interpolants, the resulting G∇LS formulation is

$$a^s(\overline{\mathbf{u}}^h, \mathbf{u}^h) + (\tau_1 \rho A\omega^2 \frac{\partial \overline{w}^h}{\partial x}, \rho A\omega^2 \frac{\partial w^h}{\partial x})_{\tilde{\Omega}} \quad +(\tau_2[\rho I\omega^2 - \kappa GA]\frac{\partial \overline{\theta}^h}{\partial x}, [\rho I\omega^2 - \kappa GA]\frac{\partial \theta^h}{\partial x})_{\tilde{\Omega}}$$
$$= \mathrm{L}(\overline{\mathbf{u}}^h) - (\tau_1 \frac{\partial q}{\partial x}, \rho A\omega^2 \frac{\partial \overline{w}^h}{\partial x})_{\tilde{\Omega}} \quad .$$

The GGLS contribution to the element dynamic stiffness matrix is

$$\tilde{\mathbf{k}}^e = \begin{bmatrix} r_1 & 0 & -r_1 & 0 \\ & r_2 & 0 & -r_2 \\ & & r_1 & 0 \\ & \text{symmetric} & & r_2 \end{bmatrix} \quad , \tag{10.17}$$

where,

$$r_1 = \tau_1(\rho A\omega^2)^2/h \quad , \tag{10.18}$$

$$r_2 = \tau_2(\rho I\omega^2 - \kappa GA)^2/h \quad . \tag{10.19}$$

Remark:

1. If τ_1 is set to zero, and

$$r_2 = -h\kappa GA/12 \quad , \tag{10.20}$$

where h is the element length, the effect of selective reduced integration is recovered. Hence selective integration is a special case of G∇LS over all frequencies, even for $\omega = 0$, i.e., statics.

10.2.2 Dispersion analysis and eigenvector accuracy

Dispersion analysis and the accuracy of the associated eigenvectors are used in this study both as design criteria for determination of the optimal τ parameters and as a means of assessing the accuracy of different methods. A brief outline of the manner in which the finite element dispersion relations are found is given next, for more details see [51, 120]. The homogeneous finite element matrix equations for an infinite uniform mesh are formed; these matrix equations yield the following difference stencils for the w_n equation:

$$z_{13}w_{n-1} + z_{23}\theta_{n-1} + (z_{11} + z_{22})w_n + (z_{12} + z_{34})\theta_n + z_{13}w_{n+1} + z_{14}\theta_{n+1} = 0 \quad (10.21)$$

and for the θ_n equation:

$$z_{14}w_{n-1} + z_{24}\theta_{n-1} + (z_{12} + z_{34})w_n + (z_{22} + z_{44})\theta_n + z_{23}w_{n+1} + z_{24}\theta_{n+1} = 0 \quad . \quad (10.22)$$

An exponential solution is assumed for the nodal unknowns:

$$\mathbf{d}_n = \mathbf{u}_0 e^{ikhn} = \left\{ \begin{array}{c} w_0 \\ \theta_0 \end{array} \right\} e^{ikhn} \quad , \quad (10.23)$$

where $i = \sqrt{-1}$, h is the nodal spacing and k is the wave number. Substitution of the assumed exponential form into the stencil equations results in the conditions for allowed waves in the finite element mesh:

$$\left[\begin{array}{cc} 2z_{13}\lambda + z_{11} + z_{33} & -2iz_{23}\eta \\ 2iz_{23}\eta & 2z_{24}\lambda + z_{22} + z_{44} \end{array} \right] \left\{ \begin{array}{c} w_0 \\ \theta_0 \end{array} \right\} = \mathcal{F}\mathbf{u}_0 = 0 \quad (10.24)$$

where $\lambda = \cos(kh)$, $\eta = \sin(kh)$. The matrix, $\mathcal{F}$, in (10.24) is called the Fourier matrix [51, 120]. Setting the determinant of the Fourier matrix to zero yields the finite element dispersion relation for the Timoshenko beam:

$$\alpha_1\lambda^2 + \alpha_2\lambda + \alpha_3 = 0 \quad , \quad (10.25)$$

where

$$\alpha_1 = 4(z_{13}z_{24} + z_{23}^2) \quad , \quad (10.26)$$

$$\alpha_2 = 2(z_{24}(z_{11} + z_{33}) + z_{13}(z_{22} + z_{44})) \quad (10.27)$$

and

$$\alpha_3 = (z_{11} + z_{33})(z_{22} + z_{44}) - (z_{12} + z_{34})^2 - 4z_{23}^2 \quad . \quad (10.28)$$

The superscript ^{h} is used to denote wave numbers that satisfy the finite element dispersion relation (i.e., k^h satisfies (10.25)). These wave numbers are called the numeric wave numbers.

Once the allowed wave numbers for the finite element mesh are obtained via dispersion analysis, one may examine the accuracy of the eigenvectors associated with each wave number. The eigenvectors of the Fourier matrix are obtained from (10.24) . The ratio of the rotation to the displacement is

$$A^h = \frac{\theta_0^h}{w_0^h} = \frac{2z_{24}\lambda^h + z_{22} + z_{44}}{2iz_{23}\eta^h} \quad . \quad (10.29)$$

Eigenvector accuracy for Timoshenko beams has also been studied by Jasti [85].

10.2.3 Design parameters for zero dispersion error

Next, the method by which the optimal design parameters τ_1 and τ_2 are selected is described. The τ parameters that yield a finite element dispersion relation that matches the analytic dispersion relation are sought. There are two values of λ that satisfy (10.25) which correspond to two pairs of numeric wave numbers $\pm k_1^h$ and $\pm k_2^h$. There are also two pairs of wave numbers that satisfy the the analytic dispersion relation [47]. Substituting the exact wave numbers into the finite element dispersion relation results in

$$\alpha_1 \lambda_1^2 + \alpha_2 \lambda_1 + \alpha_3 = 0 \quad , \tag{10.30}$$

$$\alpha_1 \lambda_2^2 + \alpha_2 \lambda_2 + \alpha_3 = 0 \quad , \tag{10.31}$$

where $\lambda_1 = \cos(k_1 h)$ and $\lambda_2 = \cos(k_2 h)$ with k_1 and k_2 satisfying the analytic dispersion relation. The coefficients α_i contain the design parameters; (10.30) and (10.31) are two nonlinear equations in τ_1 and τ_2 which must be satisfied for zero dispersion error. These nonlinear equations may be solved in closed form for the τ's which give zero dispersion error; the expressions for the optimal values are given in [50, 52]. These optimal values for τ are obtained in terms of the Galerkin element stiffness matrices and the wave numbers satisfying the analytic dispersion relation.

Performing a limiting analysis of the optimal τ's by expanding in powers of ω yields:

$$\lim_{\omega \to 0} \hat{\tau}_1 = \lim_{\omega \to 0} \hat{\tau}_1 (\rho A \omega^2)^2 / h = -\rho A \omega^2 h / 4 \tag{10.32}$$

$$\lim_{\omega \to 0} \hat{\tau}_2 = \lim_{\omega \to 0} \hat{\tau}_2 (\rho I \omega^2 - \kappa G A)^2 / h = -\kappa G A h / 12 + \rho \omega^2 h \left(\frac{-EI}{6 \kappa G} + \frac{I}{12} + \frac{7 A h^2}{360} \right) \tag{10.33}$$

For statics $\hat{\tau}_1$ plays no role in the GGLS formulation, as these terms enter only through the mass contribution. The value of $\hat{\tau}_2$ limits to that of SRI, (10.20) ; hence SRI is the zero frequency limit of the zero dispersion error GGLS_{opt} formulation.

10.2.4 Design parameters for enhanced Fourier matrix accuracy

Another possible criteria of accuracy is to examine the discrete Fourier matrix compared to the exact Fourier matrix. If one assumes the exact traveling wave solution at the nodes of a uniform finite element mesh and that $kh \ll 1$, one may design a method that minimizes certain elements of the difference between the exact and discrete Fourier matrices while still eliminating shear locking. This choice of parameters is

$$r_1 = -\rho A \omega^2 h / 6 \quad , \tag{10.34}$$

$$r_2 = -\rho I h \omega^2 / 6 - h \kappa G A / 12 \quad , \tag{10.35}$$

which turns out to be the element mass and stiffness matrix for SRI with a lumped mass approximation (lumped using Lobatto quadrature [69]). Denote this element as $\text{GGLS}_{\ell m}$. This GGLS method engenders an alteration to the force vector as τ_1

is non-zero. This differs from the standard lumped mass approximation in which no alteration to the force vector occurs. It will be shown that this element is superior to the SRI-consistent mass element but not as accurate as the optimal choice of the τ's.

10.3 Results for Timoshenko beams

Results are presented for a steel beam, $E = 210 \times 10^{10}\ dynes/cm^2$, $\nu = 0.29$ and $\rho = 7.8\ g/cm^2$. The beam length $L = 100.0\ cm$, is simply supported at both ends with a rectangular cross-section, unit width and thickness $t = 0.15\ cm$. The shear correction factor, κ is taken to be 5/6. The implementation of the optimal τ parameters of Section 10.2.3 is compared to results using a selective reduced integrated (SRI) element and the GGLS method corresponding to selective reduced integration with mass lumping ($\text{GGLS}_{\ell m}$) of Section 10.2.4.

It is interesting to note that the τ parameters used in this study are real, negative quantities. Hence, the GGLS contribution serves to reduce the stiffness of the standard Galerkin formulation. This results in $\sqrt{\tau}$ that is a pure imaginary number. In most GGLS and GLS formulations the design parameters add stability to the formulation; here the GGLS actually reduces the stability of the formulation in order to enhance the accuracy.

10.3.1 Dispersion relations for the Timoshenko beam

Next, the dispersion relations and the accuracy of the eigenvector ratios for the model problem are studied. These results are presented for values of $\Re(kh) < \pi$ which corresponds to two elements per wavelength, where $\Re$ denotes the real part of a complex quantity. This is the cut-off frequency of the dispersion relations above which the real wave numbers become complex. A more physical limit would be four elements per wavelength ($\Re(kh) < \pi/2$), as two linear shape functions do not possess sufficient minima and maxima to represent the variation of the response over a wavelength while four such shape functions do [56, 57]. In Fig. 10.1, the finite element dispersion relations, obtained from (10.25) , for the GGLS_{opt} formulation and the SRI element are compared to the analytic dispersion relation. As the frequency range plotted is below the cut-in of the second anti-symmetrical mode, one of the wave numbers satisfying the dispersion relation is real, corresponding to a propagating wave and the other is purely imaginary, corresponding to a decaying wave. The GGLS_{opt} formulation matches the analytic dispersion relation, as required by the method. At low frequencies, the SRI element performs fairly well with the qualitative behavior of the dispersion relations being replicated. The error in the real wave number (denoted k_{prop}) is less than 3% for discretizations finer than ten elements per wavelength. Above the ten elements per wavelength level, the imaginary root locus diverges rapidly away from the exact dispersion relation. In fact, this wave-number locus becomes complex (an oscillatory-decaying wave) for $\omega h > 100000.0\ cm/s$ and thus completely misrepresents the analytic behavior of the dispersion relation. The real wave-number locus remains real at these higher frequencies, maintaining the

character of the analytic solution. However, the error in this branch increases with frequency.

The finite element dispersion error for the $GGLS_{\ell m}$ element are significantly lower than for the SRI formulation, with an error in the real component of the wave number less than one percent for discretizations finer than ten elements per wavelength [49]. The errors in the eigenvectors are discussed in [49, 52, 85].

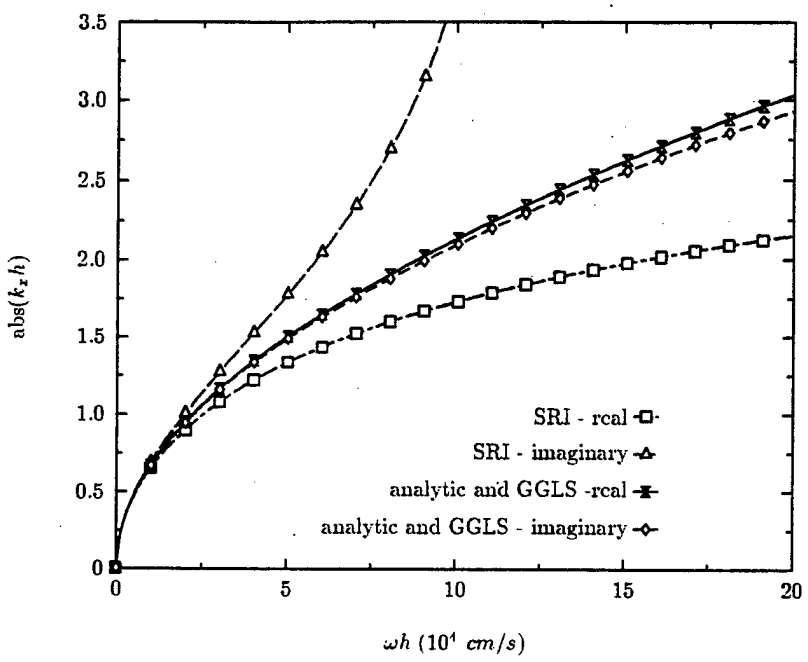

Figure 10.1: Analytic and SRI finite element dispersion relations for a Timoshenko beam. Steel beam, $h/t = 20/3$.

10.3.2 Displacement results for the Timoshenko beam

A finite element discretization of the model problem with interelement spacing of $h = 1.0\ cm$ is considered. Only the displacement is presented here as the rotation results follow the same trends. In order to demonstrate the performance of the GGLS formulation, the frequency is set to 7550 Hz which corresponds to $\omega h \approx 47500.0\ cm/s$. At this frequency, the analytic wave number corresponds to 4.30 elements per wavelength ($k_{prop}h = 1.46$), a very coarse discretization. The results comparing the SRI element to the exact solution are shown in Fig. 10.2. These results clearly demonstrate the impact of the phase error as seen in the finite element dispersion results. For the finite element solution, the number of half wavelengths over the beam is twenty-one while for the analytic solution there are twenty-three. While refining the finite element mesh, the approximate solution will experience a resonance before converging

to the analytic solution; i.e., the error will get worse before converging monotonically. Also, there is a large error at the drive point where the SRI element fails to the reproduce solution around this discontinuity. Results at the same frequency and discretization using the GGLS$_{\ell m}$ element (not shown) also are poor due to the high phase error for this discretization.

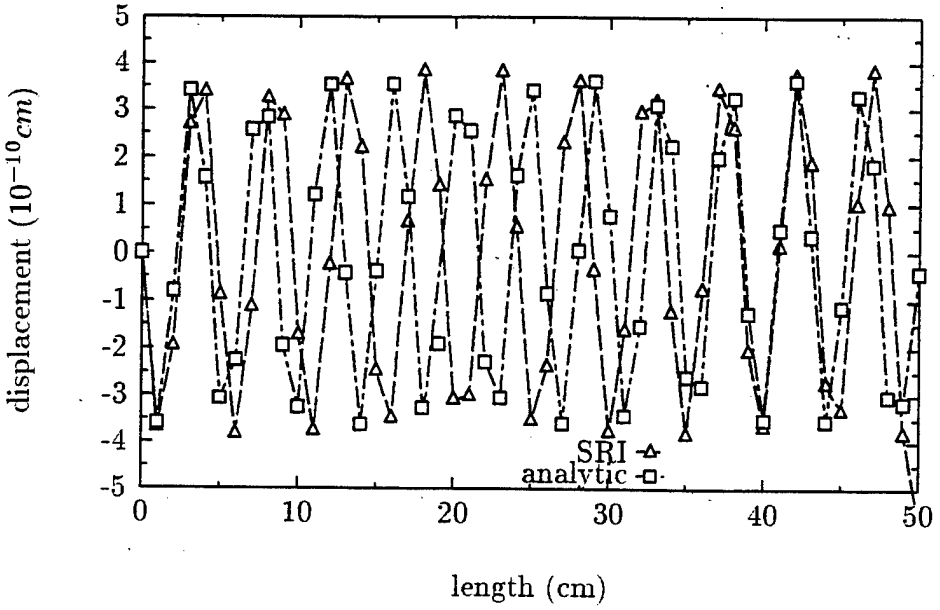

Figure 10.2: Comparison of exact and SRI finite element displacement for a steel beam, $h/t = 20/3$, frequency of 7550 Hz.

In Fig. 10.3 the result for the GGLS$_{opt}$ element is shown. The GGLS$_{opt}$ method provides a dramatic improvement in accuracy over the SRI and GGLS$_{\ell m}$ methods. The phase is exactly replicated over the entire length of the beam. The response around the drive point is also well reproduced; the essential behavior of the situation is well represented. There is an error in the amplitude of the standing wave pattern over the length of the beam. This amplitude error is exacerbated as ωh is increased, although the phase continues to be exactly represented. The amplitude error is partially due to errors in the eigenvectors.

10.3.3 L_2 error and discretization rules

The displacement results presented in the previous section give a good qualitative feel for the accuracy of these methods. Quantitative error measures using the L_2 norm are given next. The error in the displacement is defined as

$$e_w = w^h - w \quad , \tag{10.36}$$

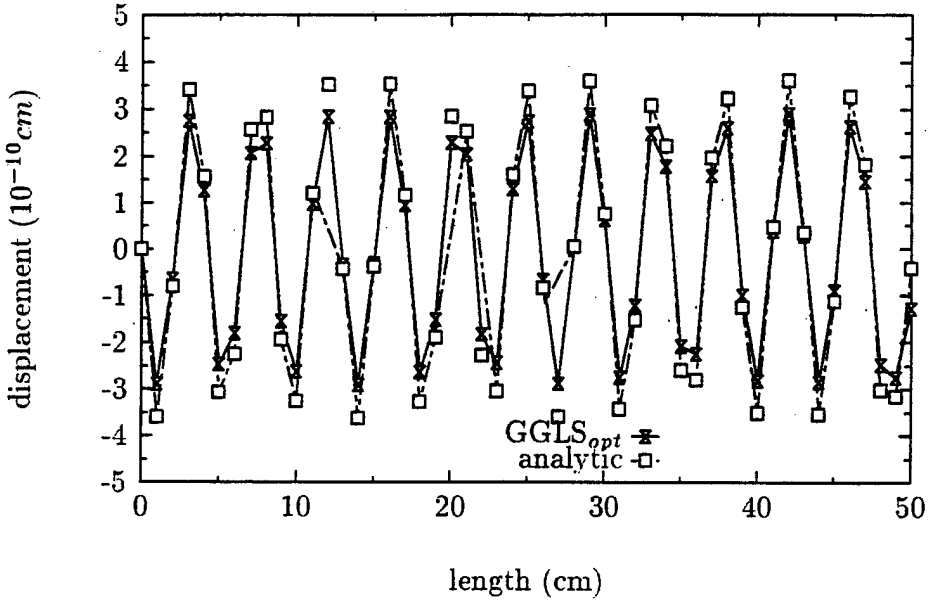

Figure 10.3: Comparison of exact and GGLS$_{opt}$ finite element displacement for a steel beam, $h/t = 20/3$, frequency of 7550 Hz.

where w is the exact solution and w^h is the finite element approximation. The L_2 norm is

$$||w|| = (\int_0^L w^2\, dx)^{1/2} \quad . \tag{10.37}$$

The convergence rates of the three methods are studied under uniform refinement. The optimal convergence rate for the linear interpolation is Ch^2 [69], i.e. $||e|| \sim Ch^2$, where C is independent of h, but will be seen to depend on frequency. The L_2 convergence of the rotation is not presented here as those results follow a similar trend [52].

The convergence rates for the displacement at $f = 7550.0\ Hz$ is shown in Fig. 10.4. In this plot the normalized L_2 error is plotted versus the number of elements used in the discretization of half the beam (n_{el}). In order to obtain a one percent normalized error, the GGLS$_{opt}$ method requires one-third the number of elements needed by the GGLS$_{\ell m}$ method and one-fifth the number of elements needed by the SRI element. The convergence rates for all three methods asymptote to the optimal rate. However, the GGLS$_{opt}$ method achieves that optimal rate with fewer elements. Examination of the error for the SRI element reveals that an increase in error the occurs before monotonic convergence with mesh refinement. This effect is due to a numerical (false) resonance that is caused by the poor phase accuracy of the SRI element.

In [49, 52] it is noted that with increasing frequency the dynamic correction afforded by the GGLS$_{opt}$ method increases as well. Therefore, the difference between the L_2 error curves also increases indicating that the constant in the convergence rate

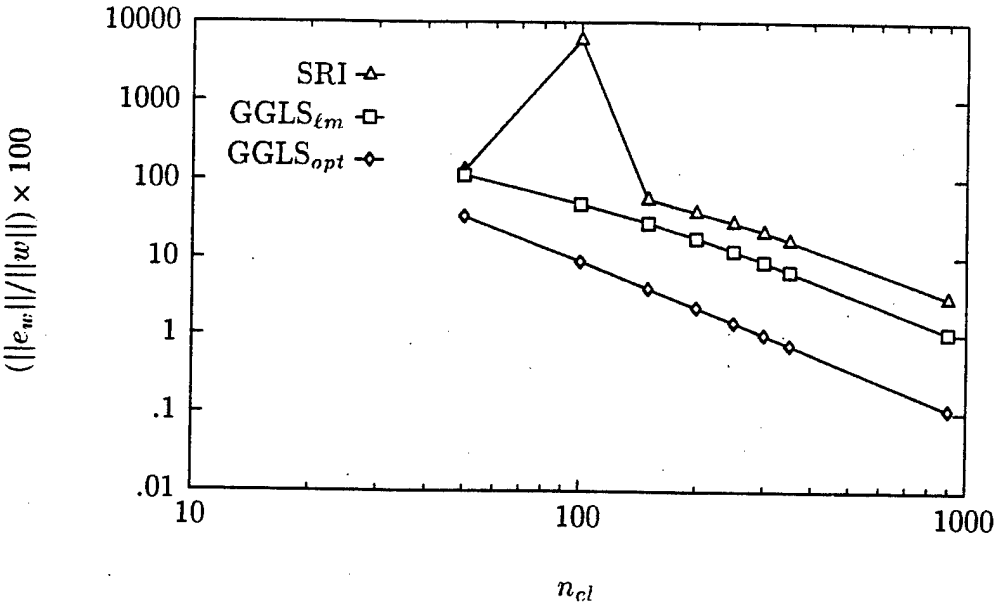

Figure 10.4: Normalized L_2 error (in percent) for the beam displacement of the model problem at $7550.0Hz$.

is frequency dependent.

Because the propagating solution dominates the beam response, the important scale for this problem is the normalized wave number, $k_{prop}h$, where k_{prop} is the real, propagating wave number. It is customary to consider the equivalent scale of elements per wavelength in quantifying discretization requirements. Note, if more than one scale is important, such as when a boundary layer is present, then multiple scales are required to quantify discretization requirements.

Table 10.1 summarizes numerical experience for uniform refinement of finite element approximations using the various finite element approaches discussed in this paper. These values represent the minimum number of elements required for adequate representation of the solution (roughly a 10–20 percent relative error).

Table 10.1: Discretization summary.

method	**minimum discretization**
GGLS$_{opt}$	4.5–5 elements/wavelength
GGLS$_{\ell m}$	12–15 elements/wavelength
SRI	24 elements/wavelength

10.4 Coupled Fluid-plate Differential Equations

In this section, new finite element methods for Reissner-Mindlin plates coupled to an acoustic fluid are developed using the GGLS framework. The new method combines the optimal GGLS parameters for the *in vacuo* beam, presented in the previous section, with a GLS method in the fluid. The superior accuracy characteristics of the new method are demonstrated using the complex wave-number dispersion analysis technique described in [51] as well as through numerical experiments.

First, the governing differential equations for the coupled system are briefly recounted. Let $\Omega \in \mathbb{R}^2$ represent the region which the acoustic fluid occupies and the curve Γ denote the fluid-structure interface and the parameterization of the mid-surface of the plate. The domain interior to Γ, i.e. $\mathbb{R}^2 \setminus \Omega$, is taken to be evacuated. Using the operator definitions for the structural variables from (10.1) , (i.e., the Timoshenko beam matrix differential operator), the coupled equations for the fluid-pressure, $p : \Omega \mapsto \mathbb{C}$ and the displacement $\mathbf{u} : \Gamma \mapsto \mathbb{C}^2$ including the effects of fluid loading are

$$\mathcal{L}_s \mathbf{u} = \mathbf{q} - \hat{\mathbf{n}}^s p \qquad \text{on } \Gamma \quad , \tag{10.38}$$

$$\mathcal{L}_f p = 0 \qquad \text{in } \Omega \quad , \tag{10.39}$$

where $\hat{\mathbf{n}}^s$ is the outward normal from the plate accounting for the rotational degree of freedom, $\mathcal{L}_f$ is the Helmholtz operator. The homogeneous Helmholtz equation is considered with the extension to the inhomogeneous case being straightforward. The fluid pressure is coupled to the structural displacement through the continuity of normal displacement boundary condition

$$\hat{\mathbf{n}} \cdot \nabla p = \rho_0 \omega^2 \hat{\mathbf{n}}^s \cdot \mathbf{u} \qquad \text{on } \Gamma \quad , \tag{10.40}$$

where $\hat{\mathbf{n}}$ is the outward normal from the plate. The fluid pressure must also satisfy radiation boundary conditions which we express in terms of the DtN condition on the truncation boundary, $\partial\mathcal{B}_R$, as

$$-Mp = p_{,n} \qquad \text{on } \partial\mathcal{B}_R \quad , \tag{10.41}$$

where M is the DtN operator appropriate to $\partial\mathcal{B}_R$ [41, 98] and $p_{,n}$ is the normal derivative of the pressure. As mentioned in Chapter 4, this is the exact boundary condition producing a problem that is equivalent to the original infinite domain problem. This boundary condition involves a infinite sum of harmonics. When implemented in practice, the sum is truncated and an approximate boundary condition results. The effect of the number of terms taken in the series on the accuracy and uniqueness of the formulation is discussed by Givoli [41, 98] and Harari [56, 58].

10.5 Variational Equations for the Coupled System

Next, the variational equations of the coupled system are given. The variational equations may be written as

$$a^s(\overline{\mathbf{u}}, \mathbf{u}) + (\overline{\mathbf{u}}, \hat{\mathbf{n}}p)_\Gamma = L^s(\overline{\mathbf{u}}) \quad , \tag{10.42}$$

$$a^f(\overline{p}, p) + (\overline{p}\hat{\mathbf{n}}^s, \rho_0\omega^2\mathbf{u})_\Gamma + (\overline{p}, Mp)_{\partial\mathcal{B}_R} = 0 \quad , \tag{10.43}$$

where $\overline{p}$ and $\overline{\mathbf{u}}^T = \{\overline{w} \;\; \overline{\theta}\}$ are the weighting functions. Any natural boundary conditions for p on Γ are enforced via essential boundary conditions on the normal displacement. The structural operator $a^s(\cdot,\cdot)$ is defined in (10.4)-(10.6). The operator $a^f(\cdot,\cdot)$ is

$$a^f(\overline{p}, p) := \int_\Omega [\nabla\overline{p} \cdot \nabla p - k_0^2\overline{p}p]\, d\Omega \quad . \tag{10.44}$$

The weak form of the problem is: Given $\mathbf{q}$, appropriate boundary conditions for $\mathbf{u}$ and p, find $(\mathbf{u}, p) \in \mathcal{S}_\mathbf{u} \times \mathcal{S}_p$ such that for all $(\overline{\mathbf{u}}, \overline{p}) \in \mathcal{V}_\mathbf{u} \times \mathcal{V}_p$ the variational equations, (10.42) and (10.43), are satisfied.

10.6 Galerkin/Generalized Least-squares Finite Element Formulations for Coupled Problems

In this section, the GGLS method for the fluid-loaded plate is presented. We will study methods with one least-squares operator each for the fluid and structural equations. Further, the GGLS$_{opt}$ method for the structural equations described earlier in this chapter is coupled to the GLS method of Harari and Hughes [56, 57] for the Helmholtz equation. The finite element interpolations of the displacement and pressure are $\mathbf{u}^h$ and p^h, respectively. Linear interpolation is used for the plate variables and bilinear interpolation is used for the acoustic pressure.

With these assumptions, the GGLS equations may be written as

$$A^s_{GGLS}(\overline{\mathbf{u}}^h, \mathbf{u}^h) + (\overline{\mathbf{u}}^h, \hat{\mathbf{n}}^s p^h)_\Gamma + (\mathbf{H}\mathcal{L}_s\overline{\mathbf{u}}^h, \mathbf{H}\hat{\mathbf{n}}^s p^h)_{\tilde{\Gamma}} = L^s(\overline{\mathbf{u}}^h) \quad , \tag{10.45}$$

$$A^f_{GLS}(\overline{p}^h, p^h) + (\overline{p}^h\hat{\mathbf{n}}, \rho_0\omega^2\mathbf{u}^h)_\Gamma + (\overline{p}^h, Mp^h)_{\partial\mathcal{B}_R} = 0 \quad , \tag{10.46}$$

where

$$A^f_{GLS} = a^f(\overline{p}^h, p^h) + (\mathcal{L}_f\overline{p}^h, \tau_f\mathcal{L}_f p^h)_{\tilde{\Omega}} \quad , \tag{10.47}$$

$$A^s_{GGLS}(\overline{\mathbf{u}}^h, \mathbf{u}^h) = a^s(\overline{\mathbf{u}}^h, \mathbf{u}) + (\mathbf{H}\mathcal{L}_s\overline{\mathbf{u}}^h, \mathbf{H}\mathcal{L}_s\mathbf{u}^h)_{\tilde{\Gamma}} \quad , \tag{10.48}$$

where $\mathbf{H}$ is the G∇LS matrix differential operator including the design parameters τ_1 and τ_2 see [50, 52]; τ_f is the GLS design parameter for the acoustic pressure. The τ_1 terms inherent to the GGLS$_{opt}$ method result in a new fluid-pressure coupling term, $(\mathbf{H}\mathcal{L}_s\overline{\mathbf{u}}^h, \mathbf{H}\hat{\mathbf{n}}^s p^h)_{\tilde{\Gamma}}$. This term adds an unsymmetric component to the formulation. This non-symmetry has implications when evaluating computational efficiency and storage requirements.

In choosing the design parameters for the coupled problem the τ's determined optimal for the uncoupled model problems are used. Therefore for the beam, the $GGLS_{opt}$ approach is used. The structural methodology is coupled consistently to the GLS formulation of Harari and Hughes [56, 57] for the Helmholtz equation, where they derive the τ_f which yields zero dispersion error for a one-dimensional acoustic medium. The value of τ_f is given in [57]. The accuracy of the new method arising from the consistent coupling of the GGLS plate and GLS fluid methods is studied.

10.7 Finite Element Dispersion Relations for the Fluid-loaded Plate

To study the accuracy of the new formulation, the model problem of the infinite fluid-loaded plate is used. This problem was studied in detail in [51] and discussed in [85], and we will here outline the manner in which these dispersion relations are derived. We use the finite element dispersion relations to determine the accuracy of the new design.

To obtain the finite element dispersion relations for the fluid-loaded Reissner-Mindlin plate, a uniform mesh in the fluid and structure is used, see Fig. 10.5. Just as for uncoupled systems, the assembly of the finite element matrix equations results in repetitive stencils for the fluid and structural variables.

Exponential solutions in the plate and fluid are assumed as follows,

$$w_n = w_0 e^{ik_x n\Delta x} = w_0 \mu_x^n \quad , \tag{10.49}$$

$$\theta_n = \theta_0 e^{ik_x n\Delta x} = \theta_0 \mu_x^n \quad , \tag{10.50}$$

$$p_{n,m} = p_0 e^{ik_x n\Delta x} e^{ik_y m\Delta y} = p_0 \mu_x^n \mu_y^m \quad , \tag{10.51}$$

where k_x and k_y are the wave numbers of the coupled system, n and m are the node indices (see Fig. 10.5); Δx and Δy are the interelement spacing in the x and y directions. Substitution of the assumed forms into the stencils yields a non-standard condition for the existence of allowed waves in the coupled system. By seeking non-zero solutions for the pressure amplitude, the non-standard condition is reduced to a standard determinantal condition from which the non-trivial solutions are calculated. For the details of these calculations see [51].

The allowed waves in the finite element mesh are to be compared to the analytic dispersion relations for the fluid-loaded Reissner-Mindlin plate which are quintic in k_x. For a description of the analytic dispersion relations see [25, 131, 132] for a detailed comparison of the analytic and finite element dispersion relations for the coupled system see [51].

We recount some of the important points regarding the k_x dependence of the wave numbers satisfying the dispersion relations. There are five branches of the dispersion relations. One is a purely real branch which is denoted as the subsonic loci (wave speed less than the acoustic wave speed). This wave number is most important as it corresponds to a flexural mode which dominates the surface displacement. The next most important branches are the two evanescent wave-number loci. The wave

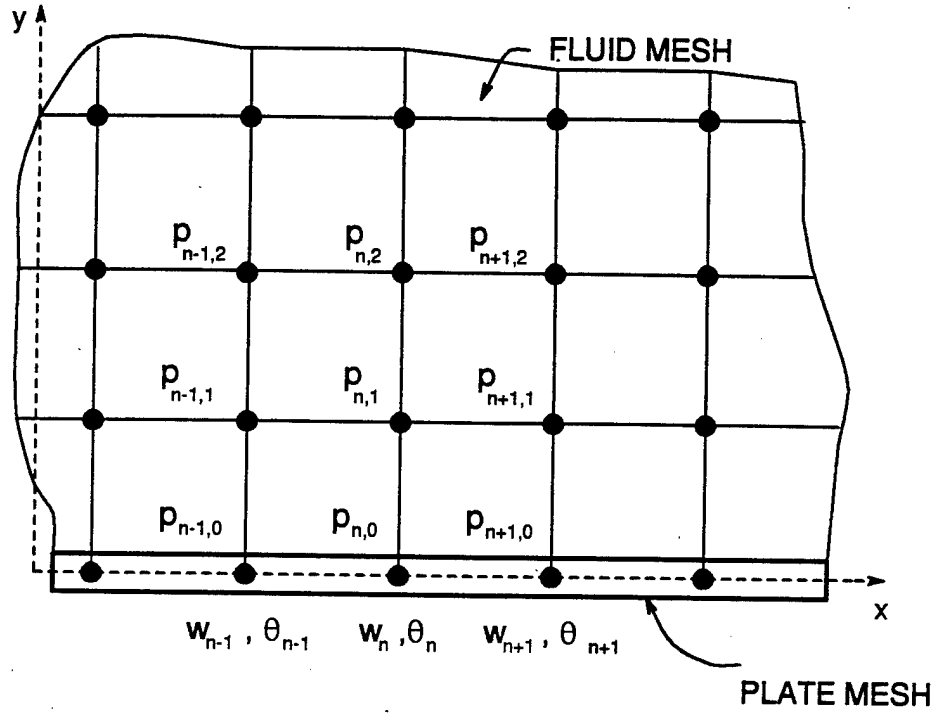

Figure 10.5: Mesh for the fluid-loaded plate.

numbers on these loci are complex conjugates of each other over the entire frequency range and consist a small real part and dominant decaying or imaginary part. The final two wave-number loci, whose relation to one another changes with frequency (although they exist as complex conjugates over much of the frequency range) are called the leaky wave-number loci. The k_x dependence of the leaky wave numbers, whose contribution is considered least important over the frequencies studied, is that of a predominantly real part with a relatively smaller imaginary part. The discussion of the importance of the various wave-number loci involves a discussion of branch cuts in the complex plane (see [25, 49, 51, 131]).

The qualitative similarity of the finite element dispersion relations to the analytic dispersion relations for the Galerkin and GGLS$_{opt}$-GLS formulation is excellent. We do not present these curves but rather move directly to quantitative error plots to demonstrate clearly the superior accuracy of the new methods with regard to dispersion error.

The phase and amplitude error of the k_x wave-number loci are presented. These plots are for steel plates in water; the plate material properties were described in Section 10.3, and for water we have taken $\rho_0 = 1.0gr/cm^3$ and $c_0 = 148100$ cm/s. The phase and amplitude error plots for the SRI plate element coupled to the Galerkin fluid approximation are shown in Fig. 10.6 and Fig. 10.7, respectively. For the new GGLS method, the phase error is shown in Fig. 10.8 and the amplitude error in Fig. 10.9. The GGLS error plots demonstrate the improvement obtained using the new approach. The error in the important subsonic wave-number loci remains below two percent over the entire frequency range. The evanescent wave-number branch is perfectly replicated up to the cut-off frequency for this branch in the k_y direction (which occurs at a value of π around $\omega h/c_0 = 2.7$ [51]). If we consider vertical branch cuts from $\pm k_0$ in the complex plane for the square roots in the analytic dispersion relation (see, e.g. [25]), the leaky wave-number root only enters the first Riemann sheet for $\omega h/c_0 > 1.0$. The wave numbers may only exist as free waves when on the first Riemann sheet. A particular wave number is only considered important when it may exist as a free wave. For these frequencies the accuracy of this branch, both phase and amplitude error of the leaky wave loci remains below three percent. The standard Galerkin approach has an error which increases with frequency and is greater than five percent over this frequency range.

The GGLS approach has a lower error than the standard Galerkin approach for every branch of the dispersion relation at frequencies where free waves are possible. This superior accuracy was attained by a consistent combination of optimal methods for the uncoupled systems. The complex wave-number dispersion analysis methodology developed in [51] enables an error estimate for the new method to be obtained in a general setting.

10.8 Fluid-loaded Plate Numerical Experiment

In this section, a two dimensional fluid-loaded plate problem is solved numerically. The results of the new formulation are compared to that of the standard Galerkin

approach. In Fig. 10.10, a schematic of four interconnected plates immersed in an infinite fluid is shown. The long side of the rectangular configuration is 6.0 cm while the short side is 1.0 cm. The plates are steel with a thickness of 0.15 cm. The plate material parameters are given in Section 10.3. The DtN boundary is at $R = 6.5$ cm. The forcing function for this problem is a unit point load (one dyne) in the vertical direction at $x = 3.0$ cm and $y = 0.0$ cm. The plate admits longitudinal motion as well as transverse displacement and rotation. The plates are rigidly connected with continuity of displacement and rotation conditions at the joints. Hence, the longitudinal force will excite both extensional and transverse waves in the plate system. Longitudinal motion has been added into the finite element model, although we have not discussed the implementation (for details see, e.g., [69]). Due to the symmetry of the loading, the solutions exhibit amplitude symmetry about the horizontal axis.

Results for the frequency $k_0 = 2.0$ cm^{-1} is presented. Different meshes were used to for comparing convergence and accuracy. The number of elements used in each mesh is given in Table 10.2. The meshes are used at both frequencies, and a typical mesh is shown in Fig. 10.11. These meshes are generated in the following manner. The circumferential spacing is uniform on the plate and on the DtN boundary with a radial line connecting the inner plate node to the DtN node. The radial spacing of the nodes along each line is uniform, except for the first four nodes in the fluid, whose spacing is half that of the other nodes. The finest mesh differs from the other three in that the DtN radius is truncated and the domain boundary is placed at $R = 4.0$ cm.

Table 10.2: Meshes for plate problem.

Mesh name	Circumferential elements	Total elements
coarse	56	1904
intermediate	140	4760
fine	224	9408
finest (truncated)	420	14280

Two methods are used to discretize the structure and fluid variables. One method is the standard Galerkin approach which consists of SRI elements for the transverse vibration of the plate, Galerkin elements for the longitudinal plate vibrations and acoustic fluid elements. The other method is the GGLS approach which consists of the $GGLS_{opt}$ method for the transverse plate vibrations and the GLS method for the longitudinal plate vibrations and the acoustic fluid elements. The use of GLS for one-dimensional and two-dimensional wave propagation is described in [56, 57].

10.8.1 Results for $k_0 = 2.0$ cm^{-1}

The pressure and displacement amplitudes of the fluid-loaded plate at $k_0 = 2.0$ cm^{-1} are studied. For the solutions obtained in this section, convergence is considered

attained when less than a five percent change in nodal amplitude occurs between meshes.

The pressure amplitude contours for the intermediate mesh GGLS approximation is shown in Fig. 10.12. A converged solution is attained by the intermediate mesh GGLS solution. In addition to convergence of the amplitude of the solution, the spatial variation of the pressure and displacement on the fluid-plate interface is examined. For the converged solution, the wavelength with which the amplitude varies is the same as the subsonic wavelength. The subsonic flexural wave dominates the response and the correspondence between the analytic and numeric results gives further confidence as to the accuracy of the approximation. The fine mesh Galerkin solution is shown in Fig. 10.13. The intermediate mesh Galerkin solution (not shown) bears a qualitative resemblance to the converged solution. However, the pressure amplitudes are four time greater than the converged solution. This large error is due to the poor phase accuracy of the SRI plate element giving rise to "numeric" or false resonance behavior as seen in the *in vacuo* plate finite element models. The fine mesh solution has an amplitude error of about fifty percent, similar to the error in the coarse mesh GGLS solution. Due to memory restrictions of the available computational platform, a converged Galerkin solution was not obtainable on the original domain using the uniform mesh. In order to approach the converged solution, a retracted DtN boundary was used to shrink the computational domain. This reduction in the size of the domain allowed for the additional refinement necessary to capture the solution.

These qualitative statements about the error can be made quantitative by examining the normal plate displacement and the DtN pressure amplitude for the two methods on the various meshes. The results for the normal plate displacement obtained through the GGLS method are shown in Fig. 10.14. The rapid convergence of the GGLS approach is seen as the intermediate mesh provides sufficient resolution to obtain the converged solution.

The results for the normal plate displacement obtained through the Galerkin approach are shown in Fig. 10.15. An increase in amplitude error with mesh refinement from the coarse to the intermediate mesh occurs. This is due to the poor phase accuracy of the Galerkin approach and this effect can also been seen in the full *in vacuo* beam results. From the intermediate mesh to the finest mesh, the finite element solution converges monotonically to the actual solution. Under the Galerkin approach, one must use the fine mesh (9408 elements) to exceed the accuracy of the coarse mesh GGLS solution (1904 elements). The finest mesh solution (using the truncated domain) for the Galerkin scheme achieves the converged result.

The pressure amplitude on the DtN boundary for GGLS solution and for the Galerkin solution contain similar information as to the magnitude of the amplitude errors. These results show the propagation of the amplitude errors of the normal displacement on the surface of the structure out to the farfield [49].

The GGLS approach achieves the converged result on the intermediate mesh while the truncated finest mesh is required for the Galerkin method to attain a similar but less accurate solution on the smaller domain. Next, storage and computational requirements of the application of the two methods on these two meshes are compared. Let n^s_{eqns} and n^u_{eqns} denote the number of equations required for satisfactory accuracy

to be achieved by the symmetric Galerkin and the unsymmetric GGLS approaches respectively. Noting that each plate node has three degrees of freedom, we have for the finest mesh $n^s_{eqns} = 15120$ and for the intermediate mesh $n^u_{eqns} = 5040$. Let b_s and b_u denote the mean half bandwidth of the meshes for the symmetric Galerkin and unsymmetric GGLS solution schemes respectively. Note also that for the unsymmetric method, the upper and lower bandwidths are the same. For this frequency, $b_s = 400$ (finest mesh) and $b_u = 136$ (intermediate mesh). The storage requirement for the symmetric method is $b_s n^s_{eqns}$ and for the unsymmetric formulation $2b_u n^u_{eqns}$; the ratio of the storage requirement for the Galerkin approach to that for the GGLS approach is 4.4. Considering asymptotic estimates of floating point operation counts (flops) for direct solution of the matrix equations, the number of flops for the symmetric band solver is approximately $n^s_{eqns}(b_s^2 + 3b_s)$ and for the unsymmetric band solver $2n^u_{eqns}b_u^2$ [45]. The ratio of the flop estimates for the direct solution of the equations resulting from the Galerkin approach to that for the GGLS approach is 13.0. Hence, significant storage and computational gains are achieved by the GGLS approach. A mesh similar to the finest mesh used on the full domain would correspond to more than 25,000 elements and in that case the indicated advantage of the GGLS approach over the Galerkin solution scheme would be even greater. Note, any added cost of calculating the design parameters for the GLS and GGLS methods has been neglected in the analysis; these would be proportional to the number of total elements if all elements were of different size. Reduction in the amount of calculations needed for the design parameters is achieved when elements have the same characteristic size.

By using the GGLS approach for this problem, we were able to obtain the solution on the original domain. In addition to a reduction in the storage requirements, the amount of computational effort is also reduced using the GGLS approach. The benefits gained from the GGLS method increase with frequency, as the correction from the least-squares addition becomes more important.

Remarks:

1. The unsymmetric component of the GGLS method only enters on the fluid-structure interface, other than this the method is completely symmetric. Advantage may be made of this fact to easily reduce the storage requirements from $2b_u n^u_{eqns}$ to $b_u n^u_{eqns} + n_{fsi} b_u$, where n_{fsi} is the number of nodes on the fluid-structure interface.

2. In the numerical study undertaken, a very regular mesh was used. The only refinement of the mesh to the anticipated solution was that smaller elements were used close to the structure, to capture the subsonic field. Much of the circumferential refinement of the uniform mesh necessary to resolve the solution was needed primarily on the fluid-structure interface and such refinement was not as important on the DtN boundary. As the subsonic waves propagate through the fluid, a filtering effect occurs, smoothing the solution greatly. A re-meshing strategy that truly adapts to the character of the solution would yield great significant benefits, for it is the reduction of the number of elements on the DtN boundary where the greatest decrease in profile could be achieved.

A successful refinement scheme would locate a greater density of elements near surface of the structure and fewer elements at the DtN boundary. Such a refinement scheme would yield a reduction in storage and computation for both the Galerkin and GGLS schemes see Chapter 9.

3. The exterior structural acoustics problem was studied here. The manner in which the GGLS method was designed, by using model uncoupled problems to obtain the design parameters, did not prejudice the methodology toward either the interior or exterior problem. Hence, it is anticipated that this new method would yield substantial accuracy enhancement for the interior problem as well as the already demonstrated superiority for the exterior problem.

10.9 Future Work

An area of future research is the application of GGLS techniques to finite element models for Reissner-Mindlin plates for arbitrary quadrilateral geometry. One approach might be to combine GLS and G∇LS methods to achieve this result. Application of GGLS methods to mixed plate elements that have no shear locking or spurious modes (such as the Hughes and Tezduyar [80] or the Bathe and Dvorkin [13] approaches) to enhance the accuracy of these elements with regard to dynamics is currently under study. Also interesting would be the examination of the effect of nonuniform meshes on the accuracy of GGLS. GGLS methods may be applied to geometrically axisymmetric and general shell configurations to enhance the accuracy and this too is of great interest.

Finally, an important area of future work is the development rigorous proofs for the convergence of these methods. For statics, it would be valuable to show the dependence of the convergence of these methods on the element size to thickness ratio just as Arnold [7] has done for the Galerkin approximation for the Timoshenko beam.

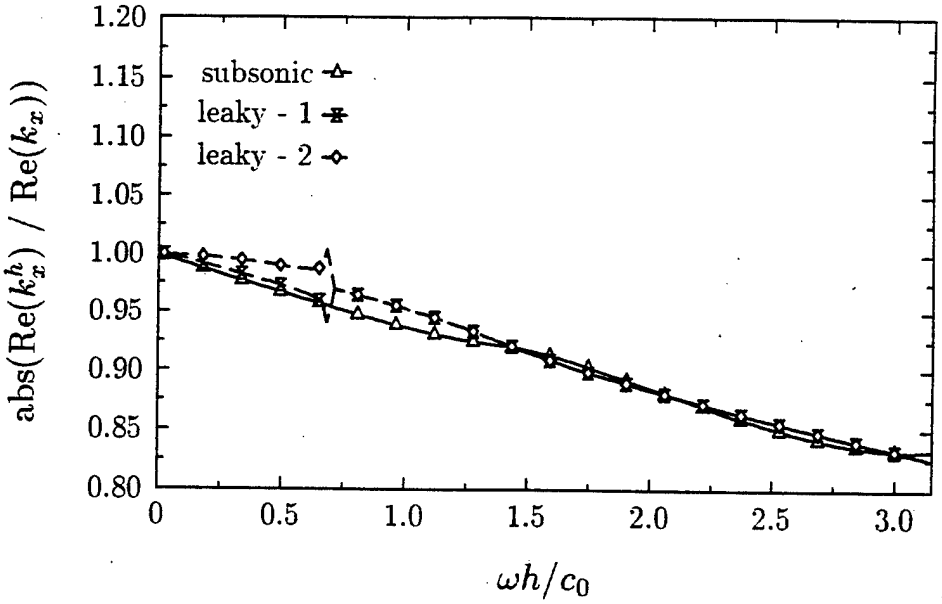

Figure 10.6: Phase error for the real components of k_x wave numbers for a fluid-loaded plate. Finite elements: SRI for the plate and Galerkin for the fluid. Steel plate in water, h/t = 1.0.

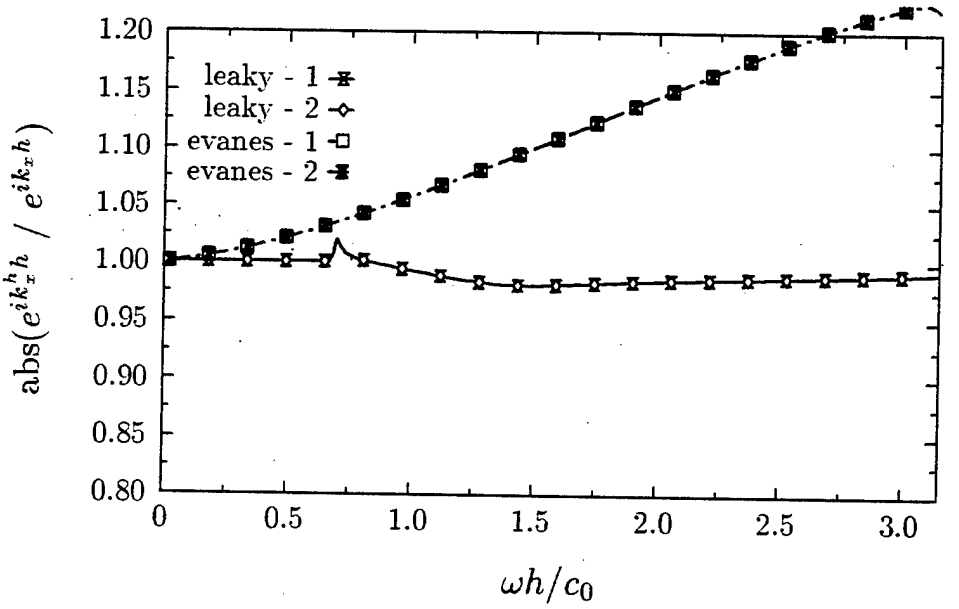

Figure 10.7: Amplitude error for the real components of k_x for a fluid-loaded plate. Finite elements: SRI for the plate and Galerkin in the fluid. Steel plate in water, h/t = 1.0.

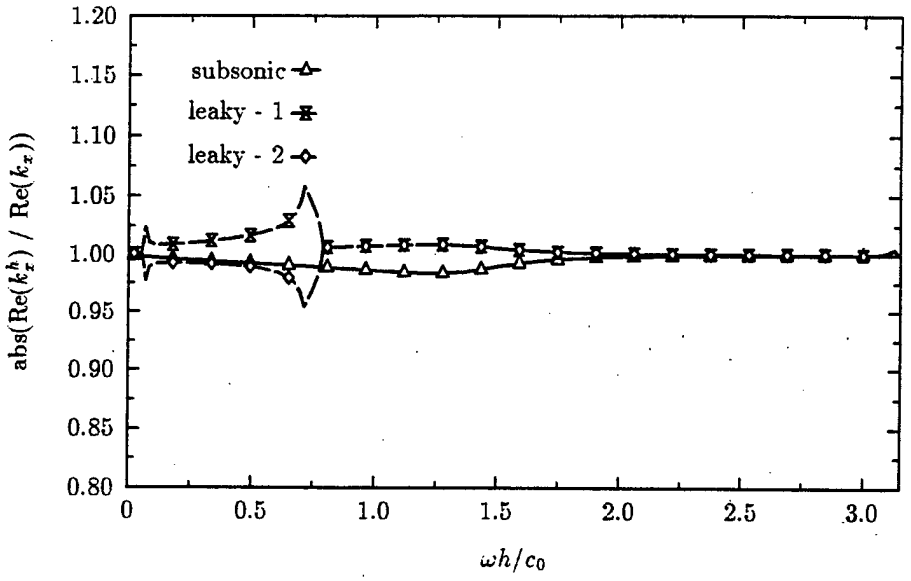

Figure 10.8: Phase error for the real components of k_x wave numbers for a fluid-loaded plate. Finite elements: $GGLS_{opt}$ for the plate and GLS in the fluid. Steel plate in water, h/t = 1.0.

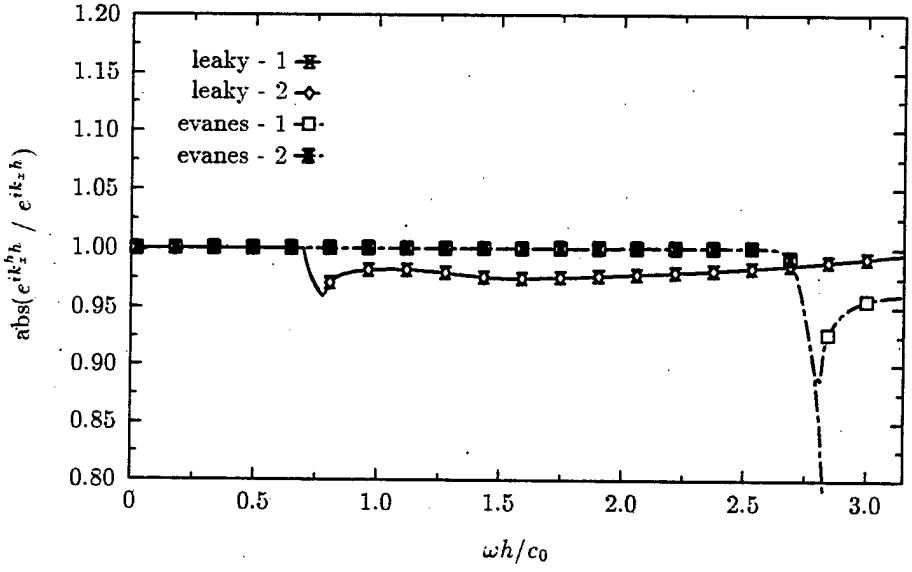

Figure 10.9: Phase error for the real components of k_x wave numbers for a fluid-loaded plate. Finite elements: $GGLS_{opt}$ for the plate and GLS in the fluid. Steel plate in water, h/t = 1.0.

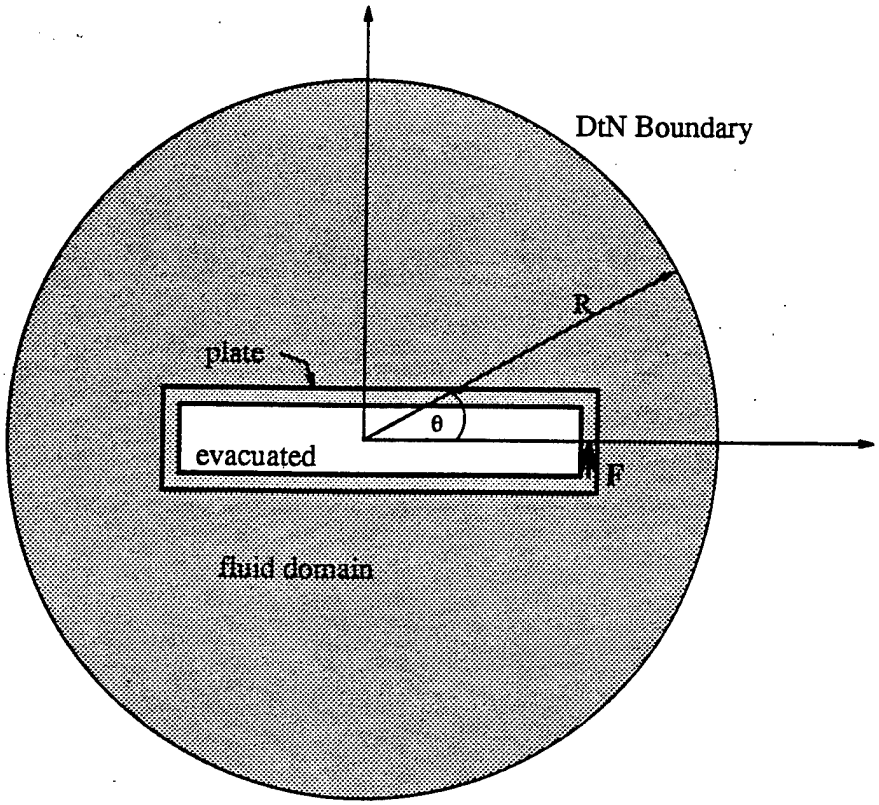

Figure 10.10: Schematic of four plate problem.

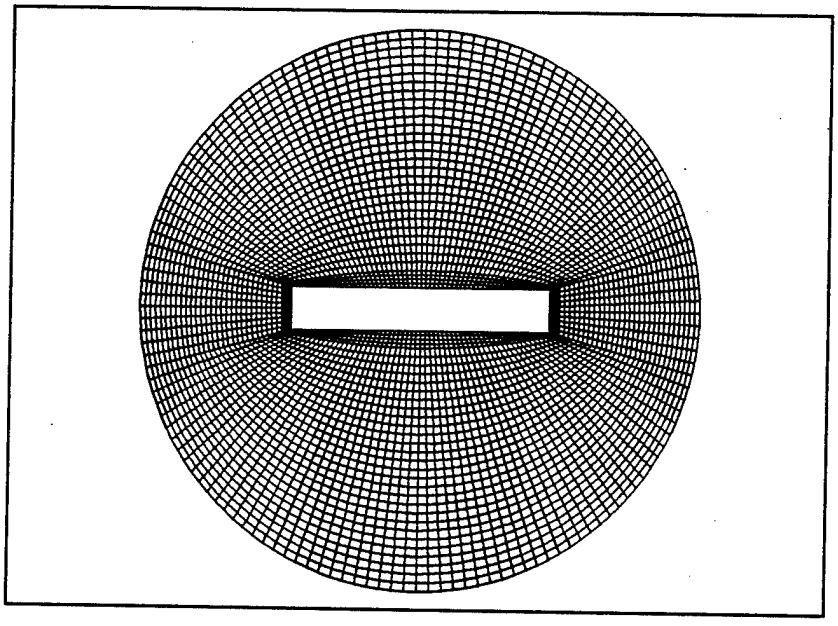

Figure 10.11: Intermediate mesh.

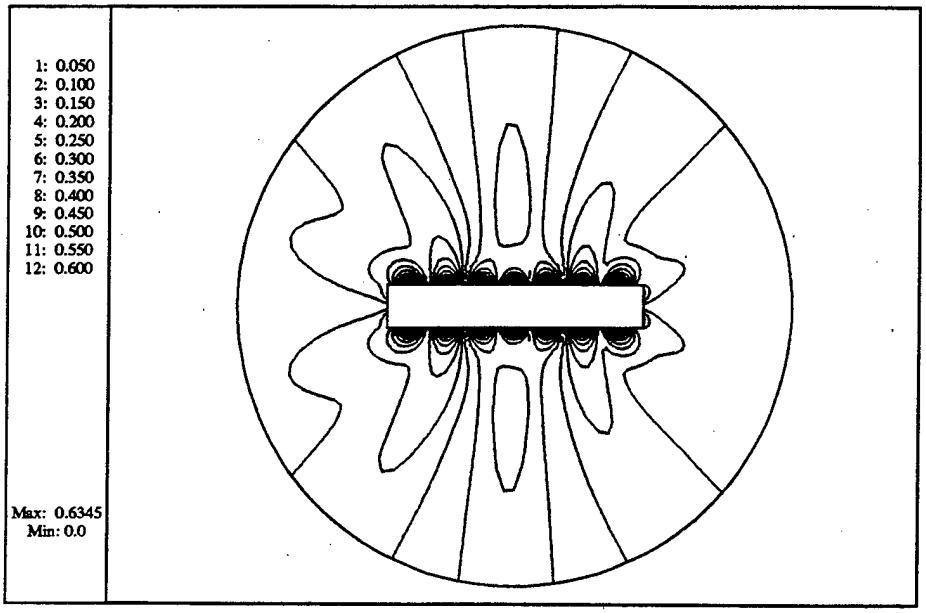

Figure 10.12: Pressure amplitude contours results for GGLS finite element method, intermediate mesh $k_0 = 2.0\ cm^{-1}$.

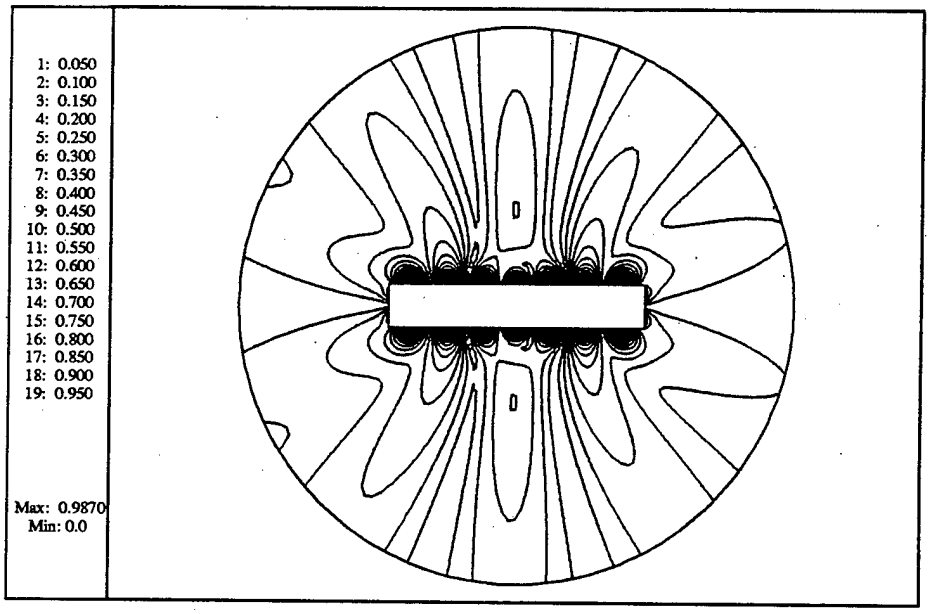

Figure 10.13: Pressure amplitude contours results for Galerkin finite element method, fine mesh, $k_0 = 2.0\ cm^{-1}$.

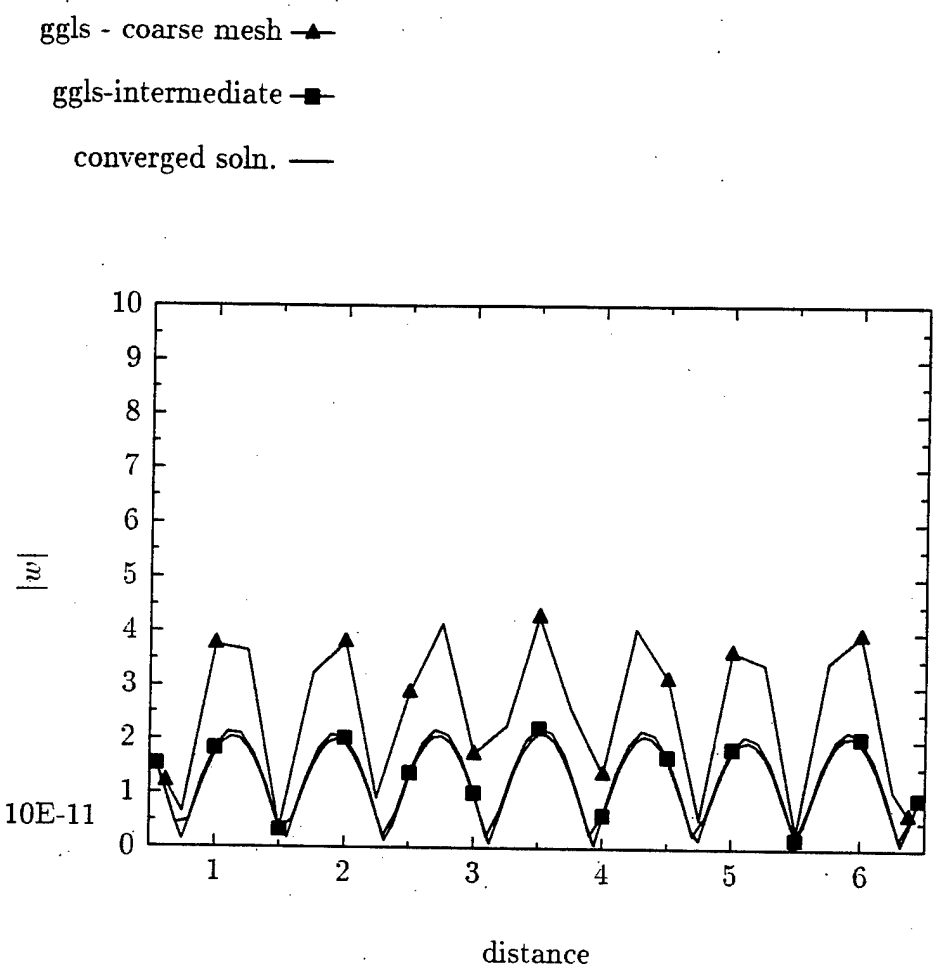

Figure 10.14: Amplitude of the normal displacement on the upper plate for GGLS finite element method, $k_0 = 2.0\ cm^{-1}$.

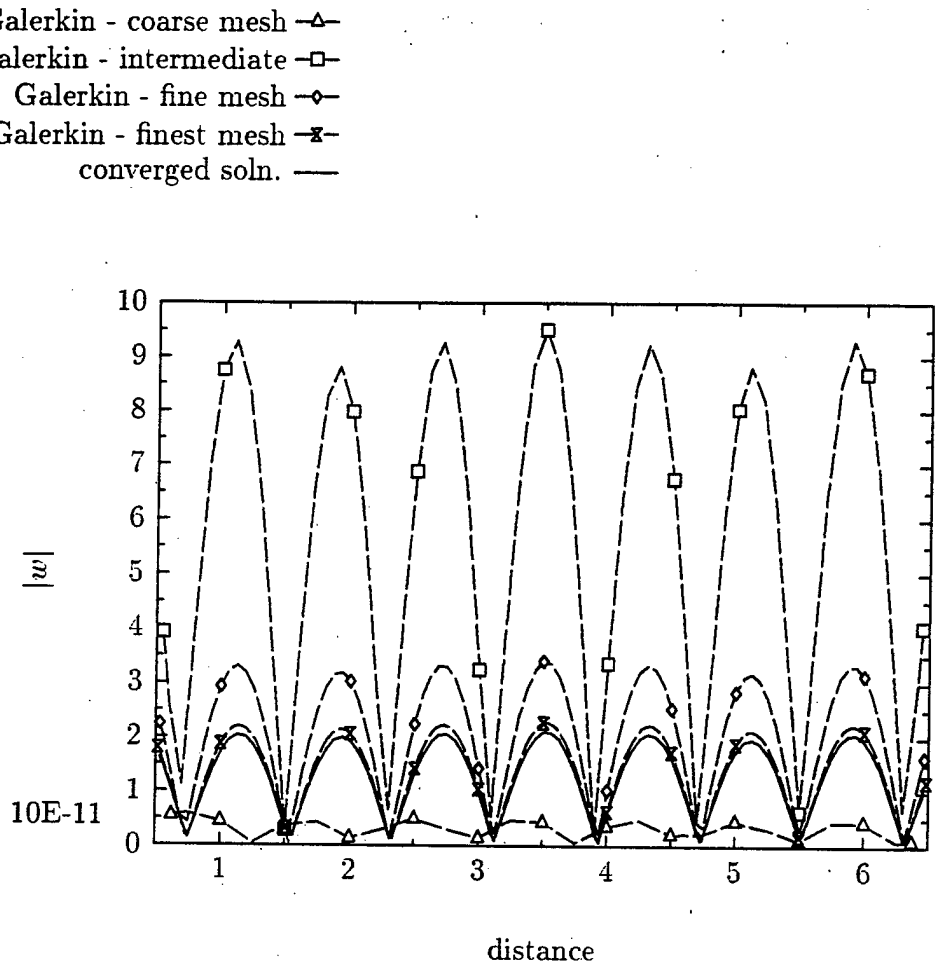

Figure 10.15: Amplitude of the normal displacement on the upper plate for Galerkin finite element method, $k_0 = 2.0\ cm^{-1}$.

Chapter 11

Space-time Finite Element Methods for Transient Structural Acoustics

The design of new space-time finite element formulations for solution of the transient structural acoustics problem in exterior domains are presented. The development and results presented in this chapter are drawn from [143, 146, 148, 149, 150, 151]. The formulation is based on a time-discontinuous Galerkin Least-Squares variational equation for both the structure and the acoustic fluid together with their interaction. The result is an algorithm for time-dependent wave propagation with the desired combination of good stability and high accuracy. The method is especially useful for the application of hierarchical hp-adaptive solution strategies for unstructured space-time meshes. The formulation employs a finite computational fluid domain surrounding the structure and incorporates exact time-dependent non-reflecting (radiation) boundary conditions on the fluid truncation boundary. New time-dependent non-reflecting boundary conditions for the acoustic wave equation are developed based on the exact impedance relation through the Dirichlet-to-Neumann (DtN) map in the frequency domain. Time-dependent counterparts are obtained through an inverse Fourier transform procedure. Optimal stability estimates and convergence rates are reported together with a discussion of the positive form of the resulting space-time matrix equations. Representative numerical examples involving transient radiation achieved by the new method for structural acoustics.

11.1 Introduction

This chapter is concerned with the design of new computational methods for transient structural acoustics. The methods are discussed in greater detail in [143, 146, 148, 149, 150, 151]. The solution method is based on a new space-time Galerkin/Least-squares variational formulation for structural acoustics which utilizes discontinuous in time shape functions. Important attributes of the time-discontinuous technology for transient structural acoustics include a natural framework for; (i) the application of self-adaptive solution strategies for unstructured space-time finite element discretiza-

tions, (*ii*) the implementation of high-order accurate time-dependent non-reflecting boundary conditions, and (*iii*) high-order accurate and unconditionally stable solution algorithms.

For linear problems characterized by a relatively small range of frequencies, a transient solution may be obtained indirectly through a sequence of time-harmonic solutions in the frequency domain followed by an inverse Fourier transform. Considerable progress has been made in the development of numerical methods for the time-harmonic exterior structural acoustics problem (see previous chapters). Still, a direct time-domain approach to solution of transient problems is necessary whenever nonlinearities occur and may be advantageous for some classes of linear problems including real-time dynamic control and optimization. For example, in problems characterized by broad frequency spectra, such as short pulse wave propagation, the indirect approach may not be computationally feasible since it requires a large number of solutions in the frequency domain for any reasonably accurate sweep of the problem band width. Previous direct time-domain approaches to the transient structural acoustics problem involving the interaction of vibrating structures submerged in an infinite acoustic fluid have employed (i) boundary element methods based on Kirchhoff's retarded potential integral formulation [68, 109, 111, 112, 115], (ii) Taylor-Galerkin methods, e.g. [128] and (iii) semi-discrete methods which employ standard Galerkin finite element methods in space and finite difference techniques for integrating in time (also referred to as the method of lines), see e.g. [124, 125, 126]. However it is well known that these standard methods are not optimal for general transient wave propagation problems; especially those involving sharp gradients in the solution arising in the complex radiation and scattering fields in the vicinity of fluid-structure interfaces and near inhomogeneities such as stiffeners and structural joints.

Boundary element methods based on the direct time integration of Kirchhoff's retarded potential boundary integral suffer from unsymmetric and dense matrices and, more importantly, can be extremely memory intensive due to the convolution in time required by the time-dependent free-space Green's function used in the kernel of the boundary integral. When used for medium to long time calculations, the boundary integral approach requires storage of a large pool of historical data during the solution process that can quickly become prohibitive when solving large-scale fluid-structure interaction problems. Semi-discrete finite element methods developed within the context of structural dynamics e.g. the Newmark [116] and Hilber, Hughes, and Taylor [66] algorithms will generally not adequately capture all the important solution features appearing in physically realistic transient structural acoustics applications. Other difficulties include the incorporation of high-order accurate absorbing boundary conditions and truly self-adaptive schemes in a semidiscrete finite element formulation for transient wave propagation in infinite domains.

Motivated by the success of Galerkin/Least-squares stabilization methods for the time-harmonic problem [60, 152], it is natural to extend these ideas to the transient problem through a direct time-domain approach. The solution methods described in this chapter and [143, 148, 146, 149, 150, 151] are based on a new space-time Galerkin/Least-squares finite element formulation for structural acoustics which utilizes discontinuous in time shape functions. The proposed method employs the si-

multaneous discretization of the spatial and temporal domains and is based on a new time-discontinuous variational formulation for the coupled fluid/structure system. The discontinuous Galerkin method in time was first introduced by Lesaint and Raviart [106] in the context of neutron transport. In this approach, the concept of space-time slabs is employed which allow for discretizations that are discontinuous in time and offers great flexibility in the discretization; in particular through the possibility of using space-time meshes oriented in along space-time characteristics. The resulting space-time algorithm gives a general solution to the fundamental problem of constructing a finite element method for transient structural acoustics with the desired combination of good stability and high accuracy. Stability is obtained through the introduction of temporal jump operators which give rise to a natural high-frequency dissipation required for the accurate resolution of sharp gradients in the physical solution. Additional stability is obtained by a least-squares modification which guarantees maximum norm stability, consistency, error localization and accurate shock resolution. The order of accuracy of the solution is related to the order of the finite element spatial and temporal basis functions, and can be specified to any accuracy and for general unstructured discretizations in space and time.

In addition to the advantages cited above, the space-time finite element approach provides a powerful framework for unified and simultaneous spatial and temporal adaptivity of the discretization. This is especially useful in the application of self-adaptive solution strategies for transient structural acoustics, in which both spatial and temporal enhancement can efficiently capture waves propagating along space-time characteristics. Furthermore the use of space-time hp-adaptive discretization strategies, where a combination of mesh size refinement/unrefinement (h-adaptivity), and finite element basis enrichment (p-adaptivity), can easily be accommodated in the time-discontinuous formulation. Because the temporal and spatial domains are treated in a consistent manner in the space-time variational equations, the method gives rise to a firm mathematical foundation from which rigorous *a posteriori* error estimates useful for reliable and efficient adaptive schemes may be established, see e.g. [28, 55, 89, 91].

Discontinuous Galerkin (DG) space-time methods with residual based stabilization such as Galerkin/Least-squares (GLS) methods; also referred to as the Streamline Diffusion (SD) or Streamline Upwind Petrov-Galerkin (SUPG) methods in the context of fluid flows, have successfully been applied to first-order hyperbolic systems of partial differential equations by Johnson, Hughes and colleagues, see e.g. [70, 88, 93], and are now widely used in many applications arising in computational fluid dynamics (CFD), including problems governed by the compressible Euler and Navier-Stokes equations [64, 134, 136], advection-diffusion problems [76], and large-eddy and turbulence modeling [84].

Classical linear structural acoustics equations can be converted to first-order hyperbolic form and these methods are thus immediately applicable. However, in this approach, the coupled state vector consists of structural displacements, velocities and stresses, as well as acoustic pressure and velocity components, which is computationally uneconomical. Recently, Hughes and Hulbert [77, 81, 82] have successfully extended the time-discontinuous Galerkin space-time method to second-order hyper-

bolic equations in the context of transient elastodynamics. Based on the success of the time-discontinuous method for elastodynamics, it is desirable to extend this technology to the coupled structural acoustics problem involving the second-order wave equation governing acoustics and the equations of elastodynamics for the structure. For the coupled equations, scalar velocity potential is chosen as the solution variable for the acoustic fluid, while the displacement vector is used for the structure. As a consequence of this choice of variables, the coupled variational equations give rise to a positive matrix form, which in the context of the space-time finite element formulation, allows for the proof of the unconditionally stability and convergence of the method.

For time-harmonic analysis it is possible to obtain an exact non-reflecting boundary condition on a separable truncation boundary through the Dirichlet-to-Neumann (DtN) map [98], in the frequency domain. Motivated by the good stability and accuracy properties of the DtN map in the frequency domain it is natural to attempt to extend these ideas to the time-domain. A direct time-dependent counterpart to the DtN map can be obtained through a convolution integral in time, resulting in a boundary condition that is non-local in both space and time dimensions. Unfortunately, while this condition is stable and exact for solutions consisting of the first N wave harmonics by design, the implementation requires storage of all previous solutions up to the current time step, and is not feasible for large-scale computations.

A time-dependent counterpart to the DtN map which retains the property of being exact for the first N wave harmonics on the truncation boundary has been derived in Thompson and Pinsky [143, 146, 150] by replacing the temporal convolution integral with local temporal derivatives. Two alternative sequences of time-dependent non-reflecting boundary conditions starting from the DtN map in the frequency domain have been obtained; the first involves both time and spatial derivatives (local in time and local in space version), and the second involves time derivatives while retaining a spatial integral (local in time and nonlocal in space version).

As the order of these and other non-reflecting boundary conditions increases they become increasingly difficult to implement in a semidiscrete setting due to the occurrence of high-order time derivatives on the fluid truncation boundary. It is shown that the time-discontinuous Galerkin space-time method provides a natural variational setting for the incorporation of high-order accurate, local in time non-reflecting boundary conditions by allowing for the use of standard C^0 continuous finite element interpolations in time.

11.2 The Transient Structural Acoustics Problem

Consider the coupled system illustrated in Figure 11.1, consisting of the computational domain $\Omega = \Omega_f \cup \Omega_s$, composed of a fluid domain Ω_f, and structural domain Ω_s. The fluid boundary $\partial\Omega_f$, is divided into the fluid-structure interface boundary Γ_i, and the artificial boundary Γ_∞. The structural boundary $\partial\Omega_s$, is composed of the fluid-structure interface boundary Γ_i and a traction boundary Γ_σ. The infinite

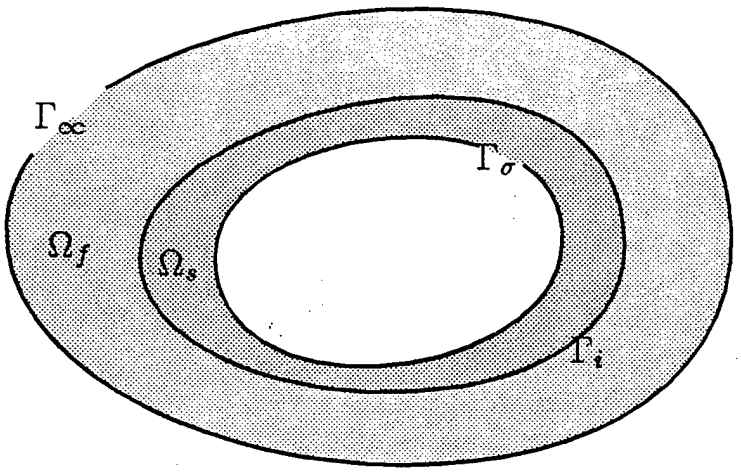

Figure 11.1: Coupled system for the exterior fluid-structure interaction problem, with artificial boundary Γ_∞ enclosing the finite computational domain $\Omega = \Omega_f \cup \Omega_s$.

domain outside the artificial boundary is denoted by Ω_∞. The temporal interval of interest is $I =]0, T[$ and the number of spatial dimensions is d.

The structure is governed by the equations of elastodynamics while the fluid equations are derived under the usual linear acoustic assumptions of an inviscid, compressible fluid with small disturbance. The strong form of the fluid-structure initial boundary-value problem is given by:

Find $\boldsymbol{u} : \bar{\Omega}_s \times [0,T] \mapsto \mathbf{R}^d$, *and* $\phi : \bar{\Omega}_f \times [0,T] \mapsto \mathbf{R}^1$, *such that*

$$\nabla \cdot \boldsymbol{\sigma} - \rho_s \ddot{\boldsymbol{u}} = \mathbf{0} \quad \text{in } Q_s \equiv \Omega_s \times I \tag{11.1}$$

$$\boldsymbol{\sigma} = \boldsymbol{C} : \nabla^s \boldsymbol{u} \quad \text{in } Q_s \equiv \Omega_s \times I \tag{11.2}$$

$$\nabla^2 \phi - a^2 \ddot{\phi} = f \quad \text{in } Q_f \equiv \Omega_f \times I \tag{11.3}$$

$$\dot{\boldsymbol{u}} \cdot \boldsymbol{n} = \nabla \phi \cdot \boldsymbol{n} \quad \text{on } \Upsilon_i \equiv \Gamma_i \times I \tag{11.4}$$

$$\boldsymbol{\sigma} \cdot \boldsymbol{n} = \rho_f \dot{\phi} \boldsymbol{n} \quad \text{on } \Upsilon_i \equiv \Gamma_i \times I \tag{11.5}$$

$$\boldsymbol{\sigma} \cdot \boldsymbol{n} = \bar{\boldsymbol{t}} \quad \text{on } \Upsilon_\sigma \equiv \Gamma_\sigma \times I \tag{11.6}$$

$$\nabla \phi \cdot \boldsymbol{n} = -\mathbf{S}_m \phi \quad \text{on } \Upsilon_\infty \equiv \Gamma_\infty \times I \tag{11.7}$$

In the above, $\boldsymbol{u}(\boldsymbol{x}, t)$ with $\boldsymbol{x} \in \Omega_s$, is the structural displacement vector, $\boldsymbol{\sigma}$ is the symmetric Cauchy stress tensor, and $\phi(\boldsymbol{x}, t)$ with $\boldsymbol{x} \in \Omega_f$, is the scalar acoustic velocity potential. The phase velocity of acoustic wave propagation is denoted by $c > 0$, with slowness $a = c^{-1}$ and $\rho_s > 0$ and $\rho_f > 0$ are the reference densities of the structure and fluid respectively. The acoustic source loading is given by f and the prescribed traction on the structure is $\bar{\boldsymbol{t}}$. A superposed dot indicates partial differentiation with respect to time t, and ∇^s refers to the symmetric gradient. The acoustic pressure, p, and the acoustic velocity, $\boldsymbol{v}$, are related to the velocity potential by $p = -\rho_f \dot{\phi}$ and $\boldsymbol{v} = \nabla \phi$.

As a consequence of the above coupled second-order system of hyperbolic equa-

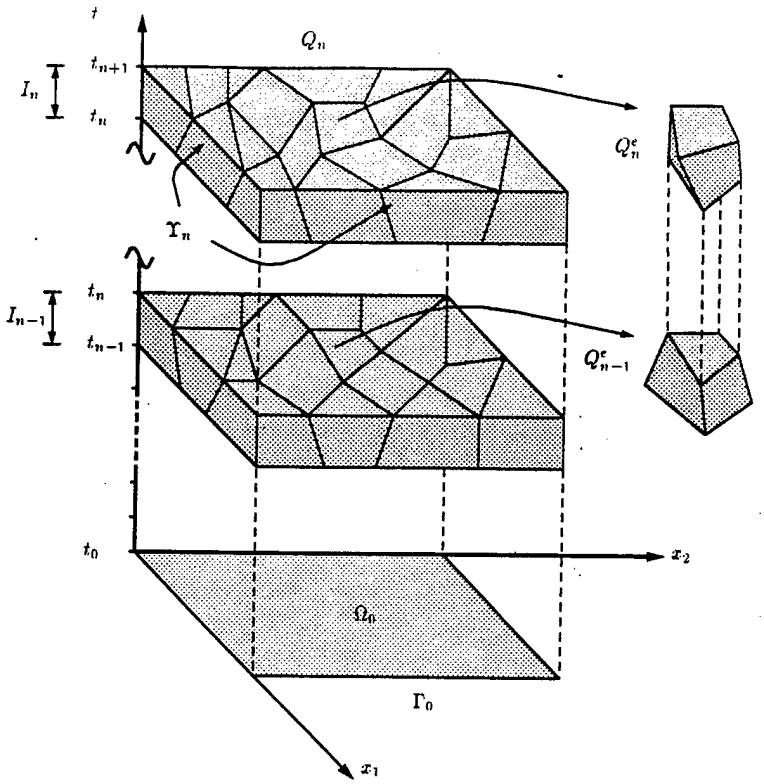

Figure 11.2: Illustration of two consecutive space-time slabs with unstructured finite element meshes in space-time.

tions, we have the initial conditions,

$$\boldsymbol{u}(\boldsymbol{x},0) = \boldsymbol{u}_0(\boldsymbol{x}) \; ; \qquad \dot{\boldsymbol{u}}(\boldsymbol{x},0) = \dot{\boldsymbol{u}}_0(\boldsymbol{x}) \qquad \boldsymbol{x} \in \Omega_s \qquad (11.8)$$

$$\phi(\boldsymbol{x},0) = \phi_0(\boldsymbol{x}) \; ; \qquad \dot{\phi}(\boldsymbol{x},0) = \dot{\phi}_0(\boldsymbol{x}) \qquad \boldsymbol{x} \in \Omega_f \qquad (11.9)$$

Equation (11.1) governs the linear momentum balance of the structure, while (11.2) is the constitutive relationship written here for linear elasticity. Equation (11.3) is the acoustic scalar wave equation, Equation (11.4) is the normal velocity compatibility condition across the fluid-structure interface, and (11.5) represents the fluid pressure acting on the structure. Equation (11.6) is the applied traction. Equation (11.7) is the radiation boundary condition imposed on the artificial boundary Γ_∞ which approximates the asymptotic behavior of the solution at infinity, as described by the Sommerfeld radiation condition, which asserts that at infinity all waves are outgoing. The specific definition of the operator $\mathbf{S}_m$ relating Dirichlet to Neumann data on the boundary is described in Section 11.5.

11.3 Space-time Finite Element Formulation

The development of the space-time method proceeds by considering a partition of the time interval, $I =]0, T[$, of the form: $0 = t_0 < t_1 < \ldots < t_N = T$, with $I_n =]t_n, t_{n+1}[$. Using this notation, $Q_n^s = \Omega_s \times I_n$, and $Q_n^f = \Omega_f \times I_n$ are the nth space-time slabs for the structure and fluid respectively. For the nth space-time slab, the spatial domain

is subdivided into $(n_{el})_n$ elements. and the interior of the e^{th} element is defined as Q_n^e. Figure 11.2 shows an illustration of two consecutive space-time slabs Q_{n-1} and Q_n for the fluid where the superscript is omitted for clarity.

Within each space-time element, the trial solution and weighting function are approximated by pth-order polynomials in $\boldsymbol{x}$ and t. These functions are assumed $C^0(Q_n)$ continuous throughout each space-time slab, but are allowed to be discontinuous across the interfaces of the slabs. This feature of the time-discontinuous method, allows for the general use of high-order elements and spectral-type interpolations in both space and time. The collections of finite element interpolation functions are given by the spaces,

Trial structural displacements

$$\mathcal{S}^h = \bigcup_{n=0}^{N-1} \mathcal{S}_n^h, \qquad \mathcal{S}_n^h = \left\{ \boldsymbol{u}^h(\boldsymbol{x},t) \middle| \boldsymbol{u}^h \in (C^0(Q_n^s))^d \,,\, \boldsymbol{u}^h\big|_{Q_n^{se}} \in (\mathcal{P}^p(Q_n^{se}))^d \right\}$$

Trial fluid potential

$$\mathcal{T}^h = \bigcup_{n=0}^{N-1} \mathcal{T}_n^h, \qquad \mathcal{T}_n^h = \left\{ \phi^h(\boldsymbol{x},t) \middle| \phi^h \in C^0(Q_n^f) \,,\, \phi^h\big|_{Q_n^{fe}} \in \mathcal{P}^p(Q_n^{fe}) \right\}$$

where $\mathcal{P}^p$ denotes the space of pth-order polynomials and C^0 denotes the space of continuous functions. For clarity, prescribed displacements and velocity potential boundary conditions were not defined, i.e. only natural boundary conditions are given. As a result the trial function spaces and weighting spaces are identical, i.e. $\mathcal{S}^h = \mathcal{V}^h$ and $\mathcal{T}^h = \mathcal{W}^h$.

Before stating the space-time variational equations, it is useful to introduce the following notation.

$$\begin{aligned}
(\boldsymbol{w}^h \,,\, \boldsymbol{u}^h)_{\Omega_s} &= \int_{\Omega_s} \boldsymbol{w}^h \cdot \boldsymbol{u}^h \, d\Omega \\
a(\boldsymbol{w}^h \,,\, \boldsymbol{u}^h)_{\Omega_s} &= \int_{\Omega_s} \nabla \boldsymbol{w}^h \cdot \boldsymbol{\sigma}(\nabla \boldsymbol{u}^h) \, d\Omega \\
(w^h \,,\, \phi^h)_{\Omega_f} &= \int_{\Omega_f} w^h \, \phi^h \, d\Omega \\
(w^h \,,\, \phi^h)_{\Gamma} &= \int_{\Gamma} w^h \, \phi^h \, d\Gamma \\
(w^h \,,\, \phi^h)_{Q_n} &= \int_{t_n}^{t_{n+1}} (w^h \,,\, \phi^h)_{\Omega} \, dt
\end{aligned}$$

The meaning of other similar terms may be inferred from these.

11.4 New Space-time Variational Equations

The space-time variational formulation is obtained from a weighted residual of the governing equations and incorporates time-discontinuous jump terms. The specific

form of this new formulation is designed such that unconditional stability for arbitrary space-time finite element discretizations can be proved through a functional analysis of the method. The time-discontinuous Galerkin formulation can be stated formally as:

Within each space-time slab, $n = 0, 1, ..., N-1$; Find $(\boldsymbol{u}^h, \phi^h) \in \mathcal{S}_n^h \times \mathcal{T}_n^h$, such that $\forall (\boldsymbol{w}^h, w^h) \in \mathcal{V}_n^h \times \mathcal{W}^h$, the following coupled variational equations are satisfied,

$$G_s(\boldsymbol{w}^h, \boldsymbol{u}^h, \phi^h)_n = 0 \tag{11.10}$$

$$G_f(w^h, \boldsymbol{u}^h, \phi^h)_n = 0 \tag{11.11}$$

where

$$\begin{aligned} G_s(\boldsymbol{w}^h, \boldsymbol{u}^h, \phi^h)_n = & \int_{t_n}^{t_{n+1}} (\dot{\boldsymbol{w}}^h, \rho_s \ddot{\boldsymbol{u}}^h)_{\Omega_s} dt + \int_{t_n}^{t_{n+1}} a(\dot{\boldsymbol{w}}^h, \boldsymbol{u}^h)_{\Omega_s} dt \\ & - \int_{t_n}^{t_{n+1}} (\dot{\boldsymbol{w}}^h \cdot \boldsymbol{n}, \rho_f \dot{\phi}^h)_{\Gamma_i} dt - \int_{t_n}^{t_{n+1}} (\dot{\boldsymbol{w}}^h, \bar{\mathbf{t}})_{\Gamma_\sigma} dt \\ & + (\dot{\boldsymbol{w}}^h(t_n^+), \rho_s [\![\dot{\boldsymbol{u}}^h(t_n)]\!])_{\Omega_s} + a(\boldsymbol{w}^h(t_n^+), [\![\boldsymbol{u}^h(t_n)]\!])_{\Omega_s} \end{aligned} \tag{11.12}$$

$$\begin{aligned} G_f(w^h, \boldsymbol{u}^h, \phi^h)_n = & \int_{t_n}^{t_{n+1}} (\dot{w}^h, \rho_f a^2 \ddot{\phi}^h)_{\Omega_f} dt + \int_{t_n}^{t_{n+1}} (\nabla \dot{w}^h, \rho_f \nabla \phi^h)_{\Omega_f} dt \\ & + \int_{t_n}^{t_{n+1}} (\dot{w}^h, \rho_f \dot{\boldsymbol{u}}^h \cdot \boldsymbol{n})_{\Gamma_i} dt - \int_{t_n}^{t_{n+1}} (\dot{w}^h, \rho_f f)_{\Omega_f} dt \\ & + (\dot{w}^h(t_n^+), a^2 \rho_f [\![\dot{\phi}^h(t_n)]\!])_{\Omega_f} + (\nabla w^h(t_n^+), \rho_f [\![\nabla \phi^h(t_n)]\!])_{\Omega_f} \\ & + G_\infty(w^h, \phi^h)_n \end{aligned} \tag{11.13}$$

In the operator G_s, the terms evaluated over $\Omega_s \times I_n$, weakly enforce the momentum balance in the structure while in G_f, the terms evaluated over $\Omega_f \times I_n$, weakly enforce the scalar wave equation over the interior domain of the space-time slab. Fluid-structure interaction is accomplished through the coupling operators defined on the fluid-structure interface $\Gamma_i \times I_n$. The operator G_∞, incorporates the time-dependent radiation boundary conditions on the boundary Γ_∞, and will be described later in Section 11.5.

An important component in the success of the space-time method is the incorporation of discontinuous temporal jump terms at each space-time slab interface.

$$[\![w^h(t_n)]\!] = w^h(\boldsymbol{x}, t_n^+) - w^h(\boldsymbol{x}, t_n^-)$$

These jump operators weakly enforce initial conditions across time slabs and are crucial for obtaining an unconditionally stable algorithm for unstructured space-time

finite element discretizations with high-order interpolations. The specific form of these jump operators are designed such that a natural norm emanates from the variational equation and satisfies a strong coercivity condition. From a Fourier analysis, it can be shown that the jump operators introduce beneficial numerical dissipation for frequencies above the spatial resolution limit.

The method is applied in one space-time slab at a time; data from the end of the previous slab are employed as initial conditions for the current slab. Introducing space-time finite element approximations for $\boldsymbol{u}^h$ and ϕ^h into the variational equations leads to the coupled system of algebraic equations to be solved in sequence for each time interval $I_n =]t_n\,,\, t_{n+1}[,\ n = 0, 1, \cdots N-1$:

$$\begin{bmatrix} \boldsymbol{K}_s & \boldsymbol{A} \\ \boldsymbol{A}^T & \boldsymbol{K}_f \end{bmatrix} \begin{Bmatrix} \boldsymbol{d} \\ \boldsymbol{\phi} \end{Bmatrix} = \begin{Bmatrix} \boldsymbol{f}_s \\ \boldsymbol{f}_f \end{Bmatrix} \tag{11.14}$$

where $\boldsymbol{d}$ and $\boldsymbol{\phi}$ are the global solution vectors for time interval I_n, $\boldsymbol{K}_s$ is the matrix emanating from the structural operator G_s, and $\boldsymbol{K}_f$ is the matrix emanating from the fluid operator G_f, and $\boldsymbol{A}$ is the fluid-structure coupling matrix.

$$\boldsymbol{A} \;=\; \mathop{\mathbf{A}}_{e=1}^{n_{el}} \int_{t_n}^{t_{n+1}} \int_{\Gamma_i^e} \rho_f \boldsymbol{N}_{s,t}^{eT} \boldsymbol{n} \boldsymbol{N}_{f,t}^{e}\, d\Gamma^e\, dt \tag{11.15}$$

where $\boldsymbol{N}_s^e(\boldsymbol{x}, t) \in Q_n^s$ and $\boldsymbol{N}_f^e(\boldsymbol{x}, t) \in Q_n^f$ are the e^{th} element shape functions for the structure and fluid respectively.

11.5 Non-reflecting Boundary Conditions

A new sequence of time-dependent non-reflecting boundary conditions which are exact for the first N spherical wave harmonics on Γ_∞ are developed. We start with the exact time-harmonic solution to the reduced wave equation (Helmholtz equation) in the exterior domain Ω_∞, expressed through the frequency-dependent non-local Dirichlet-to-Neumann map on the boundary Γ_∞. With harmonic time dependence $e^{-i\omega t}$, frequency $\omega > 0$, and the boundary Γ_∞ restricted to be a sphere of radius $r = R$ in $\mathbb{R}^3$, the exact non-local Dirichlet-to-Neumann (DtN) boundary condition is [98],

$$\frac{\partial \phi}{\partial n}(R, \theta, \varphi) = \sum_{n=0}^{\infty} z_n(kR) \int_{\Gamma_\infty} s_n(\theta, \varphi, \theta', \varphi')\ \phi(R, \theta', \varphi')\ d\Gamma' \tag{11.16}$$

where the DtN kernels $s_n,\ n = 0, 1, 2, \cdots$ are given by,

$$s_n = \sum_{j=0}^{n}{}' \alpha_{nj} P_n^j(\cos\varphi) P_n^j(\cos\varphi') \cos j(\theta - \theta') \tag{11.17}$$

$$\alpha_{nj} = \frac{(2n+1)(n-j)!}{2\pi R^2 (n+j)!} \tag{11.18}$$

with impedance coefficients,

$$z_n(kR) = \frac{kh_n'(kR)}{h_n(kR)} \tag{11.19}$$

In the above, $k = \omega/c$ is the acoustic wavenumber, $0 \le \theta < 2\pi$ is the circumferential angle and $0 \le \varphi < \pi$ is the polar angle for a spherical truncation boundary of radius $r = R$. The differential surface area is $d\Gamma = R^2 \sin\varphi d\theta d\varphi$, P_n^j are associated Legendre functions of the first kind, and h_n are spherical Hankel functions of the first kind of order n. The prime on h_n indicates differentiation with respect to its argument, and the prime after the sum indicates that a factor of $1/2$ multiplies the term with $j = 0$.

In [143, 150] it is shown that when the solution on the boundary Γ_∞ contains only a finite number of spherical harmonics, then (11.16) can be transformed into an exact condition which is local in both $\boldsymbol{x}$ and t. The transformation is based on the ideas of Givoli and Keller [42], where a spatially local counterpart to the non-local *DtN* map **S** was obtained for the two-dimensional Helmholtz equation. The extension to three-dimensions was given by Harari [56]. Use is also made of the special property of spherical Hankel functions h_n which have the unique feature of being exactly represented by a finite and convergent series up to order n:

$$h_n(kR) = h_0(kR)\left[(-i)^n \sum_{j=0}^{n} \frac{(n+j)!}{j!(n-j)} \left(\frac{-1}{2ikR}\right)^j\right], \quad n = 0, 1, 2, \cdots \tag{11.20}$$

As this series involves only inverse powers of the nondimensional wavenumber (ikR) and the zero order term $h_0 = e^{ikR}/(ikR)$ can be factored out of the sum, an inverse Fourier transform can be found which yields a local in time counterpart to the DtN map.

The sequence of local boundary conditions is obtained by truncating the DtN map given in (11.16), so that the sum over n extends over the finite range $n = 0, 1, \cdots N-1$, and expressing the first N terms in the DtN map as:

$$\frac{\partial\phi}{\partial n}(R, \theta, \varphi) = \sum_{n=0}^{N-1} z_n(kR)\, Y_n(\theta\,,\, \varphi) \tag{11.21}$$

where

$$Y_n(\theta\,,\, \varphi) = \sum_{j=0}^{n}{}' P_n^j(\cos\varphi)(A_{nj}\cos j\theta + B_{nj}\sin j\theta) \tag{11.22}$$

are spherical surface harmonics of order n, with nonlocal coefficients A_{nj} and B_{nj}. The initial goal is to replace the nonlocal spatial integrals embedded in the coefficients A_{nj} and B_{nj} with local spatial derivatives. This can be accomplished by recognizing that Y_n can be interpreted as eigenfunctions of the Laplace-Beltrami operator

$$\Delta_\Gamma := \frac{1}{\sin\varphi}\frac{\partial}{\partial\varphi}\left(\sin\varphi\frac{\partial}{\partial\varphi}\right) + \frac{1}{\sin^2\varphi}\frac{\partial^2}{\partial\theta^2} \tag{11.23}$$

with eigenvalues $\lambda = -n(n+1)$, so that

$$[n(n+1)]^m Y_n = (-\Delta_\Gamma)^m Y_n \tag{11.24}$$

This property of the spherical harmonics suggests writing the impedance coefficients as a series of powers of $n(n+1)$:

$$z_n(kR) = \sum_{m=0}^{N-1} [n(n+1)]^m \beta_m(kR), \qquad n = 0, 1, \cdots, N-1 \tag{11.25}$$

This is a system of N linear equations for the N unknown values $\beta_m, m = 0, 1, \cdots N$. Using (11.25) to replace z_n in (11.21) gives,

$$\frac{\partial \phi}{\partial n}(R, \theta, \varphi) = \sum_{n=0}^{N-1} \sum_{m=0}^{N-1} \beta_m(kR) \left[n(n+1)\right]^m Y_n(\theta\,,\, \varphi) \tag{11.26}$$

Now using (11.24) to replace $[n(n+1)]^m Y_n$ with the high-order tangential derivatives $(-\Delta_\Gamma)^m Y_n$, and using the assumption that the solution ϕ on Γ_∞ contains only the first N spherical harmonics, the following sequence of local radiation boundary conditions is obtained:

$$\frac{\partial \phi}{\partial n} \quad = \quad \sum_{m=0}^{N-1} \beta_m(kR) \, (-\Delta_\Gamma)^m \phi \qquad \text{on} \quad \Gamma_\infty \tag{11.27}$$

where the values of $\beta_m(kR)$ are obtained by solving the $N \times N$ linear algebraic system (11.25). Since this sequence follows directly from the truncated DtN map, these radiation boundary operators are exact for waves consisting of the first N spherical harmonics. In this case, the nonlocal spatial integrals have been replaced by a linear map expressed in terms of the differential operator $(\Delta_\Gamma)^m$.

The next step is to obtain an exact local in time counterpart to (11.27) through an inverse Fourier transform. To this end use is made of the finite series expansion for the spherical Hankel functions embedded in the coefficients $\beta_m(kR)$. The procedure is explicated by deriving the first two local in time counterparts in the sequence (11.27).

11.5.1 New exact time-dependent boundary conditions

For the first operator in the sequence corresponding to $N = 1$, the system (11.25) reduces to the simple result $z_0(kR) = \beta_0(kR)$, so that the local DtN condition (11.27) specializes to,

$$\frac{\partial \phi}{\partial n} \quad = \quad \frac{k h_0'(kR)}{h_0(kR)} \phi \tag{11.28}$$

For clarity, set $h_n := h_n(kR)$, and use the relation $h_0' = -h_1$ and (11.20) with $n = 1$, i.e.

$$h_1 = \left(\frac{1}{kR} - i\right) \, h_0 \tag{11.29}$$

to obtain a simplified expression for (11.28):

$$\frac{\partial \phi}{\partial n} \quad = \quad \left(ik - \frac{1}{R}\right) \phi \tag{11.30}$$

The time-dependent counterpart to (11.30) is obtained by direct application of the inverse Fourier transform, in effect, replacing every occurrence of the operator $(-ik)^m$ by $(\frac{1}{c}\frac{\partial}{\partial t})^m$ with the result,

$$\mathbf{B}_1 \phi := \frac{\partial \phi}{\partial n} + \frac{1}{R}\phi + \frac{1}{c}\dot{\phi} = 0 \tag{11.31}$$

This condition is perfectly absorbing for only axially symmetric spherical waves (outgoing wave harmonic $n = 0$).

To obtain a high-order accurate boundary condition, take $N = 2$, so that the system (11.25) yields, $\beta_0 = z_0$ and $\beta_1 = (z_1 - z_0)/2$, and (11.27) becomes,

$$\frac{\partial \phi}{\partial n} = z_0 \phi + \frac{1}{2}(z_0 - z_1)\Delta_\Gamma \phi \tag{11.32}$$

Clearing the common denominator $h_0 h_1$ and using the recurrence relation,

$$h_n' = h_{n-1} - \left(\frac{n+1}{kR}\right) h_n\,, \qquad n = 1, 2, \cdots \tag{11.33}$$

in conjunction with (11.20) and after some algebraic manipulation, we obtain the simplified form,

$$\left(\frac{1}{R} - ik\right)\frac{\partial \phi}{\partial n} \quad = \quad \left(k^2 + \frac{2ik}{R} - \frac{1}{R^2}\right)\phi + \frac{1}{2R^2}\Delta_\Gamma \phi \tag{11.34}$$

Since this expression involves only terms in powers of $(ik)^m$, the inverse Fourier transform is readily obtained with the desired result,

$$\mathsf{B}_2\phi := \frac{\partial \phi}{\partial n} + \frac{R}{c}\frac{\partial \dot{\phi}}{\partial n} + \frac{R}{c^2}\ddot{\phi} + \frac{2}{c}\dot{\phi} + \frac{1}{R}\phi - \frac{1}{2R}\Delta_\Gamma \phi = 0 \tag{11.35}$$

This higher-order accurate local boundary condition is perfectly absorbing for the first two spherical wave harmonics of orders $n = 0$ and $n = 1$. Expressions for the exact time-dependent local boundary conditions for higher-order harmonics $N = 3, 4, \cdots$, will involve higher-order temporal and tangential derivatives, and are obtained using the same procedure as indicated for $N = 1, 2$; see [143, 150].

This new sequence of local time-dependent boundary conditions provide increasing accuracy with order N which, however, is also a measure of the difficulty of implementation. In general, the Nth-order condition contains all the even tangential and temporal derivatives up to order $2(N-1)$. Because the time-discontinuous formulation allows for the use of C^0 interpolations to represent the high-order time derivatives, it is possible to implement this sequence of time-dependent absorbing boundary conditions up to any order desired. However for high-order operators in the sequence extending beyond $N \geq 3$, the lowest possible order of spatial continuity on the artificial boundary that can be achieved after integration by parts is C^{N-2}. For these high-order operators a layer of boundary elements adjacent to Γ_∞, possessing high-order tangential continuity on Γ_∞ are needed.

To obtain non-reflecting boundary conditions which possess the important property of locality in time, without the requirement of high-order tangential continuity, a local in time counterpart to the spatially nonlocal DtN map (11.16) is derived which exactly represents the first N spherical wave harmonics. This new sequence of boundary conditions retains the nonlocal spatial integral, yet replaces the time-convoluted DtN map with higher-order local time derivatives. This new sequence of time-dependent boundary conditions has the advantage that when implemented in the time-discontinuous finite element formulation, standard C^0 interpolation functions may be used for both the space and time variables. Consider the first term in

the truncated DtN series with $N = 1$, then (11.16) reduces to,

$$\frac{\partial \phi}{\partial n} = z_0 \int_{\Gamma_\infty} \phi \, s_0 \, d\Gamma' \tag{11.36}$$

where $s_0 = 1/(4\pi R^2)$ and $z_0 = kh_0'/h_0$. Using $h_0' = -h_1$ and (11.20) and clearing the denominator h_0 gives the alternate form,

$$\frac{\partial \phi}{\partial n} = \left(ik - \frac{1}{R}\right) \int_{\Gamma_\infty} \phi \, s_0 \, d\Gamma' \tag{11.37}$$

Taking the inverse Fourier transform results in the local in time but nonlocal in space boundary condition,

$$\mathbf{B}_1 \phi := \frac{\partial \phi}{\partial n} + \int_{\Gamma_\infty} \left(\frac{1}{c}\dot{\phi} + \frac{1}{R}\phi\right) s_0 \, d\Gamma' = 0 \tag{11.38}$$

This condition is perfectly absorbing for axially symmetric spherical waves.

For $N = 2$, the first two terms in the truncated DtN series (11.16) take the form,

$$\frac{\partial \phi}{\partial n} = z_0 \int_{\Gamma_\infty} \phi \, s_0 \, d\Gamma' + z_1 \int_{\Gamma_\infty} \phi \, s_1 \, d\Gamma' \tag{11.39}$$

Using the definition for $z_n(kR)$ and relations (11.20), (11.33) and clearing the common denominator $h_0 h_1$ we obtain the alternative form,

$$\left(\frac{1}{R} - ik\right) \frac{\partial \phi}{\partial n} = \left(k^2 + \frac{2ik}{R} - \frac{1}{R^2}\right) \int_{\Gamma_\infty} \phi \, s_0 \, d\Gamma' + \left(k^2 + \frac{2ik}{R} - \frac{2}{R^2}\right) \int_{\Gamma_\infty} \phi \, s_1 \, d\Gamma' \tag{11.40}$$

Direct application of the inverse Fourier transform gives

$$\begin{aligned} \mathbf{B}_2 \phi := \frac{\partial \phi}{\partial n} + \frac{R}{c}\frac{\partial \dot{\phi}}{\partial n} &+ \int_{\Gamma_\infty} \left(\frac{R}{c^2}\ddot{\phi} + \frac{2}{c}\dot{\phi} + \frac{1}{R}\phi\right) s_0 \, d\Gamma' \\ &+ \int_{\Gamma_\infty} \left(\frac{R}{c^2}\ddot{\phi} + \frac{2}{c}\dot{\phi} + \frac{2}{R}\phi\right) s_1 \, d\Gamma' = 0 \end{aligned} \tag{11.41}$$

where s_0 and s_1 are defined in (11.17). This condition is perfectly absorbing for the first two spherical wave harmonics of order $n = 0$ and $n = 1$.

Similarly for $N = 3$ [143, 150],

$$\mathbf{B}_3 \phi := \phi_{,n} + \frac{2R}{c}\phi_{,nt} + \frac{4R^2}{3c^2}\phi_{,ntt} + \frac{R^3}{3c^3}\phi_{,nttt} \tag{11.42}$$

$$\begin{aligned} &+ \int_{\Gamma_\infty} \left(\frac{R^3}{3c^4}\phi_{,tttt} + \frac{5R^2}{3c^3}\phi_{,ttt} + \frac{10R}{3c^2}\phi_{,tt} + \frac{3}{c}\phi_{,t} + \frac{1}{R}\phi\right) s_0 \, d\Gamma' \\ &+ \int_{\Gamma_\infty} \left(\frac{R^3}{3c^4}\phi_{,tttt} + \frac{5R^2}{3c^3}\phi_{,ttt} + \frac{11R}{3c^2}\phi_{,tt} + \frac{4}{c}\phi_{,t} + \frac{2}{R}\phi\right) s_1 \, d\Gamma' \\ &+ \int_{\Gamma_\infty} \left(\frac{R^3}{3c^4}\phi_{,tttt} + \frac{5R^2}{3c^3}\phi_{,ttt} + \frac{13R}{3c^2}\phi_{,tt} + \frac{6}{c}\phi_{,t} + \frac{3}{R}\phi\right) s_2 \, d\Gamma' = 0 \end{aligned} \tag{11.43}$$

This condition is perfectly absorbing for the first three spherical wave harmonics of order $n = 0, 1, 2$. These are nonlocal operators that involve a spatial integral yet retain the important property of locality in time. In general, the boundary operators in this sequence will have higher-order time derivatives up to $2(N-1)$. When implemented in the discontinuous space-time finite element formulation, standard $C^0(\Gamma_\infty \times I_n)$ continuous interpolations may be used on the radiation boundary in both the space and time dimensions.

11.5.2 Space-time finite element implementation

The most direct approach in which to implement the exact time-dependent boundary conditions is to define a linear operator $\mathbf{S}_m$ as,

$$\mathbf{B}_m(\phi) := \frac{\partial \phi}{\partial n} + \mathbf{S}_m(\phi) \tag{11.44}$$

which implies

$$\frac{\partial \phi}{\partial n} = -\mathbf{S}_m \phi \qquad \text{on } \Gamma_\infty \tag{11.45}$$

In this way, the boundary conditions are expressed in a form relating Dirchlet-to-Neumann data. For example, the first three local in space and time operators $\mathbf{S}_m$ for m equal to 1,2 and 3 are:

$$\mathbf{S}_1\phi = \frac{1}{R}\phi + \frac{1}{c}\phi_{,t} \tag{11.46}$$

$$\mathbf{S}_2\phi = \frac{1}{2R}(2 - \Delta_\Gamma)\phi + \frac{1}{c}\left(2 + R\frac{\partial}{\partial r}\right)\phi_{,t} + \frac{R}{c^2}\phi_{,tt} \tag{11.47}$$

$$\begin{aligned}\mathbf{S}_3\phi = {} & \frac{1}{24R}(24 - 14\Delta_\Gamma - (\Delta_\Gamma)^2)\phi + \frac{1}{2c}\left(6 - \Delta_\Gamma + 4R\frac{\partial}{\partial r}\right)\phi_{,t} \\ & + \frac{R}{6c^2}\left(20 - \Delta_\Gamma + 8R\frac{\partial}{\partial r}\right)\phi_{,tt} + \frac{R^2}{3c^3}\left(5 + R\frac{\partial}{\partial r}\right)\phi_{,ttt} + \frac{R^3}{3c^4}\phi_{,tttt}\end{aligned} \tag{11.48}$$

These boundary conditions are incorporated into the finite element method as a natural boundary condition, i.e., they are enforced weakly in both time and space. For example, the operator defined on Γ_∞ in Eq. (11.13) for the second-order boundary condition $m = 2$ is given by:

$$G_\infty(w^h, \phi^h)_n = \int_{t_n}^{t_{n+1}} (\dot{w}^h, \mathbf{S}_2\phi^h)_{\Gamma_\infty}\, dt + d_2(\dot{w}^h(t_n^+), [\![\dot{\phi}^h(t_n)]\!])_{\Gamma_\infty} + d_0(w^h(t_n^+), [\![\phi^h(t_n)]\!])_{\Gamma_\infty} \tag{11.49}$$

where the space-time integral on the boundary is defined as,

$$\int_{t_n}^{t_{n+1}} (\dot{w}^h, \mathbf{S}_2\phi^h)_{\Gamma_\infty}\, dt = d_0(\dot{w}^h, \phi^h)_{(\Upsilon_\infty)_n} + d_1(\dot{w}^h, \dot{\phi}^h)_{(\Upsilon_\infty)_n} + d_2(\dot{w}^h, \ddot{\phi}^h)_{(\Upsilon_\infty)_n} \tag{11.50}$$

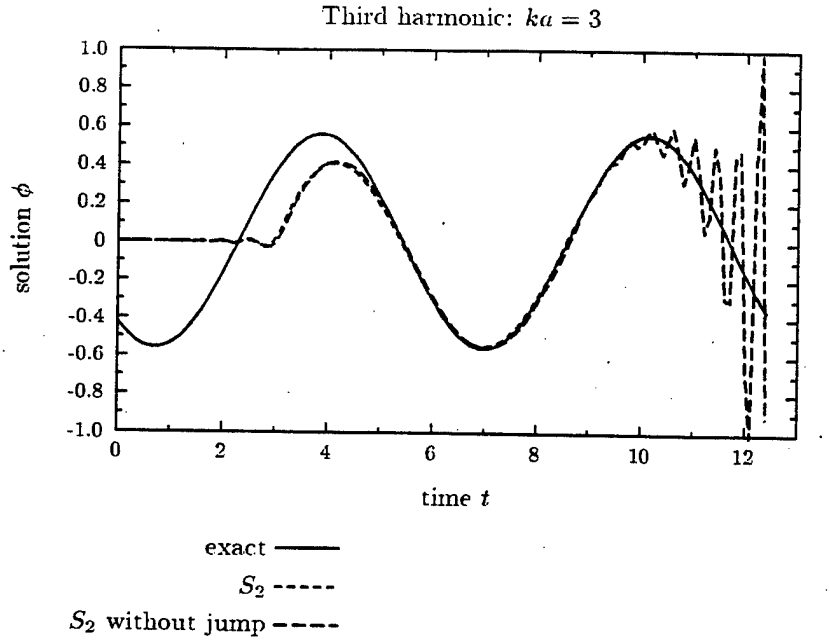

Figure 11.3: Space-time finite element solution of radiating cylinder. Results at the artificial boundary Γ_∞ show that temporal jump terms are required on Γ_∞ for stability.

and

$$d_0(\dot{w}^h\,,\,\phi^h)_{(\Upsilon_\infty)_n} = \frac{\rho_f}{R}\int_{t_n}^{t_{n+1}} (\dot{w}^h\,,\,\phi^h)_{\Gamma_\infty}\,dt + \frac{\rho_f}{2R}\int_{t_n}^{t_{n+1}} (\dot{w}^h_{,\varphi}\,,\,\phi^h_{,\varphi})_{\Gamma_\infty}\,dt + \frac{\rho_f}{2R}\int_{t_n}^{t_{n+1}} (\dot{w}^h_{,\theta}\,,\,\csc^2(\varphi)\,\phi^h_{,\theta})_{\Gamma_\infty}\,dt \tag{11.51}$$

$$d_1(\dot{w}^h\,,\,\dot{\phi}^h)_{(\Upsilon_\infty)_n} = \frac{2\rho_f}{c}\int_{t_n}^{t_{n+1}} (\dot{w}^h\,,\,\dot{\phi}^h)_{\Gamma_\infty}\,dt + \frac{\rho_f R}{c}\int_{t_n}^{t_{n+1}} (\dot{w}^h\,,\,\dot{\phi}^h_{,r})_{\Gamma_\infty}\,dt \tag{11.52}$$

$$d_2(\dot{w}^h\,,\,\ddot{\phi}^h)_{(\Upsilon_\infty)_n} = \frac{\rho_f R}{c^2}\int_{t_n}^{t_{n+1}} (\dot{w}^h\,,\,\ddot{\phi}^h)_{\Gamma_\infty}\,dt \tag{11.53}$$

In the above expressions, continuity requirements due to second-order tangential derivatives in the Laplace-Beltrami operator Δ_Γ, are relaxed on the artificial boundary Γ_∞, by using integration by parts.

The form of the terms defined in (11.49) involving temporal jump operators evaluated on the boundary Γ_∞, can be inferred from eqns. (11.51) and (11.53). These consistent jump terms act to weakly enforce continuity of ϕ^h and $\dot{\phi}^h$ between space-time-slabs at the boundary Γ_∞. These additional operators are needed in order to ensure unconditional stability for the solution and are the crucial element that enable generalization of the time-discontinuous space-time finite element method to handle unbounded domains.

Figure 11.3 illustrates how the space-time solution can become unstable as outgoing waves are transmitted through Γ_∞, if the temporal jump terms defined in (11.49) are omitted. The result shows the numerical solution of transient radiation from a

cylinder that is driven to steady-state. The solid line is the exact time-harmonic solution. When the jump terms are included, the local boundary condition, $\mathbf{S}_2$, displays the correct transient solution for short time, (time less than 6 seconds), and then quickly assumes the exact steady-state solution. When the jump terms are omitted, the solution quickly becomes unstable, generating large spurious oscillations.

11.6 Galerkin/Least-squares Stabilization

In order to add additional stability to the time-discontinuous Galerkin space-time formulation, and in addition, prove that the method converges for arbitrary space-time discretizations and higher-order interpolations, local residuals of the governing differential equations in the form of least-squares are added to the Galerkin variational equations. The Galerkin/least-squares addition to the variational equation for the fluid is,

$$\begin{aligned} G^f_{GLS}(w^h\,,\,\boldsymbol{u}^h\,,\,\phi^h)_n &= G_f(w^h\,,\,\boldsymbol{u}^h\,,\,\phi^h)_n + (\rho_f c^2 \tau \mathcal{L}_1 w^h\,,\,(\mathcal{L}_1\phi^h - f))_{\tilde{Q}^f_n} \\ &+ (\rho_f c^2 s \mathcal{L}_2 w^h\,,\,\mathcal{L}_2\phi^h)_{(\tilde{\Upsilon}_\infty)_n} + (\rho_f c^2 s \mathcal{L}_3 w^h\,,\,\mathcal{L}_3\phi^h)_{(\tilde{\Upsilon}_i)_n} \\ &+ (\rho_f c^2 s [\![w^h_{,n}(\boldsymbol{x})]\!]\,,\,[\![\phi^h_{,n}(\boldsymbol{x})]\!])_{(\tilde{\Upsilon}^e)_n} \end{aligned}$$

where $(\mathcal{L}_1 w^h - f = \nabla^2 w^h - a^2 \ddot{w}^h - f)$ is the residual for the wave equation, $(\mathcal{L}_2 w^h = w^h_{,n} + \mathbf{S}_m w^h)$ is the radiation boundary residual, and $(\mathcal{L}_3 w^h = w^h_{,n} - \dot{\boldsymbol{u}} \cdot \boldsymbol{n})$ is the interface boundary residual. In the above expressions, a tilde refers to integration over element interiors and τ and s are local mesh parameters designed to improve desirable high frequency numerical dissipation without degrading the accuracy of the underlying Galerkin method. For the structural equation (11.12) similar least-squares terms are added, see [143]. Consistency of the method is clear from the fact that a sufficiently smooth exact solution of the coupled initial/boundary-value problem satisfies the variational equations identically.

11.7 Stability and Convergence Analysis

In this section, results are summarized from a stability and convergence analysis of the space-time finite element formulation for the exterior structural acoustics problem [143, 149]. A natural measure of stability for the coupled structural acoustics problem is the total energy for the system:

$$\mathsf{E}(\boldsymbol{u}\,,\,\phi) := \mathcal{E}_s(\boldsymbol{u}) + \mathcal{E}_f(\phi) \tag{11.54}$$

where the energy for the structure is,

$$\mathcal{E}_s(\boldsymbol{u}) = \frac{1}{2}\,(\dot{\boldsymbol{u}}\,,\,\rho_s \dot{\boldsymbol{u}})_{\Omega_s} + \frac{1}{2}\,a(\boldsymbol{u}\,,\,\boldsymbol{u})_{\Omega_s} \tag{11.55}$$

while the energy for the acoustic fluid is,

$$\mathcal{E}_f(\phi^h) = \frac{1}{2}\,\rho_f\,||a\dot{\phi}^h||^2_{\Omega_f} + \frac{1}{2}\,\rho_f\,||\nabla\phi^h||^2_{\Omega_f} \tag{11.56}$$

11.7.1 A priori energy estimates

In the absence of forcing terms, i.e., $\bar{\boldsymbol{t}} = \mathbf{0}$ and $f = 0$, and for $\mathbf{S}_1$, it has been proved in [143, 149] that the following energy decay inequality holds for the coupled space-time formulation:

$$\begin{aligned} & \mathcal{E}_s(\boldsymbol{u}^h(t_{n+1}^-)) + \mathcal{E}_f(\phi^h(t_{n+1}^-)) + \frac{1}{2R}||\phi^h(t_{n+1}^-)||^2_{\Gamma_\infty} + \frac{1}{c}\int_0^{t_{n+1}} ||\dot{\phi}^h(t)||^2_{\Gamma_\infty}\, dt \\ \leq\ & \mathcal{E}_s(\boldsymbol{u}_0)) + \mathcal{E}_f(\phi_0)) \end{aligned} \tag{11.57}$$

for $n = 0, 1, 2, \cdots, N-1$. This result states that the total energy in the fluid-structure system, plus the energy absorbed through the radiation boundary, is always less than, or equal to the initial energy in the system. A corollary to this estimate is that the computed total energy for the system plus the radiation energy absorbed through the artificial boundary at the end of a time step is always less than or equal to the total energy at the previous time step for arbitrary step sizes, i.e.

$$\begin{aligned} & \mathcal{E}_s(\boldsymbol{u}^h(t_{n+1}^-)) + \mathcal{E}_f(\phi^h(t_{n+1}^-)) + \frac{1}{2R}||\phi^h(t_{n+1}^-)||^2_{\Gamma_\infty} + \frac{1}{c}\int_{t_n}^{t_{n+1}} ||\dot{\phi}^h(t)||^2_{\Gamma_\infty}\, dt \\ \leq\ & \mathcal{E}_s(\boldsymbol{u}^h(t_n^-)) + \mathcal{E}_f(\phi^h(t_n^-)) + \frac{1}{2R}||\phi^h(t_n^-)||^2_{\Gamma_\infty} \end{aligned} \tag{11.58}$$

for $n = 0, 1, 2, \cdots N-1$. Results (11.57) thru (11.58) both imply that *the space-time formulation presented is unconditionally stable.* See [143] for an analogous result for the interior problem where no radiation boundary conditions are present.

11.7.2 A priori error estimates

To study the convergence rates of the space-time finite element formulation for the exterior structural acoustics problem the following space-time mesh size parameters are introduced. For the structural domain Ω_s, $h_s = \max\{c_L\Delta t\,,\, \Delta x\}$ where c_L is the dilatational wave speed and Δx and Δt are maximum element diameters in space and time, respectively. For the fluid domain Ω_f, $h_f = \max\{c\Delta t\,,\, \Delta x\}$ where c is the acoustic wave speed. Assuming that the exact solution to the strong form of the initial/boundary value problem with $\mathbf{S}_1$ is sufficiently smooth in the sense that,

$$\boldsymbol{u} \in (H^{k+1}(Q_s))^d \quad \text{and} \quad \phi \in H^{p+1}(Q_f) \tag{11.59}$$

and assuming standard finite element interpolation estimates hold, then it has been proved in [143, 149] that the following error estimate holds for the time-discontinuous Galerkin/Least-squares formulation,

$$|||\boldsymbol{E}|||^2 \quad \leq \quad c(\boldsymbol{u})\, h_s^{2k-1} + c(\phi)\, h_f^{2p-1} \tag{11.60}$$

where k and p are the finite element interpolation orders for the structure and fluid respectively. In the above, the error is defined as

$$\boldsymbol{E} = \{\boldsymbol{e}\,,\, e\} \qquad \text{where} \qquad \boldsymbol{e} = \boldsymbol{u}^h - \boldsymbol{u} \quad \text{and} \quad e = \phi^h - \phi, \tag{11.61}$$

and $c(\boldsymbol{u})$ and $c(\phi)$ are values that are independent of the mesh size parameters h_s and h_f. The norm in which convergence is measured is given by,

$$
\begin{aligned}
|||\boldsymbol{E}|||^2 \quad = \quad & \mathcal{E}_s(\boldsymbol{e}(0^+)) + \sum_{n=1}^{N-1} \mathcal{E}_s([\![\boldsymbol{e}(t_n)]\!]) + \mathcal{E}_s(\boldsymbol{e}(T^-)) \\
+ \quad & \mathcal{E}_f(e(0^+)) + \sum_{n=1}^{N-1} \mathcal{E}_f([\![e(t_n)]\!]) + \mathcal{E}_f(e(T^-)) \\
+ \quad & \frac{1}{2R}||e(0^+)||^2_{\Gamma_\infty} + \sum_{n=1}^{N-1} \frac{1}{2R}|||[\![e(t_n)]\!]|||^2_{\Gamma_\infty} + \frac{1}{2R}||e(T^-)||^2_{\Gamma_\infty} \\
+ \quad & \sum_{n=0}^{N-1} \frac{1}{c}\int_{t_n}^{t_{n+1}} (\dot{e}(t)\,,\, \dot{e}(t))_{\Gamma_\infty}\, dt \\
+ \quad & \sum_{n=0}^{N-1} \Big\{ (\mathcal{L}_s\boldsymbol{e}\,,\, \rho_s^{-1}\boldsymbol{\tau}\mathcal{L}_s\boldsymbol{e})_{\tilde{Q}_n^s} \\
+ \quad & ([\![\boldsymbol{\sigma}(\nabla\boldsymbol{e})(\boldsymbol{x})]\!]\cdot\boldsymbol{n}\,,\, \rho_s^{-1}\boldsymbol{s}[\![\boldsymbol{\sigma}(\nabla\boldsymbol{e})(\boldsymbol{x})]\!]\cdot\boldsymbol{n})_{(\tilde{\Upsilon}_s)_n} \\
+ \quad & (\boldsymbol{\sigma}(\nabla\boldsymbol{e})\cdot\boldsymbol{n}\,,\, \rho_s^{-1}\boldsymbol{s}\boldsymbol{\sigma}(\nabla\boldsymbol{e})\cdot\boldsymbol{n})_{(\Upsilon_\sigma)_n} \\
+ \quad & (\boldsymbol{\sigma}(\nabla\boldsymbol{e})\cdot\boldsymbol{n} - \rho_f\dot{\boldsymbol{e}}\boldsymbol{n}\,,\, \rho_s^{-1}\boldsymbol{s}\boldsymbol{\sigma}(\nabla\boldsymbol{e})\cdot\boldsymbol{n} - \rho_f\dot{\boldsymbol{e}}\boldsymbol{n})_{(\Upsilon_i)_n} \\
+ \quad & ||c\tau^{1/2}\mathcal{L}_1 e||^2_{\tilde{Q}_n^f} + ||cs^{1/2}\mathcal{L}_2 e||^2_{(\tilde{\Upsilon}_\infty)_n} \\
+ \quad & ||cs^{1/2}[\![e_{,n}(\boldsymbol{x})]\!]||^2_{(\tilde{\Upsilon}_f)_n} \\
+ \quad & (\dot{\boldsymbol{e}}\cdot\boldsymbol{n} - e_{,n}\,,\, c^2 s\dot{\boldsymbol{e}}\cdot\boldsymbol{n} - e_{,n})_{(\Upsilon_i)_n}\Big\}
\end{aligned}
\tag{11.62}
$$

In the above expression $\mathcal{L}_s\boldsymbol{u}^h$ is the residual for the structure. This norm emanates naturally from the coupled fluid-structure variational equations (11.12) and (11.13). The error estimate is optimal in the sense that the finite element error converges at the same rate as the interpolate. This result indicates that the error for the coupled system is controlled by the convergence rates in both the structure and the fluid. In other words, for an accurate solution to the coupled fluid-structure problem, discretizations for both the structural domain and the fluid domain must be adequately resolved.

11.7.3 Numerical confirmation of error estimates

To verify the numerical convergence rates of the space-time finite element formulation, the response of the one-dimensional wave equation in the semi-infinite interval $0 \leq x < \infty$ was calculated by introducing a truncation boundary at $L = 4$, and imposing an exact non-reflecting boundary condition at this position. The exact boundary condition for this problem is the 'plane-wave damper',

$$\phi_{,x}(L,t) = -(1/c)\dot{\phi}(L,t) \tag{11.63}$$

The left end ($x = 0$) is fixed. A transient pulse is initiated at $x_0 = 2.4$ as,

$$\phi_0(x) = \frac{1}{4}\left(1 - \cos\frac{2\pi}{\lambda}(x - x_0)\right)^2 \tag{11.64}$$

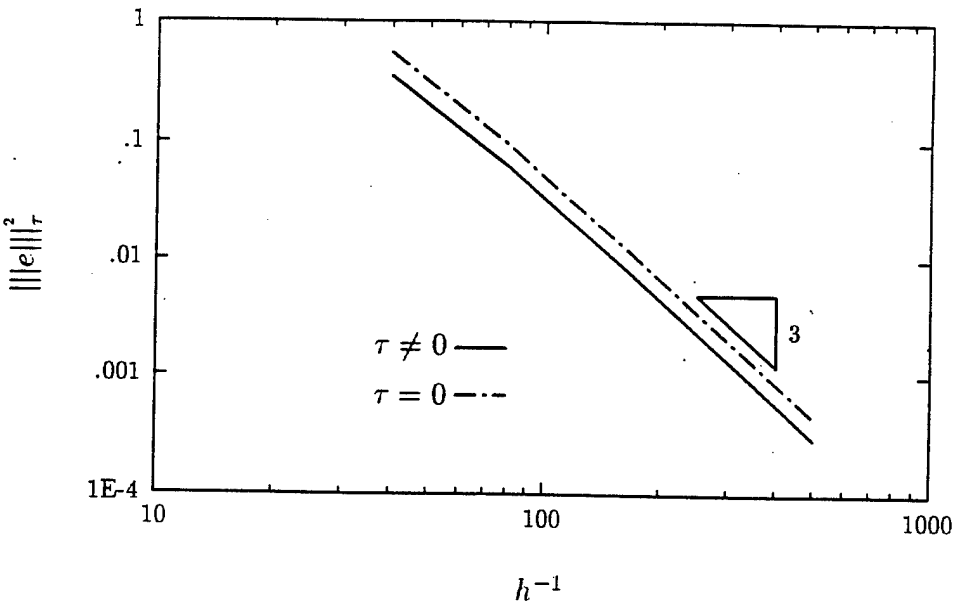

Figure 11.4: Convergence of the numerical error employing the $Q2$ element; $h = h_f$ is the element mesh size parameter. Results confirm the convergence rate $(2p-1) = 3$ for $p = 2$.

with wavelength $\lambda = 0.8$. The response was calculated for the time interval $0 \leq t \leq T = 1.8$. Each space-time slab was discretized with a uniform mesh of 160 biquadratic elements. Figure 11.4 shows the error computed using the Galerkin/least-squares formulation at time $T = 1.8$. This result confirms that a cubic rate of convergence is obtained as predicted by (11.60).

11.8 Representative Numerical Examples

A number of numerical examples are described to demonstrate the effectiveness of the time-discontinuous space-time finite element method to accurately model transient radiation and scattering from geometrically complex structures. The problems investigated are primarily designed to assess the performance of the local non-reflecting boundary conditions. For all the numerical results presented, the GLS mesh parameters are set to zero and standard quadratic finite element shape functions are used in both the time and space dimensions. Additional numerical examples are reported in [143, 146, 150, 151].

11.8.1 Nonconcentric spherical radiator

Consider a sphere of radius $r = a$, pulsating with a uniform sine pulse, $\phi(a,t) = \sin \omega t$ and $\omega = \pi$, during the short time interval $t \in [0,1]$. Initial conditions are set to zero and the wave speed is $c = 1$. The exact solution to this problem is an outgoing

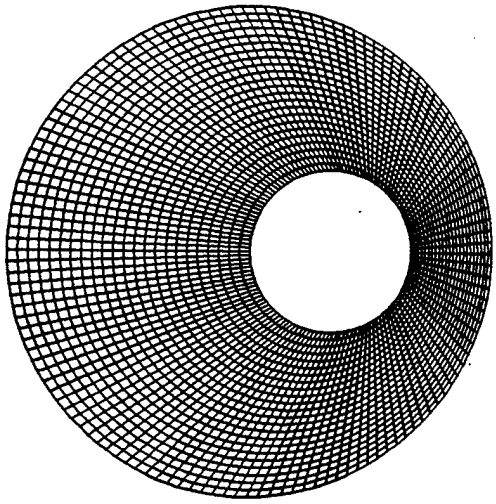

Figure 11.5: Computational domain for a sphere shifted from the center of a spherical non-reflecting boundary. Upper half modeled with 1518 axisymmetric elements using quadratic interpolation.

spherical wave of short duration with a $1/r$ amplitude decay:

$$\phi(r\,,\,t) \quad = \quad \left(\frac{a}{r}\right)\sin\omega(t-\bar{r}/c) \tag{11.65}$$

where $\bar{r} = r - a$ is the radial distance from the spherical radiator and $(t-\bar{r}/c) \in [0,1]$.

If the radiating sphere is placed concentric with a spherical artificial boundary then for the radiation field given in (11.65), the problem is trivial in that the first order $\mathbf{S}_1$, and the higher order local non-reflecting boundary conditions are all exact by design. In order to obtain a challenging problem, the radiating sphere is shifted from the center of the spherical artificial boundary Γ_∞, to a nonconcentric position. In this example, the radiating sphere is offset by a distance a, with the radius of Γ_∞ set at $R = 3a$, see Figure 11.5. With this positioning, wave fronts traveling outward along radial lines will strike the artificial boundary at oblique angles. The closer the radiating sphere gets to the edge of Γ_∞, the more acute this angle becomes, making it increasingly difficult for the local boundary conditions to transmit outgoing waves without spurious reflection.

Figure 11.5 shows the computational domain discretized with 1518 axisymmetric elements. Figure 11.6 shows the elevated contours of the time-discontinuous Galerkin solution using the second-order local boundary operator $\mathbf{S}_2$ defined in (11.47) applied to Γ_∞. In the upper left corner of Figure 11.6, the solution is shown at the end of the initial sine pulse at time $t = 1$. As time progresses, the initial pulse propagates outward from the sphere as a uniform spherical wave pulse of decreasing amplitude. After $t = 1$, the spherical pulse begins to pass through the artificial boundary Γ_∞ with negligible reflection. These results illustrate the remarkable performance of the second-order operator $\mathbf{S}_2$ to transmit waves striking the artificial boundary at rather severe angles.

For comparison, this same problem was solved with the low-order boundary operator $\mathbf{S}_1$. Figure 11.7 shows a plot of the solution on the artificial boundary Γ_∞ at the axis of symmetry, $\varphi = 0$. The solution using $\mathbf{S}_2$ shows the correct amplitude and phase for the outgoing pulse, and shows no observable reflections behind the wave front. In contrast, the solution using $\mathbf{S}_1$ shows an increase in the maximum amplitude of the outgoing pulse as well as significant reflections, as manifested by the non-zero amplitudes appearing for times $t > 2$.

11.8.2 Scattering from a geometrically complex cylinder

As a final example, consider the space-time finite element solution of the time-dependent scattering from a rigid cylinder with conical-to-spherical end caps and a large length to diameter ratio. Figure 11.8 illustrates the finite element spatial discretization of the computational domain bounded internally by the lateral projection of the benchmark cylinder, and externally by a circular artificial boundary. A total of 1600 space-time elements are used for this example.

For this two-dimensional problem, we have implemented the sequence of high-order approximate local boundary conditions described in [125] and [126], which are based on the radial asymptotic solution to the wave equation in two-dimensions. In particular, the following second-order local time-dependent boundary operator is used for this problem.

$$S_2\phi = \frac{1}{2R}(3/4 - \frac{\partial^2}{\partial\theta^2})\phi + \frac{3}{2c}\dot{\phi} + \frac{R}{c}\frac{\partial\dot{\phi}}{\partial r} + \frac{R}{c^2}\ddot{\phi} \tag{11.66}$$

The pulse $f = \delta(x_0, y_0)\sin\omega t$ and $t \in [0, 3]$, is positioned inside the computational domain simulating an oblique incident wave during a short time period. The numerical simulation is continued until just prior to reaching the practical disappearance of the signal from the domain. This example represents a challenging problem where the multiple-scales involving the ratio of the wavelength to cylinder diameter and cylinder length dimension play a critical role in the complexity of the resulting scattered wave field.

The numerical simulation starts with the initial pulse shown in Figure 11.8 at $t = 3$. The accompanying figures show the contours of the scattering phenomena from the cylinder with homogeneous Neumann boundary conditions on the wet surface, i.e. 'rigid' boundary conditions. At $t = 6$ the incident pulse has expanded in a cylindrical wave and has just reached the boundaries of the rigid cylinder. At the artificial boundary, the wave front is allowed to pass through the boundary with no reflection. At $t = 9$, the wave has begun to reflect off the rigid boundary, creating a complicated backscattered wave. As time passes, the originally cylindrical incident wave has been scattered into a part that travels along the upper part of the cylinder, and a part that diffracts around the backside.

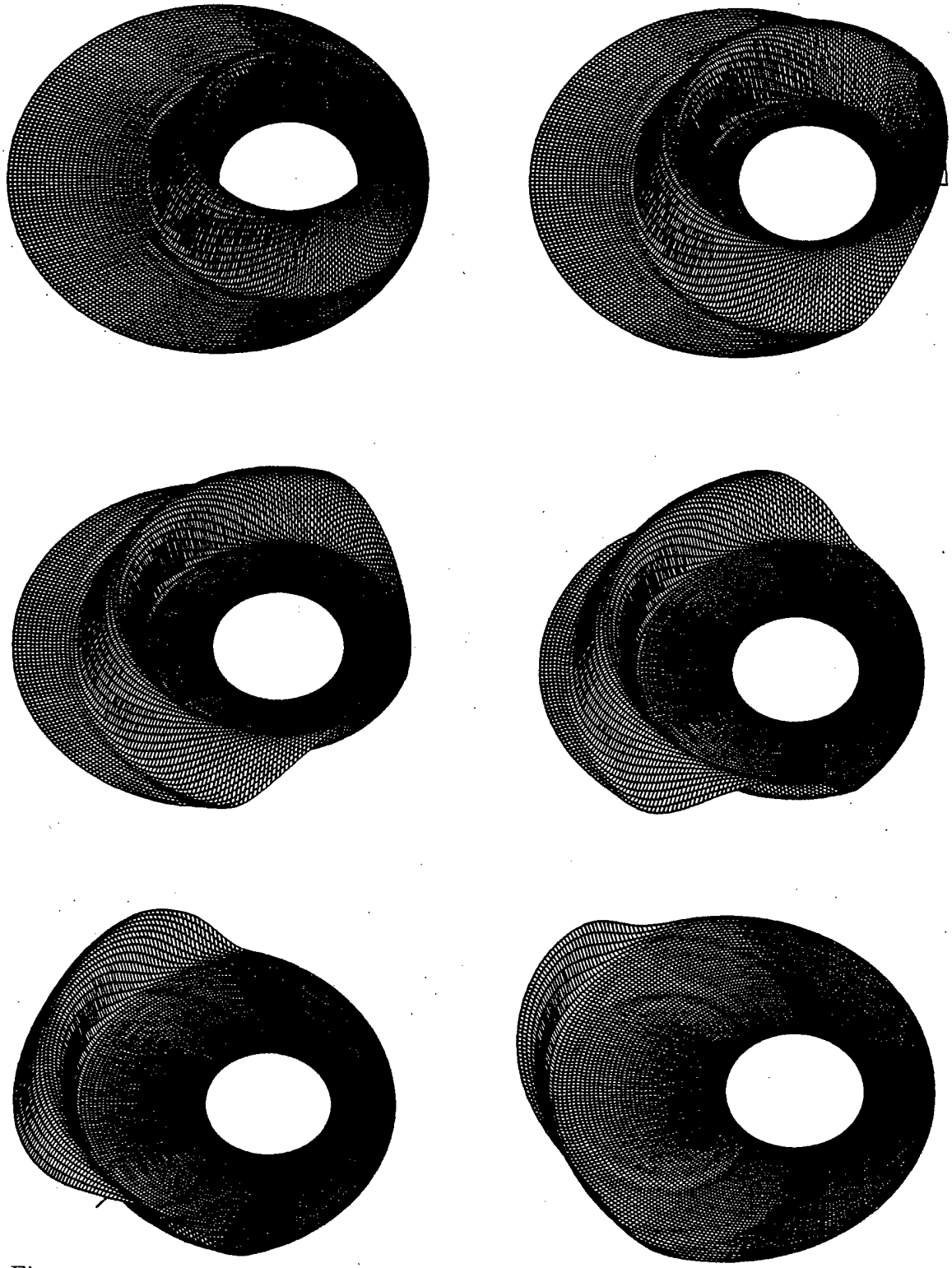

Figure 11.6: Radiation from a nonconcentric sphere. Elevated solution contours shown at the end of the initial pulse at $t = 1$ and later times $t = 1.5$ through $t = 3.5$ in increments of $\Delta t = 0.5$.

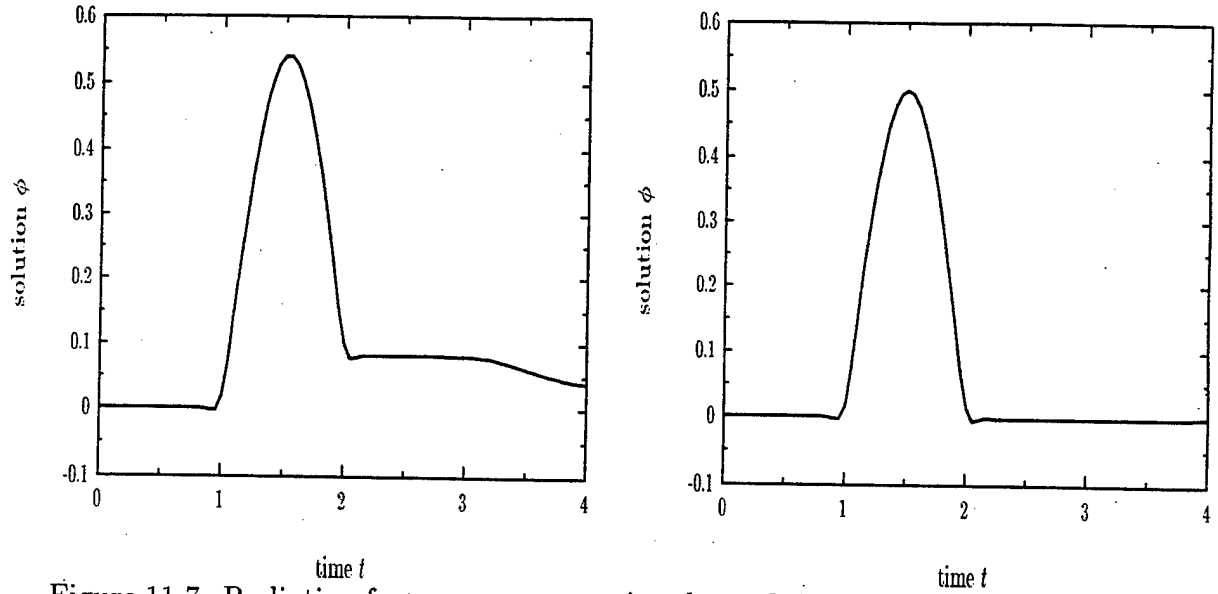

Figure 11.7: Radiation from a nonconcentric sphere: Solution on the artificial boundary Γ_∞, at the axis of symmetry $\varphi = 0$. (left) S_1 local boundary condition. (right) S_2 local boundary condition.

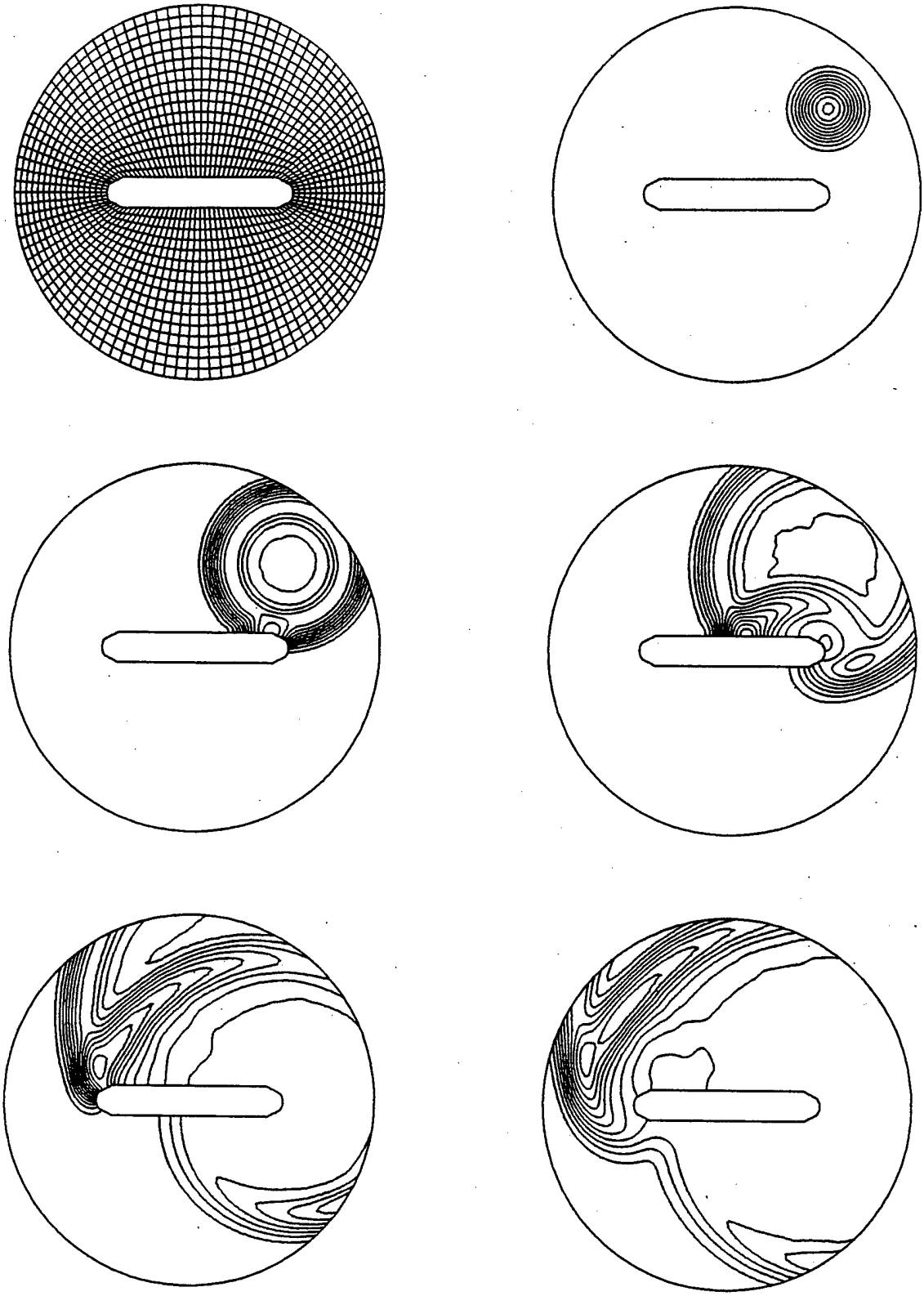

Figure 11.8: Scattering from a geometrically complex rigid structure due to point source. Solution contours shown for initial pulse at $t = 3$ and later times $t = 6, 9, 15, 18$

Chapter 12

Conclusions

In this work we have presented finite element methods for boundary-value problems of structural acoustics with particular reference to exterior domains. Finite element techniques are based on a general-purpose methodology and, by their nature, are not restricted to linear, isotropic and homogeneous problems. This is in contrast to boundary elements, the numerical methods that are prevalent in this field. Our goal was to construct discrete formulations for these problems that are mathematically rigorous, simple to implement and computationally efficient, while retaining the full generality of finite element technology. Computed solutions must represent wave phenomena accurately, yet not deteriorate when physical features are not sufficiently resolved by the numerical mesh.

The DtN approach provides a suitable basis for the computation of solutions to exterior problems by defining a bounded computational domain with appropriate boundary conditions for such problems, precluding singular behavior in finite element models. The solution of the boundary-value problem in a bounded domain obtained by the DtN method is identical to the solution of the boundary-value problem in the original domain, restricted to the computational domain. As such, the solution obtained by the DtN method is unique for all wave numbers. DtN boundary conditions are therefore non-reflective in accordance with the radiation condition that they replace. Subject to geometric considerations, there are no restrictions on the location of the artificial boundary. Analysis of the truncated operator shows that it fails to completely inhibit the reflection of higher modes, allowing non-unique solutions to occur at their harmonics. However, as long as the number of terms in the DtN map respects the bound (3.22) in terms of the wave number nondimensionalized by the radius of the artificial boundary, uniqueness of solutions is guaranteed. Based on these simple results it is easy to automate software to verify that a minimum number of terms in the operator is present, or to set the number of terms if desired. The result of this analysis is verified numerically by examining the dependence of the conditioning of the ensuing discrete equations on the number of terms in the boundary operator. In accordance with the theoretical prediction, the coefficient matrices are well conditioned as long as at least the required number of terms is employed in the map. Other parameters of the problem, such as the geometrically nondimensionalized wave number (by a length scale of the body) and the numerically nondimensionalized wave number, were not found to bring about the kind of degradation in conditioning

that is associated with non-unique solutions. Employing the local approximation of the DtN map retains uniqueness of solutions for all wave numbers. Overall, we found the DtN method to be a viable approach for defining appropriate boundary conditions on bounded domains, significantly increasing the appeal of finite elements for the computation of exterior problems.

Discrete formulations were derived on the basis of computational problems defined by the DtN method. Numerical techniques were constructed by the standard Galerkin method and variants thereof, obtained by appending residuals of the Euler-Lagrange equations in least-squares form to the Galerkin equation. These variants were designed to enhance certain properties and yet retain advantageous features of Galerkin formulations, while adding virtually no complexity in implementation.

We initially analyzed in detail numerical solutions to model problems with plane wave solutions describing physical phenomena that include propagation and decay. Solutions obtained by the Galerkin method were acceptable only with a relatively high degree of mesh refinement. We designed the Galerkin/least-squares finite element method with DtN boundary conditions to be suitable for obtaining robust numerical solutions to the Helmholtz equation in unbounded domains over the entire range of interest, achieving high accuracy of the phase and magnitude without requiring excessive resolution. Finite element methods are thus rendered economically competitive. Galerkin/least-squares solutions are exceptionally accurate on the artificial boundary which is crucial to the representation of the far field by the DtN method. When physical phenomena are not sufficiently resolved by the mesh, the Galerkin/least-squares method is designed to damp out the numerical solution. *Superior behavior is thus exhibited by the Galerkin/least-squares finite element method with DtN boundary conditions in the entire range of propagation and decay. This is the scheme that we advocate for computing solutions to problems of time-harmonic acoustics.*

We have shown that high-order finite element discretizations display frequency bands where the solutions take the form of harmonic decaying waves. In these 'stopping' bands, the solutions are not purely propagating (real wavenumbers) but are attenuated (complex wavenumbers). In order to interpret the solution within the stopping bands, the standard finite element dispersion analysis technique has been extended to include complex wavenumbers. By allowing for complex wavenumbers, a complete characterization of the stopping bands in the frequency spectrum of hierarchical p-version and spectral finite element discretizations has been obtained. The most important conclusions from this study are:

1. High-order elements display increased phase accuracy compared to low-order elements for the same number of degrees of freedom.

2. For large spectral orders, the width of the first few stopping bands are very small and the amplitude attenuation is minimal. Thus for high-order finite element discretizations, the first few stopping bands in the frequency spectrum are not of practical significance.

3. For well resolved waves, spectral elements using Lagrange interpolation in con-

junction with Lobatto quadrature show slightly improved phase accuracy compared to hierarchic finite elements. For frequencies extending beyond the limit of resolution, both dispersion and amplitude attenuation errors increase the most for spectral elements.

In multi-dimensional configurations, employing geometrically graded meshes in the close vicinity of disturbances (boundaries and concentrated sources) may improve the solution, but outside that neighborhood the use of uniform discretizations is recommended, although not required. The selection of optimal Galerkin/least-squares mesh parameters for multi-dimensional wave propagation was considered. The GLS parameter τ is designed from the criterion that numerical phase error be minimized over all directions of wave propagation. Results from both the Fourier analysis and numerical examples verify that as the wave resolution is decreased, the degradation in phase accuracy present in the Galerkin solution is reduced and in some cases eliminated by the proper choice of the GLS parameter τ. Extensions of GLS to three-dimensions was also presented. An analysis of the Galerkin/Gradient Least-squares (G∇LS) method for multi-dimensional wave propagation indicated that G∇LS and GLS have similar dispersion characteristics for uniform, linear finite element discretizations.

A global convergence analysis of the Galerkin/least-squares method for the reduced wave equation in the entire range of acoustic phenomena, with error bounds obtained for the case of unresolved waves, guarantees good performance of the method on configurations of practical interest. By virtue of employing DtN boundary conditions, convergence of the numerical solution to the exact solution is with mesh refinement, without expanding the computational domain. Numerical calculations confirm the performance of these formulations for general multi-dimensional configurations.

This work clearly demonstrates that finite element methods are economically competitive with boundary element methods for obtaining solutions to problems of time-harmonic acoustics. Despite the fact that boundary elements need less equations to discretize the same physical problem, the structure possessed by the finite element equations often leads to an overall computational advantage. In the context of direct solution techniques, finite element methods are more cost-effective for smaller problems and boundary element methods gain a computational edge for relatively large problems. The symmetry and bandedness of the matrices that emanate from finite elements bring the crossover very near, and at times beyond, the limit of problem size to which direct solvers are applicable, rendering the direct solution of finite element equations more economical in most of the range of problems on which direct solvers are employed. As a rule, iterative solution techniques are applicable to large-scale problems. For iterative solvers, we found boundary elements to be more economical in the lower part of the problem-size range, and finite elements on the higher end of the scale. By effective utilization of the element-based data structure inherent in finite elements the crossover is lowered sufficiently to cause the range in which finite elements are more economical to coincide with most of the range in which iterative solvers are practical. To summarize, in the examples considered herein, we found finite element methods to be more cost-effective than boundary element methods within the range

of applicability of each solution technique.

Comparing the two solution strategies demonstrates that efficient implementation of iterative techniques has the potential of being more cost-effective for all problems of interest, as long as the equations are well-conditioned, motivating wider acceptance of iterative strategies. Nevertheless, we expect direct solvers, by virtue of their reliability and predictability, to be retained in commercial codes for relatively small problem-size applications. This work indicates that unlike many traditional numerical applications, set-up costs may constitute a significant portion of the computational expense, pointing to opportunities for considerable savings by addressing these issues alongside economizing equation-solving strategies.

By and large, the results of this study lead us to conclude that the use of boundary element techniques for this class of problems, to the exclusion of other methods, cannot be supported solely on the basis of cost. The only clear-cut advantage boundary elements hold over finite elements appears to be in boundary discretization vs. domain discretization. In three-dimensional problems, the resulting simplification of mesh generation is indeed substantial. However, the general-purpose applicability, robustness and mathematical structure, and overall flexibility of finite element methods (in allowing such tradeoffs as reducing wave number restrictions at added computational cost by simply appending layers of elements to the mesh) highlight their attractiveness, justifying further development of effective finite element methods to complement prevalent boundary element methods.

Numerical results presented demonstrate the superiority of QMR over other gradient-type iterative methods for solving problems in acoustics. The hierarchical basis preconditioner, based on a careful selection of the associated multilevel splitting, and employed in conjunction with QMR results in a very efficient iterative strategy for solving large-scale acoustics problems on massively parallel computers. Current results are based on the effectiveness of these algorithms for uncoupled problems in two-dimensions. It is expected that the iterative solver and the proposed preconditioner will also prove effective for the coupled problem. Extension to three-dimensional problems needs further investigation.

Key technologies needed for adaptive analysis were presented, with results showing significant computational efficiency engendered through adaptivity. A residual-based a posteriori error estimator was presented for both the Galerkin and Galerkin Least-Squares finite element formulations of the Helmholtz equation. The error estimator is an upper bound on the L_2 norm of the error; the use of this norm is important since the Helmholtz operator lacks positive-definiteness, preventing the use of an energy norm. An adaptive strategy was outlined which produces an element size distribution from the estimated error distribution. In combination with the advancing front mesh generator of Peraire [122], these technologies were implemented for the problem of non-uniform radiation from a rigid infinite circular cylinder, with $ka = 2\pi$. Optimal convergence rates were obtained for both uniform and adaptive mesh refinement. However, the adaptive meshes required over three times fewer elements for a given level of accuracy. These results were translated into a cost savings, in terms of both computation and storage, based on the cost of a direct solver. Relative to Galerkin computations on a uniform mesh, adaptivity was shown to be twenty times more

efficient in terms of computation time and over eight times more efficient in terms of required storage. The combination of GLS and adaptivity produced a savings of a factor of forty in computation time.

The Galerkin/Gradient Least-squares member of the family of Galerkin/Generalized Least-squares (GGLS) methods was applied to the solution of Timoshenko beam problems. This method was designed for optimality with regard to wave propagation characteristics. Results of the implementation of this method demonstrate its superiority over standard methods for the steady-state beam vibration problem. This new method results in a fivefold decrease in the required minimum discretization over the selective reduced integration element with a consistent mass approximation. It was shown that the selective reduced integrated element and a modified version of selective reduced integration with mass lumping can both be considered GGLS methods. Other variants of GGLS can be formed by different selection of the τ's. The use of GGLS methods to enhance the accuracy of the approximation to fluid-loaded structures has garnered significant benefits. The application of these methods for more complicated geometries and three dimensional calculations is an area of future work.

A new space-time finite element method for solution of the transient structural acoustics problem in exterior domains was presented. The formulation is based on a new time-discontinuous Galerkin/Least-squares variational equation for both the structure and the acoustic fluid together with their interaction. The resulting space-time algorithm gives for the first time a general solution to the fundamental problem of constructing a finite element method for transient structural acoustics with unstructured meshes in space-time and the desired combination of good stability and high accuracy.

Desirable attributes of the new computational method for transient structural acoustics include a natural framework for the design of rigorous *a posteriori* error estimates for self-adaptive solution strategies for unstructured space-time discretizations, and the implementation of high-order accurate time-dependent non-reflecting boundary conditions. Furthermore, through the use of acoustic velocity potential and structural displacement as the solution variables, the space-time method is unconditionally stable and converges at an optimal rate in a norm which is stronger than the total energy norm. High-order accuracy is obtained simply by raising the order of the space-time polynomial basis functions; both standard nodal interpolation and hierarchical shape functions are accommodated.

New time-dependent non-reflecting boundary conditions which are exact for the first N spherical wave harmonics have been developed for the scalar wave equation in three space dimensions. Two new sequences of time-dependent non-reflecting boundary operators were derived; the first involves both time and spatial derivatives (local in time and local in space version), and the second involves time derivatives yet retains a spatial integral (local in time and nonlocal in space version). The development of these boundary conditions began with the truncated Dirichlet-to-Neumann (DtN) map in the frequency domain. Time-dependent boundary conditions were obtained by an inverse Fourier transform. The time-discontinuous Galerkin space-time formulation provides a natural variational setting for the incorporation of these local in time boundary conditions.

Numerical solutions obtained for the time-dependent acoustic radiation from a nonconcentric sphere demonstrated the improved accuracy that results from the implementation of the high-order non-reflecting boundary conditions in the space-time variational formulation. In particular, results confirm the superiority of the second-order local non-reflecting boundary condition $\mathbf{S}_2$, in comparison to the first-order $\mathbf{S}_1$ boundary condition. It has also been demonstrated that with proper usage, the second-order non-reflecting boundary condition $\mathbf{S}_2$, when implemented in the space-time finite element method, is sufficiently accurate to capture the important physics associated with a complicated transient scattering problem involving some rather severe geometric and time scales.

This work has concentrated on the computation of solutions to problems of structural acoustics. We expect Galerkin/least-squares finite element methods with DtN boundary conditions to provide a suitable framework for obtaining numerical solutions to related exterior problems, such as electromagnetic waves. Examining such opportunities may be a thrust of future work.

Acknowledgment

This research was supported by the U.S. Office of Naval Research under Contracts N00014-92-J-1774, N00014-89-J-1951, N00014-89-K-0027 and N00014-88-K-0446. Isaac Harari was also supported during a portion of this work by the Center for Absorption in Science, Ministry of Immigrant Absorption, State of Israel.

The authors wish to thank Najib Abboud, Paul Barbone, Ralph Kleinman and Arif Masud for numerous helpful discussions; Louise Couchman and Al Tucker for raising many of the issues addressed in this work at ONR/DARPA Structural Acoustics review meetings; Avi Elazar and Eyal Shmueli for computing the conditioning of the coefficient matrices; Dan Givoli for his comments and for the use of his modification to the DLEARN finite element code for the reduced wave equation with DtN boundary conditions; and Ken Morgan and Jaime Peraire for use of their mesh generator.

Bibliography

[1] N. N. Abboud. *A Mixed Finite Element Formulation for the Transient and Harmonic Exterior Fluid-structure Interaction Problem.* PhD thesis, Stanford University, 1990.

[2] N. N. Abboud and P. M. Pinsky. Finite element solution and dispersion analysis for the transient structural acoustics problem. *Applied Mechanics Reivews*, 43:381–388, 1990.

[3] N. N. Abboud and P. M. Pinsky. Finite element dispersion analysis for the three-dimensional second-order scalar wave equation. *International Journal for Numerical Methods in Engineering*, 35:1183–1218, 1992.

[4] M. Ainsworth and J. T. Oden. A procedure for a posteriori error estimation for *h-p* finite element methods. *Computer Methods in Applied Mechanics and Engineering*, 101:73–96, 1992.

[5] M. Ainsworth and J. T. Oden. A unified approach to a posteriori error estimation using element residual methods. *Numerische Mathematik*, 65:23–50, 1993.

[6] S. Amini, C. Ke, and P. J. Harris. Iterative solution of boundary element equations for the exterior Helmholtz problem. In R. J. Bernhard and R. F. Keltie, editors, *Numerical Techniques in Acoustic Radiation, NCA Vol. 6*, pages 123–128. ASME, New York, 1989.

[7] D. N. Arnold. Discretization of a model parameter dependent problem. *Numerische Mathematik*, 37:405–421, 1981.

[8] R. J. Astley, G. J. Macaulay, and J.-P. Coyette. Mapped wave envelope elements for acoustical radiation and scattering. *Journal of Sound and Vibration*, 170:97–118, 1994.

[9] O. Axelsson. Conjugate gradient type methods for unsymmetric and inconsistent systems of linear equations. *Linear Algebra and its Applications*, 29:1–16, 1980.

[10] I. Babuška and W. C. Rheinboldt. A posteriori error estimates for the finite element method. *International Journal for Numerical Methods in Engineering*, 12:1597–1615, 1978.

[11] R. E. Bank and A. Weiser. Some a posteriori error estimators for elliptic partial differential equations. *Mathematics of Computation*, 44:283–301, 1985.

[12] H. J. Barbosa and T. J. R. Hughes. The finite element method with Lagrange multipliers on the boundary: Circumventing the Babuška-Brezzi condition. *Computer Methods in Applied Mechanics and Engineering*, 85:109–128, 1991.

[13] K.-J. Bathe and E. N. Dvorkin. A four-node plate bending element based on Mindlin/Reissner theory and a mixed interpolation. *International Journal for Numerical Methods in Engineering*, 21:367–383, 1985.

[14] A. Bayliss, C. Goldstein, and E. Turkel. An iterative method for the Helmholtz equation. *Journal of Computational Physics*, 49:443–457, 1983.

[15] A. Bayliss and E. Turkel. Radiation boundary conditions for wave-like equations. *Communications in Pure and Applied Mathematics*, 33:707–725, 1980.

[16] H. Berryman, J. Saltz, W. Gropp, and R. Mirchandaney. Krylov methods preconditioned with incompletely factored matrices on the CM-2. Technical Report 89-54, NASA Langley Research Center, ICASE, Hampton, VA, 1989.

[17] P. Bettess. Infinite elements. *International Journal for Numerical Methods in Engineering*, 11:53–64, 1977.

[18] P. Bettess. Operation counts for boundary integral and finite element methods. *International Journal for Numerical Methods in Engineering*, 17:306–308, 1981.

[19] A. J. Burton and G. F. Miller. The application of integral equation methods to the numerical solution of some exterior boundary-value problems. *Proceedings of the Royal Society of London*, A. 323:201–210, 1971.

[20] G. Chertock. Integral equation methods in sound radiation and scattering from arbitrary structures. Research and Development Report 3538, David W. Taylor Naval Ship Research and Development Center, Bethesda, Maryland, 1971.

[21] P. G. Ciarlet. *The Finite Element Method for Elliptic Problems.* North-Holland, Amsterdam, 1978.

[22] L. G. Copely. Fundamental results concerning integral representations in acoustic radiation. *The Journal of the Acoustical Society of America*, 44:28–32, 1968.

[23] R. Courant and D. Hilbert. *Methods of Mathematical Physics*, volume I. Interscience Publishers, New York, 1953.

[24] J.-P. Coyette and K. R. Fyfe. An improved formulation for acoustic eigenmode extraction from boundary element models. In R. J. Bernhard and R. F. Keltie, editors, *Numerical Techniques in Acoustic Radiation, NCA Vol. 6*, pages 139–144. ASME, New York, 1989.

[25] D. G. Crighton. The free and forced waves on a fluid-loaded elastic plate. *Journal of Sound and Vibration*, 63:225–235, 1979.

[26] K. A. Cunefare, G. Koopman, and K. Brod. A boundary element method for acoustic radiation valid for all wavenumbers. *The Journal of the Acoustical Society of America*, 85:39–48, 1989.

[27] J. Douglas, Jr and J. Wang. An absolutely stabilized finite element method for the Stokes flow. *Mathematics of Computation*, 52:495–508, 1989.

[28] K. Eriksson and C. Johnson. Adaptive finite element methods for linear parabolic problems. *SIAM Journal on Applied Mathematics*, 28:43–77, 1991.

[29] G. C. Everstine and A. Quezon. User's guide to the coupled NASTRAN/Helmholtz equation capability (NASHUA) for acoustic radiation and scattering. NSRDC Technical Report DTRC CMLD-88/03, David Taylor Research Center, Bethesda, Maryland, 1988.

[30] F. Feng. Asymptotic radiation conditions for reduced wave equation. *Journal of Computational Mathematics*, 2, 1984.

[31] R. M. Ferencz. *Element-by-element Preconditioning Techniques for Large-scale, Vectorized Finite Element Analysis in Nonlinear Solid and Structural Analysis.* PhD thesis, Stanford University, 1989.

[32] R. Fletcher. Conjugate gradient methods for indefinite systems. In G. A. Watson, editor, *Proc. Dundee Conference on Numerical Analysis, 1975, Lecture Notes in Mathematics 506*, pages 73–89, Berlin, 1976. Springer-Verlag.

[33] L. P. Franca. Analysis and finite element approximation of compressible and incompressible linear isotropic elasticity based upon a variational principle. *Computer Methods in Applied Mechanics and Engineering*, 76:259–273, 1989.

[34] L. P. Franca and E. G. Dutra do Carmo. The Galerkin gradient least-squares method. *Computer Methods in Applied Mechanics and Engineering*, 74:41–54, 1989.

[35] L. P. Franca, S. L. Frey, and T. J. R. Hughes. Stabilized finite element methods: I. Application to the advective-diffusive model. *Computer Methods in Applied Mechanics and Engineering*, 95:253–276, 1992.

[36] L. P. Franca and T. J. R. Hughes. Two classes of mixed finite element methods. *Computer Methods in Applied Mechanics and Engineering*, 69:89–129, 1988.

[37] L. P. Franca and R. Stenberg. Error analysis of some Galerkin/least-squares methods for the elasticity equations. *SIAM Journal on Numerical Analysis*, 28:1680–1697, 1991.

[38] R. W. Freund. Transpose-Free quasi-minimal residual methods for non-Hermitian linear systems. Numerical Analysis 92-07, AT&T, Bell Laboratories. 1992.

[39] R. W. Freund and N. M. Nachtigal. QMR: A quasi-minimal residual method for non-Hermitian linear systems. *Numerische Mathematik*, 60:315–339, 1991.

[40] D. Givoli. *Numerical Methods for Problems in Infinite Domains.* Elsevier, Amsterdam, 1992.

[41] D. Givoli and J. B. Keller. A finite element method for large domains. *Computer Methods in Applied Mechanics and Engineering*, 76:41–66, 1989.

[42] D. Givoli and J. B. Keller. Non-reflecting boundary conditions for elastic waves. *Wave Motion*, 12:261–279, 1990.

[43] D. Givoli and J. B. Keller. Special finite elements for use with high-order boundary conditions. *Computer Methods in Applied Mechanics and Engineering*, 1994. Accepted.

[44] D. Givoli, I. Patlashenko, and J. B. Keller. High order boundary conditions and finite elements for infinite domains. TAE Report 735, Department of Aerospace Engineering, Technion — Israel Institute of Technology, Haifa, Israel, 1995. Submitted to *Computer Methods in Applied Mechanics and Engineering*.

[45] G. H. Golub and C. F. van Loan. *Matrix Computations.* John Hopkins, Baltimore, 1983.

[46] P. P. Goswami, T. J. Rudolphi, F. J. Rizzo, and D. J. Shippy. A boundary element model for acoustic-elastic interaction with applications in ultrasonic NDE. *Journal of Nondestructive Evaluation*, 9:101–112, 1990.

[47] K. Graff. *Waves in Elastic Solids.* Ohio State Univ. Press, Cols., OH, 1975.

[48] A. Greenbaum, C. Li, and H. Z. Chao. Parallelizing preconditioned conjugate gradient algorithms. *Computer Physics Communications*, 53:295–309, 1989.

[49] K. Grosh. *Design and Analysis of Computational Methods for Structural Acoustics.* PhD thesis, Stanford University, 1994.

[50] K. Grosh and P. M. Pinsky. New generalized Galerkin least squares finite element methods for wave propagation in timoshenko beams. In *SIAM Second Intl. Conf. on Math. and Numer. Aspects of Wave Prop., Univ. of Delaware*, pages 237–245, 1993.

[51] K. Grosh and P. M. Pinsky. Complex wave-number dispersion analysis of Galerkin and Galerkin least squares methods for fluid-loaded plates. *Computer Methods in Applied Mechanics and Engineering*, 113:67–98, 1994.

[52] K. Grosh and P. M. Pinsky. Design of Galerkin generalized least squares methods for Timoshenko beams. *Computer Methods in Applied Mechanics and Engineering*, 1995. Accepted.

[53] M. J. Grote and J. B. Keller. On nonreflecting boundary conditions. *Journal of Computational Physics*, 1995. Submitted.

[54] H. R. Hall and R. J. Bernhard. Total least squares solutions to acoustic boundary element models. In R. J. Bernhard and R. F. Keltie, editors, *Numerical Techniques in Acoustic Radiation, NCA Vol. 6*, pages 145–152. ASME, New York, 1989.

[55] P. Hansbo and C. Johnson. Adaptive streamline diffusion methods for compressible flow using conservation variables. *Computer Methods in Applied Mechanics and Engineering*, 87:267–280, 1991.

[56] I. Harari. *Computational Methods for Problems of Acoustics with Particular Reference to Exterior Domains.* PhD thesis, Stanford University, 1991.

[57] I. Harari and T. J. R. Hughes. Finite element methods for the Helmholtz equation in an exterior domain: Model problems. *Computer Methods in Applied Mechanics and Engineering*, 87:59–96, 1991.

[58] I. Harari and T. J. R. Hughes. Analysis of continuous formulations underlying the computation of time-harmonic acoustics in exterior domains. *Computer Methods in Applied Mechanics and Engineering*, 97:103–124, 1992.

[59] I. Harari and T. J. R. Hughes. A cost comparison of boundary element and finite element methods for problems of time-harmonic acoustics. *Computer Methods in Applied Mechanics and Engineering*, 97:77–102, 1992.

[60] I. Harari and T. J. R. Hughes. Galerkin/least-squares finite element methods for the reduced wave equation with non-reflecting boundary conditions in unbounded domains. *Computer Methods in Applied Mechanics and Engineering*, 98:411–454, 1992.

[61] I. Harari and T. J. R. Hughes. What are C and h?: Inequalities for the analysis and design of finite element methods. *Computer Methods in Applied Mechanics and Engineering*, 97:157–192, 1992.

[62] I. Harari and T. J. R. Hughes. Stabilized finite element methods for steady advection-diffusion with production. *Computer Methods in Applied Mechanics and Engineering*, 114:165–191, 1994.

[63] I. Harari and T. J. R. Hughes. Studies of domain-based formulations for computing exterior problems of acoustics. *International Journal for Numerical Methods in Engineering*, 37:2935–2950, 1994.

[64] G. Hauke and T. J. R. Hughes. A unified approach to compressible and incompressible flows. *Computer Methods in Applied Mechanics and Engineering*, 113:389–395, 1994.

[65] M. R. Hestenes and E. Steifel. Methods of conjugate gradients for solving linear systems. *Journal of Research of the National Bureau of Standards*, 49:409–436, 1952.

[66] H. M. Hilber, T. J. R. Hughes, and R. L. Taylor. Improved numerical dissipation for time integration algorithms in structural dynamics. *Earthquake Engineering and Structural Dynamics*, 5:283–292, 1977.

[67] G. C. Hsiao, R. E. Kleinman, R.-X. Li, and P. M. van den Berg. Residual error — a simple and sufficient estimate of actual error in solutions of boundary integral equations. In C. B. S. Grilli and A.-D. Cheng, editors, *Proceedings of the Fifth International Conference on Boundary Element Technology, Vol. 1: Fluid and Potential Problems*, pages 73–83. (Computational Mechanics Publications, Boston, MA), 1990.

[68] H. Huang, G. C. Everstine, and Y. F. Wang. Retarded potential techniques for the analysis of submerged structures impinged by weak shock waves. In T. Belytschko and T. L. Geers, editors, *Computational Methods for Fluid-Structure Interaction Problems*, volume AMD Vol. 26, pages 83–93. ASME, 1977.

[69] T. J. R. Hughes. *The Finite Element Method: Linear Static and Dynamic Finite Element Analysis.* Prentice-Hall, Englewood Cliffs, NJ, 1987.

[70] T. J. R. Hughes. Recent progress in the development and understanding of SUPG methods with special reference to the compressible Euler and Navier-Stokes equations. *International Journal for Numerical Methods in Engineering*, 7:1261–1275, 1987.

[71] T. J. R. Hughes and F. Brezzi. On drilling degrees of freedom. *Computer Methods in Applied Mechanics and Engineering*, 72:105–121, 1989.

[72] T. J. R. Hughes and A. Brooks. A multi-dimensional upwind scheme with no crosswind diffusion. In T. J. R. Hughes, editor, *Finite Element Methods for Convection Dominated Flows, AMD Vol. 34*, pages 19–35. ASME, New York, 1979.

[73] T. J. R. Hughes and L. P. Franca. A new finite element formulation for computational fluid dynamics: VII. The Stokes problem with various well-posed boundary conditions: Symmetric formulations that converge for all velocity/pressure spaces. *Computer Methods in Applied Mechanics and Engineering*, 65:85–96, 1987.

[74] T. J. R. Hughes and L. P. Franca. A mixed finite element method formulation for Reissner-Mindlin plate theory: Uniform convergence of all higher-order spaces. *Computer Methods in Applied Mechanics and Engineering*, 67:223–240, 1988.

[75] T. J. R. Hughes, L. P. Franca, and M. Balestra. A new finite element formulation for computational fluid dynamics: V. Circumventing the Babuška-Brezzi condition: A stable Petrov-Galerkin formulation of the Stokes problem accommodating equal-order interpolations. *Computer Methods in Applied Mechanics and Engineering*, 59:85–99, 1986.

[76] T. J. R. Hughes, L. P. Franca, and G. M. Hulbert. A new finite element formulation for computational fluid dynamics: VIII. The Galerkin/least-squares method for advective-diffusive equations. *Computer Methods in Applied Mechanics and Engineering*, 73:173–189, 1989.

[77] T. J. R. Hughes and G. M. Hulbert. Space-time finite element methods for elastodymamics: Formulations and error estimates. *Computer Methods in Applied Mechanics and Engineering*, 66:339–363, 1988.

[78] T. J. R. Hughes and M. Mallet. A new finite element formulation for computational fluid dynamics: III. The generalized streamline operator for multidimensional advective-diffusive systems. *Computer Methods in Applied Mechanics and Engineering*, 58:305–328, 1986.

[79] T. J. R. Hughes and F. Shakib. Computational aerodynamics and the finite element method. In *AIAA 25th Aerospace Sciences Meeting*, Reno, Nevada, 1988.

[80] T. J. R. Hughes and T. E. Tezduyar. Finite elements based upon Mindlin plate theory with particular reference to the four-node bilinear isoparametric element. *ASME Journal of Applied Mechanics*, 46:587–596, 1981.

[81] G. M. Hulbert. *Space-time Finite Element Methods for Second-order Hyperbolic Equations.* PhD thesis, Stanford University, 1989.

[82] G. M. Hulbert and T. J. R. Hughes. Space-time finite element methods for second-order hyperbolic equations. *Computer Methods in Applied Mechanics and Engineering*, 84:327–348, 1990.

[83] B. M. Irons. A frontal solution program for finite element analysis. *International Journal for Numerical Methods in Engineering*, 2:177–202, 1970.

[84] K. Jansen, Z. Johan, and T. J. R. Hughes. Implementation of a one-equation turbulence model within a stabilized finite element formulation of a symmetric advective-diffusive system. *Computer Methods in Applied Mechanics and Engineering*, 105:405–433, 1993.

[85] R. V. Jasti. *Mixed Finite Element Methods for Structural Acoustics.* PhD thesis, Stanford University, 1992.

[86] Z. Johan, T. J. R. Hughes, and F. Shakib. A globally convergent matrix-free algorithm for implicit time-marching schemes arising in finite element analysis

in fluids. *Computer Methods in Applied Mechanics and Engineering*. 87:281–304, 1991.

[87] C. Johnson. Streamline diffusion methods for problems in fluid mechanics. In R. H. Gallagher, G. F. Carey, J. T. Oden, and O. C. Zienkiewicz, editors, *Finite Element Methods in Fluids*, volume 6, pages 251–261. Wiley, Chichister, 1986.

[88] C. Johnson. *Numerical Solutions of Partial Differential Equations by the Finite Element Method.* Cambride University Press, Cambridge, 1987.

[89] C. Johnson. Adaptive finite element methods for diffusion and convection problems. *Computer Methods in Applied Mechanics and Engineering*, 82:301–322, 1990.

[90] C. Johnson. Finite element methods for flow problems. Technical Report 787, AGARD, 7 Rue Ancelle, 92299 Neuilly sur Seine, France, 1992.

[91] C. Johnson. Discontinuous Galerkin finite element methods for second order hyperbolic problems. *Computer Methods in Applied Mechanics and Engineering*, 107:117–129, 1993.

[92] C. Johnson and P. Hansbo. Adaptive finite element methods in computational mechanics. *Computer Methods in Applied Mechanics and Engineering*, 101:143–181, 1992.

[93] C. Johnson, U. Nävert, and J. Pitkäranta. Finite element methods for linear hyperbolic problems. *Computer Methods in Applied Mechanics and Engineering*, 45:285–312, 1984.

[94] C. Johnson and J. Saranen. Streamline diffusion methods for the incompressible Euler and Navier-Stokes equations. *Mathematics of Computation*, 47:1–18, 1986.

[95] D. S. Jones. Integral equations for the exterior acoustic problem. *The Quarterly Journal of Mechanics and Applied Mathematics*, 27:129–142, 1974.

[96] M. C. Junger and D. Feit. *Sound and Structures.* M.I.T. Press, Cambridge, MA, 1986.

[97] A. Karafiat, J. T. Oden, and P. Geng. Variational formulations and *hp*-boundary element approximations for hypersingular integral equations for Helmholtz exterior boundary-value problems in two dimensions. *International Journal of Engineering Science*, 31:649–672, 1993.

[98] J. B. Keller and D. Givoli. Exact non-reflecting boundary conditions. *Journal of Computational Physics*, 82:172–192, 1989.

[99] D. W. Kelly. The self-equilibration of residuals and complementary a posteriori error estimates in the finite element method. *International Journal for Numerical Methods in Engineering*, 20:1491–1506, 1984.

[100] S. M. Kirkup. *Solution of Exterior Acoustic Problems by the Boundary Element Method.* PhD thesis, Brighton Polytechnic. Brighton, U.K., 1989.

[101] R. E. Kleinman and G. F. Roach. Boundary integral equations for the three-dimensional Helmholtz equation. *SIAM Review*, 16:214–236, 1974.

[102] R. E. Kleinman, G. F. Roach, L. S. Scheutz, and J. Shirron. An iterative solution to acoustic scattering by rigid objects. *The Journal of the Acoustical Society of America*, 84:385–391, 1988.

[103] G. Krishnasamy, L. W. Schmerr, T. J. Rudolphi, and F. J. Rizzo. Hypersingular boundary intergal equations: Some applications in acoustic and elastic wave scattering. *ASME Journal of Applied Mechanics*, 57:404–414, 1990.

[104] V. D. Kupradze. Fundamental problems in the mathematical theory of diffraction (steady state processes). NBS Report 2008, National Bureau of Standards, 1952. Translated by C. D. Benster.

[105] H. Lamb. *Hydrodynamics.* Cambridge University Press, Cambridge, sixth edition, 1932.

[106] P. Lesaint and P. A. Raviart. On a finite element method for solving the neutron transport equation. In C. de Boor, editor, *Mathematical Aspects of Finite Elements in Partial Differential Equations*, pages 89–123, New York, 1974. Academic Press.

[107] Y. Liu and F. J. Rizzo. A weakly-singular form of the hypersingular boundary integral equation applied to 3-D acoustic wave problems. *Computer Methods in Applied Mechanics and Engineering*, 96:271–287, 1992.

[108] A. F. D. Loula, T. J. R. Hughes, L. P. Franca, and I. Miranda. Mixed Petrov-Galerkin methods for the Timoshenko beam problem. *Computer Methods in Applied Mechanics and Engineering*, 63:133–154, 1987.

[109] Y. P. Lu. The application of retarded potential techniques to submerged dynamic structural systems. In R. P. Shaw and W. Pilkey, editors, *Proceedings of the 2nd Int. Symposium Innovative Numerical Analysis for the Applied Engineering Sciences*, pages 59–68, 1980.

[110] G. D. Manolis and D. E. Beskos. Dynamic response of lined tunnels by an isoparametric boundary element method. *Computer Methods in Applied Mechanics and Engineering*, 36:291–307, 1983.

[111] W. J. Mansur and C. A. Brebbia. Formulation of the boundary element method for transient problems governed by the scalar wave equation. *Applied Mathematical Modelling*, 6:307–311, 1982.

[112] W. J. Mansur and C. A. Brebbia. Further developments on the solution of the transient scalar wave equation. In C. A. Brebbia, editor, *Topics in Boundary Element Research*, volume 2, Berlin, 1984. Springer-Verlag.

[113] J. A. Meijerink and H. A. van der Vorst. An iterative solution method for linear systems of which the coefficient matrix is a symmetric M-matrix. *Mathematics of Computation*. 31:148–162, 1977.

[114] P. M. Morse and H. Feshbach. *Methods of Theoretical Physics*. volume 2. McGraw-Hill, New York, 1953.

[115] H. C. Neilson, G. C. Everstine, and Y. F. Wang. Transient response of a submerged fluid-coupled double-walled shell structure to a pressure pulse. *The Journal of the Acoustical Society of America*, 70(6):1776–1782, 1981.

[116] N. M. Newmark. A method of computation for structural dynamics. *Journal of Engineering Mechanics, ASCE*, pages 67–94, 1959.

[117] J. T. Oden, L. Demkowicz, and J. K. Bennighof. Fluid-structure interaction in underwater acoustics. *Applied Mechanics Reivews*, 43:374–380, 1990.

[118] J. T. Oden, L. Demkowicz, W. Rachowicz, and T. A. Westermann. Toward a universal *h-p* adaptive finite element strategy, part 2. a posteriori error estimation. *Computer Methods in Applied Mechanics and Engineering*, 77:113–180, 1989.

[119] C. Paige and M. Saunders. Solution of sparse indefinite systems of linear equations. *SIAM Journal on Numerical Analysis*, 12:617–629, 1975.

[120] K. C. Park and D. L. Flaggs. A Fourier analysis of spurious mechanisms and locking in the finite element method. *Computer Methods in Applied Mechanics and Engineering*, 46:65–81, 1984.

[121] K. C. Park and D. L. Flaggs. A symbolic Fourier synthesis of a one-point integrated quadrilateral plate element. *Computer Methods in Applied Mechanics and Engineering*, 48:805–812, 1985.

[122] J. Peraire, M. Vahdati, K. Morgan, and O. C. Zienkiewicz. Adaptive remeshing for compressible flow computations. *Journal of Computational Physics*, 72:449–466, 1987.

[123] P. M. Pinsky and N. N. Abboud. Transient finite element analysis of the exterior structural acoustics problem. In R. J. Bernhard and R. F. Keltie, editors, *Numerical Techniques in Acoustic Radiation, NCA Vol. 6*, pages 35–48. ASME, New York, 1989.

[124] P. M. Pinsky and N. N. Abboud. Finite element solution of the transient exterior structural acoustics problem based on the use of radially asymptotic boundary operators. *Computer Methods in Applied Mechanics and Engineering*, 85:311–348, 1991.

[125] P. M. Pinsky and L. L. Thompson. Accuracy of local non-reflecting boundary conditions for time-dependent structural acoustics. In *Structural Acoustics*, volume NCA-Vol.12/AMD-Vol.128, pages 153–160. ASME, 1991.

[126] P. M. Pinsky, L. L. Thompson, and N. N. Abboud. Local high order radiation boundary conditions for the two-dimensional time-dependent structural acoustics problem. *The Journal of the Acoustical Society of America*. 91(3):1320–1335, 1992.

[127] Y. Saad and M. H. Schultz. GMRES: A generalized minimal residual algorithm for solving nonsymmetric linear systems. *SIAM Journal on Scientific and Statistical Computing*, 7:856–869, 1986.

[128] A. Safjan, L. Demkowicz, and J. T. Oden. Adaptive finite element methods for hyperbolic systems with application to transient acoustics. *International Journal for Numerical Methods in Engineering*, 32:677–707, 1991.

[129] A. H. Schatz. An observation concerning Ritz-Galerkin methods with indefinite bilinear forms. *Mathematics of Computation*, 28:959–962, 1974.

[130] H. A. Schenck. Improved integral formulation for acoustic radiation problems. *The Journal of the Acoustical Society of America*, 44:41–58, 1968.

[131] J. F. M. Scott. The free modes of propagation of an infinite fluid-loaded shell thin cylindrical shell. *Journal of Sound and Vibration*, 125:241–290, 1988.

[132] C. Seren and S. I. Hayek. Acoustic radiation from an insonified elastic plate with a line discontinuity. *The Journal of the Acoustical Society of America*, 86:195–209, 1989.

[133] A. F. Seybert and T. K. Rengarajan. The use of CHIEF to obtain unique solutions for acoustic radiation using boundary integral equations. *The Journal of the Acoustical Society of America*, 81:1299–1306, 1987.

[134] F. Shakib. *Finite Element Analysis of the Compressible Euler and Navier-Stokes Equations*. PhD thesis, Stanford University, 1988.

[135] F. Shakib, T. J. R. Hughes, and Z. Johan. A multi-element group preconditioned GMRES algorithm for nonsymmetric systems arising in finite element analysis. *Computer Methods in Applied Mechanics and Engineering*, 75:415–456, 1989.

[136] F. Shakib, T. J. R. Hughes, and Z. Johan. A new finite element formulation for computational fluid dynamics: X. the compressible Euler and Navier-Stokes equations. *Computer Methods in Applied Mechanics and Engineering*, 89:141–219, 1991.

[137] R. P. Shaw. Integral equation methods in acoustics. In C. A. Brebbia, editor, *Boundary Elements X*, volume 4, pages 221–244, Berlin, 1988. Springer-Verlag.

[138] D. J. Silvester and N. Kechkar. Stabilised bilinear-constant velocity-pressure finite elements for the conjugate gradient solution of the Stokes problem. *Computer Methods in Applied Mechanics and Engineering*, 79:71–86, 1990.

[139] I. Stakgold. *Boundary Value Problems of Mathematical Physics*. volume II. Macmillan, New York, 1968.

[140] J. R. Stewart. *Adaptive Finite Element Methods for the Helmholtz Equation in Exterior Domains*. PhD thesis, Stanford University, Stanford, CA, 1995.

[141] G. Strang and G. J. Fix. *An Analysis of the Finite Element Method*. Prentice-Hall, Englewood Cliffs, NJ, 1973.

[142] R. L. Taylor, E. L. Wilson, and S. J. Sackett. Direct solution of equations by frontal and variable band, active column methods. In W. Wunderlich, E. Stein, and K.-J. Bathe, editors, *Nonlinear Finite Element Analysis in Structural Mechanics*, pages 521–552. Springer-Verlag, Berlin, 1981.

[143] L. L. Thompson. *Design and Analysis of Space-Time and Galerkin Least-Squares Finite Element Methods for Fluid-Structure Interaction in Exterior Domains*. PhD thesis, Stanford University, April 1994.

[144] L. L. Thompson and P. M. Pinsky. Complex wavenumber Fourier analysis of hierarchic p-version and spectral elements. SUDAM Report 93-1, Stanford University, January 1993.

[145] L. L. Thompson and P. M. Pinsky. A multi-dimensional Galerkin least-squares finite element method for time-harmonic wave propagation. In e. a. R. Kleinman, editor, *Second International Conference on Mathematical and Numerical Aspects of Wave Propagation*, pages 444–451. SIAM, 1993.

[146] L. L. Thompson and P. M. Pinsky. New space-time finite element methods for fluid-structure interaction in exterior domains. In *Computational Methods for Fluid/Structure Interaction, AMD Vol. 178*, pages 101–120. ASME, New York, 1993.

[147] L. L. Thompson and P. M. Pinsky. Complex wavenumber Fourier analysis of the p-version finite element method. *Computational Mechanics*, 13(4):255–275, 1994.

[148] L. L. Thompson and P. M. Pinsky. A new space-time finite element method for transient structural acoustics. *The Journal of the Acoustical Society of America*, 1994. Submitted.

[149] L. L. Thompson and P. M. Pinsky. A space-time finite element method for structural acoustics in infinite domains, part I: Formulation, stability, and convergence. *Computer Methods in Applied Mechanics and Engineering*, 1994. Submitted.

[150] L. L. Thompson and P. M. Pinsky. A space-time finite element method for structural acoustics in infinite domains, part II: Exact time-dependent non-reflecting boundary conditions. *Computer Methods in Applied Mechanics and Engineering*, 1994. Submitted.

[151] L. L. Thompson and P. M. Pinsky. A space-time finite element method for the exterior structural acoustics problem: Time-dependent radiation boundary conditions in two spatial dimensions. *International Journal for Numerical Methods in Engineering*, 1994. Submitted.

[152] L. L. Thompson and P. M. Pinsky. A Galerkin least squares finite element method for the two-dimensional Helmholtz equation. *International Journal for Numerical Methods in Engineering*, 38:371–397, 1995.

[153] C. H. Wilcox. *Scattering Theory for the d'Alembert Equation in Exterior Domains*. Springer-Verlag, Berlin, 1975.

[154] E. L. Wilson. Solution of sparse stiffness matrices for structural systems. In I. S. Duff and G. W. Stewart, editors, *Sparse Martix Proceedings 1978*, pages 1–24, Philadelphia, 1979. SIAM.

[155] D. M. Young and K. C. Jea. Generalized conjugate-gradient acceleration of nonsymmetrizable iterative methods. *Linear Algebra and its Applications*, 34:159–194, 1980.

[156] H. Yserentant. Hierarchical bases of finite-element spaces in the discretization of nonsymmetric elliptic boundary value problems. *Computing*, 35:39–49, 1985.

[157] H. Yserentant. On the multi-level splitting of finite element spaces. *Numerische Mathematik*, 49:379–412, 1986.